Tectonomagmatic Controls on the Çöpler Epithermal Au and Cevizlidere Porphyry Cu-Au-Mo Deposits (Central Eastern Turkey) and the Genesis of the Porphyry-Epithermal Mineralization at the Çöpler Epithermal Au Deposit

by

Ali Imer

A thesis submitted in partial fulfillment of the requirements for the degree of

Doctor of Philosophy

Department of Earth and Atmospheric Sciences
University of Alberta

ABSTRACT

The Munzur Mountains in central eastern Turkey are an emerging belt of intrusion-related precious and base metal deposits. Two recent discoveries, the Çöpler epithermal Au and Cevizlidere porphyry Cu-Mo-Au deposits, lie 50 km apart and are located along the northern and southern margins of the Munzur Mountain range, respectively.

The Çöpler deposit is centered around shallow-level dioritic to granodioritic intrusive rocks of the Çöpler-Kabataş magmatic complex, which have been emplaced into a succession of regionally metamorphosed Late Paleozoic–Mesozoic sedimentary rocks and Mesozoic carbonate rocks. Cevizlidere is also formed in association with porphyritic diorites and granodiorites cross-cutting the Paleozoic limestones.

^{40}Ar/^{39}Ar dating of two igneous biotite samples from Çöpler yielded plateau ages of 43.75±0.26 Ma and 44.19±0.23, whereas igneous hornblende from a third sample yielded a plateau age of 44.13±0.38. These ages closely overlap with ^{40}Ar/^{39}Ar ages of hydrothermal sericite (44.44±0.28 Ma) and biotite (43.84±0.26 Ma), and Re–Os ages from two molybdenite samples (44.6±0.2 and 43.9±0.2 Ma).

Two biotite separates obtained from syn-mineral diorite porphyry from Cevizlidere yielded ^{40}Ar/^{39}Ar ages of 25.49±0.10 Ma and 25.10±0.14 Ma. ^{40}Ar/^{39}Ar age of hydrothermal biotite (24.73±0.08 Ma) and Re-Os ages of two molybdenite separates (24.90±0.10 Ma and 24.78±0.10 Ma) are slightly younger than the cooling ages of the diorite porphyry.

Geochronological data suggests that the duration of magmatic-hydrothermal activity in both districts was short-lived (<1 m.y.) and that porphyry-style mineralization developed shortly

after magma emplacement. No suitable minerals were found that could be used to date the epithermal system at Çöpler, but it is inferred to be close in age to the precursor porphyry system.

The whole-rock geochemical characteristics of the intrusive rocks from the Çöpler-Kabataş magmatic complex and Cevizlidere are consistent with derivation from subduction-modified mantle sources. Although the area is tectonically complex, regional comparisons suggest that the intrusive system at Çöpler was formed in a back-arc setting behind the Southern Neotethys arc, in response to Paleocene slab roll-back and upper-plate extension. Cevizlidere was formed in a similar tectonic setting in the late Oligocene during a period of regional extension, following a period of contractional deformation and magmatic quiescence. The kinematic switch at this time was possibly related to the break-off of the Southern Neotethys oceanic slab prior to the Arabia–Eurasia continent-continent collision, implying a pre-collisional timing for the Cevizlidere deposit.

Çöpler features a centrally-located subeconomic porphyry Cu-Au system characterized by a potassically-altered (biotite-K-feldspar-magnetite) core overprinted by a more extensive phyllic (quartz-sericite) alteration zone. The potassic alteration zone is associated with M-type hairline magnetite and B-type quartz ± magnetite ± sulfide veinlets, whereas the enveloping phyllic-altered assemblages contain abundant D-type quartz-pyrite and lesser polymetallic quartz-sulfide veinlets.

Overprinting intermediate-sulfidation epithermal mineralization is divided into two stages. Main-stage epithermal mineralization is characterized by carbonate-sulfide veinlets consisting of arsenical pyrite, arsenopyrite, marcasite, chalcopyrite, tennantite/tetrahedrite,

galena, and sphalerite. Late-stage sooty pyrite veinlets contain some realgar and orpiment and are associated with zones of extensive carbonate alteration. Manto-type carbonate-replacement zones sporadically occurring in the distal portions of the porphyry system also constitute a significant gold resource.

Polyphase brine inclusions (~47–62 wt.% NaCl equiv.) in early B-type quartz ± magnetite ± sulfide veinlets were trapped with low salinity (~3–5.5 wt.% NaCl equiv.) vapor-rich inclusions at temperatures ~390°C and at a depth of ~1.5 km under lithostatic conditions. Fluids associated with the overprinting phyllic alteration were slightly cooler (~370°C) and less saline (37–42 wt.% NaCl equiv.). Fluid inclusions in carbonate-sulfide veinlets trapped moderate salinity (4–15 wt.% NaCl equiv.) fluids at ~290°C, whereas sooty pyrite veinlets were formed from low temperature (~100°C) and low to moderate salinity (1–14 wt.% NaCl equiv.) fluids.

Combined fluid inclusion and stable isotope data indicate that the Au mineralizing system at Çöpler progressed from a high temperature porphyry system towards a relatively low temperature intermediate-sulfidation epithermal system. The early stages of epithermal mineralization developed from cooling and neutralization of predominantly magmatic-sourced hydrothermal fluids, whereas some involvement of meteoric waters was recorded during late-stage epithermal mineralization. Overall, the porphyry-epithermal system at Çöpler was structurally and lithologically controlled, and the role of carbonate cover rocks as a pressure seal and also as a neutralizing agent was critical for its formation.

PREFACE

This thesis comprises five chapters, three of which have been prepared in manuscript format. Chapter 2 has been published in Mineralium Deposita in 2013 (volume 48), whereas Chapter 3 has been published online (in June 2014) in the same journal and is pending publication in a print volume at the time of writing of this thesis. A modified version of Chapter 4 is intended to be submitted as a co-authored article.

Findings presented in this thesis are based on 5 months of fieldwork completed over three field seasons between 2006 and 2008. Fieldwork involved logging and sampling of drill core from the Çöpler and Cevizlidere deposits, geological and alteration mapping at Çöpler, and regional sampling of the igneous exposures along the eastern Taurides. Over 300 drill core samples were collected in Çöpler; another 32 drill core samples were collected from Cevizlidere, and a total of 31 outcrop samples were collected from regional exposures. Collected samples were described at the macro scale and photographed on site. Mapping at Çöpler was carried out at the scale of 1:5,000, and previously mapped (by company geologists) deposit geology was checked and revised.

I did all of the sample collection, preliminary sample preparation for lithogeochemical, radiogenic, and stable isotope analyses, and carried out petrographic, fluid inclusion, and electron microprobe work as well as data synthesis and manuscript writing. Jeremy P. Richards is the thesis advisor and the second author in all three manuscripts. He contributed to regional- and deposit-scale sampling in Çöpler in 2006 and 2007, did a preliminary site visit to the Cevizlidere prospect in 2004, and assisted in data interpretation and manuscript writing.

Robert A. Creaser (University of Alberta) is a co-author in Chapters 2 and 3 and provided Re-Os geochronological data. Terry L. Spell (University of Nevada at Las Vegas) is a co-author in Chapter 3 and provided ^{40}Ar/^{39}Ar geochronological data. Karlis Muehlenbachs (University of Alberta) is a co-author in Chapter 4 and provided stable isotope data for Chapter 4.

Geological and exploration data including deposit- and district-scale geological maps, drill logs and assays, and reserve estimate reports for the Çöpler and Cevizlidere projects were provided in digital format by Alacer Gold Corp. and Rio Tinto plc., respectively. I have modified the company maps presented in Chapters 2–4.

^{40}Ar/^{39}Ar step-heating data presented in Chapter 2 was collected by T. Ullrich at the Pacific Centre for Isotopic and Geochemical Research (PCIGR) Noble Gas Laboratory (University of British Columbia). Sulfur isotope analyses were performed by Stephen Taylor (University of Calgary) and oxygen and carbon isotope analyses of carbonate minerals were carried out by Ezgi Ünal-İmer at the Stable Isotope Laboratory of the University of Queensland (Australia). Electron microprobe analysis was performed at the University of Alberta under guidance of Sergei Matveev.

Most of the polished thin sections for transmitted and reflected light microscopic analyses were prepared at the University of Alberta, whereas fluid inclusion wafers and few additional polished thin sections were prepared at the Vancouver Petrographics Ltd. and Vancouver GeoTech Labs. Whole-rock lithogeochemical analyses were conducted at the Actlabs Laboratories in Ontario, Canada.

In memory of my parents,
Arsal and Ersin İmer

"… O earth, what changes hast thou seen!
There where the long street roars, hath been
The stillness of the central sea.

The hills are shadows, and they flow
From form to form, and nothing stands;
They melt like mist, the solid lands,
Like clouds they shape themselves and go."

- Lord Alfred Tennyson, *In Memoriam*, Section 123

ACKNOWLEDGMENTS

I would like to thank my supervisor Jeremy Richards for all his guidance and support, and also for his never-ending patience for the past few years.

I would also like to thank my supervisory committee members Sarah Gleeson and Martyn Unsworth for their valuable suggestions on my research project.

Rob Creaser was critical at various stages of this research and provided high quality Re-Os geochronological data as well as valuable comments on the manuscripts. Sincere thanks are extended to Karlis Muehlenbachs, Terry Spell, and Thomas Ullrich for their contributions to the project. Stephen Taylor is thanked for providing sulfur isotope data.

Financial support for this project was mainly provided by the National Sciences and Engineering Research Council of Canada (NSERC) through a Discovery grant to Jeremy Richards. Additional financial support by the Society of Economic Geologists through three separate Student Research Grants between 2007 and 2009 is also appreciated.

This project would not have been possible without the support of Alacer Gold Corp. and Rio Tinto plc. Special thanks are due to Firuz Alizade and İlhan Poyraz of Alacer and Gerard Rheinberger of Rio Tinto for permission to study the Çöpler and Cevizlidere deposits, respectively. I also would like to thank Alacer geologists Ali E. Özden, Can Tekin, Selçuk Uz, Aşkın Sarpay, İbrahim Güney, and Adnan Erdoğan for their assistance and discussions during fieldwork. Mehtap Yurdakul of the Ankara office of Rio Tinto kindly arranged the visit to Ovacık in 2008, and Tolga Tosun, Levent Çığ, and Mustafa Şaylı accompanied me to the site. Orhan Karaman was also helpful during regional sampling in June 2008.

I am grateful to the people of İliç and Çöpler for their warm hospitality. There are too many to mention individually but I do want to mention Ahmet Çoban, Recep Çoban, İlhami Gül, and Erdal Mürekkepçi as they patiently dealt with my myriad of requests around the core shed.

Numerous people at the EAS dedicated their valuable time to me over the years. Sergei Matveev, Mark Labbe, and Don Resultay and staff of the front office and the Digital Imaging Facility are greatly appreciated for their help.

Hakan Akan deserves a special “Thank you” for always being there for me. To my partners in crime in Edmonton: Andreas Enggist, Guadalupe Maldonado Sanchez, Rares Bistran, Mary Borrero, Yi Zhao, Osbaldo Zamora Vega, Ernesto Pecoits, Natalie Aubet, Gideon Lambiv Dzemua, Nelson Bernal, Mauricio Castillo, and Carlos Portillo – many thanks for memorable times. I must also mention my fellow office mates and friends from the research group: James Scott, Suzanne Byron, Micheal Moroskat, Bronwen Wallace, and Rui Wang. Beyond Edmonton, I would like to thank Guia Morelli, Donata Morelli, and Andrea Picanza for the good times in Brisbane and to Tonguç Uysal for making my life easier in Australia.

Finally, I would like to thank my family, particularly to my wife Ezgi, for their endless support and encouragement. Ezgi had to bear part of the burden with me throughout the years and even ran few stable isotope analyses for me so that I could finish earlier.

TABLE OF CONTENTS

LIST OF FIGURES

LIST OF TABLES

LIST OF SYMBOLS AND ABBREVIATIONS

Measurement Units

%	percent
‰	per mil
°	degrees
<	less than
>	greater than
~	approximately
amu	atomic mass unit
a.s.l.	above sea level
C	Celsius
cm	centimeter
g	gram
h	hour
km	kilometer
m	meter
Ma	million annum
mg	milligram
min	minute
mm	millimeter
mol	mole
Moz	million ounces
mV	millivolt
my	million year
pg	picogram
ppb	parts per billion
ppm	parts per million
t	ton (metric)
Th	homogenization temperature
$Th_{(L-V)}$	homogenization temperature to the liquid state via a bubble-point transition
Tm_{ice}	ice final melting temperature
VCDT	Vienna Canyon Diablo Troilite
VSMOW	Vienna Standard Mean Ocean Water
δ	delta
λ	decay constant
μm	micrometer
σ	standard deviation

Analytical Methods

EMPA	electron microprobe analysis
ICP	inductively coupled plasma
INAA	instrumental neutron activation analysis
MS	mass spectrometry

TD	total dissolution

Abbreviations (General)

alt	altered
ca	circa
d.l.	detection limit
E	east
e.g.	for example
equiv.	equivalent
HFSE	high field strength element
HREE	heavy rare earth element
i.e.	that is
IOCG	iron oxide copper-gold
LILE	large ion lithophile element
LOI	loss-on-ignition
LREE	light rare earth element
MREE	medium rare earth element
MSWD	mean square weighted deviation
N	north
REE	rare earth element
S	south
t	model age
TAB	Tauride-Anatolide Block
UTM	Universal Transverse Mercator
W	west
wk	weak
WGS	World Geodetic System
wt	weight

Minerals, Elements, Alteration Facies, and Rock Units

Ag	silver
Al	aluminium
Ar	argon
As	arsenic
Au	gold
Ba	barium
bar	barite
bt	biotite
Ca	calcium
CaF_2	calcium fluoride
carb	carbonate
chl	chlorite
Cl	chlorine
CO_2	carbon dioxide
cp	chalcopyrite
cpx	clinopyroxene
Cu	copper
Dy	dysprosium
ep	epidote
Eu	europium
Fe	iron
fl	fluorite
gn	galena
grd	granodiorite
hb	hornblende
HCl	hydrochloric acid
hm	hematite
HNO_3	nitric acid

K	potassium
Ksp	potassium feldspar
La	lanthanum
lst	limestone
mag	magnetite
Mo	molybdenum
mo	molybdenite
mrb	marble
N	nitrogen
Nb	niobium
Ni	nickel
ol	olivine
orp	orpiment
Os	osmium
Pb	lead
phyl	phyllic
plag	plagioclase feldspar
pot	potassic
prop	propylitic
Pt	platinum
py	pyrite
qz	quartz
Re	rhenium
rea	realgar
rhod	rhodochrosite
S	sulfur
Sb	antimony
ser	sericite
Sm	samarium
sp	sphalerite
Sr	strontium
Ta	tantalum
Ti	titanium
ten	tennantite
tet	tetrahedrite
U	uranium
W	tungsten
Y	yttrium
Yb	ytterbium
Zn	zinc
Zr	zirconium

CHAPTER 1: INTRODUCTION

1.1 Porphyry-epithermal systems

With the advent of plate tectonics in the 1970s and following the seminal paper of Sillitoe (1972), convergent margins have increasingly become primary targets for mineral exploration, particularly for porphyry Cu±Mo±Au and epithermal Au-Ag-base metal deposits. In these tectonic settings, porphyry and epithermal deposits are commonly found in close relationship with subduction-related magmas, but they otherwise belong to distinct physicochemical environments of mineralization as indicated by their respective ore fluid characteristics.

Porphyry deposits typically form from high temperature (~350°–700°C), near neutral to slightly acidic magmatic fluids exsolved from shallow level (2–5 km depth) intrusions of intermediate to felsic composition (Einaudi et al., 2003; Richards, 2003; Seedorff et al., 2005; Sillitoe, 2010). Epithermal deposits, on the other hand, form at relatively shallow depths (typically <1 km), from lower temperature (100°–300°C) and lower salinity (commonly <5 wt.% NaCl equiv.) fluids (Cooke and Simmons, 2000; Simmons et al., 2005).

The most recent and widely accepted classification of epithermal deposits, as proposed by Sillitoe and Hedenquist (2003), recognizes two end-member mineralization styles, with these end-members reflecting contrasting fluid characteristics. The high-sulfidation (HS) class of epithermal deposits (also known as "acid-sulfate-type"; Hayba et al., 1985; Heald et al., 1987) are associated with acidic fluids (under high sulfur and oxygen fugacities) of magmatic origin, whereas low-sulfidation (LS) epithermal deposits (also known as "adularia-sericite-type"; op. cit., and Albino and Margolis, 1991) form from near-neutral pH fluids (under moderate sulfur and oxygen fugacities) that are dominated by groundwaters. The role of magmatism in the latter group is much less pronounced, and is usually limited to supply of heat for the mineralizing hydrothermal system.

Intermediate-sulfidation (IS) epithermal deposits ("carbonate-base metal Au deposits" of Corbett and Leach, 1998) form part of the same epithermal spectrum and share some characteristics of HS and LS deposits. Similar to HS epithermal deposits, ore fluids in IS deposits are usually of magmatic origin, but their alteration chemistries indicate near-neutral pH conditions. In addition, ore fluids in IS systems usually have higher salinities (>5 up to ~23 wt.% NaCl equiv.; Albinson et al., 2001; Sillitoe and Hedenquist, 2003; Simmons et al., 2005) when compared to HS and LS systems, in keeping with their relatively high base metal contents.

In many districts porphyry and epithermal deposits occur in close proximity to each other, and in few others paragenetically late epithermal mineralization is found superimposed on top of early porphyry mineralization due to extreme telescoping (Sillitoe, 1994). This implies a genetic link between porphyry and epithermal deposits, which was already recognized in the early 1990s by detailed studies in some world-known districts such as in the Maricunga and El Indio Belts in Chile (Jannas et al., 1990; Vila and Sillitoe, 1991), in the Baguio district in Philippines (Cooke and Bloom, 1990), and in Porgera in Papua New Guinea (Richards, 1992). Later studies by Arribas et al. (1995) and Muntean and Einaudi (2001) demonstrated in detail that porphyry and epithermal ore formation in a district may indeed develop contemporaneously from a single magmatic-hydrothermal source, and may thus form a continuum of hydrothermal processes.

1.2 Turkish porphyry-epithermal systems and thesis objectives

As mentioned earlier, porphyry and epithermal deposits are spatially associated with convergent margins, and therefore a majority of the world's known porphyry and epithermal deposits are concentrated along two extensive orogenic belts: the Circum-Pacific belt and the Alpine-Himalayan belt.

The ~10,000 km-long Alpine-Himalayan orogenic belt extends from western Europe through Turkey, Iran, and Pakistan to Tibet and China. This belt mainly formed as a result of convergence between the Afro-Arabian, Eurasian, and Indian plates, and therefore has recorded a long history of continental rifting/ocean opening, subduction, and collision. In 1977, Janković recognized that a wealth of metallic ore deposits are closely associated with the volcano-plutonic arcs of this orogenic belt and coined the name "Tethyan-Eurasian Metallogenic Belt (TEMB)" to broadly define this relationship in a metallogenic context.

Turkey, as a part of the TEMB, has recently emerged as an important producer of precious and base metals in Europe as a result of increased exploration activities. The western part of Turkey is so far the most prospective region as it hosts numerous epithermal deposits of varying size as well as several important porphyry deposits, including the Kışladağ porphyry Au, Halilağa porphyry Cu-Au, and Efemçukuru, Ovacık, and Kirazlı epithermal Au deposits (Fig. 1.1).

Despite its potential, only a small number of deposits have been discovered in eastern Turkey, and among these the Çöpler epithermal Au and Cevizlidere porphyry Cu-Mo-Au deposits (Fig. 1.1) are the most important discoveries. Both deposits are located along the eastern Tauride Mountains, in a geologically complex region where extensive neotectonic zones have been juxtaposed against ancient Paleotethyan and Neotethyan sutures, and as such regional geological relationships are often complex and ambiguous.

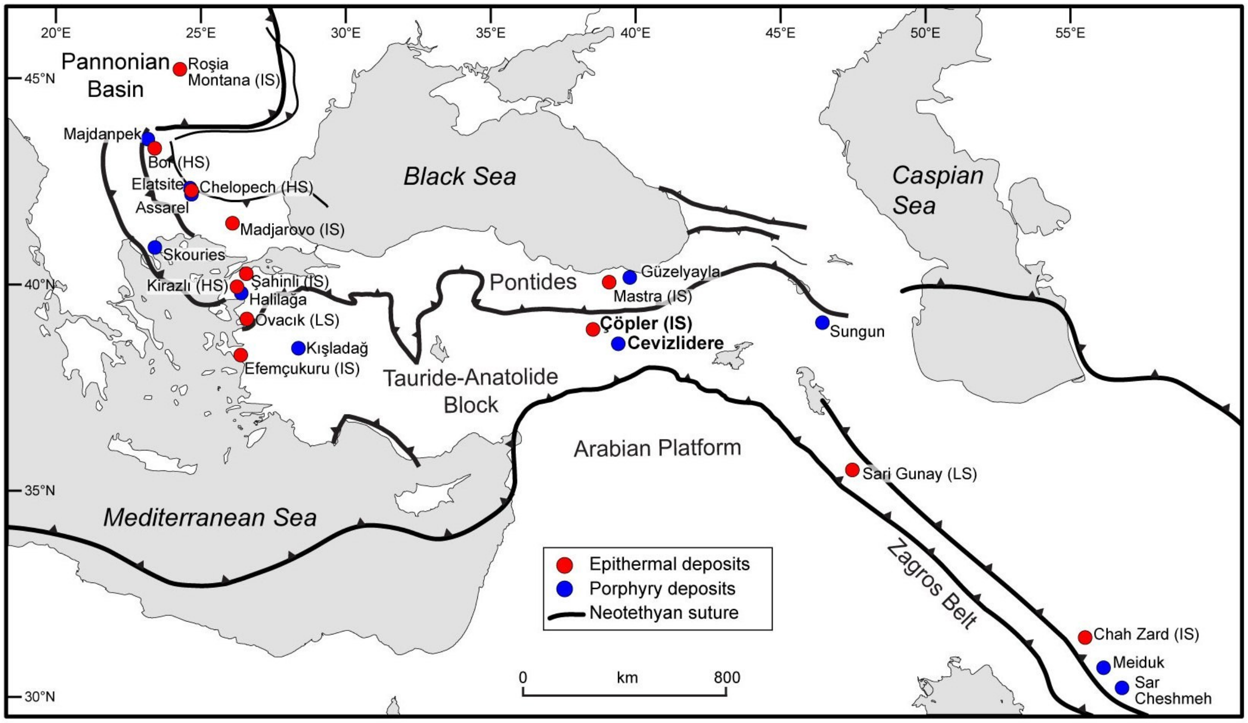

Figure 1.1 Map showing locations of the Çöpler and Cevizlidere deposits together with other important porphyry and epithermal deposits located in southeastern Europe, Turkey, and Iran. Also shown are the major Neotethyan sutures of the eastern Mediterranean region (after Okay and Tüysüz, 1999). Abbreviations: IS = intermediate-sulfidation, HS = high-sulfidation, LS = low-sulfidation

Very few studies have been published on the general geological features as well as on the tectonomagmatic evolution of this region (e.g., Özgül and Turşucu, 1984; Robertson et al., 2007; Kaymakçı et al., 2006 and 2010; Kuşcu et al., 2010 and 2013), and descriptions of both the Çöpler and Cevizlidere deposits are lacking in the literature. Therefore, this project is designed to investigate primarily: (1) the timing of magmatism and ore formation, nature of magmatism, and tectonomagmatic controls in both Çöpler and Cevizlidere districts (Chapters 2 and 3), and (2) the spatiotemporal evolution of the magmatic-hydrothermal system at Çöpler (Chapter 4).

1.3 References

Albino GV, Margolis J (1991) Differing styles of adularia-sericite epithermal deposits – contrasts in geologic setting and mineralogy [abst.]. Geol Soc Am Abstracts with Program 23:A230.

Albinson T, Norman DI, Cole D, Chomiak B (2001) Controls on formation of low-sulfidation epithermal deposits in Mexico: Constraints from fluid inclusion and stable isotope data: Soc Econ Geol Spec Publ 8:1–32.

Arribas A Jr, Hedenquist JW, Itaya T, Okada T, Concepcion RA, Garcia JS Jr (1995) Contemporaneous formation of adjacent porphyry and epithermal Cu-Au deposits over 300 ka in northern Luzon, Philippines. Geology 23:337–340.

Cooke DR, Bloom MS (1990) Epithermal and subjacent porphyry mineralization, Acupan, Baguio District, Philippines: a fluid-inclusion and paragenetic study. J Geochem Expl 35:297–340.

Cooke DR, Simmons SF (2000) Characteristics and genesis of epithermal gold deposits. Rev. Econ. Geol. 13:221–244.

Corbett GJ, Leach TM (1998) Southwest Pacific Rim gold-copper systems: Structure, alteration and mineralization. Soc Econ Geol Spec Publ 6:236 p.

Einaudi MT, Hedenquist JW, Inan EE (2003) Sulfidation state of fluids in active and extinct hydrothermal systems: Transitions from porphyry to epithermal environments. Soc Econ Geol Spec Publ 10:285−313.

Hayba DO, Bethke PM, Heald P, Foley NK (1985) Geologic, mineralogic, and geochemical characteristics of volcanic-hosted epithermal precious metal deposits. Rev Econ Geol 2:129–167.

Heald P, Foley NK, Hayba DO (1987) Comparative anatomy of volcanic-hosted epithermal deposits: Acid sulfate and adularia-sericite types. Econ Geol 82:1–26.

Janković S (1977) The copper deposits and geotectonic setting of the Tethyan Eurasian Metallogenic Belt. Miner Deposita 12:37–47.

Jannas RR, Beane RE, Ahler BA, Brosnahan DR (1990) Gold and copper mineralization at the El Indio deposit, Chile: J Geochem Explor 36:233–266.

Kaymakçı N, İnceöz M, Ertepınar P (2006) 3D-architecture and Neogene evolution of the Malatya Basin: Inferences for the Kinematics of the Malatya and Ovacık Fault Zones. Turk J Earth Sci 15:123–154.

Kaymakçı N, İnceöz M, Ertepınar P, Koç A (2010) Late Cretaceous to Recent kinematics of SE Anatolia (Turkey). In: Sosson M, Kaymakçı N, Stephenson RA, Bergerat F, Starostenko V (eds) Sedimentary Basin Tectonics from the Black Sea and Caucasus to the Arabian Platform. Geol Soc Lond Spec Publ, 340:409–435.

Kuşcu İ, Gençalioğlu-Kuşcu G, Tosdal RM, Ulrich TD, Friedman R (2010) Magmatism in the southeastern Anatolian orogenic belt: transition from arc to post-collisional setting in an evolving orogen. In: Sosson M, Kaymakçı N, Stephenson RA, Bergerat F, Starostenko V (eds) Sedimentary Basin Tectonics from the Black Sea and Caucasus to the Arabian Platform. Geol Soc Lond Spec Publ 340:437–460.

Kuşcu İ, Tosdal RM, Gençalioğlu-Kuşcu G, Friedman R, Ullrich TD (2013) Late Cretaceous to Middle Eocene Magmatism and Metallogeny of a Portion of the Southeastern Anatolian Orogenic Belt, East-Central Turkey. Econ Geol 108:641–666.

Muntean JL, Einaudi MT (2001) Porphyry-epithermal transition: Maricunga Belt, northern Chile. Econ Geol 96:743–772.

Özgül N, Turşucu A (1984) Stratigraphy of the Mesozoic carbonate sequence of the Munzur Mountains (Eastern Turkey). In: Tekeli O, Göncüoğlu MC (eds) Geology of the Taurus Belt. Proceedings of the International Tauride Symposium. Mineral Research and Exploration Institute of Turkey (MTA) Publications, Ankara, Turkey, pp 173–180.

Richards JPR (1992) Magmatic-hydrothermal transitions in alkalic systems: Porgera gold deposit, Papua New Guinea. Geology 20:547–550.

Richards JPR (2003) Tectono-magmatic precursors for porphyry Cu-(Mo-Au) deposit Formation. Econ Geol 98:1515−1533.

Robertson AHF, Parlak O, Rızaoğlu T, Ünlügenç Ü, İnan N, Taşlı K, Ustaömer T (2007) Tectonic evolution of the South Tethyan ocean: evidence from the Eastern Taurus Mountains (Elazığ region, SE Turkey). In: Ries AC, Butler RWH, Graham RH (eds) Deformation of the Continental Crust: The Legacy of Mike Coward. Geol Soc Lond Spec Publ 272:231–270.

Seedorff E, Dilles JH, Proffett JM Jr, Einaudi MT, Zurcher L, Stavast WJA, Johnson DA, Barton MD (2005) Porphyry deposits: Characteristics and origin of hypogene features. Econ Geol 100th Anniversary Vol:251−298.

Sillitoe RH (1972) A plate tectonic model for the origin of porphyry copper deposits. Econ Geol 67:184−197.

Sillitoe RH (1994) Erosion and collapse of volcanoes: Causes of telescoping in intrusion-centered ore deposits. Geology 22:945−948.

Sillitoe RH (2010) Porphyry copper systems. Econ Geol 105:3–41.

Sillitoe RH, Hedenquist JW (2003) Linkages between volcanotectonic settings, ore-fluid compositions, and epithermal precious metal deposits. Soc Econ Geol Spec Publ 10:315–343.

Simmons SF, White NC, John DA (2005) Geological characteristics of epithermal precious and base metal deposits. Econ Geol 100th Anniversary Vol: 485–522.

Vila T, Sillitoe RH (1991) Gold-rich porphyry systems in the Maricunga belt, northern Chile. Econ Geol 86:1238−1260.

CHAPTER 2: AGE AND TECTONOMAGMATIC SETTING OF THE EOCENE ÇÖPLER-KABATAŞ MAGMATIC COMPLEX AND PORPHYRY-EPITHERMAL AU DEPOSIT, EAST CENTRAL ANATOLIA, TURKEY*

* A version of this chapter has been published in Mineralium Deposita (volume 43, June 2013), co-authored by Jeremy P. Richards (University of Alberta) and Robert A. Creaser (University of Alberta).

2.1 Introduction

Convergent and collisional orogens worldwide are host to a wide range of magmatic rocks and associated mineral deposit types (e.g., Janković, 1977; Solomon, 1990; Hedenquist and Lowenstern, 1994; Kesler, 1997; Barley et al., 2002; Richards, 2003a and 2009; Bierlein et al., 2009). The Tethyan Alpine-Himalayan Belt stands as one of the best examples of such an orogenic system, with a large endowment of magmatic-hydrothermal ore deposits including porphyry Cu±Mo±Au and epithermal Au-Ag deposits (Janković, 1977; Richards, 2003b; Hou and Cook, 2009; Yiğit, 2009).

The recently discovered (in 1998) Çöpler gold deposit is located ~120 km southwest of the city of Erzincan in central eastern Turkey (Fig. 2.1). The deposit consists of early, low-grade porphyry-type Cu-Au mineralization overprinted by intermediate-sulfidation epithermal-style Au mineralization. Çöpler is the first significant gold discovery in eastern Anatolia, a region which had remained mostly unexplored prior to the late 1990s. With total reserves in excess of 4.5 million ounces (Moz) Au equivalent (~96 million metric tonnes at 1.49 g/t Au; http://www.alacergold.com), Çöpler currently ranks as the second largest gold deposit in Turkey after the Kışladağ porphyry Au deposit in western Anatolia (~460 million metric tonnes at 0.71 g/t Au; http://www.eldoradogold.com).

Porphyry-epithermal mineralization at Çöpler is spatially associated with the middle Eocene calc-alkaline Çöpler-Kabataş intrusive complex, which was emplaced into a narrow structural corridor along the northern flank of the eastern Taurus mountain range. The magmatic complex lies on the northeastern margin of the Tauride-Anatolide orogenic block (TAB), within a region of structural complexity where the modern Eurasia–Arabia collision zone is juxtaposed against at least two different suture zones marking the closure of former Neotethyan ocean basins (Fig. 2.1, 2.2). During the Late Mesozoic–Cenozoic, basin closure along both margins of the TAB was accompanied by northward subduction and continental arc magmatism. This was followed by Late Cretaceous collision in the Pontides, and protracted periods of subduction-related and post-subduction magmatism from the middle Eocene onwards.

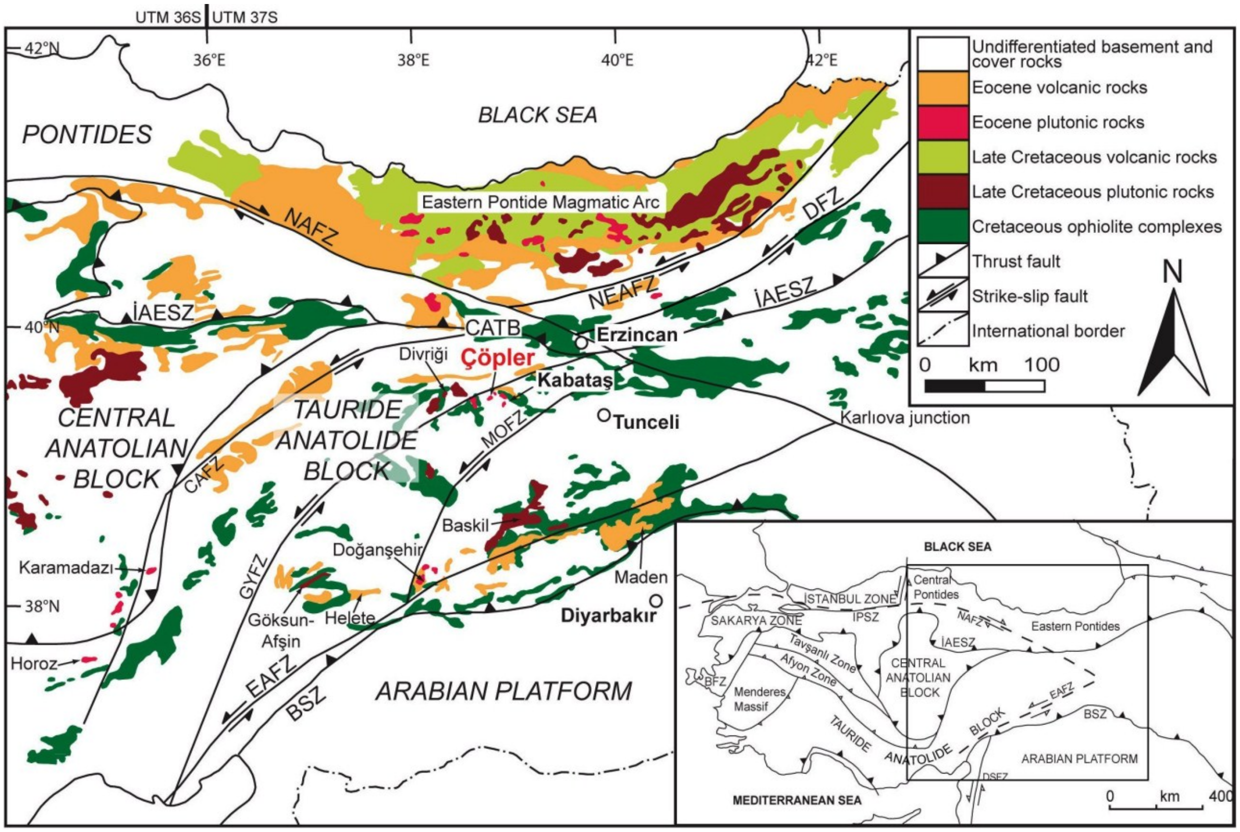

Figure 2.1 Simplified geological map showing the distribution of Late Cretaceous to Eocene magmatic rocks and Cretaceous ophiolite complexes of eastern Anatolia (modified from MTA, 1989 and Bozkurt, 2001). Areas shown in white represent undifferentiated Paleozoic–Mesozoic basement rocks and Tertiary sedimentary/volcanic cover. Karlıova junction marks the intersection of the North and East Anatolian Fault Zones. Inset map shows the major tectonic elements of Turkey (Okay and Tüysüz, 1999). Box indicates the area of the main map. Abbreviations: BFZ = Bornova Flysch Zone; BSZ = Bitlis Suture Zone; CAFZ = Central Anatolian Fault Zone; CATB = Central Anatolian Thrust Belt; DFZ = Dumlu Fault Zone; DSFZ = Dead Sea Fault Zone; EAFZ = East Anatolian Fault Zone; GYFZ = Göksu-Yazyurdu Fault Zone; İAESZ = İzmir-Ankara-Erzincan Suture Zone; IPSZ = Intra-Pontide Suture Zone; MOFZ = Malatya-Ovacık Fault Zone; NAFZ = North Anatolian Fault Zone; NEAFZ = North East Anatolian Fault Zone

Although these regional magmatic and tectonic events have been the subject of several studies, understanding the geotectonic significance of the Çöpler-Kabataş magmatic complex and nearby igneous rocks of similar age and chemistry has been hindered by a lack of geological and geochronological data. The distal positioning of these intrusive centers relative to the established Late Cretaceous–Eocene arc magmatic belts in the Pontides and in southeast Anatolia (Baskil–Maden; Fig. 2.1) has led to conflicting interpretations regarding the nature and source of magmatism. Proposed models for the Eocene central-eastern Tauride magmatic belt have ranged from typical continental arc settings (Özer and Öner, 1999) to post-collisional tectonic settings in which magmatism was induced by slab steepening and break-off either (1) along the northern margin of the TAB (Önal et al., 2005), or (2) along the southern margin of the Tauride-Anatolide Block (Kuşcu et al., 2007 and 2010).

This contribution provides new data on the age, geology, and geochemistry of the Çöpler-Kabataş magmatic complex and associated porphyry deposit, in order to place it more clearly in a regional tectonomagmatic and metallogenic context.

2.2 Tectonic Framework of Central Turkey

Turkey forms part of the extensive Alpine-Himalayan Orogenic Belt that stretches from SW Europe to SE Asia, and comprises largely an assemblage of continental fragments of Tethyan origin. These continental fragments, once separated by Neotethyan basins, were amalgamated during convergence between the Eurasian and Afro-Arabian plates since at least late Mesozoic times (Fig. 2.2).

The ~1500-km-long Tauride-Anatolide Block (TAB), which hosts the Çöpler gold deposit, is the largest of these continental fragments. During the Late Permian–Early Triassic, the TAB and other Cimmerian continents (including the laterally adjacent Central Iranian Block), started to detach from the northern Gondwana margin, initiating the southern Neotethys Ocean basin (Şengör and Yılmaz, 1981; Robertson and Dixon, 1984; Stampfli et al., 1991). Closure of this ocean basin commenced in the Early Cretaceous by north-dipping subduction along the Bitlis Suture (Fig. 2.2), accompanied by continental arc development (~88–73 Ma) along the active southern margin of the TAB (Baskil and Göksun-Afşin arcs, Fig. 2.1; Şengör and Yılmaz, 1981; Yazgan and Chessex, 1991; Yılmaz, 1993; Rızaoğlu et al., 2009). At the end of the Mesozoic, subduction-related calc-alkaline magmatic activity in the TAB was interrupted, possibly due to a decrease in the rate of convergence between Arabia and Eurasia (Dewey et al., 1989) or roll-back of the southern Neotethys slab (Robertson et al., 2007; Kaymakçı et al., 2010). This subsequently led to widespread back-arc extension in the central and eastern part of the

TAB. In the Eocene, arc magmatism along this margin resumed with eruption of the mafic-to-intermediate composition Maden-Helete lavas, while back-arc magmatism occurred intermittently along ENE-trending transcurrent fault systems throughout the central and eastern Taurides (Fig. 2.1; Yazgan, 1984; Yılmaz, 1993; Yiğitbaş and Yılmaz, 1996a; Elmas and Yılmaz 2003; Robertson et al., 2007). The Çöpler-Kabataş intrusive complex was formed during this period in the TAB. Final closure of the southern Neotethys Ocean along the Bitlis Suture took place during the Miocene, when the Arabian Platform collided with the TAB, which by this time was already part of the southern Eurasian margin (Dewey et al., 1986; Şengör and Yılmaz, 1981; Yiğitbaş and Yılmaz, 1996b; Okay et al., 2010).

Contemporaneous with development of the southern Neotethys Ocean in the Early Mesozoic, a back-arc basin known as the İzmir-Ankara-Erzincan Ocean (or northern Neotethys; Fig. 2.2) was formed to the north of the TAB (Robertson and Pickett, 2000; Stampfli, 2000; Tekin, et al., 2002; Okay et al., 2006). This short-lived basin was closed in the Cretaceous, first by intra-oceanic subduction of unknown polarity, and then by northward subduction beneath the Eurasian margin to form the Eastern Pontide Magmatic Arc (Fig. 2.1, 2.2). Collision between the Pontides and the TAB occurred in the Late Cretaceous, with obduction of ophiolites onto the north-facing margin of the TAB (Fig. 2.1, 2.2; Okay and Şahintürk, 1997; Rice et al., 2006; Tüysüz and Tekin, 2007).

In the Paleocene, continued N–S-directed convergence along the collisional belt resulted in transpressional deformation of the eastern Pontides, accompanied by folding, thrusting, and uplift (Okay and Şahintürk, 1997; Kaymakçı et al., 2000). Collapse of the crustally thickened orogen occurred during the middle Eocene, initiating an episode of post-collisional calc-alkaline magmatism (50–41 Ma) mainly within ENE- and E–W-trending extensional basins in the Pontides, and along the İzmir-Ankara-Erzincan Suture Zone (Fig. 2.1; Okay and Şahintürk, 1997; Topuz et al., 2005; Keskin et al., 2008).

The Miocene collision of Eurasia and Arabia along the Bitlis Suture heralded the start of continent–continent (as opposed to microplate–continent) collision in this region. Collision was followed by uplift and extensive deformation of eastern Anatolia, and by westward migration of the main Anatolian Block along two new regional strike-slip structures, the North and East

Anatolian Fault Zones. These faults are roughly coincident with the pre-existing Neotethyan sutures (Fig. 2.1; Dewey et al., 1986). Widespread post-collisional volcanism occurred throughout Anatolia from the Miocene onwards. In eastern Anatolia, it has been suggested that this volcanic activity was associated either with delamination of the sub-continental lithospheric mantle (Pearce et al., 1990; Göğüş and Pysklywec, 2008) or with slab steepening and break-off following collision (Keskin 2003; Şengör et al., 2003; Faccenna et al., 2006; Lei and Zhao, 2007). In contrast, in western Anatolia this volcanism is attributed to Miocene to Recent extensional tectonics related to the opening of the Aegean back-arc (McKenzie and Yılmaz, 1991).

2.3 Regional Geological and Structural Setting of the Tauride-Anatolide Block

The eastern part of the TAB consists of a number of tectonomagmatic and stratigraphic units including the Paleozoic–Mesozoic Keban metamorphic massif, the Munzur allochthon (Late Triassic–Cretaceous platform and deep marine carbonates), Cretaceous ophiolite complexes, Late Cretaceous and Cenozoic igneous rocks, and Cenozoic sedimentary cover rocks of the Sivas Basin; Fig. 2.3; Michard et al., 1984; Özgül and Turşucu 1984; Özer 1994). The Munzur allochthon was overthrust onto the Permo–Triassic metamorphic basement in the Late Cretaceous (Özgül and Turşucu, 1984), forming an extensive east–west-trending mountain range between Tunceli to the south and Erzincan to the north (Fig. 2.1). The steep topography of the allochthon gradually diminishes outwards towards the surrounding Late Cretaceous–Tertiary sedimentary basins.

The Munzur allochthon comprises a thick succession of deep marine and platform-type carbonate rocks (Özgül and Turşucu, 1984; Tunç et al., 1991). Its northern flank has been extensively overlain by tectonic slivers of Cretaceous ophiolitic rocks and melange that were accreted during Late Cretaceous dextral transpression associated with closure of the İzmir-Ankara-Erzincan ocean basin (Özgül et al., 1981; Yılmaz, 1985; Kaymakçı et al., 2000; Yalınız et al., 2000; Okay et al., 2001). Both carbonate rocks and obducted ophiolites were later intruded and covered by igneous rocks of varying composition during three distinct magmatic episodes: an early bimodal alkaline intrusive event during the Late Cretaceous, a more voluminous calc-alkaline intrusive and extrusive event in the Eocene, and a widespread bimodal volcanic event in the Miocene.

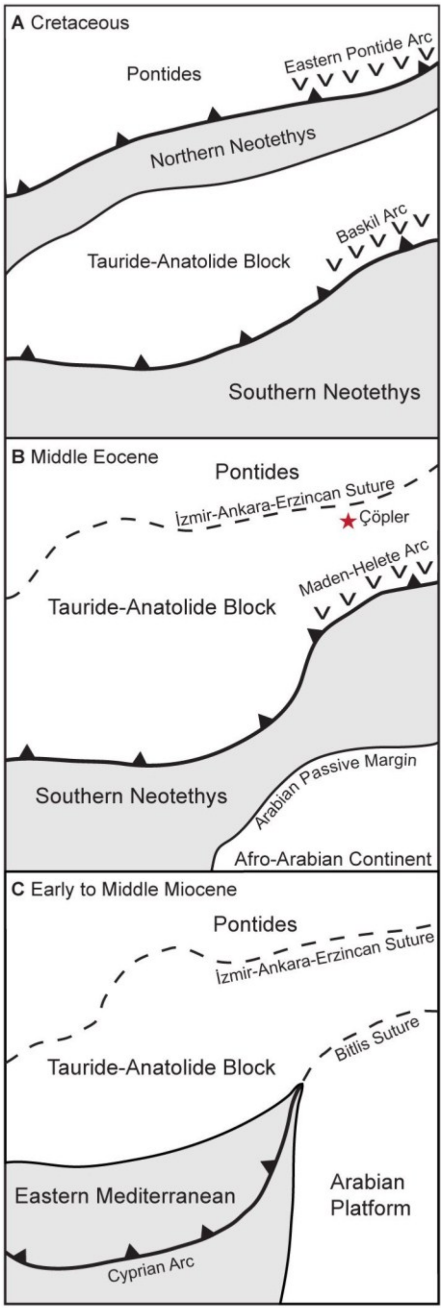

Figure 2.2 Simplified sketch diagram showing the Neotethyan evolution of the Tauride-Anatolide Block and traces of Neotethyan suture zones from (A) Cretaceous to (B) middle Eocene, to (C) Miocene times (after Robertson, 1998). Also shown are the approximate locations of the Çöpler deposit and the magmatic arcs that are referred in the text. Note the southward jump of the southern Neotethyan subduction zone during the Miocene (as shown in C).

The oldest magmatic phase in the vicinity of the Munzur allochthon is represented by sporadic exposures of Late Cretaceous bimodal intrusions including the Murmano and Dumluca plutons near Divriği, and several small intrusive centers located near Hekimhan (Fig. 2.1, 2.3). Intrusive rocks of this stage are typically alkaline syenite-quartz monzonite and diorite-gabbro suites with ages between ~76–74 Ma (Zeck and Ünlü, 1991; Yılmaz et al., 1993, Kadıoğlu et al., 2006; Boztuğ et al., 2007; Kuşcu et al., 2007 and 2010; Marschik et al., 2008; Özgenç and İlbeyli, 2009; this study). Emplacement of these bimodal plutons seems to coincide with break-up and collapse of the thickened eastern TAB crust, the result of which was a reversal in stress directions and a switch from transpression to transtension. From Late Cretaceous until middle Eocene time, this transtensional period led to the opening of several ENE-trending sedimentary basins (Cater et al., 1991; Temiz et al., 1993), and exhumation of metamorphic complexes (Gautier et al., 2002; Umhoefer et al., 2007; Whitney et al., 2008), mainly along Cretaceous thrust fault systems reactivated as sinistral strike-slip faults (Fig. 2.1, 2.3; Koçyiğit and Beyhan, 1998; Poisson et al., 1996; Fayon et al., 2001).

Eocene magmatic rocks are widely scattered throughout the northeastern Taurides, and include the Çöpler-Kabataş magmatic complex, the Çaltı and Bizmişen plutons, and an east–west-trending belt of volcano-sedimentary rocks that crop out adjacent to the İzmir-Ankara-Erzincan Suture Zone (Fig. 2.1, 2.3). Intrusive rocks consist of calc-alkaline diorite, quartz diorite, granodiorite, and quartz monzonite, and volcanic rocks range from basaltic andesite to rhyolite (Özer and Öner, 1999; Önal et al., 2005; Kuşcu et al., 2007; Keskin et al., 2008). Although their geochemical characteristics are similar to global arc magmas, the Eocene igneous rocks do not form a continuous narrow magmatic belt as in many volcanic arcs, but rather occur as isolated intrusive and volcanic complexes localized in structurally favourable sites, and distal to the presumed coeval subduction zone and arc to the south.

The Karamadazı, Horoz, and Doğanşehir plutons are other regionally significant Eocene intrusive systems, which follow the same general structural trend to the southwest (Fig. 2.1; see discussion below). All three plutons are reported to be Eocene in age (~50–48 Ma), and consist of felsic to intermediate sub-alkaline lithologies (Gençalioğlu-Kuşcu et al., 2001; Karaoğlan and Parlak, 2006; Karaoğlan et al., 2009; Kadıoğlu and Dilek, 2010; Kuşcu et al., 2010).

Throughout the northeastern TAB, much of the Late Cretaceous–Middle Eocene magmatism appears to have been controlled by two prominent ENE-trending structures, the sinistral Central Anatolian and Göksu-Yazyurdu Fault Zones (Fig. 2.1), which accommodated a component of the transtensional deformation. Shallow level pluton emplacement is favored at times of oblique transtensional or transpressional movement (e.g., Hutton 1982 and1990; Glazner 1991; Román-Berdiel et al., 1997; Tosdal and Richards, 2001). During the Eocene transtensional period, a total sinistral displacement of 74 km is recorded along the Central Anatolian Fault Zone (Koçyiğit and Beyhan, 1998), but the offset along the Göksu-Yazyurdu Fault Zone to the south is not known.

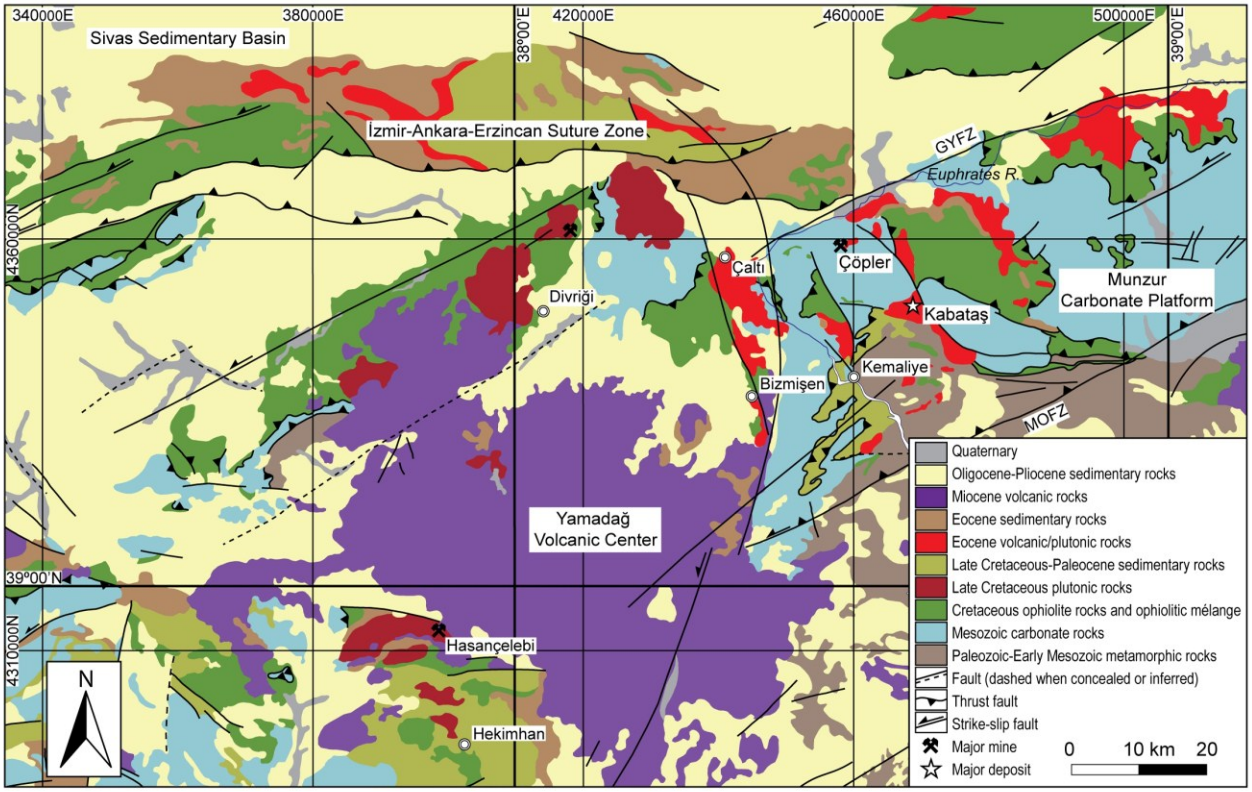

Figure 2.3 Simplified geological map of the eastern Tauride-Anatolide Block. Compiled from the 1:500,000 geological map of Turkey, Sivas and Erzurum quadrangles (MTA, 2002a, b; UTM Zone 37S). Structural data are modified from Kaymakçı et al. (2006). Abbreviations: GYFZ = Göksu-Yazyurdu Fault Zone; MOFZ = Malatya-Ovacık Fault Zone.

The northeastern TAB experienced a final stage of widespread post-collisional magmatism in the Miocene, erupted along strike-slip fault systems. For example, basaltic trachyandesite to dacite volcanic rocks form the 19–11 Ma Yamadağ volcanic center to the southwest of Çöpler (Fig. 2.3; Arger et al., 2000; Kürüm et al., 2008; Ekici et al., 2009). These magmas are interpreted to have formed during post-collisional readjustments by melting of subduction-modified lithospheric sources remnant from earlier Neotethyan subduction events (Arger et al., 2000; Keskin 2003; Kürüm et al., 2008; Ekici et al., 2009).

2.4 Local Geological Setting of the Çöpler Au Deposit

The Çöpler gold deposit is located in the central eastern part of the TAB, along the northern flanks of the Munzur Mountains, roughly 3 km southeast of the Euphrates River (Fig. 2.3). The deposit is spatially related to an Eocene composite stock forming the northwestern extension of the Çöpler-Kabataş magmatic complex (Fig. 2.4, 2.5), which intruded a basement of Late Paleozoic–Cretaceous sedimentary and ophiolitic rocks (Fig. 2.3–6). The intrusive system at Çöpler is exposed within a 1 x 2 km wide, bowl-shaped, ENE-trending structural window (the Çöpler window; Fig. 2.4, 2.5), along which block-faulted rocks have been exposed underneath the regional thrust sheet of the Munzur carbonate allochthon. The intrusive complex appears to post-date thrusting, and locally intrudes the base of the thrust sheet causing contact-metamorphism to marble.

2.4.1 Paleozoic–Mesozoic Basement Units

The basement in the Çöpler area consists of an 800 m-thick succession of regionally metamorphosed Permo–Triassic siliciclastic sedimentary rocks, which belong to the Yoncayolu Formation of the Keban metamorphic massif (Özgül and Turşucu, 1984). This unit is exposed in the western part of the Çöpler window and in the vicinity of Kabataş village (Fig. 2.4, 2.5). The metasedimentary succession consists of uniformly alternating layers of shelf-type clastic rocks, which underwent low-grade greenschist facies metamorphism in conjunction with Late Cretaceous obduction of ophiolites onto the northern TAB margin (Özgül et al., 1981; Özgül and Turşucu, 1984). These rocks are characterized by a mineral assemblage of chlorite + quartz ± sericite ± epidote; however, brown-colored biotite-rich, and pale green-colored diopside-rich hornfels are locally developed at contacts with the Eocene intrusions.

Structurally overlying the metamorphic basement is the Late Triassic to Cretaceous allochthonous Munzur carbonate platform, which displays an overall younging trend from south to north (Özgül and Turşucu, 1984). The northern section of this allochthon, which is exposed between Çöpler and Kabataş villages, consists of a 300 m-thick succession of Cenomanian to

Campanian rudist-bearing limestones (Özgül and Turşucu, 1984). The base of the limestone succession is poorly-exposed, but in the southwestern sector of the Çöpler window metasedimentary rock injections into the Munzur limestone were observed (Fig. 2.7A). These textures are interpreted to reflect south-vergent décollement thrusting of the carbonate platform during the Campanian–Maastrichtian interval (Özgül et al., 1981; Özgül and Turşucu, 1984). The limestones are metamorphosed to sugary-textured white marble for several hundred meters around the intrusive contacts (Fig. 2.5).

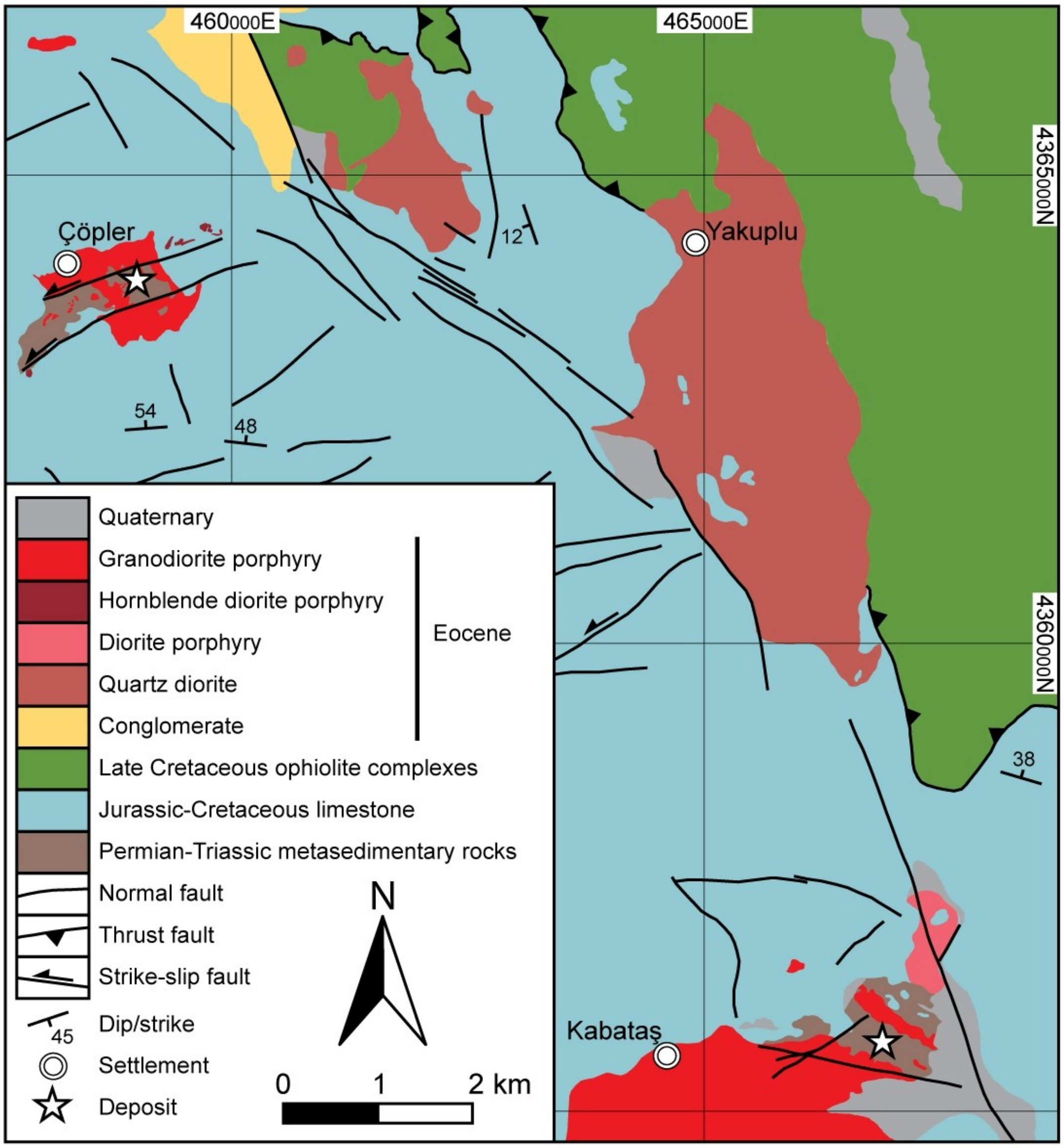

Figure 2.4 Geological map of the Çöpler-Kabataş magmatic complex, modified from Özer (1994).

2.4.2 The Eocene Çöpler-Kabataş Magmatic Complex

The Çöpler-Kabataş magmatic complex intrudes the Paleozoic–Mesozoic basement and overlying limestones as several stocks that range in width from a few hundred meters to several kilometers (Fig. 2.4). The intrusive rocks are porphyritic to equigranular and intermediate composition, with ubiquitous and abundant plagioclase (andesine). Quartz is also a common constituent of many of these igneous lithologies, whereas K-feldspar was not observed in unaltered rocks. Green-colored hornblende is the predominant mafic phase and is present in most igneous lithologies, whereas biotite and clinopyroxene are sparse.

Granodiorite porphyry: The predominant phase in the Çöpler-Kabataş magmatic complex is a granodiorite porphyry that crops out in the main Çöpler window (Fig. 2.4, 2.5), and also near Kabataş village (Fig. 2.4). At Çöpler, this unit is mainly exposed between the Çöpler North and South Faults, and also occurs as two lobes to the north and south of these structures (Fig. 2.5). Granodiorite porphyry contains abundant plagioclase, hornblende, and sparse biotite phenocrysts set in a fine-grained groundmass of plagioclase, quartz, and lesser magnetite (Fig. 2.7B, 2.8A). Euhedral to subhedral phenocrysts, ranging in size from 0.5 to 4 mm, make up to about 70 volume percent of the rock. Rounded, biotite-rich mafic xenoliths are occasionally present in the granodiorite porphyry (Fig. 2.7B). Both in Çöpler and Kabataş, granodiorite porphyry has undergone widespread hydrothermal alteration, and its least-altered varieties display weak propylitic alteration with partial replacement of mafic phases by chlorite and epidote, together with sparse carbonate.

Hornblende diorite porphyry: Hornblende diorite porphyry is exposed as several small stocks in the northeast and southwest sectors of the Çöpler window, in close association with east–west-trending structures (Fig. 2.5, 2.7C). The hornblende diorite porphyry contains abundant plagioclase and hornblende phenocrysts within a fine-grained plagioclase-quartz-magnetite groundmass, with a significantly lower phenocryst to groundmass ratio than the granodiorite porphyry (Fig. 2.8B). Its relationship with the granodiorite porphyry is unclear, because it has mostly been intensely altered. Least-altered samples of hornblende diorite porphyry exhibit weak propylitic alteration as indicated by partial replacement of hornblende by chlorite, and by the presence of sparse epidote and carbonate in the groundmass.

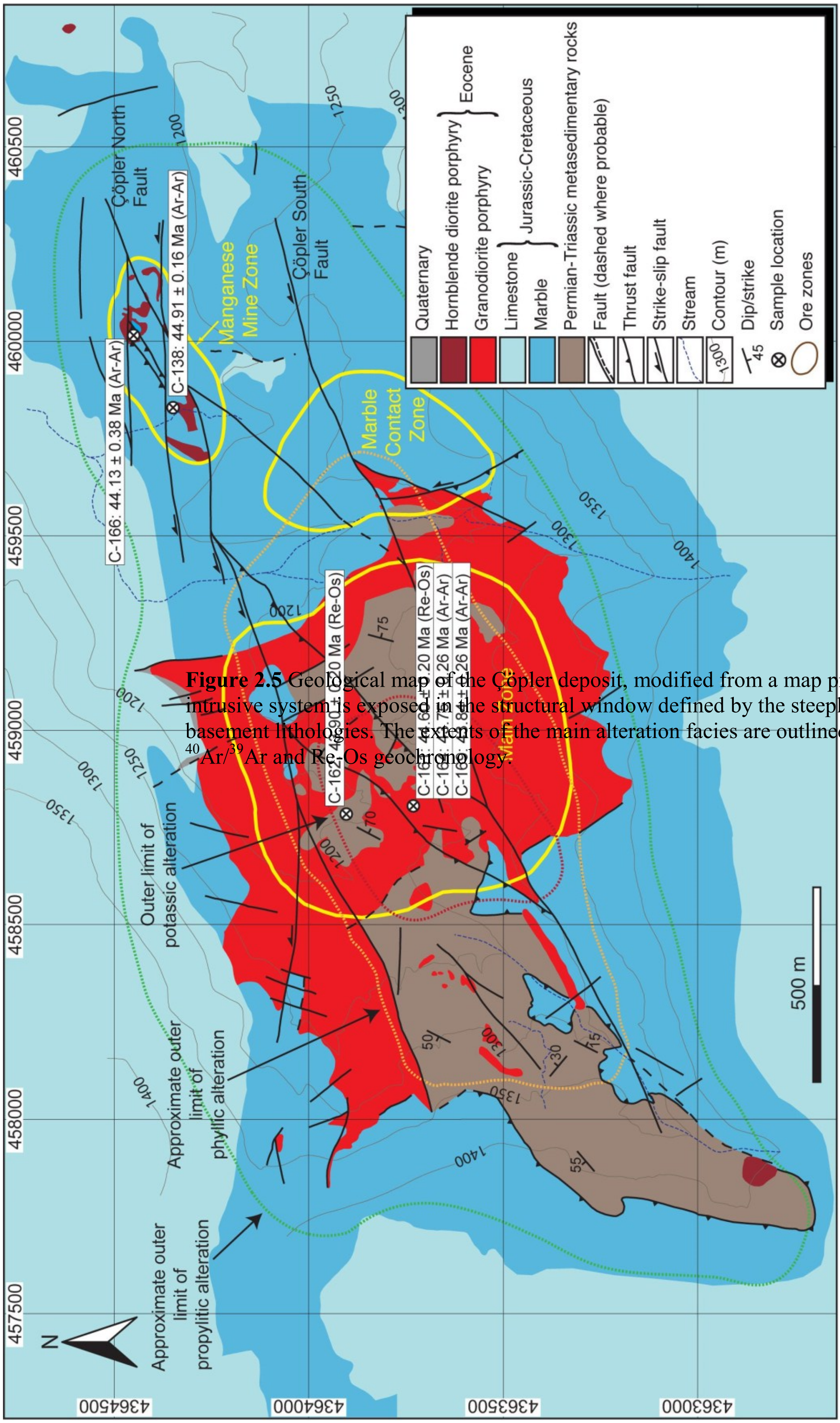

Figure 2.5 Geological map of the Çöpler deposit, modified from a map prepared by Anatolia Minerals Develop
intrusive system is exposed in the structural window defined by the steeply-dipping Çöpler North and South Fa
basement lithologies. The extents of the main alteration facies are outlined by surface projection of drillhole dat
^{40}Ar/^{39}Ar and Re-Os geochronology.

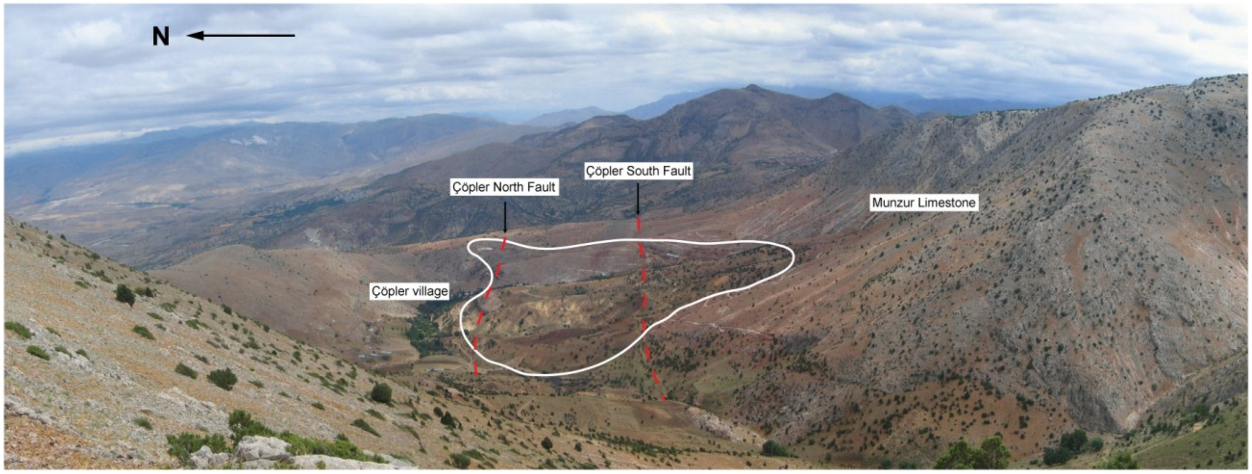

Figure 2.6 Photograph showing the main Çöpler window, looking east. Dashed red lines indicate traces of the Çöpler North and South Faults. Also outlined is the approximate extent of the porphyry–epithermal mineralization (white line; ~900 m-wide in this view). Resistant hills lying to the south and north of these faults are carbonate rocks of the Munzur platform. The main peak in the background (approximately 4 km to the east) is a Cretaceous ophiolite nappe thrust onto these carbonate rocks. The low-lying area in the far left (northeast) is part of the Tertiary Sivas Basin.

Quartz diorite: Quartz diorite occurs as NW-oriented lensoidal bodies to the east of Çöpler, along the eastern side of a NNW-trending structure (Fig. 2.4). This unit, previously named the Yakuplu Pluton (Özer, 1994; Özer and Öner, 1999), consists of medium-grained, subhedral to euhedral phenocrystic quartz, plagioclase, biotite, and hornblende, with minor magnetite (Fig. 2.7D, 2.8C). Similar to the granodiorite porphyry, quartz diorite also commonly contains mafic enclaves (Fig. 2.7D). The quartz diorite exhibits weak propylitic alteration readily recognized by crosscutting veinlets of epidote, and mafic phenocrysts partially rimmed by chlorite along with lesser amounts of epidote and carbonate.

Diorite porphyry: A relatively small stock of diorite porphyry occurs to the northeast of Kabataş (Fig. 2.4). The diorite porphyry is unaltered, and consists of phenocrystic plagioclase and clinopyroxene, in a groundmass of plagioclase microcrysts and substantial amounts of magnetite (Fig. 2.8D). Euhedral plagioclase phenocrysts (0.1–0.5 mm) display either polysynthetic twinning or oscillatory zoning, whereas clinopyroxene phenocrysts (0.2–0.5 mm) commonly occur in glomeroporphyritic clusters.

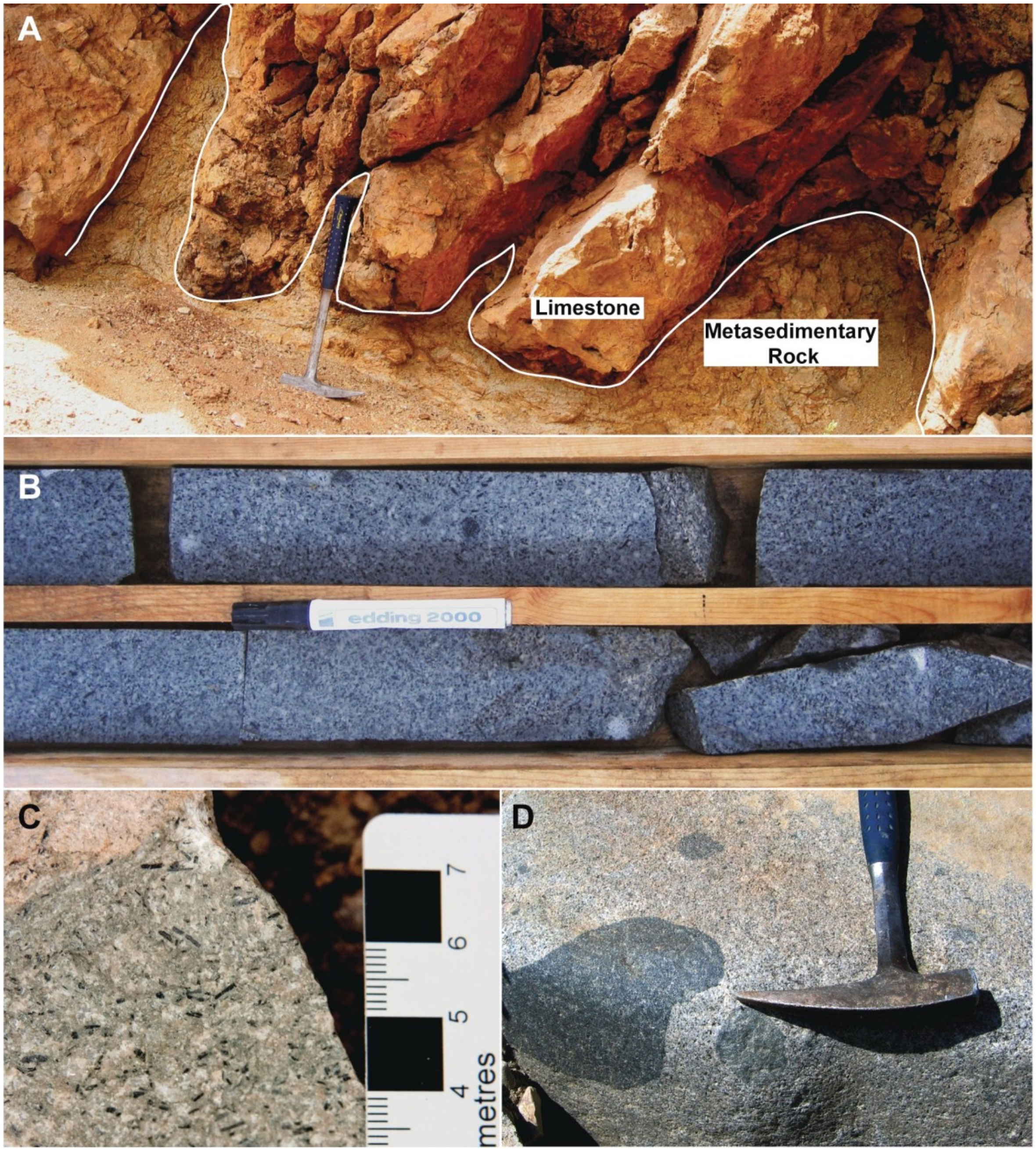

Figure 2.7 Photographs of the main lithologic units in the Çöpler-Kabataş area. (A) Permo-Triassic metasedimentary basement rocks and the overlying Munzur limestone. The contact between the two units is characterized by deformation structures with metasedimentary rock injections into the base of the overlying limestone (0457248E, 4362979N). (B) Granodiorite porphyry intrusion from the Çöpler Main Zone with centimeter-sized biotite-rich xenoliths (CDD-002, 293-294 m; 0458972E, 4363881N). (C) Relatively fresh hornblende diorite porphyry from the Manganese Mine Zone (near 0460177E, 4364450N); the slightly green coloration is due to weak propylitic alteration of the matrix. (D) Weakly propylitized quartz diorite containing hornblende- and plagioclase-rich xenoliths, exposed approximately 1 km to the east of the Çöpler area (0461485E, 4365002N).

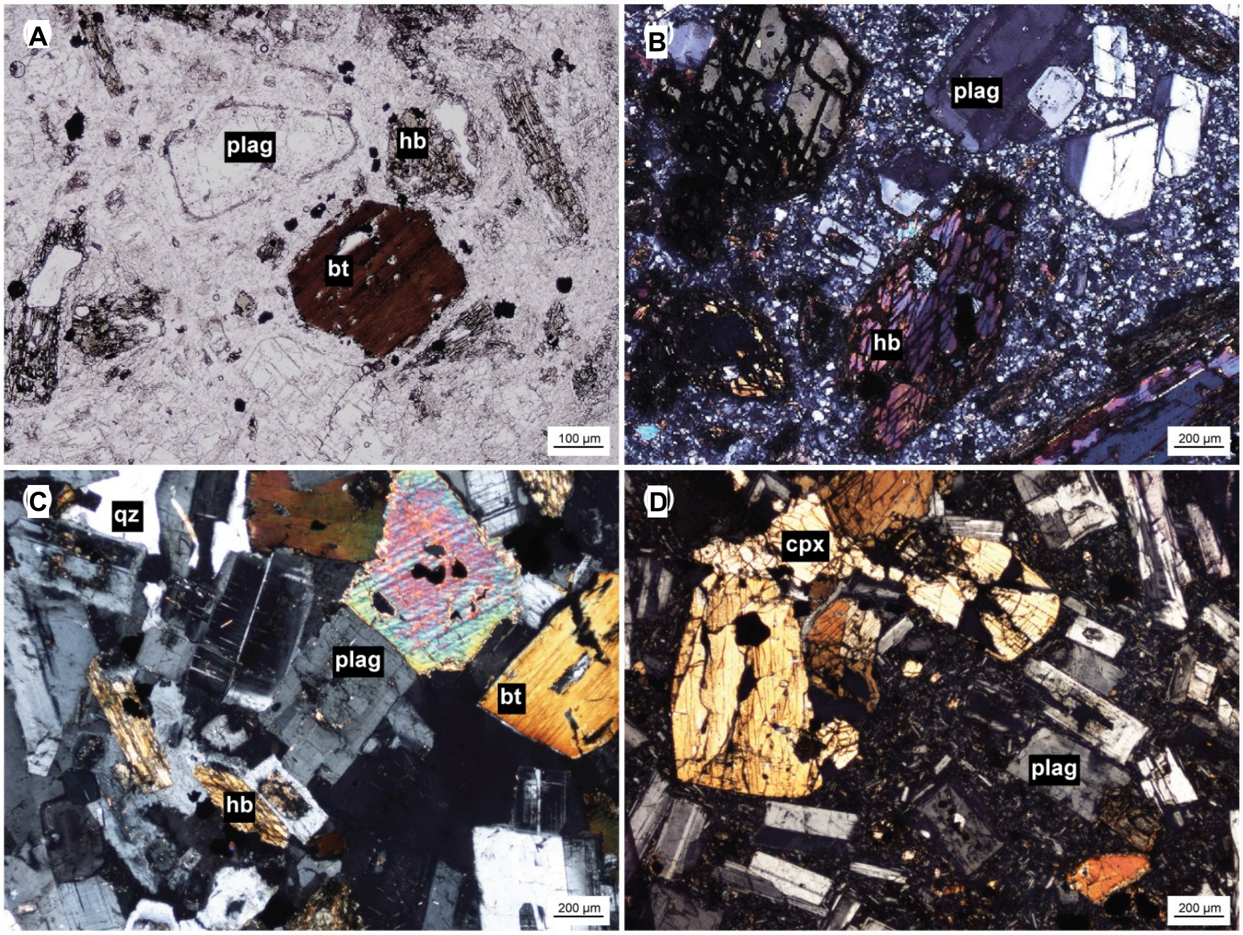

Figure 2.8 Photomicrographs in (A) plane- and (B–D) cross-polarized light of intrusive rocks from the Çöpler-Kabataş magmatic complex. (A) Granodiorite porphyry from the Çöpler Main Zone, with biotite, hornblende, and plagioclase phenocrysts, set in a groundmass of quartz, plagioclase, and magnetite (sample C-164; CDD-140, 106 m; 0458723E, 4363842N). (B) Hornblende diorite porphyry from the Çöpler Manganese Mine Zone, with large hornblende and plagioclase phenocrysts, set in a quartzofeldspathic groundmass (sample C-166; CDD-159, 26 m; 0460072E, 4364353N). (C) Equigranular quartz diorite from east of the Çöpler window, with abundant plagioclase, biotite, and lesser quartz and hornblende (sample CR-02; 0464761E, 4362274N). (D) Clinopyroxene-bearing diorite porphyry from near Kabataş, with abundant plagioclase and glomeroporphyritic clinopyroxene phenocrysts, set in a glassy groundmass containing plagioclase microcrysts (sample CR-03; 0467648E, 4362274N)

2.4.3 Structure

The Çöpler intrusive system and the underlying basement succession are disrupted by several sets of high-angle faults. The predominant structural features within the Çöpler window are the ENE-trending Çöpler North and South Faults that are related to Late Cretaceous–Eocene sinistral deformation along the regional Göksu-Yazyurdu Fault Zone (Fig. 2.5). NE–SW-trending extensional structures linking the ENE-trending faults, and E–W-trending sinistral faults also developed in relation to middle Eocene transtensional deformation, and facilitated shallow level magma emplacement and hydrothermal mineralization at Çöpler. The NE–SW-trending structures were later reactivated as reverse faults during later minor contractional deformation. A fourth set of NNW-trending faults truncates the granodiorite porphyry, and locally offsets the earlier fault sets. All structures at Çöpler have been reactivated on several occasions as evidenced by post-emplacement faulting and brecciation (Fig. 2.5).

2.5 Porphyry Cu-(Au) and Epithermal Au Mineralization and Alteration at Çöpler

A brief account of the alteration and mineralization styles at Çöpler is provided below as a context for the geochronological data. A more detailed account will appear in a later publication that focuses on ore formation.

Low-grade porphyry Cu-Au and superimposed epithermal Au mineralization occur in three different zones at Çöpler: the Main Zone, the Marble Contact Zone, and the Manganese Mine Zone (Fig. 2.5). Each zone displays distinct hydrothermal alteration and mineralization features. The Main Zone is characterized by high temperature porphyry-style alteration and Cu-(Au) mineralization centered around the granodiorite porphyry. Here, early potassic alteration, consisting of hydrothermal biotite and K-feldspar, forms an inner core with associated quartz-magnetite-chalcopyrite-pyrite ± molybdenite veinlets. The central potassic alteration zone grades outwards into a laterally more extensive phyllic alteration zone which is readily distinguished by pervasive sericite-quartz alteration and stockwork quartz-pyrite veinlets. Both alteration styles are enveloped by a propylitic alteration assemblage of chlorite-epidote-carbonate developed peripheral to the Main Zone.

Epithermal-style mineralization is locally superimposed on the early porphyry-style mineralization within the Main Zone, but is best developed in the Marble Contact and Manganese Mine Zones. The Marble Contact Zone is proximal to the Main Zone, and occupies the southeast margin of the granodiorite porphyry, whereas the Manganese Mine Zone is delimited by two E–W-trending secondary fault systems and related extensional structures in the northeastern sector of the property (Fig. 2.5). Both zones consist of Au-bearing quartz-carbonate-sulfide ± barite veins and Au-bearing manto-type carbonate replacement bodies of massive sulfides along the basal contact of the Munzur limestone, which have largely been oxidized to gossan, particularly in the Manganese Mine Zone. In these oxidized zones, hypogene Mn-carbonates (rhodochrosite or manganocalcite) have been altered to manganese wad.

2.6 Sampling and Analytical Methods

2.6.1 Sample Selection

Samples for petrographic, whole-rock geochemical and geochronological analysis were collected from diamond drill core at the Çöpler deposit, and outcrop exposures within or nearby the Çöpler-Kabataş magmatic complex. A summary of sample descriptions and locations is provided in Appendix A.

Twelve drill core and outcrop samples of least-altered (6) and altered (6) igneous rocks from the Çöpler-Kabataş magmatic complex were analyzed for their major and trace element compositions. In addition, nine other samples of fresh igneous rocks from elsewhere across the central eastern Taurides were collected and analyzed for comparison purposes. Five of these regional samples were obtained from Eocene intrusions near Bizmişen, Çaltı, Doğanşehir, Horoz, and Karamadazı (Fig. 2.1, 2.3), three samples were collected from Late Cretaceous intrusions near Divriği, and one sample was collected from the Miocene Yamadağ volcanic center to the south of Divriği.

Altered samples from the Çöpler-Kabataş magmatic complex contain either an overprinting propylitic alteration assemblage of chlorite, epidote, and carbonate, or a phyllic alteration assemblage consisting of sericite replacing mafic minerals and plagioclase, as reflected in their relatively high loss-on-ignition values (Appendix B).

Three samples containing igneous biotite and/or hornblende were selected for ^{40}Ar/^{39}Ar incremental step-heating analysis from a suite of least-altered plutonic rocks from the Çöpler-Kabataş magmatic complex. Two potassic (biotite) and phyllic (sericite) altered samples were also analyzed to constrain the timing of hydrothermal alteration related to porphyry mineralization at Çöpler. In addition, three samples of fresh rock containing igneous biotite and/or hornblende were selected from the Bizmişen, Çaltı, and Divriği intrusions in order to constrain the timing of intrusive magmatism elsewhere in the central eastern Taurides.

In order to constrain the timing of porphyry-style mineralization, two molybdenite samples obtained from quartz-magnetite-sulfide veinlets within the Çöpler Main Zone were analyzed by the Re-Os method.

2.6.2 Whole-rock geochemistry

Sample preparation and whole-rock geochemical analyses of twenty one igneous rock samples were carried out at Actlabs Laboratories in Ontario, Canada. Major and trace element compositions were obtained by a combination of inductively coupled plasma (ICP), inductively coupled plasma emission mass spectrometry (ICP-MS), and instrumental neutron activation analysis (INAA) methods. Replicate analyses of international standards indicate accuracy to within 5 relative percent for major and minor elements, and to within 10 relative percent of the standard values for trace elements. Results are listed in Appendix B, and major oxide compositions were recalculated to a volatile-free basis totalling 100 wt. % for plotting and classification purposes.

2.6.3 $^{40}Ar/^{39}Ar$ geochronology

Mineral separates of biotite, hornblende, and sericite were prepared at the University of Alberta using crushing/sieving, and standard heavy liquid and magnetic separation techniques. Individual grains were then hand-picked under a binocular microscope, and sent to the Noble Gas Laboratory, Pacific Centre for Isotopic and Geochemical Research, University of British Columbia, Canada, for analysis by T. Ullrich. Samples and flux monitors were wrapped in aluminum foil and sent for irradiation at the McMaster University reactor in Canada. After irradiation, the samples were heated in incremental steps under the defocused beam of a 10W CO_2 laser (New Wave Research MIR10) until fused. The Ar isotopic composition of the gas emitted from each step was analyzed using a VG5400 mass spectrometer. Isotopic ratios were corrected for total system blank, mass spectrometer sensitivity, mass discrimination, radioactive decay of ^{37}Ar and ^{39}Ar during and subsequent to irradiation, and interfering argon from atmospheric contamination and the irradiation of Ca, Cl, and K.

2.6.4 Re-Os geochronology

Selected quartz-magnetite-sulfide vein samples were pulverized in a porcelain disk mill, and molybdenite was then separated from other sulfide and gangue phases using heavy liquid techniques, magnetic separation, and by flotation using high-purity water. Finally, molybdenite grains were handpicked under a binocular microscope.

The ^{187}Re and ^{187}Os concentrations in molybdenite were determined by isotope dilution mass spectrometry at the University of Alberta Radiogenic Isotope Facility. Dissolution of molybdenite separates and equilibration of sample and tracer Re and Os were done using the Carius tube method (Shirey and Walker, 1995).

Samples were dissolved and equilibrated with a “mixed double” spike containing a known amount of ^{185}Re + ^{188}Os + ^{190}Os in 8 ml of reverse aqua regia (3:1, 16 N HNO_3: 12 N HCl) at 220°C for 48 hours. Os and Re were separated by solvent extraction, microdistillation, and anion chromatography techniques (Selby and Creaser, 2004). The purified Os and Re fractions were loaded onto Ba-coated Pt or Ni filaments and measured with Faraday collectors using negative thermal ionization mass spectrometry (Creaser et al., 1991; Völkening et al., 1991) on a Micromass Sector 54 mass spectrometer. Total procedure blanks are on the order of <5 pg for Re, and <2 pg for Os.

Errors (2σ) include uncertainties in Re and Os isotopic measurements, Re and Os isotope composition reproducibility of standards, calibration and gravimetric uncertainties of ^{187}Re and ^{187}Os, and uncertainties in the ^{187}Re decay constant. Uncertainties in weights of sample and tracer solution do not affect the calculated age and are not considered.

2.7 Whole-Rock Geochemistry of the Çöpler-Kabataş Magmatic Complex

The results of whole-rock geochemical analyses are listed in Appendix B.

2.7.1 Major elements

Least-altered and altered intrusive and hypabyssal igneous rocks from the Çöpler-Kabataş magmatic complex are plotted on a total alkali versus silica diagram in Figure 2.9 (after Middlemost, 1994). All least-altered samples from the Çöpler-Kabataş magmatic complex display sub-alkaline character (medium- to high-K calc-alkaline), and most plot within the granodiorite field, with silica contents ranging from 63.7 to 68.1 wt.%. Three samples have lower silica contents (between 56.4 and 58.1 wt.% SiO_2), with one least-altered sample (CR-03) and one propylitically altered sample (C-166) plotting within the diorite field, and another propylitically altered sample (CR-14) lying in the monzonite field. The slightly elevated alkali contents of the two propylitically altered samples might be due to sericitization of feldspars, and are not thought to reflect primary magma compositions. A compositional gap (between 58 and 64 wt.% SiO_2) exists between the fresh diorite porphyry (CR-03) and the rest of the least-altered igneous lithologies from the magmatic complex.

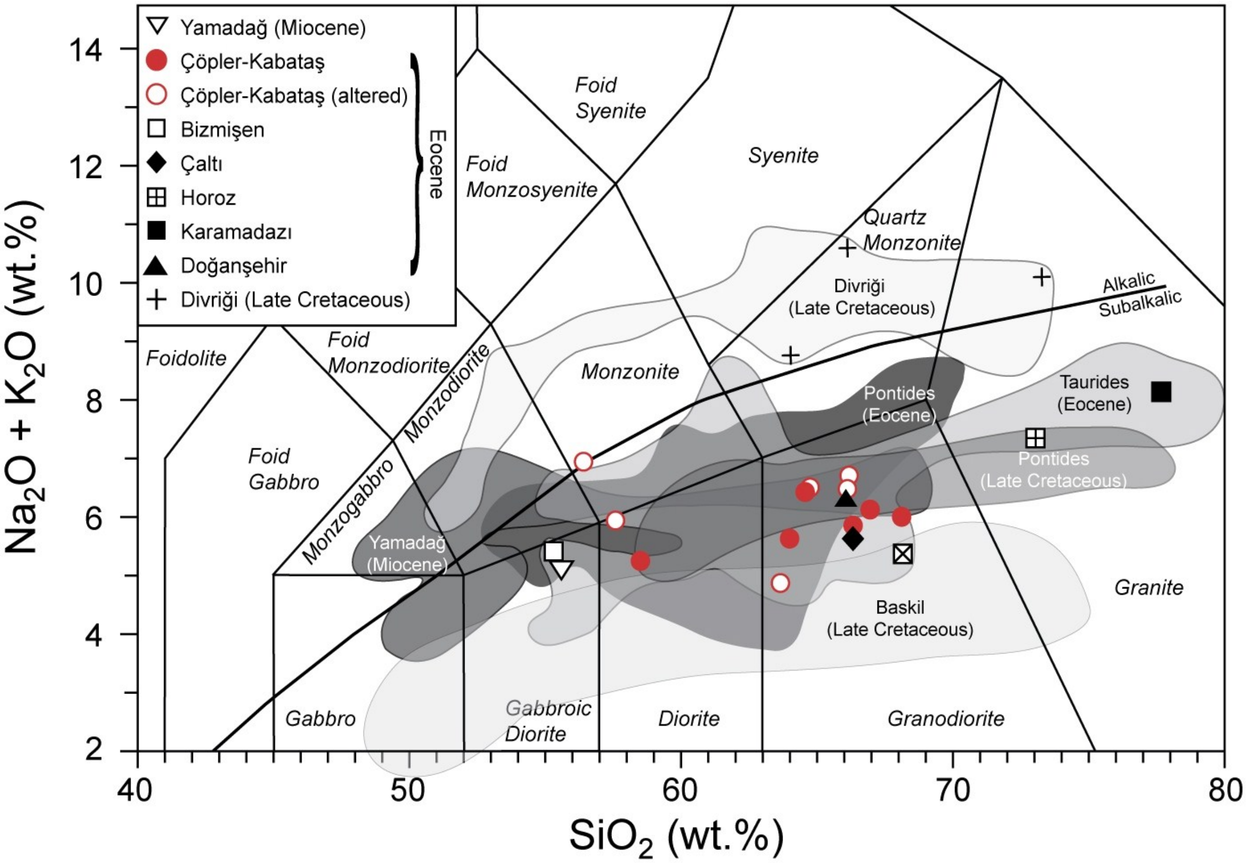

Figure 2.9 Total-alkali versus silica diagram (after Middlemost 1994) for least altered and altered intrusive rocks from the Çöpler-Kabataş magmatic complex (data recalculated 100% volatile-free) plotted together with a suite of regional samples obtained from various Late Cretaceous–Eocene intrusive systems across the central eastern Taurides, and one extrusive rock sample from the Yamadağ volcanic center. Also plotted are the ranges of compositions from the same localities as well as felsic to intermediate compositions from the Eocene Pontide magmatic belt as compiled from previously published data. Data sources: Eocene Tauride intrusions: Gençalioğlu-Kuşcu et al. (2001), Önal et al. (2005), Kadıoğlu and Dilek (2010); Divriği: Boztuğ et al. (2007); Yamadağ volcanic center: Kürüm et al. (2008); Baskil intrusive complex: Rızaoğlu et al. (2009), Pontides: Karslı et al. (2007, 2010a, b). Alkaline-subalkaline boundary from Irvine and Baragar (1971).

Major and minor oxide compositions of the least-altered magmatic rocks from the Çöpler-Kabataş magmatic complex define roughly linear trends when plotted against SiO_2 on Harker-type diagrams (Fig. 2.10), suggesting a similar parentage for these rocks. Most major oxides display weak to moderate negative trends with increasing silica content, consistent with fractional crystallization of minerals such as pyroxene, amphibole, and plagioclase, which occur as phenocryst phases. Na_2O, on the other hand shows a nearly flat trend, whereas K_2O abundance increases slightly with increasing silica content until late stages of fractionation (~67 wt.% SiO_2).

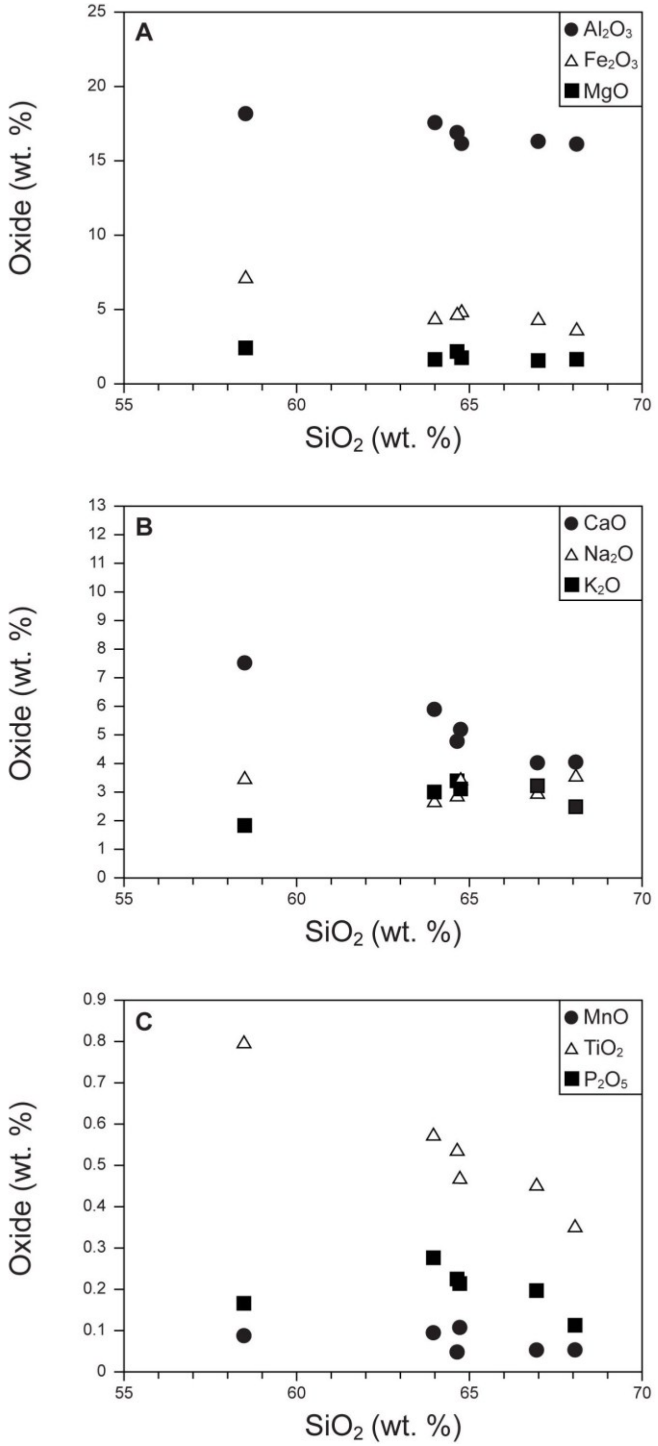

Figure 2.10 Harker diagrams showing variation of major and minor oxide abundances relative to SiO_2 for least altered intrusive rocks from the Çöpler-Kabataş magmatic complex.

2.7.2 Trace elements

All samples from the Çöpler-Kabataş magmatic complex have similar trace element compositions, as illustrated on a primitive mantle-normalized trace element diagram (Fig. 2.11). The samples are enriched in incompatible elements, particularly large ion lithophile elements (LILE) when compared to high field strength elements (HFSE). Positive peaks for Pb and Sb, and negative anomalies for Nb, Ta, and Ti are typical of magmas related to subduction (Brenan et al., 1994; Stolz et al., 1996).

Rare earth elements (REE) in Çöpler-Kabataş samples show distinctive listric-shaped patterns on a chondrite-normalized diagram (Fig. 2.12), with moderate enrichments in light rare earth elements (LREE) relative to middle (MREE) and heavy rare earth elements (HREE), and flat to upward-trending (listric) slopes between MREE and HREE (Fig. 2.12). This pattern is commonly ascribed to hornblende fractionation or residual hornblende in the source region, because hornblende preferentially partitions MREE (Frey et al., 1978; Hanson, 1980). The lack of significant europium anomalies is indicative of either oxidizing conditions (Eu^{3+} cannot be incorporated into plagioclase) and/or hydrous conditions (early plagioclase crystallization being suppressed) during evolution of the Çöpler-Kabataş magmas (Hanson, 1980; Carmichael and Ghiorso, 1990; Moore and Carmichael, 1998). The oxidized and hydrous nature of these magmas is further supported by the abundance of hornblende as a phenocryst phase, and the widespread presence of magnetite.

2.8 $^{40}Ar/^{39}Ar$ geochronology

A summary of the of $^{40}Ar/^{39}Ar$ dating results is presented in Table 2.1, and apparent age spectra are illustrated in Figure 2.13; full analytical data are listed in Appendix C. Plateau ages are defined using the criteria of Fleck et al. (1977). All samples yielded moderately- to well-defined plateaus and calculated plateau ages that are within error of the inverse isochron ages.

Igneous biotite from granodiorite porphyry (C-164), igneous hornblende from hornblende diorite porphyry (C-166), and igneous biotite from quartz diorite (CR-02) from the Çöpler intrusive complex yielded plateau ages of 43.75 ± 0.26 Ma (MSWD = 0.20), 44.13 ± 0.38 Ma

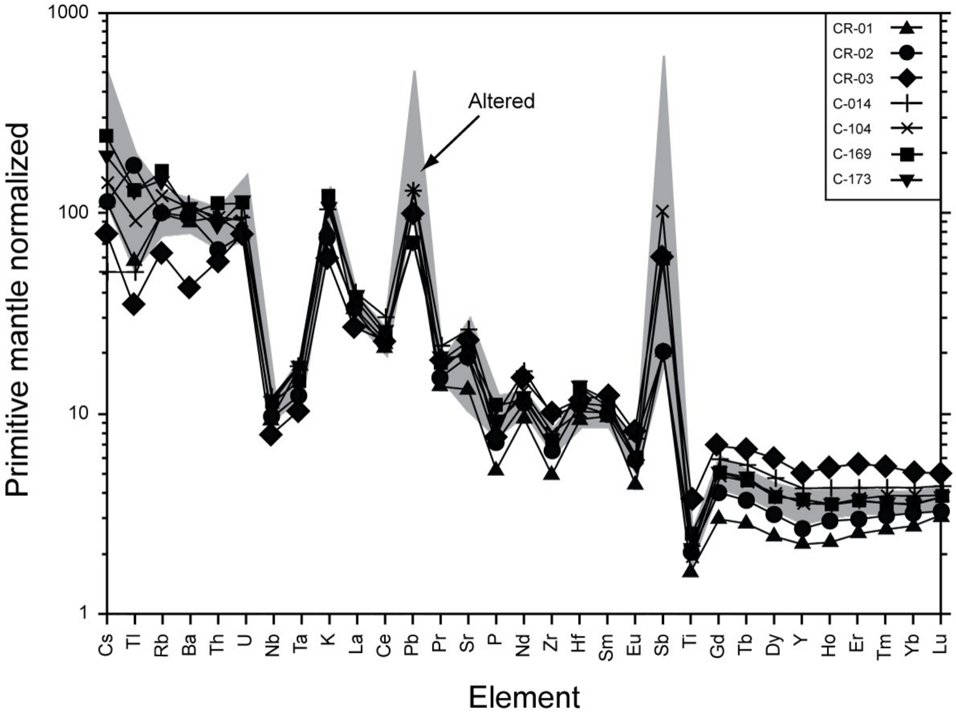

Figure 2.11 Primitive mantle-normalized trace element diagram for least altered igneous rocks from the Çöpler-Kabataş magmatic complex. Grey area represents altered samples from the region, and the close overlap between least altered and altered samples indicates that hydrothermal alteration has had minimal effect on most trace element compositions in this suite. Normalization values from Sun and McDonough (1989)

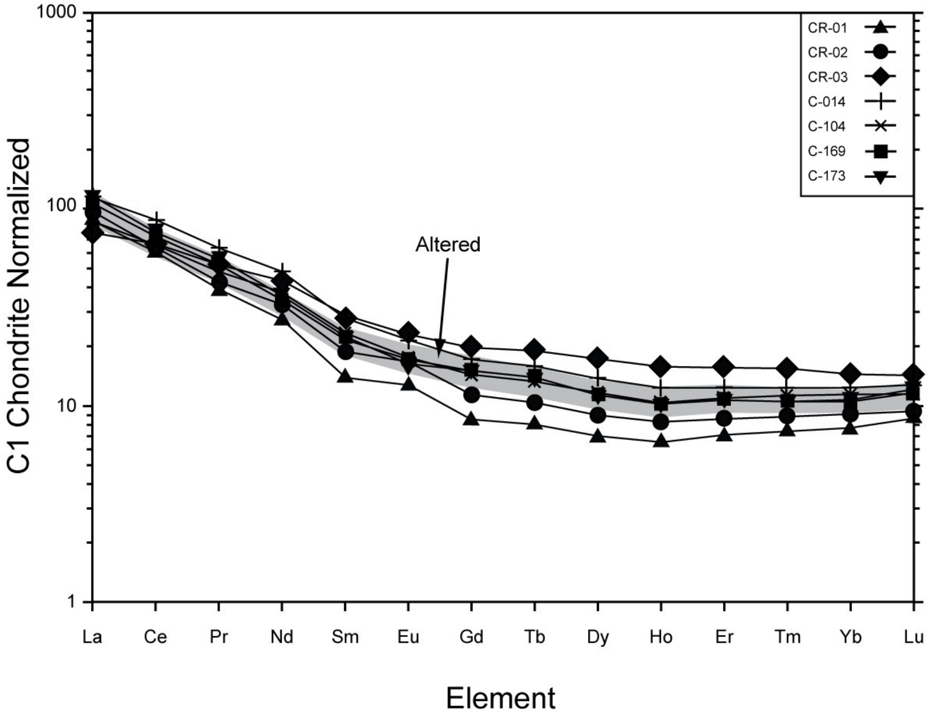

Figure 2.12 Chondrite-normalized REE diagram for least altered igneous rocks from the Çöpler-Kabataş magmatic complex. Grey area represents altered samples from the region, showing that alteration has not affected rare earth element compositions in these rocks. Normalization values from Sun and McDonough (1989)

(MSWD = 1.4), and 44.19 ± 0.23 Ma (MSWD = 0.49), respectively (Fig. 2.13A–C). These dates overlap within error and are interpreted to represent cooling ages for these samples.

^{40}Ar/^{39}Ar analysis of hydrothermal alteration minerals associated with mineralization at Çöpler yielded plateau ages close to or overlapping the ages of igneous minerals. Hydrothermal biotite from porphyry-style potassic alteration in sample C-169 yielded a plateau age of 43.84 ± 0.26 Ma (MSWD = 0.63; Fig. 2.13D). Sericite from phyllic alteration in sample C-138 yielded a downward stepping spectrum suggesting the presence of minor excess ^{40}Ar in early steps (Fig. 2.13E), but the second half of the spectrum includes an acceptable six-step plateau containing more than 50% of total ^{39}Ar released, with an age of 44.44 ± 0.28 Ma (MSWD = 1.05), which should be considered a maximum age. An alternative estimate in samples containing excess ^{40}Ar is provided by the inverse isochron age, which in this case was almost within error of the plateau age at 45.22 ± 0.74 Ma (MSWD = 0.23).

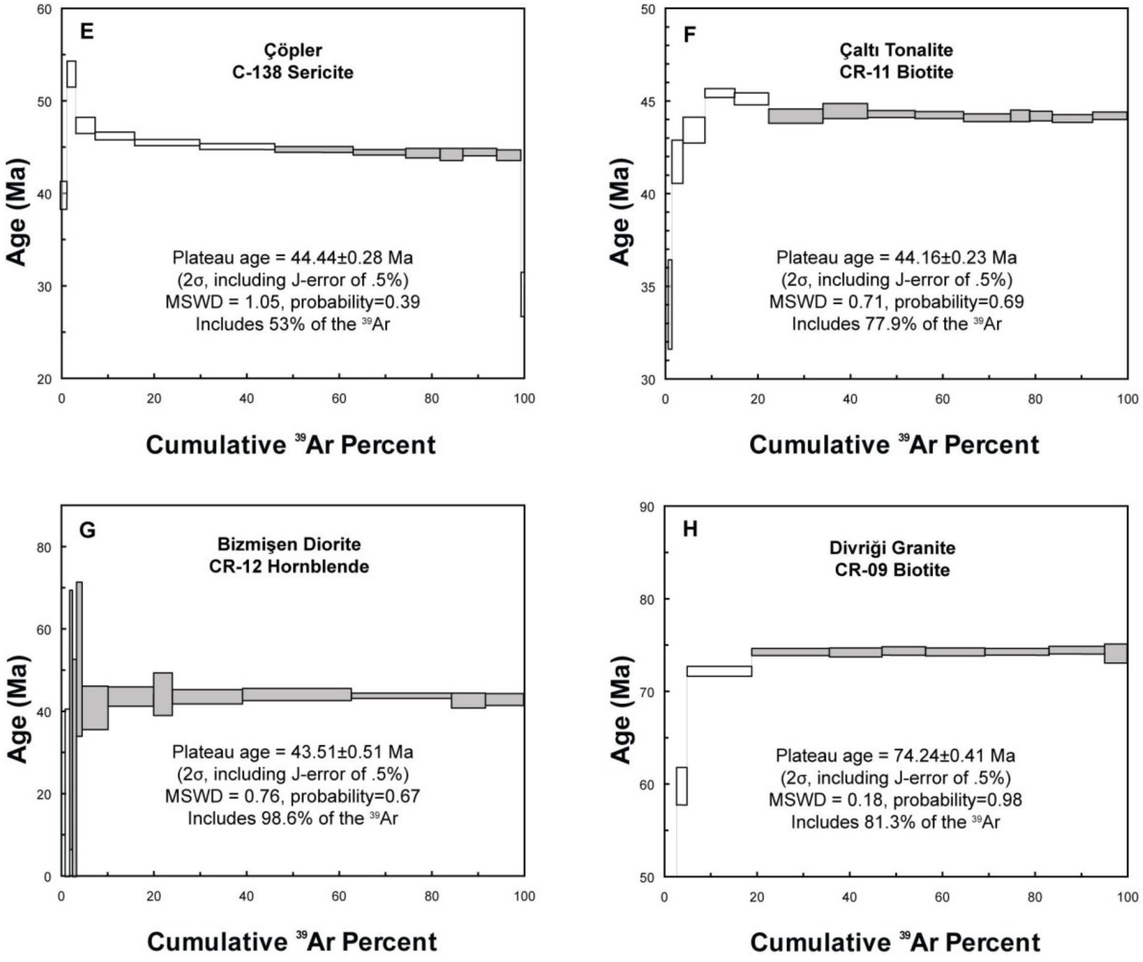

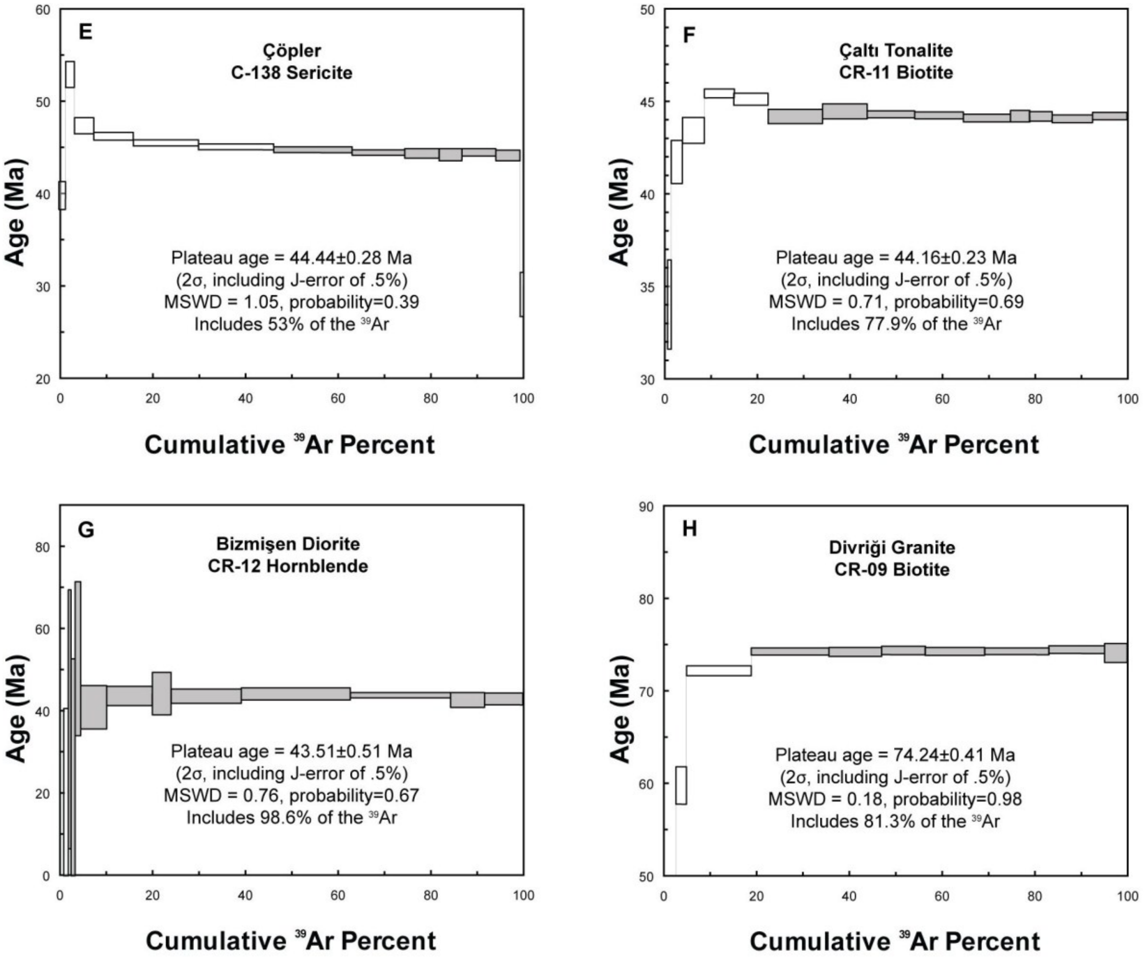

Figure 2.13 Apparent ^{40}Ar/^{39}Ar age spectra for igneous and hydrothermal minerals from the Çöpler-Kabataş magmatic complex. (A-C), hydrothermal biotite and sericite from the Çöpler porphyry deposit (D-E), and igneous biotite from nearby central eastern Tauride intrusive centers (F-H). See Appendix A for sample locations and descriptions. Locations of the samples from the Çöpler deposit are also shown in Figure 2.5. Results are summarized in Table 2.1, and full data are listed in Appendix C.

Two samples from the Çaltı (CR-11) and Bizmişen (CR-12) intrusions yielded well-defined plateau ages of 44.16 ± 0.23 Ma (MSWD = 0.71) and 43.51 ± 0.51 Ma (MSWD = 0.76), respectively (Fig. 2.13F, G), which are similar to the ages from Çöpler. A granite sample (CR-09) from the Divriği area also yielded a well-constrained plateau age of 74.24 ± 0.41 Ma (MSWD = 0.18; Fig. 2.13H), about 30 m.y. older than the Çöpler magmatic system, and consistent with the data previously published by Boztuğ et al. (2007) and Kuşcu et al. (2007).

ng results from the Çöpler-Kabataş magmatic complex and Bizmişen, Çaltı, and Divriği intrusions

Sample no.	**Lithology**	**Mineral**	**Integrated age ±2σ (Ma)**	**Plateau age ±2σ (Ma)**	**MSWD**	**No. of steps in plateau/total steps**	**% ^{39}Ar released (plateau)**	**Inverse isochron age ±2σ (Ma)**	**MSWD**	**Initial ^{40}Ar/^{36}Ar[1]**
Igneous minerals: Çöpler-Kabataş Magmatic Complex										
C-164	Granodiorite porphyry	Biotite	43.29 ± 0.21	43.75 ± 0.26	0.20	6/9	94	43.70 ± 0.28	0.19	289 ± 24
C-166	Hornblende diorite porphyry	Hornblende	44.43 ± 0.42	44.13 ± 0.38	1.4	8/11	100	43.74 ± 0.49	0.69	307 ± 12
CR-02	Quartz diorite	Biotite	43.97 ± 0.11	44.19 ± 0.23	0.49	11/18	89.5	44.17 ± 0.26	0.65	294 ± 23
Hydrothermal minerals: Çöpler										
C-169	Potassically altered porphyry	Biotite	43.22 ± 0.24	43.84 ± 0.26	0.63	11/17	90.5	43.86 ± 0.30	0.49	292.9 ± 5.1
C-138	Sericitized porphyry	Sericite	44.91 ± 0.16	44.44 ± 0.28	1.05	6/13	53	45.22 ± 0.74	0.23	148 ± 130
Igneous minerals: Çaltı and Bizmişen intrusions										
CR-11	Tonalite	Biotite	44.11 ± 0.11	44.16 ± 0.23	0.71	9/16	77.9	43.68 ± 0.26	1.4	476 ± 36
CR-12	Diorite	Hornblende	42.36 ± 1.11	43.51 ± 0.51	0.76	11/14	98.6	43.40 ± 0.64	0.82	293 ± 2.7
Igneous minerals: Divriği intrusion										
CR-09	Alkali feldspar granite	Biotite	72.89 ± 0.22	74.24 ± 0.41	0.18	7/11	81.3	74.24 ± 0.56	0.21	288 ± 45

[1] Expected composition of atmospheric argon

2.9 Re-Os geochronology

Model Re-Os ages were calculated for molybdenite samples C-161 and C-162 from Çöpler, based on the simplified isotope equation: $t = \ln(^{187}Os/^{187}Re+1)/\lambda$, where t is the model age, and λ is the ^{187}Re decay constant (1.666×10^{-11} a^{-1}; Smoliar et al., 1996). The samples yielded ages of 44.6 ± 0.2 Ma and 43.9 ± 0.2 Ma, respectively (Table 2.2), which are similar to each other, and to the ^{40}Ar/^{39}Ar ages of igneous (44.2 ± 0.3 Ma) and hydrothermal (44.4–43.8 Ma) minerals.

Table 2.2 Summary of Re-Os molybdenite data from the Çöpler deposit

Sample no.	**Sample Location**	**Drill hole: depth**	**Re (ppm)**	**^{187}Re (ppm)**	**^{187}Os (ppb)**	**Model Age (Ma)**	**Age uncertainty (±2σ) with decay constant uncertainty (Ma)**
C-161	0458723 E 4363842 N	-	7031	4419	3284	44.6	0.2
C-162	0458802 E 4363880 N	CDD-140: 180.0–180.1m	2242	1409	1031	43.9	0.2

2.10 Discussion

2.10.1 Interpretation of Geochronological Data

New geochronological data presented herein constrain the temporal relationship between magmatic and hydrothermal events at the Çöpler-Kabataş magmatic complex. With the exception of two samples, combined ^{40}Ar/^{39}Ar and Re-Os ages of igneous and hydrothermal minerals from Çöpler are analytically indistinguishable from each other suggesting rapid cooling conditions within a period of ≤1 m.y (Fig. 2.14). This is consistent with the simple intrusive history and the relatively shallow level of emplacement directly beneath the Munzur limestone, which has a maximum thickness of 1,200 m (Özgül and Turşucu, 1984; Tunç et al., 1991).

The plateau age of sericite sample obtained from phyllic-altered granodiorite porphyry (44.44 ± 0.28 Ma) and the Re-Os age of one molybdenite-bearing quartz-sulfide vein (44.6 ± 0.2 Ma) are notably older than the ^{40}Ar/^{39}Ar plateau age of igneous biotite (43.75 ± 0.26 Ma) obtained from the host granodiorite porphyry (Fig. 2.14). This discrepancy between the igneous and hydrothermal dates likely suggests thermal resetting of the igneous biotite and hornblende during high temperature potassic alteration, and therefore, at least the younger ^{40}Ar/^{39}Ar dates probably represent cooling ages rather than the crystallization age of the Çöpler intrusion. If this is the case, then the older molybdenite age can be explained by the high closure temperature of molybdenite (>700ºC; Bingen and Stein, 2003) compared to the Ar diffusion blocking temperature of biotite (280º–340ºC; McDougall and Harrison, 1999) and hornblende (~490º–580ºC; Harrison, 1981).

However, based on the close agreement between these cooling ages and the plateau age of igneous biotite (44.19 ± 0.23 Ma) from unaltered quartz diorite immediately to the east of Çöpler, it can be inferred that the hydrothermal event resetting the Ar isotopic system of igneous biotite and hornblende from Çöpler is only slightly younger than the age of pluton emplacement at the Çöpler-Kabataş magmatic complex. This interpretation is further supported by the ^{40}Ar/^{39}Ar dates of igneous biotite and hornblende from the unaltered Çaltı and Bizmişen plutons, which yielded plateau ages of 44.16 ± 0.23 Ma and 43.51 ± 0.51 Ma, respectively.

Molybdenite samples from two quartz-magnetite-sulfide veins from the Çöpler Main Zone yielded Re-Os ages of 44.6 ± 0.2 Ma and 43.9 ± 0.2 Ma, which do not overlap within error. These different ages may represent discrete pulses of molybdenite mineralization, although there is no field or petrographic evidence to confirm this hypothesis.

The timing of the paragenetically later epithermal-style mineralization, on the other hand, could not be determined due to its poor preservation. Minerals such as adularia or sericite, which may have originally been present, have been destroyed by intense weathering and oxidization of the shallow epithermal levels of the system. However, there is no evidence to suggest that this stage of mineralization was substantially later than the higher-temperature porphyry-style mineralization.

2.10.2 Petrogenesis of middle Eocene granitoids in the central eastern Taurides

The timing of cooling of the magmatic-hydrothermal system at Çöpler and the inferred crystallization age of the Çöpler-Kabataş magmatic complex (~44 Ma) overlaps with the emplacement ages of the nearby Çaltı (44.16 ± 0.23 Ma) and Bizmişen intrusions (43.51 ± 0.51 Ma), and is slightly younger than the cooling ages of the Horoz, Karamadazı, and Doğanşehir plutons (50–48 Ma; Kuşcu et al., 2007; Karaoğlan et al., 2009) located farther to the southwest. Together, these intrusive centers define a middle Eocene calc-alkaline suite in the central and eastern Taurides, with broadly similar trace element compositions (including enrichments in LREE, negative anomalies of HFSE such as Nb, Ta, Zr, and Ti, and listric-shaped REE patterns; Fig. 2.15A, 2.16A). One sample of evolved granite (CR-28) from Horoz shows stronger depletions in Ba, Sr, P, Eu, and Ti, likely due to extensive fractionation of plagioclase, apatite, and Ti-bearing phases (Fig. 2.15A, 2.16A). In general, however, the geochemical signatures of the middle Eocene granitoids of the central eastern Taurides are consistent with typical arc-related magmatic rocks formed by partial melting of metasomatized mantle wedge above a subducting slab (Brenan et al., 1994; Stolz et al., 1996; Kogiso et al., 1997).

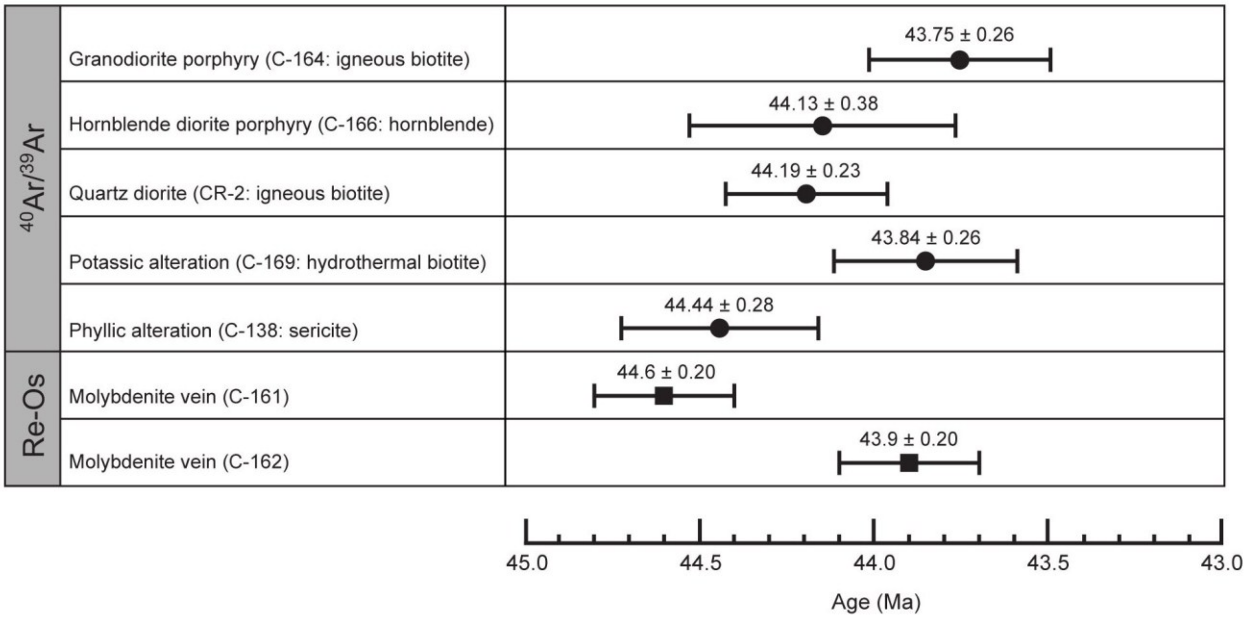

Figure 2.14 Summary of ^{40}Ar/^{39}Ar and Re-Os geochronology results for the Çöpler-Kabataş magmatic complex and the Çöpler gold deposit. ^{40}Ar/^{39}Ar dates are plateau ages and Re-Os dates are model ages. Error bars are reported at 2σ.

The central eastern Tauride granitoids are currently located approximately 140 km north of the Bitlis Suture, and about 120 km north of the Maden and Helete volcanic belt (Fig. 2.1), but these distances may have been larger prior to Miocene collision. Thus, these granitoids may have formed in a back-arc environment behind the main Maden and Helete arc and Bitlis subduction zone.

2.10.3 Late Cretaceous-Eocene Magmatism along the Southeastern TAB Margin (Taurides)

The Late Cretaceous (88–70 Ma) Baskil intrusive complex and several granitoid bodies exposed around Göksun-Afşin area represent the earliest stage of arc magmatism along the southern TAB margin. Geochemical data compiled for a range of mafic to felsic sub-alkaline lithologies (Fig. 2.9) indicate relatively un-enriched compositions compared to the Çöpler-Kabataş suite (Fig. 2.15B, 2.16B), consistent with a continental arc origin for these granitoids (Yazgan and Chessex, 1991; Parlak et al., 2006; Rızaoğlu et al., 2009).

After a period of quiescence in the Paleocene, magmatism along the southern TAB margin resumed in the middle Eocene with eruption of the Maden and Helete volcanic rocks (Fig. 2.1). These basaltic to rhyolitic rocks have sub-alkaline to mildly alkaline character, with enrichments in LILE relative to HFSE, and negative Nb and Zr anomalies (Aktaş and Robertson 1984; Yiğitbaş and Yılmaz 1996a; Elmas and Yılmaz 2003; Robertson et al., 2007). The Helete and Maden suites appear to represent the locus of middle Eocene volcanism above the southern Neotethys subduction zone (Yiğitbaş and Yılmaz 1996a; Robertson et al., 2007).

In comparison, as noted above, the broadly coeval Çöpler-Kabataş magmatic complex, located 120 km further north, likely represents a back arc magmatic system. A similar tectonomagmatic setting may also be invoked for Eocene magmatism along the transtensional Göksu-Yazyurdu and Malatya-Ovacık fault zones. Paleocene–Eocene slab roll-back beneath southeast Anatolia (Robertson et al., 2007; Kaymakçı et al., 2010) may have caused extension in the overriding plate, and subsequent initiation of these back-arc systems, and may also be responsible for the anomalous curvatures of the Bitlis sector of the southern Neotethyan subduction zone and the adjacent Cyprian arc to the southwest (Fig. 2.2C; Schellart and Lister, 2004; Wallace et al., 2009). Similar middle Eocene back-arc magmatism occurred behind the main axis of the Urumieh-Dokhtar arc in Iran (the eastern continuation of the Maden-Helete arc), producing large volumes of calc-alkaline volcanic and plutonic rocks with subduction signatures (LILE-enriched, HFSE-depleted, and LREE-enriched trace element patterns; Ahmadian et al., 2009; Allen 2009; Verdel et al., 2011; Vincent et al., 2005).

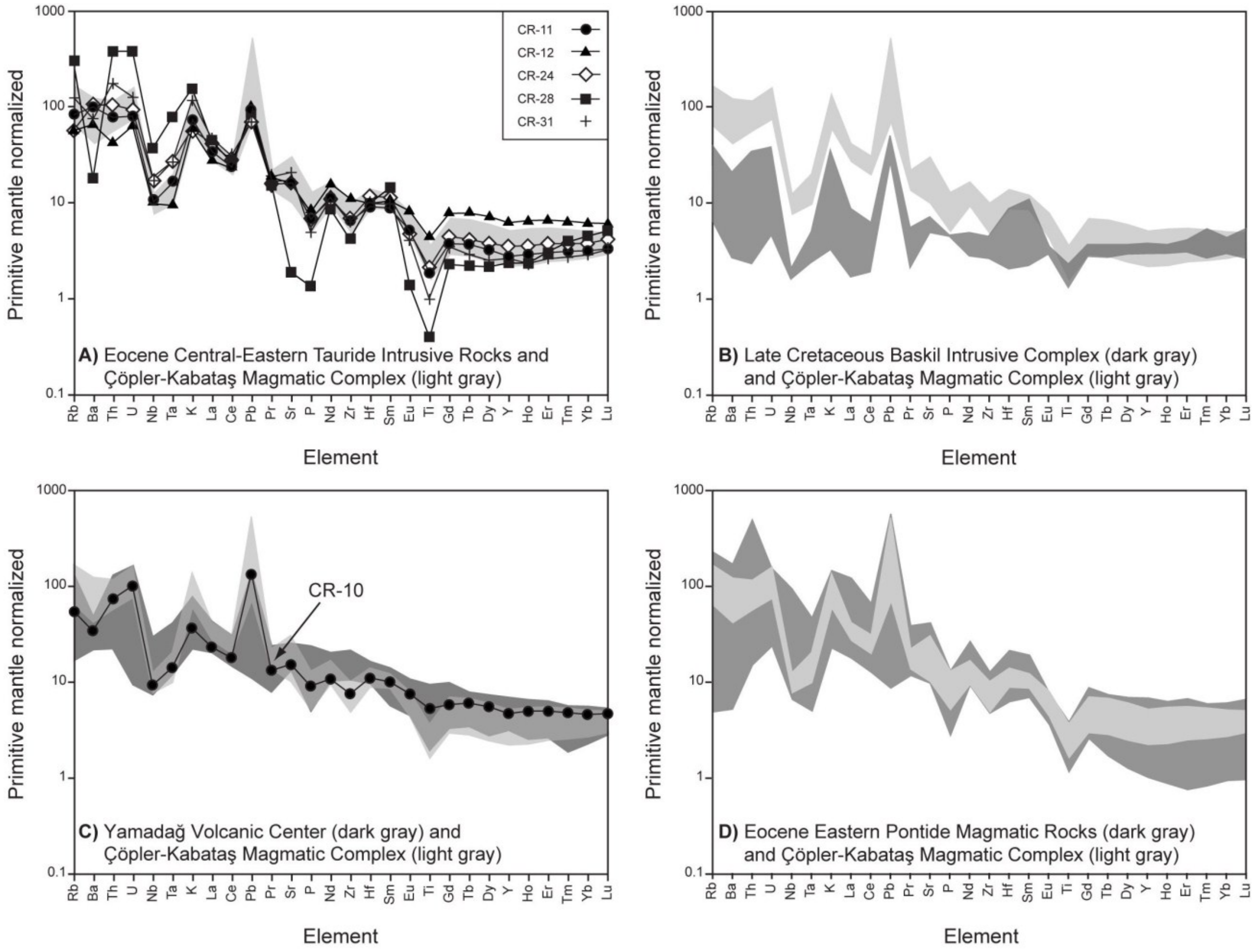

Figure 2.15 Primitive mantle-normalized trace element diagrams, showing compositions of (A) Eocene central-eastern Tauride plutonic rocks, (B) the Late Cretaceous Baskil intrusive complex, (C) the Miocene Yamadağ volcanic center, (D) the middle Eocene eastern Pontide plutonic and volcanic rocks, compared with the range of compositions of igneous rocks from the Çöpler-Kabataş magmatic complex (light grey field). Data sources: Baskil intrusive complex: Rızaoğlu et al. (2009); Yamadağ volcanic center: Kürüm et al. (2008). Normalization values from Sun and McDonough (1989)

On the other hand, Kuşcu et al. (2010) argued that the middle Eocene volcanism at Maden and Helete, and the Eocene central eastern Tauride granitoids were generated in a post-collisional setting, following the termination of Late Cretaceous subduction magmatism in southeast Anatolia. According to this model, incipient rupturing of the steepened slab led to invasion of hot asthenospheric material beneath the southern TAB margin, which caused the delayed partial melting of subduction-modified mantle sources and subsequent sub-alkaline to mildly alkaline magmatism in the eastern TAB. However, a problem with this model is that it infers a pre-Eocene timing for the Eurasia–Arabia collision, which is not supported by recent tectonic reconstructions that suggest Miocene collision (e.g., Dewey et al., 1986; McQuarrie et al., 2003; Hüsing et al., 2009; Okay et al., 2010).

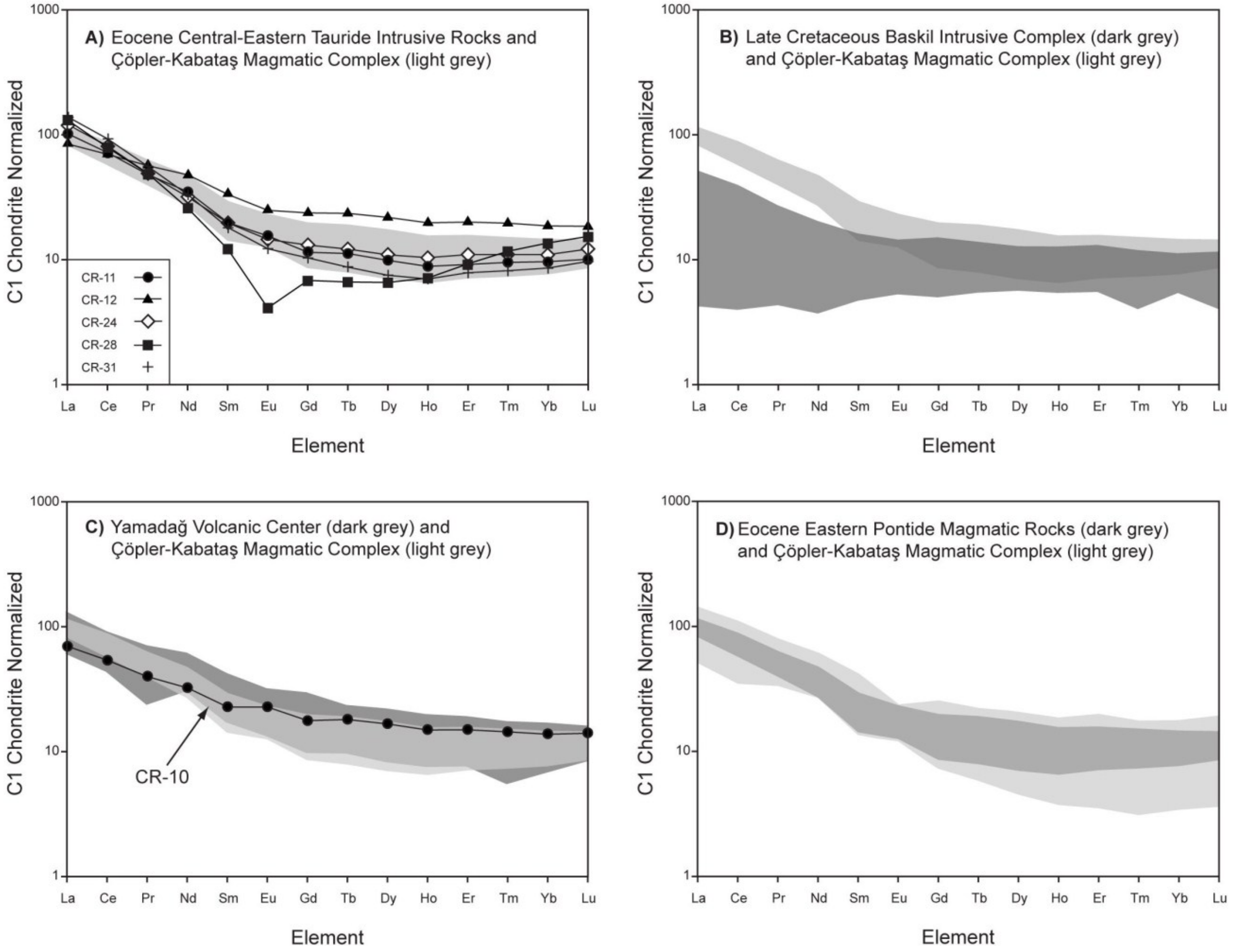

Figure 2.16 Chondrite-normalized rare earth element diagrams, showing compositions of (A) Eocene central-eastern Tauride plutonic rocks, (B) the Late Cretaceous Baskil intrusive complex, (C) the Miocene Yamadağ volcanic center, (D) the middle Eocene eastern Pontide plutonic and volcanic rocks, compared with the range of compositions of igneous rocks from the Çöpler-Kabataş magmatic complex (light grey field). Data sources: Baskil intrusive complex: Rızaoğlu et al. (2009); Yamadağ volcanic center (light grey field): Kürüm et al. (2008). Normalization values from Sun and McDonough (1989)

2.10.4 Middle Miocene post-collisional magmatism in the TAB

Post-collisional magmatism along the southern TAB margin began during the middle Miocene with eruption of large volumes of sub-alkaline to mildly alkaline mafic to felsic volcanic rocks, including the Yamadağ volcanic center. Overall, the trace element and REE profiles of the erupted magmas are broadly similar to those of middle Eocene central eastern

Tauride intrusions (Fig. 2.15C, 2.16C), suggesting derivation from a remnant subduction-modified mantle source beneath the TAB. Partial melting was possibly triggered by slab break-off following early Miocene collision (Keskin, 2003; Şengör et al., 2003; Faccenna et al., 2006) or by delamination of the sub-continental lithospheric mantle beneath eastern Anatolia (Pearce et al., 1990; Göğüş and Pysklywec, 2008).

2.10.5 Comparison with Eocene magmatism along the Northern TAB Margin (Pontides)

Middle Eocene (52–41 Ma) plutonic and volcanic successions also occur along the northern TAB margin in the eastern Pontides, and are interpreted to represent post-collisional magmatism following closure of the İzmir-Ankara-Erzincan Ocean (Okay and Şahintürk, 1997). These rocks are geochemically quite similar to the Çöpler-Kabataş magmatic rocks (Fig. 2.9, 2.15D, 2.16D), but in this case are indisputably post-collisional. This illustrates the problem of using lithogeochemistry alone as an indicator of tectonic setting, because geochemically similar magmas can be generated in back-arc and post-subduction settings.

2.10.6 Metallogenic Implications

The calc-alkaline Çöpler-Kabataş magmatic complex is argued above to have formed in a back-arc setting during the final stages of regional transtension prior to collision, and its location was controlled by a major ENE-trending sinistral fault system.

Unlike many porphyry systems that occur as clusters within orogen-parallel volcano-plutonic belts in convergent margin settings, the Çöpler Au-(Cu) deposit is positioned inland from the coeval Maden-Helete arc system. In this respect, Çöpler may have formed in a manner comparable to some other isolated Au-rich porphyry deposits such as the Bajo de la Alumbrera porphyry Cu-Au deposit in northwest Argentina, and Bingham Canyon porphyry Cu-Au-Mo deposit in western USA.

The Miocene Farallòn Negro Complex and associated Bajo de la Alumbrera porphyry Cu-Au deposit in Argentina lies about 200 km inland from the main axis of the Andean volcanic arc, and is thought to have formed during a period of flattening of subduction, with magmatism being localized by extensional structural intersections in the upper plate (Sasso and Clark, 1998; Chernicoff et al., 2002; Halter et al., 2004).

Similarly, the Bingham porphyry Cu-Au-Mo deposit is located far inland with respect to the coeval subduction zone, and is proposed to have formed during a period of incipient extension related to steepening/roll-back of the Farallon Plate during the Paleocene (Ryskamp et al., 2008; Sillitoe, 2008; Pettke et al., 2010). Pettke et al. (2010) further suggested that the parental magma at Bingham and its ore components were derived from a Proterozoic subduction-modified lithospheric mantle source, which was remelted during the Eocene tectonic activity.

In comparison, collision-related deposits such as Grasberg (Indonesia) and Ok Tedi (Papua New Guinea) are thought to have formed by remelting of subduction-modified lithospheric sources following delamination of the sub-continental lithospheric mantle (McDowell et al., 1996; Cloos et al., 2005; van Dongen et al., 2010). The similarity of magma compositions and deposit styles between these collision-related and back-arc deposits such as Çöpler suggests that there may be a continuum in terms of tectonomagmatic and metallogenic processes in these broadly subduction-related settings (Richards, 2009 and 2011).

2.11 Conclusions

The Çöpler porphyry-epithermal Au-(Cu) deposit is spatially related to middle Eocene calc-alkaline diorite and granodiorite porphyry stocks, which are interpreted to have formed in a back-arc setting behind the southern Neotethys subduction zone, shortly prior to continent–continent collision in the Miocene. Emplacement of these and other middle Eocene intrusions in the central eastern Taurides was controlled by regionally extensive, ENE-striking, strike-slip fault systems.

^{40}Ar/^{39}Ar ages of igneous minerals from intrusive rocks in the Çöpler-Kabataş magmatic complex range between 44.13 ± 0.38 and 43.75 ± 0.26 Ma, whereas hydrothermal biotite and sericite associated with porphyry-style hydrothermal alteration at Çöpler yielded ^{40}Ar/^{39}Ar ages of 43.84 ± 0.26 Ma and 44.44 ± 0.2, respectively. These dates closely overlap with the age of porphyry-type mineralization obtained from two molybdenite samples (44.6 ± 0.2 and 43.9 ± 0.2 Ma), indicating a short life span for the magmatic–hydrothermal system of ≤1 m.y., which is consistent with the relatively simple history and shallow emplacement of the intrusive system and ore deposit.

These ages are also similar to the ^{40}Ar/^{39}Ar plateau ages of igneous biotite from an unaltered quartz diorite to the east of Çöpler (44.19 ± 0.26 Ma) and igneous biotite and hornblende from the unaltered Çaltı (44.16 ± 0.23 Ma) and Bizmişen (43.51 ± 0.51 Ma) intrusions, indicating that the hydrothermal system at Çöpler developed concurrently with the ~44 Ma back-arc magmatic activity that took place in the eastern Taurides.

The back-arc setting of the Çöpler Au-(Cu) deposit can be compared to other similar porphyry Cu-Au deposits in back-arc or collisional settings, such as Bingham Canyon (USA), Bajo de la Alumbrera (Argentina), and possibly Ok Tedi (Papua New Guinea) and Grasberg (Indonesia).

2.12 References

Ahmadian J, Haschke M, McDonald I, Regelous M, RezaGhorbani M, Emami, M.H., Murata, M. (2009) High magmatic flux during Alpine-Himalayan collision: Constraints from the Kal-e-Kafi complex, central Iran. Geol Soc Am Bull 12:857–868.

Aktaş G, Robertson AHF (1984) The Maden Complex, SE Turkey: evolution of a Neotethyan active margin. In: Dixon JE, Robertson AHF (eds) The Geological Evolution of the Eastern Mediterranean. Geol Soc Lond Spec Publ 17:375–402.

Allen MB (2009) Discussion on the Eocene bimodal Piranshahr massif of the Sanadaj-Sirjan Zone, West Iran: a marker of the end of collision in the Zagros orogen. J Geol Soc Lond 166:981–982.

Arger J, Mitchell J, Westaway RWC (2000) Neogene and Quaternary volcanism of southeastern Turkey. In: Bozkurt E, Winchester JA, Piper JDA (eds) Tectonics and magmatism in Turkey and surrounding area. Geol Soc Lond Spec Publ 173:1–23.

Armstrong JT (1995) A package of correction programs for the quantitative electron microbeam x-ray analysis of thick polished materials, thin films, and particles. Microbeam Anal 4:177–200.

Barley ME, Rak P, Wyman D (2002) Tectonic controls on magmatic-hydrothermal gold mineralization in the magmatic arcs of SE Asia. In: Blundell DJ, Neubauer F, Von Quadt A (eds)

The timing and location of major ore deposits in an evolving orogen. Geol Soc Lond Spec Publ 204:39–47.

Bierlein FP, Groves DI, Cawood PA (2009) Metallogeny of accretionary orogens – The connection between lithospheric processes and metal endowment. Ore Geol Rev 36:282–292.

Bingen B, Stein H (2003) Molybdenite Re–Os dating of biotite dehydration melting in the Rogaland high-temperature granulites, S Norway. Earth Planet Sci Lett 208:181–195.

Boccaletti M, Gocev P, Manetti P (1974) Mesozoic isopic zones in the Black Sea region. Boll Soc Geol It 93:547–565.

Bozkurt E (2001) Neotectonics of Turkey – a synthesis. Geod Acta 14:3–30.

Boztuğ D (2008) Petrogenesis of the Kösedağ Pluton, Suşehri-NE Sivas, east-central Pontides, Turkey. Turk J Earth Sci 17:241–262.

Boztuğ D, Harlavan Y, Arehart GB, Satır M, Avcı N (2007) K-Ar age, whole-rock and isotope geochemistry of A-type granitoids in the Divriği-Sivas region, eastern-central Anatolia, Turkey. Lithos 97:193–218.

Boztuğ D, Jonckheere RC, Heizler M, Ratschbacher L, Harlavan Y, Tichomirova M (2009) Timing of post-obduction granitoids from intrusion through cooling to exhumation in central Anatolia, Turkey. Tectonophysics 473:223–233.

Brenan JM, Shaw HF, Phinney DL, Ryerson FJ (1994) Rutile-aqueous fluid partitioning of Nb, Ta, Hf, Zr, U and Th: implications for high field strength element depletions in island-arc basalts. Earth Planet Sci Lett 128:327–339.

Carmichael ISE, Ghiorso MS (1990) The effect of oxygen fugacity on the redox state of natural liquids and their crystallizing phases. In: Nicholls J, Russell JK (eds), Modern Methods of Igneous Petrology: Understanding Magmatic Processes. Rev Mineral, Min Soc America 24:191–212.

Cater JML, Hanna SS, Ries AC, Turner P (1991) Tertiary evolution of the Sivas Basin, central Turkey. Tectonophysics 195:29–46.

Chernicoff CJ, Richards JP, Zappettini EO (2002) Crustal lineament control on magmatism and mineralization in northwestern Argentina: Geological, geophysical, and remote sensing evidence. Ore Geology Reviews 21:127–155.

Cloos M, Sapiie B, van Ufford AQ, Weiland RJ, Warren PQ McMahon TP (2005) Collisional delamination in New Guinea: the geotectonics of subducting slab breakoff. Geol Soc Am Spec Pap 400: pp. 51.

Creaser RA, Papanastassiou DA, Wasserburg GJ (1991) Negative thermal ion mass spectrometry of osmium, rhenium and iridium. Geochim Cosmochim Acta 55:397–401.

Dewey JF, Hempton MR, Kidd WSF, Şaroğlu F, Şengör AMC (1986) Shortening of continental lithosphere: the neotectonics of Eastern Anatolia – a young collision zone. In: Coward MP, Ries AC (eds) Collision Tectonics. Geol Soc Lond Spec Publ 19:3–36.

Dewey JF, Helman ML, Turco E, Hutton DWH, Knott SD (1989) Kinematics of the western Mediterranean. In : Coward MP, Dietrich D, Park RG (eds) Alpine Tectonics. Geol Soc Lond Spec Publ 45:265–283.

Ekici T, Alpaslan M, Parlak O, Uçurum A (2009) Geochemistry of the middle Miocene collision-related Yamadağı (eastern Anatolia) calc-alkaline volcanics, Turkey. Turk J Earth Sci 18:511–528.

Elmas A, Yılmaz Y (2003) Development of an oblique subduction zone – tectonic evolution of the Tethys suture zone in southeast Turkey. Int Geol Rev 45:827–840.

Faccenna C, Bellier O, Martinod J, Piromallo C, Regard V (2006) Slab detachment beneath eastern Anatolia: a possible cause for the formation of the North Anatolian fault. Earth Planet Sci Lett 242:85–97.

Fayon AK., Whitney DL, Teyssier C, Garver JI, Dilek Y (2001) Effects of plate convergence obliquity on timing and mechanisms of exhumation of a mid-crustal terrain, the Central Anatolian Crystalline Complex. Earth Planet Sci Lett 192:191–205.

Fleck RJ, Sutter JF, Elliot DH (1977) Interpretation of discordant ^{40}Ar/^{39}Ar age-spectra of Mesozoic tholeiites from Antarctica. Geochim Cosmochim Acta 41:15–32.

Frey FA, Chappell BW, Roy SD (1978) Fractionation of rare-earth elements in the Tuolumne intrusive series, Sierra Nevada batholith, California. Geology 6:239–242.

Gautier P, Bozkurt E, Hallot E, Dirik K (2002) Dating the exhumation of a metamorphic dome: Geological evidence for pre-Eocene unroofing of the Niğde Massif (Central Anatolia, Turkey). Geol Mag 139:559–576.

Gençalioğlu-Kuşcu G, Göncüoğlu MC, Kuşcu İ (2001) Post-collisional magmatism on the northern margin of the Taurides and its geological implications: geology and petrology of the Yahyalı-Karamadazı Granitoid. Turk J Earth Sci 10:103–119.

Glazner AF (1991) Plutonism, oblique subduction, and continental growth: An example from the Mesozoic of California. Geology 19:784–786.

Govers R, Wortel MJR (2005) Lithosphere tearing at STEP faults: response to edges of subduction zones. Earth Planet Sci Lett 236:505–523.

Göğüş OH, Pysklywec RN (2008) Mantle lithosphere delamination driving plateau uplift and synconvergent extension in eastern Anatolia. Geology 36:723–726.

Guezou J-C, Temiz H, Poisson A, Gürsoy H (1996) Tectonics of the Sivas Basin: The Neogene record of the Anatolian accretion along the Inner Tauride Suture. Int Geol Rev 38:901–925.

Halter WE, Bain N, Becker K, Heinrich CA, Landtwing M, VonQuadt A, Clark AH, Sasso AM, Bissig T, Tosdal RM (2004) From andesitic volcanism to the formation of a porphyry Cu-Au mineralizing magma chamber: the Farallòn Negro Volcanic Complex, northwestern Argentina. J Volcanol Geotherm Res 136:1–30.

Hanson GN (1980) Rare earth elements in petrogenetic studies of igneous systems. Annu Rev Earth Planetary Sci 8:371–406.

Harrison TM (1981) Diffusion of ^{40}Ar in hornblende. Contrib Mineral Petr 78:324–331.

Hedenquist JW, Lowenstern JB (1994) The role of magmas in the formation of hydrothermal ore deposits. Nature 370:519–527.

Hou Z, Cook NJ (2009) Metallogenesis of the Tibetan collisional orogen: A review and introduction to the special issue. Ore Geol Rev 36:2–24.

Hutton DHW (1982) A tectonic model for the emplacement of the Main Donegal Granite, NW Ireland. J Geol Soc Lond 139:615–631.

Hutton DHW, Dempster TJ, Brown PE, Becker SD (1990) A new mechanism of granite emplacement: Intrusion in active extensional shear zones. Nature 343:452–455.

Hüsing SK, Zachariasse W-J, van Hinsbergen DJJ, Krijgsman W, İnceöz M, Harzhauser M, Mandic O, Kroh A (2009) Oligocene–Miocene basin evolution in SE Anatolia, Turkey: constraints on the closure of the eastern Tethys gateway. In: van Hinsbergen DJJ, Edwards MA, Gowers R (eds) Collision and Collapse at the Africa-Arabia-Eurasia Subduction Zone. Geol Soc Lond Spec Publ 311:107–132.

Irvine TN, Baragar WRA (1971) A guide to the chemical classification of the common volcanic rocks. Can J Earth Sci 8:523–548.

Janković S (1977) The copper deposits and geotectonic setting of the Tethyan Eurasian Metallogenic Belt. Miner Deposita 12:37–47.

Kadıoğlu YK, Dilek Y (2010) Structure and geochemistry of the adakitic Horoz granitoid, Bolkar Mountains, south-central Turkey, and its tectonomagmatic evolution. Int Geol Rev 52:505–535.

Kadıoğlu YK, Dilek Y, Foland KA (2006) Slab breakoff and syncollisional origin of the Late Cretaceous magmatism in the Central Anatolian Crystalline Complex, Turkey. In: Dilek Y, Pavlides S (eds) Postcollisional tectonics and magmatism in the Mediterranean region and Asia. Geol Soc Am Spec Pap 409:381–415.

Karaoğlan F, Parlak O (2006) Geochemistry and tectonic significance of the Doğanşehir (Malatya) granitoid. Abstracts of the 59th Geological Congress of Turkey, Ankara, 20-24 March 2006, pp. 495–496.

Karaoğlan F, Parlak O, Kloetzli U, Thöni M, Koller F, Hejl E, Rızaoğlu T (2009) Geochronology and isotope geochemistry of the ophiolites and granitoids along the southeast Anatolian orogenic belt. Abstracts of the 62nd Geological Congress of Turkey, Ankara, 13-17 April 2009, pp. 846–847.

Karslı O, Chen B, Aydın F, Şen C (2007) Geochemical and Sr-Nd-Pb isotopic compositions of the Eocene Dölek and Sarıçiçek Plutons, Eastern Turkey: Implications for magma interaction in the genesis of high-K calc-alkaline granitoids in a post-collision extensional setting. Lithos 98:67–96.

Karslı O, Dokuz A, Uysal İ, Aydın F, Chen B, Kandemir R, Wijbrans J (2010a) Relative contributions of crust and mantle to generation of Campanian high-K calc-alkaline I-type granitoids in a subduction setting, with special reference to Harşit Pluton, eastern Turkey. Contrib Mineral Petrol 160:467–487.

Karslı O, Dokuz A, Uysal İ, Aydın F, Kandemir R, Wijbrans J (2010b) Generation of the Early Cenozoic adakitic volcanism by partial melting of mafic lower crust, Eastern Turkey: Implications for crustal thickening to delamination. Lithos 114:109–120.

Kaymakçı N, White SH, Van Dijk PM (2000) Palaeostress inversion in a multiphase deformed area: kinematic and structural evolution of the Çankırı Basin (central Turkey), Part 1 – northern area. In: Bozkurt E, Winchester JA, Piper JDA (eds) Tectonics and magmatism in Turkey and surrounding area. Geol Soc Lond Spec Publ 173:295–323.

Kaymakçı N, İnceöz M, Ertepınar P (2006) 3D-architecture and Neogene evolution of the Malatya Basin: Inferences for the Kinematics of the Malatya and Ovacık Fault Zones. Turk J Earth Sci 15:123–154.

Kaymakçı N, İnceöz M, Ertepınar P, Koç A (2010) Late Cretaceous to Recent kinematics of SE Anatolia (Turkey). In: Sosson M, Kaymakçı N, Stephenson RA, Bergerat F, Starostenko V (eds) Sedimentary Basin Tectonics from the Black Sea and Caucasus to the Arabian Platform. Geol Soc Lond Spec Publ, 340:409–435.

Keskin M (2003) Magma generation by slab steepening and breakoff beneath a subduction-accretion complex: An alternative model for collision-related volcanism in Eastern Anatolia, Turkey. Geophys Res Lett 30:8046. doi:10.1029/2003GL018019.

Keskin M, Genç ŞC, Tüysüz O (2008) Petrology and geochemistry of post-collisional Middle Eocene volcanic units in North-Central Turkey: Evidence for magma generation by slab breakoff following the closure of the Northern Neotethys Ocean. Lithos 104:267–305.

Kesler SE (1997) Metallogenic evolution of convergent margins: Selected ore deposit models. Ore Geol Rev 12:153–171.

Koçyiğit A, Beyhan A (1998) A new intracontinental transcurrent structure: the Central Anatolian Fault Zone, Turkey. Tectonophysics 284:317–336.

Kogiso T, Tatsumi Y, Nakano S (1997) Trace element transport during dehydration processes in the subducted crust: 1. Experiments and implications for the origin of ocean island basalts. Earth Planet Sci Lett 148:193–205.

Kuşcu İ, Gençalioğlu-Kuşcu G, Tosdal RM (2007) Tectonomagmatic-metallogenic framework of mineralization events in the southern NeoTethyan arc, southeastern Turkey. In: Andrew CJ et al (eds) Digging Deeper. Proceedings of the 9th Biennial SGA Meeting, Dublin, 20-23 August 2007, pp. 853–856.

Kuşcu İ, Gençalioğlu-Kuşcu G, Tosdal RM, Ulrich TD, Friedman R (2010) Magmatism in the southeastern Anatolian orogenic belt: transition from arc to post-collisional setting in an evolving orogen. In: Sosson M, Kaymakçı N, Stephenson RA, Bergerat F, Starostenko V (eds) Sedimentary Basin Tectonics from the Black Sea and Caucasus to the Arabian Platform. Geol Soc Lond Spec Publ 340:437–460.

Kürüm S, Önal A, Boztuğ D, Spell T, Arslan M (2008) $^{40}Ar/^{39}Ar$ age and geochemistry of the post-collisional Miocene Yamadağ volcanics in the Arapkir area (Malatya Province), eastern Anatolia, Turkey. J Asian Earth Sci 33:229–251.

Lei J, Zhao D (2007) Teleseismic evidence for a break-off subducting slab under Eastern Turkey. Earth Planet Sci Lett 257:14–28.

Marschik R, Spikings R, Kuşcu İ (2008) Geochronology and stable isotope signature of alteration related to hydrothermal magnetite ores in Central Anatolia, Turkey. Miner Deposita 43:111–124.

McDougall I, Harrison TM (1999) Geochronology and thermochronology by the $^{40}Ar/^{39}Ar$ method. Oxford University Press, New York, Oxford, 269 p.

McDowell FW, McMahon TP, Warren PQ, Cloos M (1996) Pliocene Cu-Au bearing intrusions of the Gunung Bijih (Ertsberg) district, Irian Jaya, Indonesia : K-Ar geochronology. J Geol 104:327–340.

McKenzie D, Yılmaz Y (1991) Deformation and volcanism in western Turkey and the Aegean. Bull Tech Univ İstanbul 44:345–373.

McQuarrie, N., Stock, J.M., Verdel, C., Wernicke, B., 2003. Cenozoic evolution of Neotethys and implications for the causes of plate motions. Geophysical Research Letters 30, 2036, doi: 10.1029/2003GL017992.

Michard A, Whitechurch H, Ricou LE, Montigny R, Yazgan E (1984) Tauric subduction (Malatya-Elazığ provinces) and its bearing on tectonics of the Tethyan realm in Turkey. In: Dixon JE, Robertson AHF (eds) The Geological Evolution of the Eastern Mediterranean. Geol Soc Lond Spec Publ 17:361–373.

Middlemost EAK (1994) Naming materials in the magma/igneous rock system. Earth Sci Rev 37:215–224.

Moore G, Carmichael ISE (1998) The hydrous phase equilibria (to 3 kbar) of an andesite and basaltic andesite from western Mexico: Constraints on water content and conditions of phenocryst growth. Contrib Mineral Petrol 130:304–319.

MTA (1989) Geologic map of Turkey. Ankara, MTA, scale 1:2,000,000.

MTA (2002a) Geologic map of Turkey (Sivas Quadrangle). Ankara, MTA, scale 1:500,000.

MTA (2002b) Geologic map of Turkey (Erzurum Quadrangle). Ankara, MTA, scale 1:500,000.

Okay Aİ, Şahintürk O (1997) Geology of the eastern Pontides. In: Robinson AG (ed) Regional and Petroleum Geology of the Black Sea and Surrounding Region. Am Assoc Petrol Geol Mem 68:291–311.

Okay Aİ, Tüysüz O (1999) Tethyan sutures of northern Turkey. In: Durand B, Jolivet L, Horvath F, Seranne M (eds) Mediterranean Basins: Tertiary Extension within the Alpine Orogen. Geol Soc Lond Spec Publ 156:475–515.

Okay Aİ, Tansel İ, Tüysüz O (2001) Obduction, subduction and collision as reflected in the Upper Cretaceous-Lower Eocene sedimentary record of western Turkey. Geol Mag 138:117–142.

Okay Aİ, Satır M, Siebel W (2006) Pre-Alpide Palaeozoic and Mesozoic orogenic events in the Eastern Mediterranean region. In: Gee DG, Stephenson RA (eds) European Lithosphere Dynamics. Geol Soc Lond Mem 32:389–405.

Okay Aİ, Zattin M, Cavazza W (2010) Apatite fission-track data for the Miocene Arabia-Eurasia collision. Geology 38:35–38.

Önal A, Boztuğ D, Kürüm S, Harlavan Y, Arehart GB, Arslan M (2005) K-Ar age determination, whole-rock and oxygen isotope geochemistry of the post-collisional Bizmişen and Çaltı plutons, SW Erzincan, eastern Central Anatolia, Turkey. Geol J 40:457–476.

Özer E (1994) Stratigraphy of the Munzur mountains (Kemah-İliç-Erzincan). Bull Geol Soc Turk 37:53–64 (in Turkish with English abstract).

Özer E, Öner F (1999) Geochemical characteristics and tectonic interpretation of the Yakuplu Pluton in the northeastern Taurid Mountains, eastern Turkey. Chemie Erde 59:173–182 (in German with English abstract).

Özgenç İ, İlbeyli N (2009) Geochemical constraints on petrogenesis of Late Cretaceous alkaline magmatism in east-central Anatolia (Hasançelebi-Başören, Malatya), Turkey. Miner Petrol 95:71–85.

Özgül N, Turşucu A (1984) Stratigraphy of the Mesozoic carbonate sequence of the Munzur Mountains (Eastern Turkey). In: Tekeli O, Göncüoğlu MC (eds) Geology of the Taurus Belt. Proceedings of the International Tauride Symposium. Mineral Research and Exploration Institute of Turkey (MTA) Publications, Ankara, Turkey, pp 173–180.

Özgül N, Turşucu A, Özyardımcı N, Şenol M, Bingöl İ, Uysal S (1981) Munzur dağlarının jeolojisi. Min Res Explor Inst Turkey (MTA) Report 6995, Ankara (unpublished).

Parlak O (2006) Geodynamic significance of granitoid magmatism in the southeast Anatolian orogen: geochemical and geochronological evidence from Göksun-Afşin (Kahramanmaraş, Turkey) region. Int J Earth Sci 95:609–627.

Pearce JA, Bender JF, De Long SE, Kidd, WSF, Low PJ, Güner Y, Şaroğlu F, Yılmaz Y, Moorbath S, Mitchell JG (1990) Genesis of collision volcanism in Eastern Anatolia, Turkey. J Volcanol Geotherm Res 44:189–229.

Pettke T, Oberli F, Heinrich CA (2010) The magma and metal source of giant porphyry-type ore deposits, based on lead isotope microanalysis of individual fluid inclusions. Earth Planet Sci Lett 296:267–277.

Poisson A, Guezou J-C, Öztürk A, İnan S, Temiz H, Gürsoy H, Kavak K, Özden S (1996) Tectonic setting and evolution of the Sivas Basin, Central Anatolia, Turkey. Int Geol Rev 38:838–853.

Rızaoğlu T, Parlak O, Höck V, Koller F, Hames WE, Billor Z (2009) Andean-type active margin formation in the eastern Taurides: Geochemical and geochronological evidence from the Baskil granitoid (Elazığ, SE Turkey). Tectonophysics 473:188–207.

Rice SP, Robertson AHF, Ustaömer T (2006) Late Cretaceous-Early Cenozoic tectonic evolution of the Eurasian active margin in the Central and Eastern Pontides, northern Turkey. In: Robertson AHF, Mountrakis D (eds) Tectonic Development of the Eastern Mediterranean Region. Geol Soc Lond Spec Publ 260:413–445.

Richards JP (2003a) Tectono-magmatic precursors for porphyry Cu-(Mo-Au) deposit formation. Econ Geol 96:1515–1533.

Richards JP (2003b) Metallogeny of the Neo-Tethys arc in central Iran. In: Eliopoulos DG et al (eds) Proceedings of Mineral Exploration and Sustainable Development. Millpress, Rotterdam, pp 1237–1239.

Richards JP (2009) Postsubduction porphyry Cu-Au and epithermal deposits: Products of remelting of subduction-modified lithosphere. Geology 37:247–250.

Richards JP (2011) Magmatic to hydrothermal metal fluxes in convergent and collided margins. Ore Geol Rev 40:1–26.

Robertson AHF (1998) Mesozoic–Tertiary tectonic evolution of the Easternmost Mediterranean area: integration of marine and land evidence. In: Robertson AHF, Emeis K-C, Richter C, Camerlenghi A (eds) Proceedings of the Ocean Drilling Program, Scientific Results 160:723–782.

Robertson AHF, Dixon JE (1984) Introduction: Aspects of the Geological Evolution of the Eastern Mediterranean. In: Dixon JE, Robertson AHF (eds) The Geological Evolution of the Eastern Mediterranean. Geol Soc Lond Spec Publ 17:1–74.

Robertson AHF, Pickett EA (2000) Palaeozoic-Early Tertiary Tethyan evolution of mélanges, rift and passive margin units in the Karaburun Peninsula (western Turkey) and Chios Island (Greece). In: Bozkurt E, Winchester, JA, Piper JDA (eds) Tectonics and Magmatism in Turkey and Surrounding Area. Geol Soc Lond Spec Publ 173:43–82.

Robertson AHF, Parlak O, Rızaoğlu T, Ünlügenç Ü, İnan N, Taşlı K, Ustaömer T (2007) Tectonic evolution of the South Tethyan ocean: evidence from the Eastern Taurus Mountains

(Elazığ region, SE Turkey). In: Ries AC, Butler RWH, Graham RH (eds) Deformation of the Continental Crust: The Legacy of Mike Coward. Geol Soc Lond Spec Publ 272:231–270.

Román-Berdiel T, Gapais D, Brun J-P (1997) Granite intrusion along strike-slip zones in experiment and nature. Am J Sci 297:651–678.

Rosenbaum G, Gasparon M, Lucente FP, Peccerillo A, Miller MS (2008) Kinematics of slab tear faults during subduction segmentation and implications for Italian magmatism. Tectonics 27:TC2008. doi:10.1029/2007TC002143.

Ryskamp EB, Abbott JT, Christiansen EH, Keith JD, Vervoort JD, Tingey DG (2008) Age and petrogenesis of volcanic and intrusive rocks in the Sulphur Spring Range, central Nevada: Comparisons with ore-associated Eocene magma systems in the Great Basin. Geosphere 4:496–519.

Sasso AM, Clark, AH (1998) The Farallòn Negro Group, northwest Argentina: magmatic, hydrothermal, and tectonic evolution and implications for Cu-Au metallogeny in the Andean back-arc. SEG Newsletter 34:1 and 8–18.

Schellart WP, Lister GS (2004) Tectonic models for the formation of arc-shaped convergent zones and backarc basins. In: Sussman AJ, Weil AB (eds) Orogenic Curvature: Integrating Paleomagnetic and Structural Analyses. Geol Soc Am Spec Pap 383:237–258.

Selby D, Creaser RA (2004) Macroscale NTIMS and microscale LA-MC-ICP-MS Re-Os isotopic analysis of molybdenite: Testing spatial restrictions for reliable Re-Os age determinations, and implications for the decoupling of Re and Os within molybdenite. Geochim Cosmochim Acta 68:3897–3908.

Shirey SB, Walker RJ (1995) Carius tube digestion for low-blank rhenium-osmium analysis. Anal Chem 67:2136–2141.

Sillitoe RH (2008) Major gold deposits and belts of the North and South American Cordillera: distribution, tectonomagmatic settings, and metallogenic considerations. Econ Geol 103:663–687.

Smoliar MI, Walker RJ, Morgan JW (1996) Re-Os ages of Group IIA, IIIA, IVA, and IVB iron meteorites. Science 271:1099–1102.

Solomon M (1990) Subduction, arc reversal, and the origin of porphyry copper-gold deposits in island arcs. Geology 18:630–633.

Stampfli GM (2000) Tethyan oceans. In: Bozkurt E, Winchester JA, Piper JDA (eds) Tectonics and magmatism in Turkey and surrounding area. Geol Soc Lond Spec Publ 173:1–23.

Stampfli GM, Marcoux J, Baud A (1991) Tethyan margins in space and time. Palaeogeogr Palaeoclimatol Palaeoecol 87:373–410.

Stolz AJ, Jochum KP, Spettel B, Hofmann AW (1996) Fluid- and melt-related enrichment in the subarc mantle: Evidence from Nb/Ta variations in island-arc basalts. Geology 24:587–590.

Sun S-S, McDonough WF (1989) Chemical and isotopic systematics of oceanic basalts: Implications for mantle composition and processes. In: Saunders AD, Norry MJ (eds) Magmatism in the Ocean Basins. Geol Soc Lond Spec Publ 42:313–345.

Şengör AMC, Yılmaz Y (1981) Tethyan evolution of Turkey: a plate tectonic approach. Tectonophysics 75:181–241.

Şengör AMC, Özeren MS, Genç T, Zor E (2003) East Anatolian high plateau as a mantle-supported, north-south shortened domal structure. Geophys Res Lett 30:8045. doi:10.1029/2003GL017858.

Tekin UK, Göncüoğlu MC, Turhan N (2002) First evidence of Late Carnian radiolarians from the İzmir-Ankara suture complex, central Sakarya, Turkey: implications for the opening age of the İzmir-Ankara branch of Neo-Tethys. Geobios 35:127–135.

Temiz H, Guezou J-C, Poisson AM, Tutkun Z (1993) Tectonostratigraphy and kinematics of the eastern end of the Sivas Basin (central eastern Turkey): implications for the so-called ‘Anatolian block’. Geol J 28:239–250.

Topuz G, Altherr R, Schwarz WH, Siebel W, Satır M, Dokuz A (2005) Post-collisional plutonism with adakite-like signatures: the Eocene Saraycık granodiorite (Eastern Pontides, Turkey). Contrib Mineral Petrol 150:441–455.

Tosdal RM, Richards JP (2001) Magmatic and structural controls on the development of porphyry Cu ± Mo ± Au deposits. In: Richards JP, Tosdal RM (eds) Structural Controls on Ore Genesis. Rev Econ Geol 14:157–181.

Tunç M, Özçelik O, Tutkun Z, Gökçe A (1991) Basic geological characteristics of the Divriği-Yakuplu-İliç-Hamo (Sivas) area. Turk J Eng Environ Sci 15:225–245 (in Turkish with English abstract).

Tüysüz O, Tekin UK (2007) Timing of imbrication of an active continental margin facing the northern branch of Neotethys, Kargı Massif, northern Turkey. Cret Res 28:754–764.

Umhoefer PJ, Whitney DL, Teyssier C, Fayon AK, Casale G, Heizler MT (2007) Yo-yo tectonics in a wrench zone, Central Anatolian fault zone, Turkey. In: Till AB, Roeske SM, Sample JC, Foster DA (eds) Exhumation Associated with Continental Strike-Slip Fault Systems. Geol Soc Am Spec Pap 434:35–57.

Van Dongen M, Weinberg, RF, Tomkins, AG, Armstrong, RA, Woodhead, JD (2010) Recycling of Proterozoic crust in Pleistocene juvenile magma and rapid formation of the Ok Tedi porphyry Cu–Au deposit, Papua New Guinea. Lithos 114:282–292.

Verdel C, Wernicke BP, Hassanzadeh J, Guest B (2011) A Paleogene extensional arc flare-up in Iran. Tectonics 30:TC3008. doi: 10.1029/2010TC002809.

Vincent SJ, Allen MB, Ismail-Zadeh AD, Flecker R, Foland KA, Simmons MD (2005) Insights from the Talysh of Azerbaijan into the Paleogene evolution of the South Caspian region. Geol Soc Am Bull 117:1513–1533.

Völkening J, Walczyk T, Heumann K (1991) Osmium isotope ratio determinations by negative ion mass spectrometry. Int J Mass Spectrom Ion Proc 105:147–159.

Wallace LM, Ellis S, Mann P (2009) Collisional model for rapid fore-arc block rotations, arc curvature, and episodic back-arc rifting in subduction settings. Geochem Geophys Geosyst 10:Q01004. doi:10.1029/2008GC002220.

Whitney DL, Umhoefer PJ, Teyssier C, Fayon AK (2008) Yo-yo tectonics of the Niğde Massif during wrenching in Central Anatolia. Turk J Earth Sci 17:209–217.

Yalınız MK, Göncüoğlu MC, Özkan-Altıner S (2000) Formation and emplacement ages of the SSZ-type Neotethyan ophiolites in Central Anatolia, Turkey: palaeotectonic implications: Geol J 35:53–68.

Yazgan E (1984) Geodynamic evolution of the Eastern Taurus region. In: Tekeli O, Göncüoğlu MC (eds) Geology of the Taurus Belt. Proceedings of the International Tauride Symposium. Mineral Research and Exploration Institute of Turkey (MTA) Publications, Ankara, Turkey, pp 199–208.

Yazgan E, Chessex R (1991) Geology and tectonic evolution of Southeastern Taurus in the region of Malatya. Turk Assoc Petrol Geol Bull 3:1–42.

Yılmaz A (1985) Basic geological characteristics and structural evolution of the region between the Upper Kelkit Creek and the Munzur Mountains. Bull Geol Soc Turk 28:78–92 (in Turkish with English abstract).

Yılmaz S, Boztuğ D, Öztürk A (1993) Geological setting, petrographic and geochemical characteristics of the Cretaceous and Tertiary igneous rocks in the Hekimhan-Hasançelebi area, north-west Malatya, Turkey. Geol J 28:383–398.

Yılmaz Y (1993) New evidence and model on the evolution of Southeast Anatolian orogen. Geol Soc Am Bull 105:251–271.

Yiğit Ö (2009) Mineral deposits of Turkey in relation to Tethyan metallogeny: implications for future mineral exploration. Econ Geol 104:19–51.

Yiğitbaş E, Yılmaz Y (1996a) New evidence and solution to the Maden complex controversy of the Southeast Anatolian orogenic belt (Turkey). Geol Rund 85:250–263.

Yiğitbaş E, Yılmaz Y (1996b) Post-Late Cretaceous strike-slip tectonics and its implications for the Southeast Anatolian orogen, Turkey. Int Geol Rev 38:818–831.

Zeck HP, Ünlü T (1991) Shoshonitic, monzonitic pluton near Murmano, eastern central Turkey – a preliminary note. Bull Min Res Explor Inst Turkey (MTA) 112:47–58 (in Turkish with English abstract).

CHAPTER 3: The Late Oligocene Cevizlidere Cu-Au-Mo Deposit, Tunceli Province, Eastern Turkey*

* A version of this chapter has been published online in Mineralium Deposita (June 2014), co-authored by Jeremy P. Richards (University of Alberta), Robert A. Creaser (University of Alberta), and Terry L. Spell (University of Nevada at Las Vegas)

3.1 Introduction

Eastern Anatolia has experienced complex collisional orogenic events since at least the Late Mesozoic, relating to closure of the Neotethyan oceanic basin and ultimate collision between Eurasia and Arabia. As a result of this convergence, the orogenic belt experienced prolonged intervals of arc and back-arc magmatism during the Late Cretaceous (*ca.* 80–70 Ma) and middle Eocene (*ca.* 50–44 Ma) above the northward subducting Neotethys oceanic plate. Subduction-related magmatism was followed by a period of widespread collision-related and post-collisional volcanic activity starting in the middle Miocene (*ca.* 17 Ma; Kürüm et al., 2008) and continuing to the present day. In eastern Anatolia, several porphyry Cu±Mo±Au and epithermal Au deposits are associated with Late Cretaceous and middle Eocene subduction-related magmatic centers, such as the Çöpler porphyry-epithermal Au-Cu deposit, and the Kabataş, Nazaruşağı, and Ispendere porphyry Cu±Au±Mo deposits (Fig. 3.1; Dumanlılar 1999; Kuşcu et al., 2010, 2013; Yiğit 2009; İmer et al., 2013), whereas no such deposits are known to be associated with middle Miocene and younger volcanic centers.

Farther southeast, throughout the laterally contiguous Zagros orogenic belt in Iran, the nature and timing of Late Mesozoic–Cenozoic igneous activity is roughly similar to that of eastern Anatolia, but magmatic exposures and related porphyry- and epithermal-style mineralization are considerably more widespread, and the majority of deposits are of mid-Miocene age (Janković 1977; Richards 2003; Richards et al., 2006, 2012; Allen and Armstrong 2008; Shafiei et al., 2009; Haschke et al., 2010; Verdel et al., 2011). Nevertheless, a salient characteristic shared by both the eastern Turkish and Iranian segments of the Alpine–Himalayan orogenic belt is the scarcity of late Eocene to Oligocene magmatic rocks. This magmatic lull likely signalled the onset of Afro-Arabia–Eurasia continent–continent collision, which commenced diachronously in eastern Anatolia in the late Eocene (Yılmaz 1993; Allen and

Armstrong 2008; Allen 2009; Boulton 2009) or middle Miocene (Dewey et al., 1986; Robertson et al., 2007; Hüsing et al., 2009; Okay et al., 2010), and between the Oligocene and Miocene in central Iran (Mohajjel et al., 2003; Agard et al., 2005; Shafiei et al., 2009).

In eastern Anatolia, rare exposures of Oligocene volcanic and volcaniclastic rocks are mainly preserved within fault-bounded sedimentary basins to the north of the Bitlis Suture Zone (Fig. 3.1; Akay 1989; Akay et al., 1989; Elmas 1994). Erupted lavas, the ages of which are only stratigraphically constrained, are predominantly calc-alkaline andesites to rhyolites that geochemically resemble arc magmas (op. cit. and Elmas and Yılmaz 2003).

The Cevizlidere porphyry Cu-Mo-Au deposit is located about 45 km to the west-northwest of the city of Tunceli in eastern Anatolia (Fig. 3.1). The deposit is one of three major porphyry prospects (together with Mamlis and Sin; Fig. 3.2A) identified within a 60 km^2 area known as the Tunceli porphyry belt, and is the only one that has so far proved to be of economic interest. The deposit was initially targeted and explored by a joint venture between Rio Tinto and Alacer Gold Corp. (formerly Anatolia Minerals Development Limited) in the early 2000s, and is currently being explored by Alacer Gold Corp. Early drilling at Cevizlidere has confirmed an inferred resource of 445 million metric tonnes of ore grading at 0.38% Cu (cut-off grade at 0.20%), 0.11 g/t Au, and 48 ppm Mo (Kociumbas and Page 2009), and mineralization is open along strike to the southeast and at depth (Fig. 3.3B).

The Cevizlidere deposit is of significant importance for several reasons. First, its precursor magmatic system is one of the few well-exposed Oligocene (based on this study) magmatic centers in eastern Anatolia. Secondly, preliminary resource estimates suggest that Cevizlidere is the largest porphyry Cu system in Turkey, even though its potential has not yet been fully explored. And finally, Cevizlidere does not seem to be part of a previously documented magmatic and metallogenic belt, and hence, the tectonic and magmatic events that led to its formation are of significant interest. In this communication we present preliminary lithogeochemical and geochronological (^{40}Ar/^{39}Ar and Re-Os) data for the Cevizlidere deposit in an attempt to resolve the uncertainties relating to its origin, particularly within the context of Neotethyan subduction/closure and regional metallogeny.

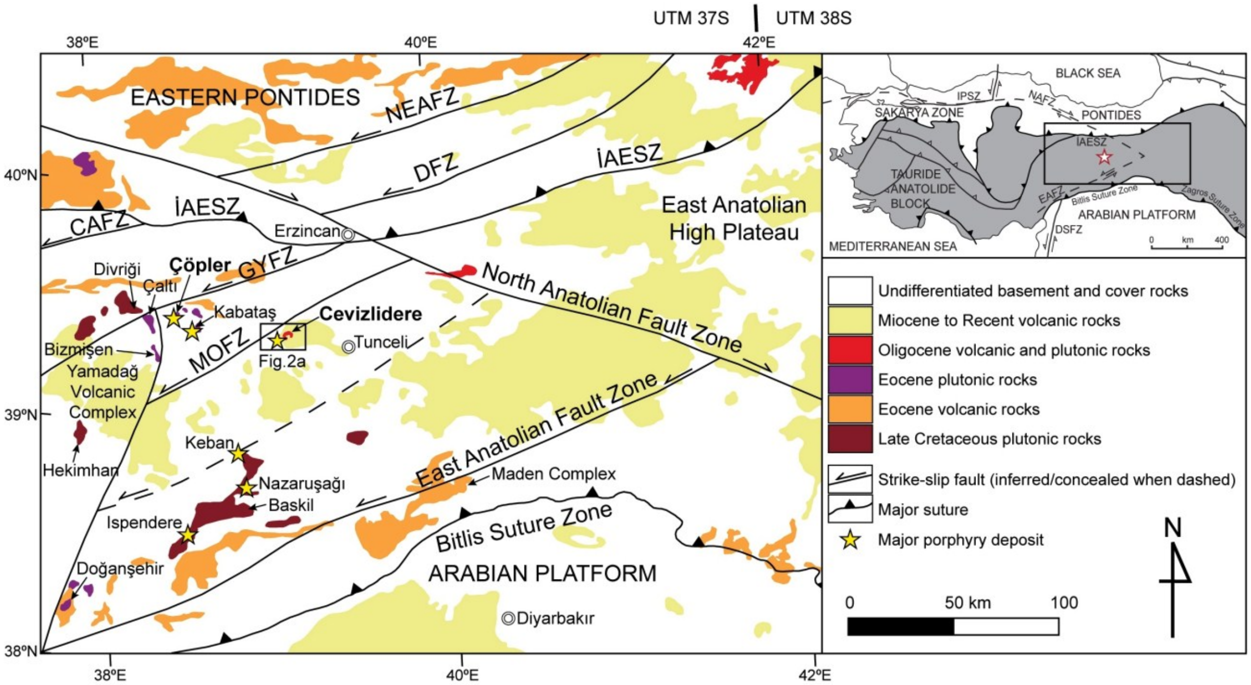

Figure 3.1 Geological map showing the distribution of Late Mesozoic–Cenozoic igneous rocks and major tectonic features of eastern Anatolia (modified from MTA, 1989). Also shown are the locations of major porphyry occurrences in the region. Box indicates the area of Fig. 3.2; inset map shows the major tectonic divisions of Turkey; the Tauride-Anatolide Block is shown as the shaded area (Okay and Tüysüz, 1999). Box in the inset indicates the area of the main map and the red star shows the approximate location of the Cevizlidere deposit. Abbreviations: CAFZ = Central Anatolian Fault Zone, DFZ = Dumlu Fault Zone, DSFZ = Dead Sea Fault Zone, EAFZ = East Anatolian Fault Zone, Göksu-Yazyurdu Fault Zone, İAESZ = İzmir-Ankara-Erzincan Suture Zone, IPSZ = Intra-Pontide Suture Zone, MOFZ = Malatya-Ovacık Fault Zone, NAFZ = North Anatolian Fault Zone, NEAFZ = North East Anatolian Fault Zone.

3.2 Sampling and Methodology

Fieldwork in this region of southeastern Turkey is difficult for security reasons, and only one visit to the area has been possible (by the second author in August 2003). In July 2008, the first author spent four days inspecting drillcore from Cevizlidere at a storage facility in the town of Ovacık. Core from six diamond drillholes completed between 2003 and 2005 was logged and sampled for petrographic study as well as for lithogeochemical and geochronological analyses. Locations and brief descriptions of these samples are given in Appendix D. Geologic descriptions given in the following section are largely based on unpublished company reports and are supplemented by drillcore observations.

Eight drillcore samples of intrusive igneous rocks were selected for lithogeochemical analysis; these comprised four least-altered and four moderately altered samples, which were sent to Actlabs Laboratories in Ontario, Canada, for lithogeochemical analysis. Major and trace element compositions of the selected samples were determined using a combination of inductively-coupled plasma (ICP), inductively-coupled plasma emission mass spectrometry (ICP-MS), and instrumental neutron activation analysis (INAA) methods (Actlabs method 4E Research plus ICP-MS). Accuracy, as determined by reproducibility of lab standards and duplicates, is typically within 5 relative percent for major-element oxides, and to within 10 relative percent for minor and trace elements.

Two samples of least-altered porphyritic rocks containing igneous biotite, and one sample of potassically altered porphyry containing hydrothermal biotite were selected for ^{40}Ar/^{39}Ar incremental step-heating analyses in order to determine the timing of magmatic cooling and porphyry-style hydrothermal alteration at Cevizlidere. Pure biotite mineral separates were analyzed by conventional step-heating analyses at the Nevada Isotope Geochronology Laboratory at the University of Nevada, Las Vegas (see Appendix E for a full description of the analytical methods).

In order to constrain the timing of mineralization at Cevizlidere, two molybdenite mineral separates were extracted from B-type quartz-magnetite-sulfide veinlets and analysed by the Re-Os geochronological method. ^{187}Re and ^{187}Os compositions were measured by isotope dilution mass spectrometry at the University of Alberta Radiogenic Isotope Facility using methods described by Selby and Creaser (2004). Details of the analytical procedures are provided in Appendix F.

3.3 Cevizlidere Geology

The Cevizlidere porphyry Cu-Mo-Au deposit is located within the Tauride-Anatolide Block (TAB), which is an E–W-elongated continental fragment of Gondwana origin (Fig. 3.1). The TAB is sandwiched between two major suture zones, the İzmir-Ankara-Erzincan Suture and the Bitlis Suture, marking strands of two former Neotethyan basins that were consumed by northward subduction during the Late Cretaceous and Late Cenozoic, respectively (Fig. 3.1; Şengör and Yılmaz 1981). The Bitlis Suture in the south separates the TAB from the Arabian Shield, whereas the İzmir-Ankara-Erzincan Suture represents the collision zone between the TAB and the Pontides to the north (Fig. 3.1). In eastern Anatolia, the terrain between these two suture zones is dissected into a series of topographic highs and intervening sedimentary basins by subparallel ENE-trending crustal-scale fault systems (Fig. 3.1; Koçyiğit and Beyhan 1998; Kaymakçı et al., 2010) and numerous lineaments, many of which possess a dominant strike-slip component.

The hinterland of the southeast Anatolian orogenic belt to the north of the Bitlis Suture Zone consists of a number of imbricated pre-Tertiary nappes that have been accreted to the southern TAB margin during the subduction of the Southern Neotethys ocean. The region in the general vicinity of the Cevizlidere deposit is floored by two of these allochthonous sheets, namely the Keban and Munzur Units, which have been derived from the northern continental margin of the Southern Neotethys (Robertson et al., 2007). The Munzur Unit to the north forms part of the eastern Tauride mountain range, and comprises a 1200 m-thick succession of platformal carbonates of Jurassic–Cretaceous age (Özgül and Turşucu 1984). The Keban Unit to the south is composed predominantly of regionally metamorphosed Carboniferous–Triassic siliciclastic and carbonate rocks, and Jurassic–Cretaceous ophiolite bodies (Michard et al., 1984; Özgül and Turşucu 1984; Robertson et al., 2007). Both allochthonous units have been progressively cut and overlain by Late Cretaceous–middle Eocene subduction-related, and middle Miocene and younger syn- and post-collisional igneous rocks.

The Late Cretaceous calc-alkaline intrusive rocks exposed near Baskil (Fig. 3.1) record the earliest phase of arc magmatism in southeast Anatolia (85–79 Ma; Yazgan and Chessex 1991; Rızaoğlu et al., 2009; Kuşcu et al., 2010, 2013), succeeded by a period of mildly alkaline bimodal magmatism from 78–69 Ma near Divriği, Hekimhan, and Keban (Fig. 3.1; Boztuğ et al., 2007; Kuşcu et al., 2010, 2013; İmer et al., 2013). Although field relationships have been established between the rocks of the former suite and porphyry-style hydrothermal alteration and mineralization at the Nazaruşağı and Ispendere prospects (Fig. 3.1; Dumanlılar et al., 1999; Kuşcu et al., 2013), there is no geochronological evidence as of yet to establish a temporal link between these magmatic and hydrothermal events. The latter suite, however, hosts several important Fe-skarn/IOCG-type deposits such as the A-Kafa, B-Kafa, and C-Placer orebodies near Divriği, the Hasançelebi deposit near Hekimhan, and a porphyry Cu-Mo system with peripheral Mo-W and Pb-Zn skarn mineralization at Keban (Fig. 3.1; Yiğit 2009; Kuşcu et al., 2013). ^{40}Ar/^{39}Ar alteration ages for these deposits range between 74–69 Ma (Kuşcu et al., 2013).

Arc/back-arc magmatism across the eastern Taurides resumed in the middle Eocene with calc-alkaline to mildly alkaline volcanism in the south (e.g., the Maden Complex; Fig. 3.1) and intermittent calc-alkaline volcanism and plutonism in the north (Fig. 3.1). Recently reported K-Ar and ^{40}Ar/^{39}Ar ages indicate that the calc-alkalic intrusive rocks of this stage were emplaced between 48 and 43 Ma into the Munzur Unit in the north (e.g., Çöpler-Kabataş, Bizmişen, and Çaltı plutons; Fig. 3.1; Önal et al., 2005; Kuşcu et al., 2010, 2013; İmer et al., 2013), whereas the southerly Doğanşehir pluton was emplaced into the southwestern edge of the Keban Unit during ~51–48 Ma (combined U-Pb zircon and ^{40}Ar/^{39}Ar biotite ages; Karaoğlan et al., 2013).

The final magmatic epoch in this region commenced in the middle Miocene with the eruption of calc-alkaline to mildly alkaline basaltic to rhyolitic volcanic rocks near Yamadağ (*ca.* 17 Ma; Fig. 3.1; Kürüm et al., 2008). To the east, collision-related calc-alkaline volcanism peaked throughout the East Anatolian High Plateau (Fig. 3.1) at ~11 Ma, and transitioned into a more within plate-type character as post-collisional volcanism migrated towards the south (Keskin, 2003) following final collision between the TAB and the Arabian Platform at 12–10 Ma (Şengör and Yılmaz, 1981; Dewey et al., 1986; Hüsing et al., 2009).

To the south of the Munzur Mountains, the Keban and Munzur allochthonous units are separated by the active ENE-striking Ovacık Fault and its associated pull-apart basin (Fig. 3.2A). This prominent structure initially developed as a normal fault during the early Miocene (Kaymakçı et al., 2006), or possibly slightly earlier given its close spatial relationship with the Oligocene plutons, and was later reactivated in the late Miocene as a sinistral structure with a considerable reverse component of movement (Kaymakçı et al., 2006). However, it is still questionable whether the Ovacık Fault represents a segment of a single crustal-scale fault system (namely the Malatya-Ovacık Fault Zone; Fig. 3.1; Koçyiğit and Beyhan, 1998; Westaway and Arger, 2001) or is an independent structural zone (Kaymakçı et al., 2006).

The host plutonic rocks of the Cevizlidere deposit are exposed near the southern edge of the Ovacık pull-apart basin (Fig. 3.2A). Here, the deposit is centered around a NW–SE-elongated composite stock, which intrudes Paleozoic limestones of the Keban Unit and unconformably overlying Paleogene andesitic lava flows (Fig. 3.2B). The exact age of these lavas is not known, but a middle Eocene age is inferred based on regional correlations with nearby intrusive centers such as the Çöpler-Kabataş magmatic complex and the Bizmişen, Çaltı, and Doğanşehir plutons, all of which were emplaced between 50 and 43 Ma (Fig. 3.1; Önal et al., 2005; Kuşcu et al., 2007, 2013; İmer et al., 2013; Karaoğlan et al., 2013).

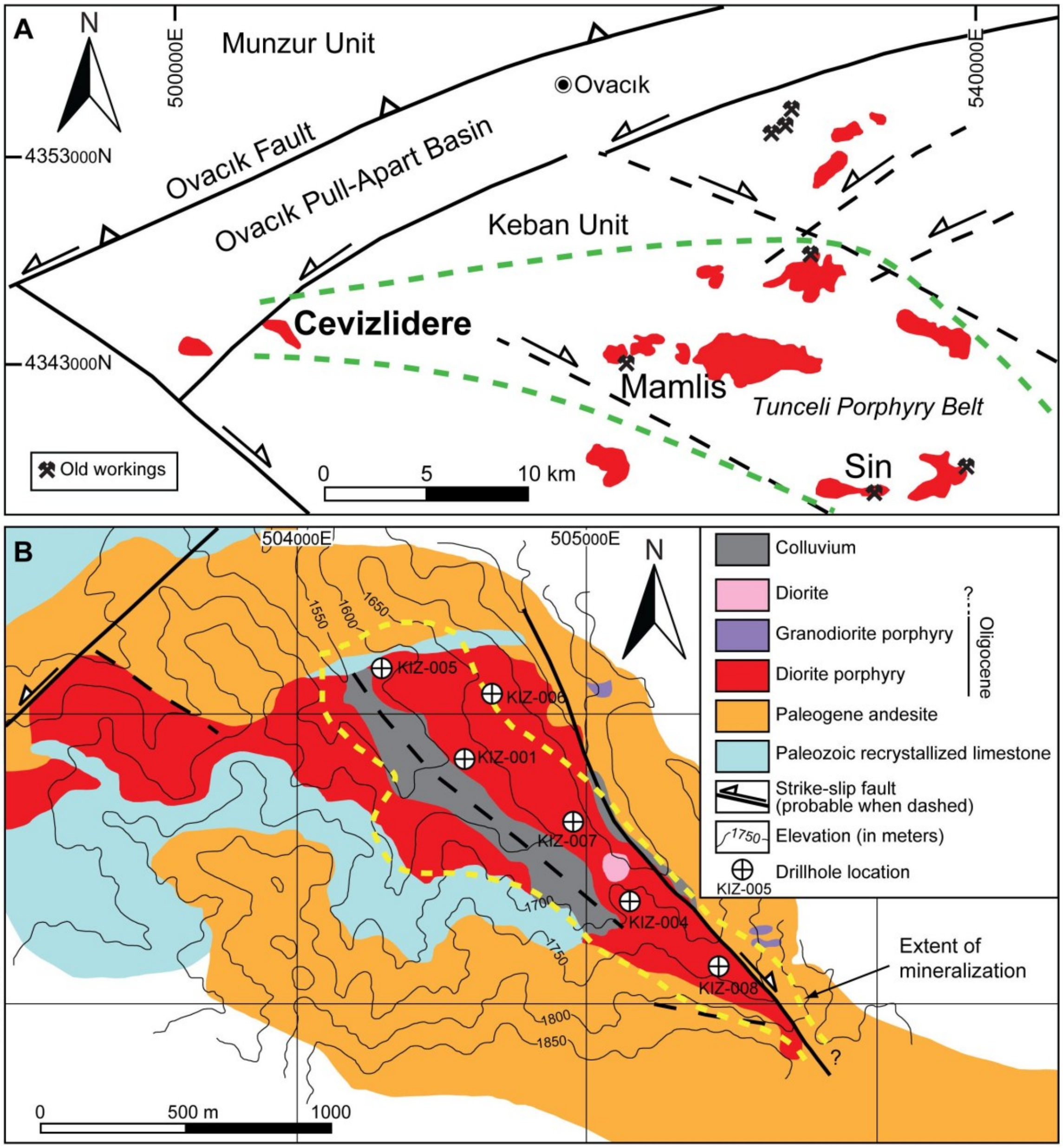

Figure 3.2 (A) Geological map showing the distribution of Oligocene intrusive centers in the Ovacık area, including the Cevizlidere, Mamlis, and Sin porphyry prospects; compiled from a map prepared by Rio Tinto geologists (structural data modified from Kaymakçı et al., 2006). (B) Geology of the Cevizlidere deposit showing the locations of sampled drillholes (modified from a map prepared by Rio Tinto geologists; UTM Zone 37S). The Tunceli Porphyry Belt (outlined by green dashed lines) contains several altered/mineralized porphyry centers including the Cevizlidere deposit and several other prospects near Mamlis and Sin, and extends towards the southeast.

The predominant intrusive phase at Cevizlidere is a diorite porphyry ("feldspar porphyry"; Kociumbas and Page 2009) which has been intruded along a NW-trending structure (Fig. 3.2B). The diorite porphyry consists of phenocrystic hornblende, biotite, plagioclase feldspar, and quartz embedded in a quartzofeldspathic and magnetite-bearing groundmass (Fig. 3.3A). In the central part of the deposit this unit has a minimum vertical extent of ~600 m as revealed by drillcore intercepts (KIZ-001; see Fig. 3.2B for location).

Granodiorite porphyry ("dacite porphyry"; Kociumbas and Page, 2009) has relatively limited exposure but it has been intersected in several drillholes (e.g., KIZ-005 and KIZ-006; Fig. 3.2B). Petrographically, it is similar to the diorite porphyry in containing abundant plagioclase with relatively smaller amounts of hornblende and biotite set in a fine-grained groundmass of quartz, plagioclase, and magnetite. However, its phenocryst content is lower than that of the diorite porphyry (Fig. 3.3B).

Within the deposit, both porphyry phases have been subjected to extensive potassic and phyllic alteration. Potassic alteration is characterized by abundant secondary K-feldspar replacing phenocrystic and groundmass plagioclase, and also by fine-grained hydrothermal biotite which occurs either as pseudomorphs after hornblende or along hairline veinlets. B-type quartz-magnetite-chalcopyrite-pyrite ± molybdenite ± bornite veinlets and disseminations of chalcopyrite and bornite are commonly observed in close association with this type of alteration (Fig. 3.3C). Copper grades associated with the potassic alteration zone range between 0.2 and 0.5 % Cu, whereas Au and Mo grades in this zone range between 0.09 and 0.15 g/t and 30 and 110 g/t, respectively.

The potassically-altered core is surrounded and partly overprinted by a zone of intense phyllic (quartz-sericite) alteration which is readily recognized at surface (Fig. 3.3D) and in drillcore by bleaching of the porphyry phases due to pervasive sericitization of mafic minerals and feldspars. Sheeted to stockwork D-type quartz-pyrite-sericite veinlets in this alteration zone carry only sparse chalcopyrite, and hypogene Cu grades are considerably lower than in the potassic alteration zone (typically <0.2 % Cu).

Both potassic and phyllic alteration zones are enveloped by a propylitic alteration halo characterized by chlorite (after mafic minerals or sericite), epidote, carbonate, and pyrite.

Carbonate alteration is also developed marginally near the intrusive-limestone contacts, and is locally accompanied by narrow skarn zones that contain Pb-Zn and minor Cu mineralization (Kociumbas and Page, 2009).

Late supergene oxidation, extending to depths of 100–150 m below surface, has caused significant redistribution of copper mineralization into a relatively high grade (~0.8–1% Cu) chalcocite blanket and a near-surface oxide zone consisting of mobile Cu minerals (Fig. 3.3E).

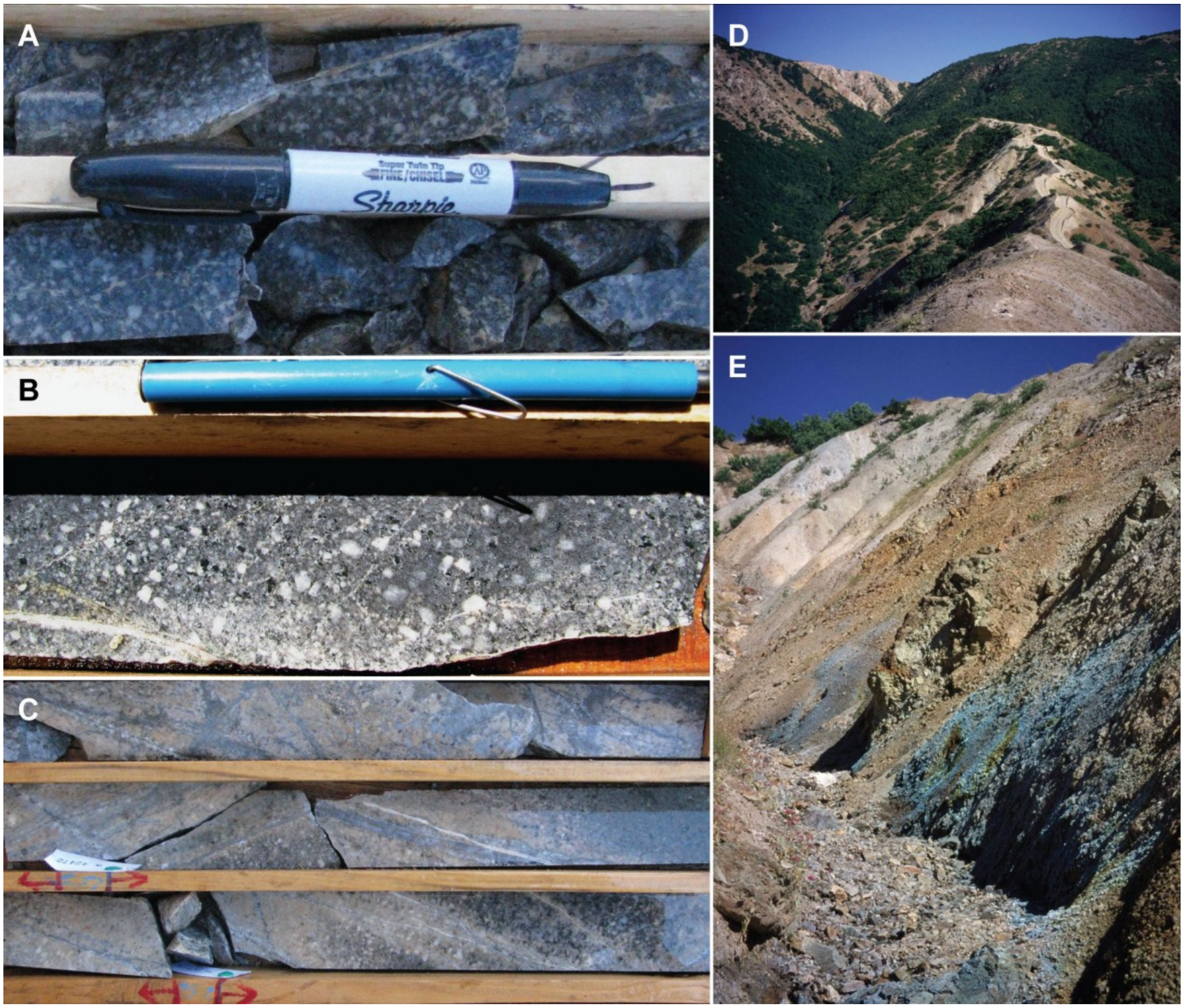

Figure 3.3 (A) Drillcore interval of least altered (slightly propylitized) diorite porphyry with abundant phenocrysts of plagioclase (white), hornblende (chloritized), and biotite (KIZ-001, 490.90–491.10 m; collar location: 504582E, 4344844N). (B) Least-altered granodiorite porphyry with partially sericitized plagioclase phenocrysts (KIZ-004, 392.30–392.45 m; collar location: 505156E, 4344350N). (C) Potassically-altered diorite porphyry with K-feldspar flooding and crosscutting A-type veinlets (KIZ-001, ~254–256 m; collar location: 504582E, 4344844N). (D) Phyllic alteration surrounding the central potassic zone at the center of the Cevizlidere prospect, view to WNW. (E) Active Cu leaching and mobilization in natural drainage, Cevizlidere prospect (WGS 84, 37S, 0504270E, 4344969N, 1274 m a.s.l.).

A circular plug of diorite crops out near the central part of the prospect and post-dates all of the other igneous phases (Fig. 3.2B; Kociumbas and Page 2009), though this unit is not intersected in any of the sampled drillholes. The dark grey diorite consists predominantly of plagioclase and hornblende phenocrysts together with subordinate biotite, and appears to post-date mineralization because it is neither altered nor mineralized (Kociumbas and Page 2009).

Structures that have been mapped in the Cevizlidere area are generally steeply-dipping and are either northeast- or northwest-trending, with the former displaying sinistral displacement and the latter, dextral (Fig. 3.2B). Although these structures are suggested to have predated pluton emplacement (Kociumbas and Page 2009), post-emplacement faulting is also evident, particularly along the northwestern margin of the deposit where the Cevizlidere stock has been sharply truncated and offset for at least 2 km along a NE-trending structure (Fig. 3.2A).

3.4 Results

3.4.1 Petrography

Petrographic study was undertaken in order to distinguish between least-altered and altered intrusive rocks from the Cevizlidere deposit. Samples suitable for whole-rock lithogeochemical and ^{40}Ar/^{39}Ar geochronological analyses were selected on the basis of this study.

All of the drillcore samples have undergone some degree of hydrothermal alteration. In the least-altered samples, hornblende crystals have been partially to completely replaced by chlorite, whereas biotite phenocrysts are partially rimmed by chlorite (Fig. 3.4A). Igneous biotite occurs in these samples as individual subhedral to euhedral grains (100–300 μm; Fig. 3.4A), commonly displaying poikilitic textures enclosing plagioclase (Fig. 3.4A) and magnetite inclusions. Magnetite also occurs as microphenocrysts in the matrix (typically ~20–50 μm). Plagioclase phenocrysts occur as subhedral to euhedral crystals with minor sericitic alteration giving them a cloudy appearance in thin section (Fig. 3.4A). Sparse patchy carbonate and minor epidote occur within the groundmass of these samples.

In potassically-altered samples, hydrothermal biotite (≤ 100 μm) is present either as patchy aggregates or scattered grains dispersed throughout the groundmass (Fig. 3.4B), as pseudomorphous clusters replacing primary hornblende grains, or as selvages bordering quartz-magnetite-sulfide veinlets. Hydrothermal magnetite occurs as anhedral to subhedral aggregates with grain sizes commonly coarser (typically 50–200 μm) than its primary igneous counterpart. Secondary K-feldspar occurs as a replacement of plagioclase phenocrysts and groundmass (Fig. 3.4B).

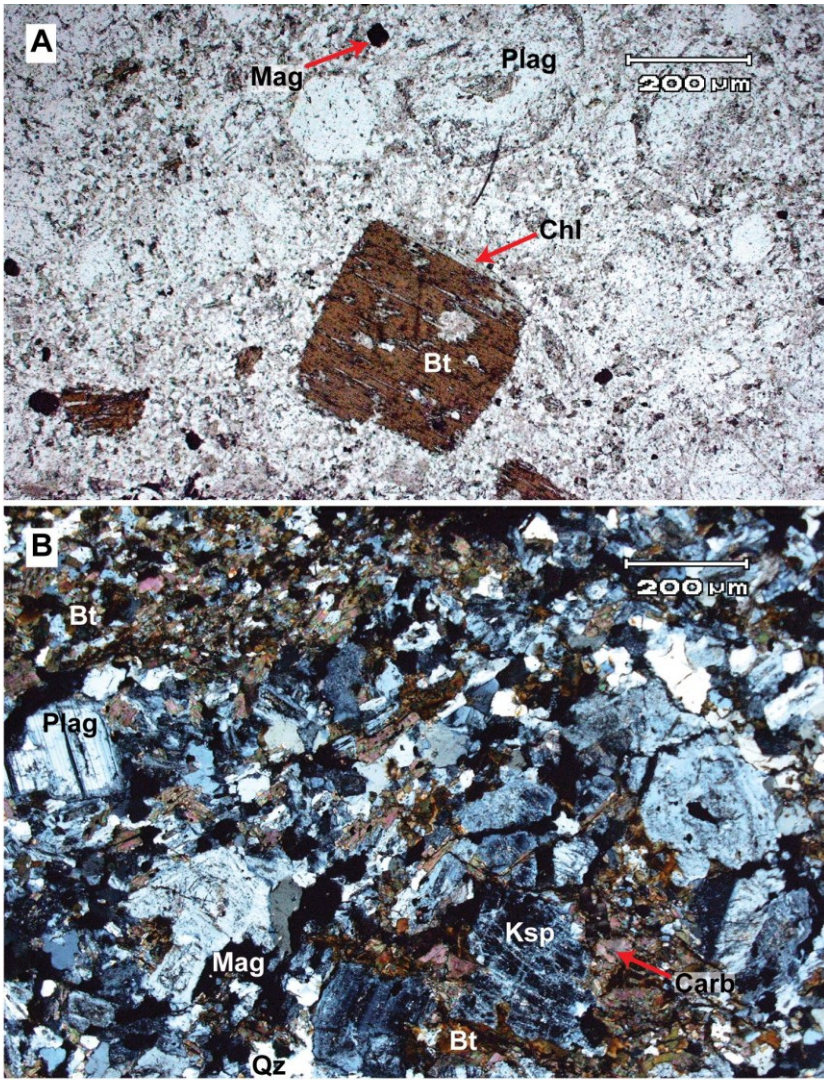

Figure 3.4 Photomicrographs showing examples of igneous and hydrothermal biotite from the Cevizlidere deposit. (A) Igneous biotite from sample K-4403 (diorite porphyry) showing incipient chlorite alteration along the rims (plane-polarized light). Plagioclase phenocrysts display cloudy appearance due to minor sericitic alteration. (B) Aggregates of hydrothermal biotite (higher birefringence colours) from sample K-7420 (granodiorite porphyry) with abundant hydrothermal magnetite and lesser secondary K-feldspar, together with relict plagioclase phenocrysts (cross-polarized light).

3.4.2 Lithogeochemistry

Major, trace, and rare earth element compositions of four least-altered and four altered samples of hypabyssal rock from the Cevizlidere deposit are provided in Appendix G. Major oxide compositions were normalized to 100% volatile-free for classification and plotting purposes. All of the Cevizlidere samples are calc-alkaline and fall within the medium-K subalkaline field when plotted on total alkali versus silica (Fig. 3.5A; after Middlemost 1994) and K_2O versus SiO_2 (Fig. 3.5B) diagrams, with most of the samples either tightly grouped within the granodiorite field or close to the diorite-granodiorite boundary (Fig. 3.5). One altered sample (K-1180) has a somewhat lower SiO_2 content than the rest of the samples and plots in the diorite field (Fig. 3.5).

Least-altered samples display weak phyllic or propylitic alteration. Phyllic altered samples are characterized by minor sericitization of plagioclase and groundmass, whereas the propylitized samples show partial to complete chloritization of hornblende together with sparse carbonate and epidote; biotite and plagioclase phenocrysts in these samples are mostly well-preserved. The remaining samples, on the other hand, have undergone moderate degrees of propylitic or potassic alteration. The alteration observed in these samples, although not intense, has likely resulted in some mobility of alkali elements and perhaps silica, but probably not to an extent that would change the petrological classification of these samples. This is further confirmed by the close correlation between the least- and moderately altered samples observed in the total alkali versus diagram (Fig. 3.5A), and the relatively small range of K_2O (1.06–1.49 wt.% K_2O; Fig. 5B) and Na_2O (3.20–4.29 wt.% Na_2O) values.

On a primitive mantle-normalized trace element diagram, least- and moderately altered samples from the Cevizlidere deposit show very similar patterns (Fig. 3.6A). They display relative enrichments in large ion lithophile elements (LILE) and prominent negative anomalies for Nb, Ta, and Ti. The overall trace element patterns of the samples appear to be largely unaffected by hydrothermal alteration, and are typical of subduction-related magmas that are formed through partial melting of metasomatized asthenospheric mantle (Brenan et al., 1994; Stolz et al., 1996; Kogiso et al., 1997).

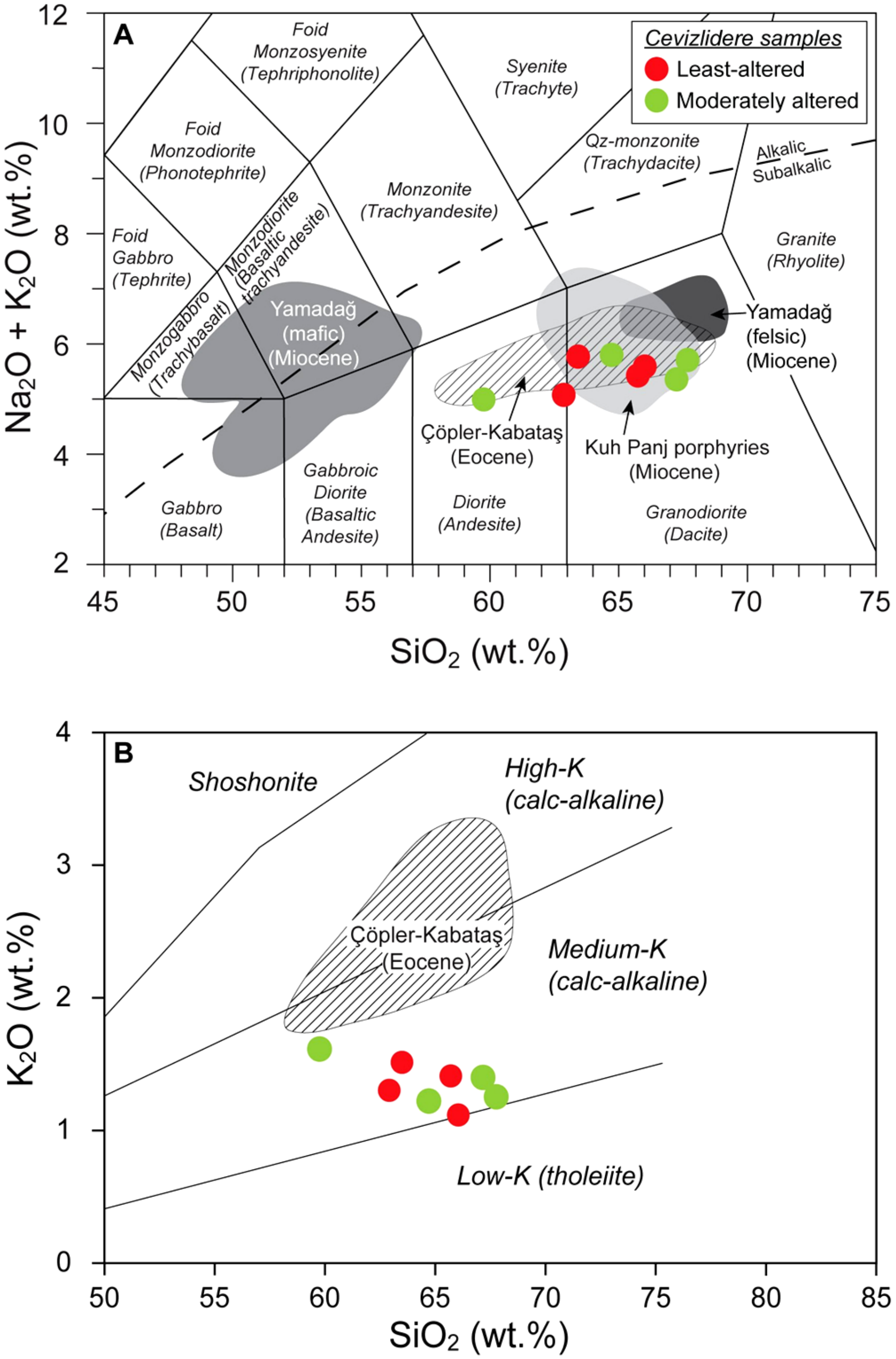

Figure 3.5 (A) Total-alkali versus silica (TAS) diagram (after Middlemost, 1994) showing the compositions of least-altered (slightly propylitized and/or sericitized) and altered (moderately propylitized and/or potassically-altered) intrusive rocks from the Cevizlidere deposit. Also plotted are the ranges of compositions of igneous rocks from the middle Eocene Çöpler-Kabataş magmatic complex (light gray field; İmer et al., 2013), the early to middle Miocene Yamadağ volcanic complex (dark gray field; Kürüm et al., 2008), and the middle Miocene Kuh Panj porphyries (hatched; Shafiei et al., 2009). Normalization values from Sun and McDonough (1989). The alkaline-subalkaline boundary is from Irvine and Baragar (1971). (B) K_2O versus SiO_2 diagram for least- and moderately altered intrusive rocks from the Cevizlidere deposit (magma series after Peccerillo and Taylor, 1976).

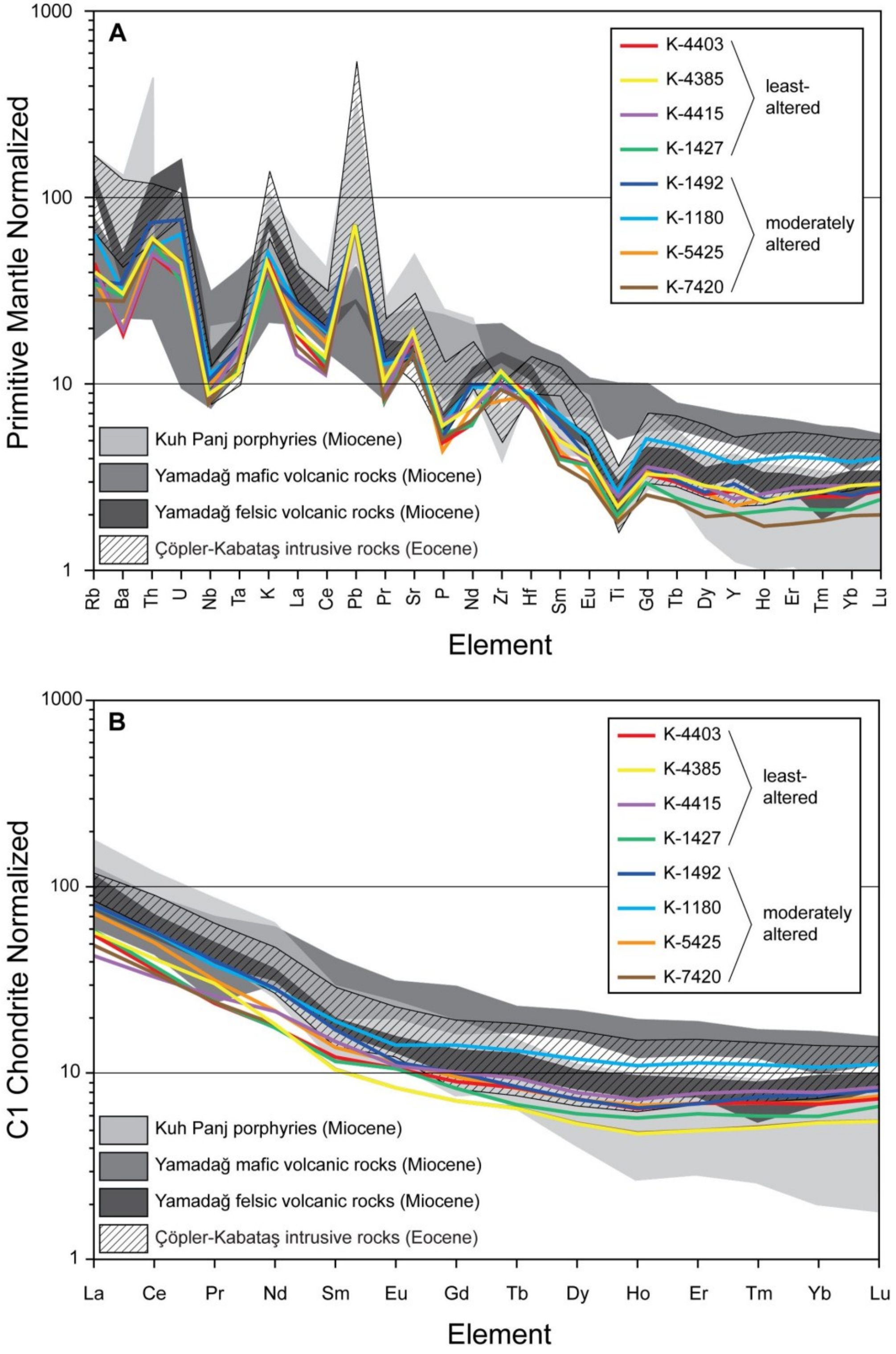

Figure 3.6 Normalized trace and rare earth element diagrams for least- and moderately altered intrusive rocks from the Cevizlidere deposit, compared with previously published data for the Çöpler-Kabataş, Yamadağ, and Kuh Panj suites (sources of other data as in Fig. 3.5). Normalization values from Sun and McDonough (1989).

On a chondrite-normalized diagram the least- and moderately altered samples are enriched in light rare earth elements (LREE; $[La/Sm]_n$ = 2.8–5; average = 4.18 ± 0.69, *n* = 8) relative to medium (MREE) and heavy rare earth elements (HREE) (Fig. 3.6B). Flat to slightly concave-upward (listric) patterns from MREE to HREE (Fig. 3.6B; $[Dy/Yb]_n$ = 0.94–1.10; average = 1.01 ± 0.05, *n* = 8) indicate hornblende fractionation because MREE preferentially partition into this mineral (Frey et al., 1978; Hanson, 1980). Analyzed samples lack significant Eu anomalies probably due to either suppression of plagioclase fractionation under hydrous conditions, and/or high magmatic oxidation state, because Eu^{+3} does not partition into fractionating plagioclase (Hanson 1980; Carmichael and Ghiorso 1990; Moore and Carmichael 1998). The slight increase observed in Sr concentrations of these samples with increasing SiO_2 contents (Fig. 3.7) rules out the possibility of significant plagioclase fractionation during the evolution of the Cevizlidere porphyries. The presence of hornblende phenocrysts and magnetite microphenocrysts also indicate that the Cevizlidere porphyries were formed from relatively oxidized and hydrous magmas. On a Sr/Y versus Y diagram (Fig. 3.8A), the Cevizlidere porphyries plot in the adakite-like field except one altered sample, whereas their La/Yb ratios (7.1–13.3) are below adakitic levels (<20; Fig. 3.8B). These characteristics further attest to the relatively oxidized and hydrous nature of the Cevizlidere magmas, and that plagioclase fractionation was insignificant during their formation.

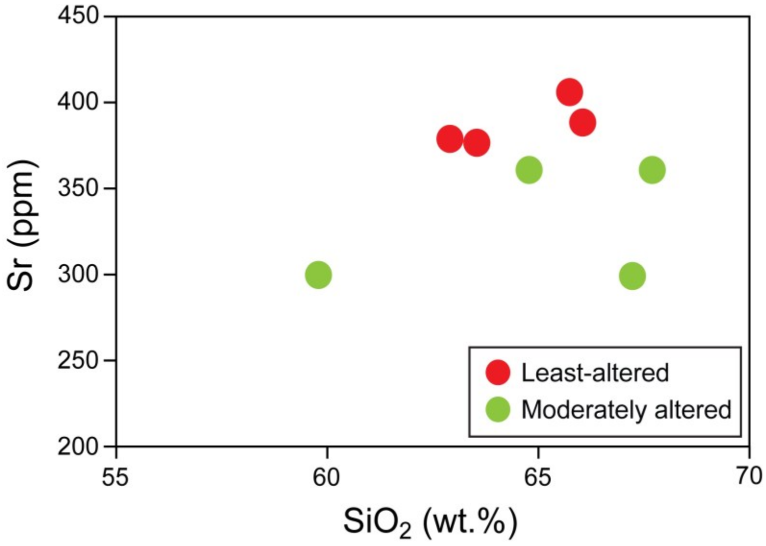

Figure 3.7 Sr versus SiO_2 diagram for least- and moderately altered intrusive rocks from the Cevizlidere deposit.

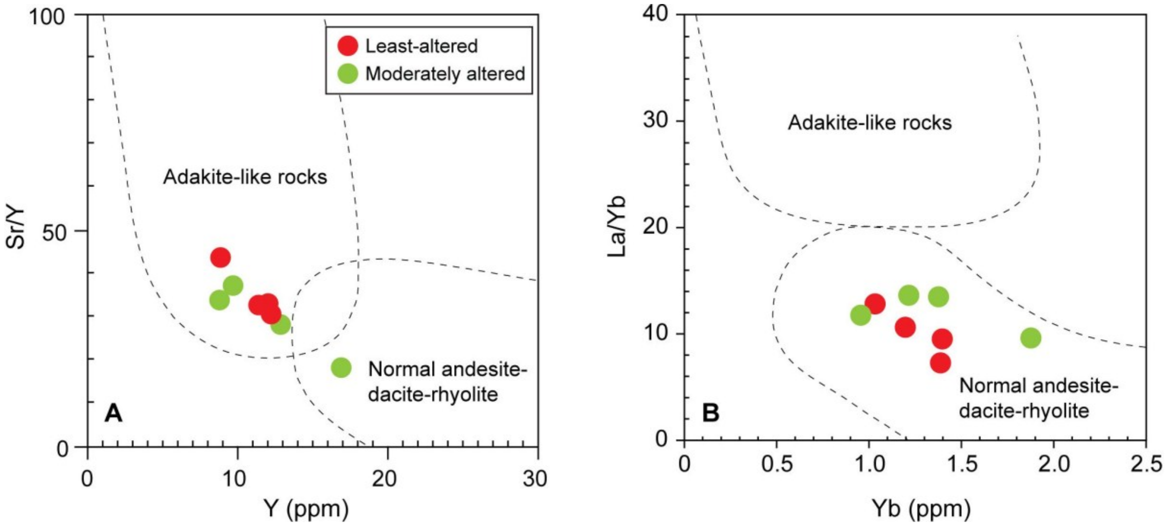

Figure 3.8 (A) Sr/Y versus Y (Defant and Drummond, 1993), and (B) La/Yb versus Yb (Castillo et al., 1999) plots of the intrusive rocks for least- and moderately altered rocks from the Cevizlidere deposit.

3.4.3 ^{40}Ar/^{39}Ar geochronology

A summary of the ^{40}Ar/^{39}Ar geochronological results for three samples of igneous and hydrothermal biotite from the Cevizlidere deposit is provided in Table 3.1, and full data are provided in Appendix H; age spectra are illustrated in Figure 3.9, and all ages are quoted with 2σ errors.

Sample K-1427: Sample K-1427 was collected from a drillcore interval of slightly propylitized diorite porphyry. Hornblende phenocrysts in this sample have been replaced by chlorite, but subhedral biotite grains have only been partially chloritized along the rims. The sample produced a flat spectrum consisting of eight steps, with an age of 25.29 ± 0.34 Ma (Fig. 3.9A). High initial and final age steps indicate that some excess ^{40}Ar was trapped during crystallization, and as a result, the inverse isochron age (25.10 ± 0.28 Ma; MSWD = 1.7; Fig. 3.9B), which is nevertheless within error of the plateau age, is selected as the preferred age for this sample.

Sample K-4403: This sample was also obtained from a least-altered drillcore interval of diorite porphyry. Relatively large hornblende phenocrysts in this sample are substantially altered to chlorite, but biotite grains are only partially rimmed by chlorite, with well-preserved inner cores. With the exception of a low age initial step, this sample yielded a flat age spectrum with an age of 25.54 ± 0.40 Ma (Fig. 3.9C). Although the total gas, plateau, and inverse isochron ages are statistically indistinguishable, the inverse isochron age (25.49 ± 0.20 Ma, MSWD = 1.4; Fig. 3.9D) is regarded as the most accurate age for this sample.

Sample K-7420: Sample K-7420 was collected from a drillcore interval displaying intense potassic alteration, and contains anhedral grains of hydrothermal biotite. This sample produced a U-shaped spectrum with high initial steps and a high final step age, but with an acceptable seven-step plateau with an age of 24.84 ± 0.36 Ma (Fig. 3.9E). However, because of the likely presence of minor amounts of excess ^{40}Ar, the inverse isochron age of 24.73 ± 0.16 Ma (MSWD = 1.4; Fig. 3.9F) is again accepted as the more accurate age estimate for this sample.

3.4.4 Re-Os geochronology

Model Re-Os ages (after Stein et al., 2001) for the two vein molybdenite separates were calculated using the simplified isotope equation: $t = \ln(^{187}\mathrm{Os}/^{187}\mathrm{Re} + 1)/\lambda$, where t is the model age, and λ is the ^{187}Re decay constant (1.666×10^{-11} a^{-1}; Smoliar et al., 1996). The model ages and 2σ errors calculated for samples KIZ-1429 and KIZ-1493 are 24.9 ± 0.10 Ma, and 24.78 ± 0.10 Ma, respectively (Table 3.2). These ages are statistically indistinguishable from each other and also indistinguishable from the ^{40}Ar/^{39}Ar age for hydrothermal biotite (24.73 ± 0.16 Ma). In addition, our new Re-Os ages are also broadly consistent with, but more precise than, a previously published Re-Os molybdenite age of 26.0 ± 0.20 Ma (Marinov et al., 2011). A meaningful comparison between this slightly older Re-Os molybdenite age and our new ages is difficult because no supporting data such as location, paragenesis, or analytical details are provided in the abstract of Marinov et al. (2011). However, we believe our results to accurately date the timing of vein formation at Cevizlidere because of the concordance of the Re-Os and ^{40}Ar/^{39}Ar ages, and the good reproducibility of standard analyses (see Appendix F).

3.5 Discussion

3.5.1 Interpretation of the ^{40}Ar/^{39}Ar biotite and Re-Os molybdenite ages

^{40}Ar/^{39}Ar dating of minerals is a powerful technique that is widely utilized in studies of porphyry systems. Discrete magmatic and hydrothermal pulses in a porphyry district can be unraveled by this method, especially when it is used in tandem with other high-precision geochronological methods such as U-Pb zircon and Re-Os molybdenite dating. However, one major drawback of ^{40}Ar/^{39}Ar dating is the possibility of thermal resetting of the dated minerals after initial crystallization, and extra care should be taken during interpretation of ^{40}Ar/^{39}Ar geochronological data obtained from magmatic and hydrothermal assemblages, particularly from minerals with relatively low closure temperatures for Ar diffusion (e.g., biotite, K-feldspar, muscovite/sericite, and illite). Resetting of Ar isotopic systematics is commonly observed in porphyry districts that have protracted and complex magmatic-hydrothermal histories (e.g., Villeneuve et al., 2001; Maksaev et al., 2004; Masterman et al., 2004; Deckart et al., 2005; Harris et al., 2008; Chiaradia et al., 2009).

In this study, two samples of magmatic biotite collected from the least altered intervals of diorite porphyry, together with another sample of hydrothermal biotite, yielded ^{40}Ar/^{39}Ar ages that overlap within error (Fig. 3.9 and Table 3.1). Although a discrimination was made between the least-altered and altered samples based on petrographic observations, the ^{40}Ar/^{39}Ar biotite ages require further testing against the possibility of thermal resetting.

Overall, ^{40}Ar/^{39}Ar step-heating analyses of all three samples produced concordant age spectra and inverse isochron ages (Fig. 3.9). Minor Ar loss detected in sample K-4403 in low temperature steps (Fig. 3.9C) probably reflects chloritization of the rims of some igneous biotite grains, but the uniform Ar degassing pattern observed in higher temperature steps suggests that chlorite alteration did not affect the bulk of the grains (*cf.* Lo and Onstott, 1989). Samples K-1427 (igneous biotite) and K-7420 (hydrothermal biotite), on the other hand, have older initial and last steps (Fig. 3.9A, E) suggesting the presence of minor amounts of excess ^{40}Ar. Nevertheless, the statistically valid plateaus in the middle parts of the spectra can be considered to provide maximum estimates of the cooling ages. Where the presence of excess ^{40}Ar is suspected, inverse isochrons commonly provide a more accurate estimate of the true age. For all three samples, the inverse isochron ages are identical within error of the plateau ages, so we are confident in the validity of these results. The y-axis intercepts of the inverse isochrons also confirm the presence of excess ^{40}Ar in samples K-1427 and K-7420, because the ^{36}Ar/^{40}Ar ratios are below the expected value for atmospheric argon (i.e., blank = 0.00338). Consequently, we accept the inverse isochron ages as the best estimates of the ages of these samples.

Table 3.1 Summary of ^{40}Ar/^{39}Ar geochronological analyses from the Cevizlidere deposit

Sample	**Lithology**	**Mineral**	**No. of steps in plateau/total steps**	**%^{39}Ar released (plateau)**	**^{40}Ar/^{39}Ar plateau age (Ma ± 2σ)**	**^{40}Ar/^{39}Ar inverse isochron age (Ma ± 2σ)**
K-1427	Diorite porphyry	Biotite (igneous)	8/11	85	25.29 ± 0.34	25.10 ± 0.28 (MSWD=1.7)
K-4403	Diorite porphyry	Biotite (igneous)	9/10	97	25.54 ± 0.40	25.49 ± 0.20 (MSWD=1.4)
K-7420	Granodiorite porphyry	Biotite (hydrothermal)	7/10	86	24.84 ± 0.36	24.73 ± 0.16 (MSWD=1.4)

The ^{40}Ar/^{39}Ar ages of the both igneous biotite separates (25.49 ± 0.20 Ma and 25.10 ± 0.28 Ma) are distinctly older than the age of hydrothermal biotite (24.73 ± 0.16 Ma) suggesting that the igneous biotites have not been reset by later hydrothermal overprinting, or by the heat of later magmatism such as the late diorite plug (Fig. 3.2B). We therefore interpret the ^{40}Ar/^{39}Ar ages of the igneous biotites to approximate the magmatic cooling age (~25.3 Ma) at 250 – 400°C, acknowledging the uncertainties introduced by the presence of minor excess ^{40}Ar and weak chloritization. The ^{40}Ar/^{39}Ar age for hydrothermal biotite (24.73 ± 0.16 Ma) is statistically indistinguishable from two molybdenite Re-Os ages of 24.90 ± 0.10 Ma and 24.78 ± 0.10 Ma, confirming that these dates accurately reflect the timing of hydrothermal alteration and mineralization at ~ 24.8 Ma. These ages further suggest that hydrothermal activity was short-lived and closely followed cooling of the intrusive rocks (i.e., within ~0.5 m.y.). The short life-span of the magmatic-hydrothermal system correlates well with many other porphyry systems globally (Arribas et al., 1995; Muntean and Einaudi 2001; Chiaradia et al., 2009), and also with theoretical estimates of the thermal duration of porphyry-related magmatism and ore formation (Cathles et al., 1997).

The combined ^{40}Ar/^{39}Ar and Re-Os isotopic data show that the Cevizlidere porphyry Cu-Au-Mo deposit is temporally unrelated to middle Eocene (~48–44 Ma; Kuşcu et al., 2010, 2013; İmer et al., 2013) porphyry-related systems such as Çöpler and Kabataş, despite their regional proximity (within 40–50 km; Fig. 3.1). Thus, the Cevizlidere deposit appears to belong to a distinct metallogenic epoch that is significantly younger than the middle Eocene porphyry-epithermal deposits hosted by back-arc-related magmatic rocks in the eastern Taurides.

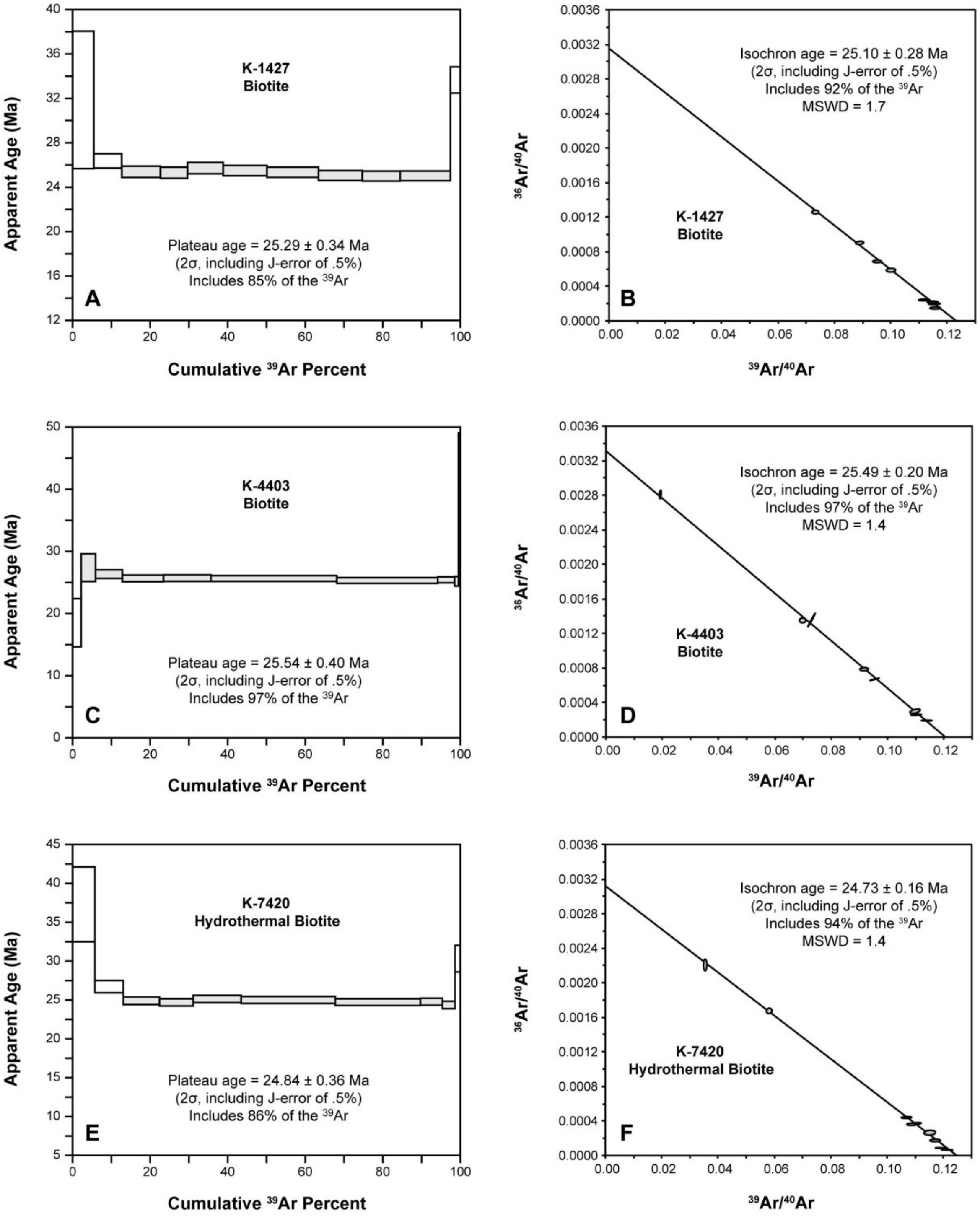

Figure 3.9 Apparent ^{40}Ar/^{39}Ar age spectra and inverse isochron plots for igneous and hydrothermal biotites from the Cevizlidere deposit.

Table 3.2 Summary of Re-Os molybdenite data from the Cevizlidere deposit

Sample	Drillhole-depth (m)	Location	Re (ppm)	± 2σ	^{187}Re (ppb)	± 2σ	^{187}Os (ppb)	± 2σ	Model Age (Ma)	Age uncertainty (± 2σ) with decay constant uncertainty (Ma)
KIZ-1429	KIZ-001: 429.50m	504582E 4344844N	775.5	2.0	487442	1261	202.3	0.1	24.90	0.10
KIZ-1493	KIZ-001: 493.50m	504582E 4344844N	724.6	1.9	455462	1178	188.1	0.1	24.78	0.10

3.5.2 *Implications for Southern Neotethys subduction and metallogeny*

In Figures 3.5A and 3.6, the compositions of the Cevizlidere intrusive rocks are compared to those of other mid–late Cenozoic igneous rocks from the eastern Taurides generated by subduction of the Southern Neotethys ocean.

The Çöpler-Kabataş magmatic complex and related porphyry-epithermal Au-Cu deposit, which was formed in the middle Eocene at ~44 Ma (Kuşcu et al., 2007, 2013; İmer et al., 2013), consists of sub-alkaline (medium- to high-K) dioritic to granodioritic intrusive rocks (Fig. 3.5A) that contain abundant hornblende and magnetite, with or without biotite (İmer et al., 2013). Major and trace element compositions are very similar to those of Cevizlidere, although the Çöpler-Kabataş suite is uniformly slightly more enriched in most trace elements including REE (Fig. 3.5A, 3.6).

Volcanic and volcaniclastic rocks of the collision-related early to middle Miocene Yamadağ Volcanic Complex (17–12 Ma; Kürüm et al., 2008) represent the earliest stage of collision-related volcanism in eastern Turkey. This volcanic assemblage is dominated by a bimodal suite comprising sub-alkaline to mildly alkaline olivine- and olivine-pyroxene-phyric basalt, trachybasalt, basaltic trachyandesite, and basaltic andesite, with minor sub-alkaline dacite (Fig. 3.5A; Kürüm et al., 2008). On a normalized trace element diagram (Fig. 3.6A), the Yamadağ volcanic rocks display broadly similar patterns to the Çöpler-Kabataş and Cevizlidere suites, with enrichments in LILE and negative Nb, Ta, and Ti anomalies. However, the overall enrichment levels of the incompatible elements in the Yamadağ volcanic rocks are slightly higher when compared to the Cevizlidere porphyries (Fig. 3.6A) consistent with their relatively alkaline nature. When plotted on a chondrite-normalized REE diagram, the Yamadağ suite shows enrichments in LREE relative to MREE and HREE (Fig. 3.6B; $[La/Sm]_n$ = 4–10, $[Dy/Yb]_n$ = 1.5–2.4) similar to the Cevizlidere porphyries, but the latter suite is relatively less enriched in LREE–HREE (Fig. 3.6B).

The above comparisons highlight the temporal evolution of the nature of magmatism in eastern Anatolia during mid–late Cenozoic times. In terms of major and trace element characteristics, the late Oligocene Cevizlidere porphyritic suite is almost indistinguishable from the middle Eocene Çöpler-Kabataş magmatic complex in that both magmatic suites comprise calc-alkaline, LILE- and LREE-enriched, and relatively MREE- and HREE-depleted intrusive rocks, which were formed from I-type, oxidized magmas with high magmatic water contents. Previous studies of the middle Eocene (50–43 Ma) plutons across the eastern Taurides (including the Çöpler-Kabataş magmatic complex) by Kuşcu et al., (2010 and 2013) interpreted these intrusive rocks as products of post-collisional magmatism. However, based on regional geological and geochronological data, İmer et al., (2013) suggested that these plutons were emplaced in a back-arc setting behind the broadly contemporaneous Southern Neotethys arc in eastern Turkey, and the close similarity in magma compositions suggest a similar tectonic setting for the Cevizlidere porphyries.

The Oligocene–Miocene boundary (23 Ma) marks a major change in the Late Cenozoic geodynamics of the eastern Mediterranean region, and is characterized by a switch from compressional to extensional tectonics, possibly due to the initiation of slab break-off below the southern margin of the TAB (Kaymakçı et al., 2010; Guest and Matthews 2011). This was followed by regional-scale subsidence, basin development (e.g., the Ovacık Basin), and exhumation throughout Turkey (Whitney and Dilek 1997; Jaffey and Robertson 2005; Boztuğ et al., 2008; Hüsing et al., 2009), the Greater Caucasus (Avdeev and Niemi 2011), and Iran (Verdel et al., 2011). The timing of calc-alkaline magmatism and related porphyry-style mineralization at Cevizlidere (~25 Ma) closely precedes the onset of this extensional tectonic regime, reflecting a transition from subduction to early collisional tectonics.

The early to middle Miocene (17–12 Ma) Yamadağ Volcanic Complex, on the other hand, is bimodal, predominantly mafic, and slightly more alkaline in character than both the

Çöpler-Kabataş and Cevizlidere magmatic suites (Fig. 3.5A). Its major and trace element characteristics indicate derivation through mixing of enriched-mantle-derived mafic magmas with felsic crustal melts. The enriched-mantle source of the Yamadağ volcanic rocks is most probably inherited from the earlier Late Cretaceous–Oligocene subduction events, as a result of upper plate extension and subsequent upwelling of hot asthenosphere beneath eastern Anatolia. In this respect, the Yamadağ Volcanic Complex may have formed in response to tectonic readjustments prior to the final collision event in eastern Anatolia, which is suggested to have taken place at ~12–10 Ma (Şengör and Yılmaz 1981).

Apart from Cevizlidere, no other porphyry and/or epithermal deposits with similar timing have been reported from eastern/southeastern Turkey. In contrast, the contiguous Iranian segment of this orogenic belt hosts several early collisional porphyry and epithermal systems including the porphyry Cu deposits of the Kerman Belt (~12 Ma; Shafiei et al., 2009), the Darreh-Zerreshk and Ali-Abad porphyry Cu deposits in central Iran (~16 Ma; Zarasvandi et al., 2007), the Dalli porphyry Cu-Au deposit (~21–19 Ma; Ayati et al., 2013), and the Sari Gunay epithermal Au deposit (~11 Ma; Richards et al., 2006). Porphyry and/or epithermal mineralization in these districts is related to early to late Miocene, predominantly sub-alkaline magmatic activity except for the Sari Gunay deposit, which is associated with mildly alkaline latitic to trachyitic volcanic rocks, interpreted to reflect its transitional timing with respect to the Arabia-Eurasia collision (Richards et al., 2006). The relatively younger timing of these Iranian deposits compared with Cevizlidere is consistent with tectonic reconstructions that suggest diachronous progression of this collisional event from northwest to southeast (Agard et al., 2005; Chiu et al., 2013).

Major and trace element compositions of the middle Miocene Kuh Panj porphyry suite, which is located in the Kerman Belt, are compared to the Cevizlidere porphyries in Figures 3.5A and 3.6. The subalkaline diorite to granodiorite intrusive rocks of the Kuh Panj deposit (Fig. 3.5A) display LILE- and LREE-enriched and Nb-Ta-Ti-depleted trace and rare earth element patterns (Fig. 3.6A; Shafiei et al., 2009; Richards et al., 2012). In comparison to the Cevizlidere porphyries, the Kuh Panj suite overlaps the range of Cevizlidere samples, but extends to greater enrichments for some incompatible elements (including LREE) and lower enrichments for HREE. Broadly similar magma compositions have also been reported for the 16 Ma (early/middle Miocene boundary) Darreh-Zerreshk and Ali-Abad porphyry Cu (Zarasvandi et al., 2007), and the early Miocene Dalli porphyry Cu-Au deposits (Ayati et al., 2013). These roughly similar geochemical and temporal characteristics between the late Oligocene Cevizlidere intrusions and the early to middle Miocene Iranian porphyry and epithermal deposits suggests a pre-collisional timing for these deposits, reflecting a final pulse of arc-related magmatism along the Southern Neotethys subduction zone.

3.6 Conclusions

Porphyry Cu-Mo-Au mineralization at Cevizlidere is related to a composite stock consisting of intermediate composition diorite to granodiorite porphyries. Both intrusive phases have undergone intense potassic and phyllic alteration as a result of porphyry-related hydrothermal activity. $^{40}Ar/^{39}Ar$ incremental step-heating analyses of igneous biotite from least-altered samples of syn-mineral diorite porphyry yielded ages of 25.49 ± 0.20 Ma and 25.10 ± 0.28 Ma. The timing of the porphyry mineralizing system at Cevizlidere is constrained by the $^{40}Ar/^{39}Ar$ age of hydrothermal biotite (24.73 ± 0.16 Ma) associated with high-temperature potassic alteration, and by Re-Os ages of two molybdenite samples (24.90 ± 0.10 Ma and 24.78 ± 0.10 Ma) obtained from B-type quartz-magnetite-sulfide veinlets.

Mineralized intrusive phases at Cevizlidere are calc-alkaline (medium-K) in composition and display trace element patterns characteristic of magmas generated in convergent margin settings. The regional geological and geochronological evidence, suggests that shallow level magmatism and associated porphyry mineralization at Cevizlidere are related to a change from compressional to locally extensional tectonics at ~25 Ma, prior to the final collision between Arabia and Eurasia (~12–10 Ma). Thus, the tectonic setting of the Cevizlidere deposit is comparable to the back-arc-related middle Eocene (~44 Ma) Çöpler epithermal Au deposit, but its late timing with respect to Neotethys subduction also suggests similarities to several early-collisional Iranian porphyry systems, including the Kerman porphyry belt, the Dalli porphyry Cu-Au deposit, and the Darreh-Zerreshk and Ali-Abad porphyry Cu deposits.

3.7 References

Agard P, Omrani J, Jolivet L, Mouthereau F (2005) Convergence history across Zagros (Iran): constraints from collisional and earlier deformation. Int J Earth Sci (Geol Rundsch) 94:401–419.

Akay E (1989) Evolution of the post-collisional cratonic basins in eastern Taurus. Bull Min Res Explor Inst Turkey (MTA) 109:53–64.

Akay E, Erkan E, Ünay E (1989) Muş Tersiyer havzasının stratigrafisi. Bull Min Res Explor Inst Turkey (MTA) 109:59–76 (in Turkish).

Allen MB (2009) Discussion on the Eocene bimodal Piranshahr massif of the Sanadaj–Sirjan Zone, West Iran: a marker of the end of collision in the Zagros orogen. J Geol Soc 166: 981–982.

Allen MB, Armstrong, HA (2008) Arabia–Eurasia collision and the forcing of mid-Cenozoic global cooling. Palaeogeogr Palaeocl 265:52–58.

Arribas A Jr, Hedenquist JW, Itaya T, Okada T, Concepcion RA, Garcia JS Jr (1995) Contemporaneous formation of adjacent porphyry and epithermal Cu-Au deposits over 300 ka in northern Luzon, Philippines. Geology 23:337–340.

Avdeev B, Niemi NA (2011) Rapid Pliocene exhumation of the central Greater Caucasus constrained by low-temperature thermochronometry. Tectonics 30:TC2009. doi:10.1029/2010TC002808.

Ayati F, Yavuz F, Asadi HH, Richards JP, Jourdan F (2013) Petrology and geochemistry of calc-alkaline volcanic and subvolcanic rocks, Dalli porphyry copper-gold deposit, Markazi Province, Iran. Int Geol Rev 55:158–184.

Boulton SJ (2009) Record of Cenozoic sedimentation from the Amanos Mountains, Southern Turkey: Implications for inception and evolution of the Arabia–Eurasia continental collision. Sediment Geol 216:29–47.

Boztuğ D, Harlavan Y, Arehart GB, Satır M, Avcı N (2007) K-Ar age, whole-rock and isotope geochemistry of A-type granitoids in the Divriği-Sivas region, eastern-central Anatolia, Turkey. Lithos 97:193–218.

Brenan JM, Shaw HF, Phinney DL, Ryerson FJ (1994) Rutile-aqueous fluid partitioning of Nb, Ta, Hf, Zr, U and Th: implications for high field strength element depletions in island-arc basalts. Earth Planet Sci Lett 128:327–339.

Carmichael ISE, Ghiorso MS (1990) The effect of oxygen fugacity on the redox state of natural liquids and their crystallizing phases. In: Nicholls J, Russell JK (eds), Modern Methods of Igneous Petrology: Understanding Magmatic Processes. Rev Mineral, Min Soc America 24:191–212.

Castillo PR, Janney PE, Solidum RU (1999) Petrology and geochemistry of Camiguin Island, southern Philippines: Insights to the source of adakites and other lavas in a complex arc setting. Contrib Mineral Petr 134:33–51.

Cathles LM, Erendi AH, Barrie T (1997) How long can a hydrothermal system be sustained by a single intrusive event? Econ Geol 92:766–771.

Chiaradia M, Vallance, J, Fontbote L, Stein H, Schaltegger U, Coder J, Richards J, Villeneuve M, Gendall I (2009) U–Pb, Re–Os, and 40Ar/39Ar geochronology of the Nambija Au-skarn and Pangui porphyry Cu deposits, Ecuador: implications for the Jurassic metallogenic belt of the Northern Andes. Miner Deposita 44:371–387.

Chiu H-Y, Chung S-L, Zarrinkoub MH, Mohammadi SS, Khatib MM, Iizuka Y (2013) Zircon U-Pb age constraints from Iran on the magmatic evolution related to Neotethyan subduction and Zagros orogeny. Lithos 162–163:70–87.

Clark AH, Ullrich TD (2004) ^{40}Ar-^{39}Ar age data for andesitic magmatism and hydrothermal activity in the Timok Massif, eastern Serbia: implications for metallogenetic relationships in the Bor copper-gold subprovince. Miner Deposit 39:256–262.

Deckart K, Clark AH, Aguilar C, Vargas R, Bertens A, Mortensen JK, Fanning M (2005) Magmatic and hydrothermal chronology of the giant Rio Blanco porphyry copper deposit, central Chile: Implications of an integrated U-Pb and ^{40}Ar/^{39}Ar database. Econ Geol 100:905–934.

Defant MJ, Drummond MS (1993) Mount St. Helens: Potential example of the partial melting of the subducted lithosphere in a volcanic arc. Geology 21:547–550.

Dewey JF, Hempton MR, Kidd WSF, Şaroğlu F, Şengör AMC (1986) Shortening of continental lithosphere: the neotectonics of Eastern Anatolia – a young collision zone. In: Coward MP, Ries AC (eds) Collision Tectonics. Geol Soc Lond Spec Publ 19:3–36.

Dumanlılar H, Aydal D, Dumanlılar Ö (1999) Geology, mineralogy and geochemistry of sulfide mineralization in the Ispendere region (Malatya). Bull Min Res Explor Inst Turkey (MTA) 121:57–82.

Elmas A (1994) An example of the active continental margin volcanism in the Late Lutetian–Late Oligocene interval in southeast Anatolia: Gövelek volcanics (Van-Erçek). Turk J Earth Sci 3:43–54.

Elmas A, Yılmaz Y (2003) Development of an oblique subduction zone – tectonic evolution of the Tethys suture zone in southeast Turkey. Int Geol Rev 45:827–840.

Frey FA, Chappell BW, Roy SD (1978) Fractionation of rare-earth elements in the Tuolumne intrusive series, Sierra Nevada batholith, California. Geology 6:239–242.

Guest B, Matthews WA (2011) A reassessment of the timing of the Arabia-Eurasia collision with regional and global implications. Geological Society of America Annual Meeting Abstracts with Programs 43, no.5, 141.

Hanson GN (1980) Rare earth elements in petrogenetic studies of igneous systems. Annu Rev Earth Planetary Sci 8:371–406.

Harris AC, Dunlap WJ, Reiners PW, Allen CM, Cooke DR, White NC, Campbell IH, Golding SD (2008) Multimillion year thermal history of a porphyry copper deposit: Application of U-Pb, $^{40}Ar/^{39}Ar$ and (U-Th)/He chronometers, Bajo de la Alumbrera copper-gold deposit, Argentina. Miner Deposit 43:295–314.

Haschke M, Ahmadian J, Murata M, McDonald I (2010) Copper mineralization prevented by arc-root delamination during Alpine-Himalayan collision in central Iran. Econ Geol 105:855–865.

Hüsing SK, Zachariasse W-J, van Hinsbergen DJJ, Krijgsman W, İnceöz M, Harzhauser M, Mandic O, Kroh A (2009) Oligocene–Miocene basin evolution in SE Anatolia, Turkey: constraints on the closure of the eastern Tethys gateway. In: van Hinsbergen DJJ, Edwards MA, Gowers R (eds) Collision and Collapse at the Africa-Arabia-Eurasia Subduction Zone. Geol Soc Lond Spec Publ 311:107–132.

İmer A, Richards JP, Creaser RA (2013) Age and tectonomagmatic setting of the Çöpler-Kabataş magmatic complex and porphyry-epithermal Au deposit, east central Anatolia, Turkey. Miner Deposit 48:557–583.

Irvine TN, Baragar WRA (1971) A guide to the chemical classification of the common volcanic rocks. Can J Earth Sci 8:523–548.

Jaffey N, Robertson A (2005) Non-marine sedimentation associated with Oligocene-Recent exhumation and uplift of the Central Taurus Mountains, S Turkey. Sediment Geol 173:53–89.

Janković S (1977) The copper deposits and geotectonic setting of the Tethyan Eurasian Metallogenic Belt. Miner Deposita 12:37–47.

Karaoğlan F, Parlak O, Robertson A, Thöni M, Klötzli U, Koller F, Okay Aİ (2013) Evidence of Eocene high-temperature/high-pressure metamorphism of ophiolitic rocks and granitoid intrusion related to Neotethyan subduction processes (Dogansehir area, SE Anatolia). In: Robertson AHF, Parlak O, Unlugenc UC (eds) Geological Development of Anatolia and the Easternmost Mediterranean Region. Geol Soc Lond Spec Publ 372:249–272.

Kaymakçı N, İnceöz M, Ertepınar P (2006) 3D-architecture and Neogene evolution of the Malatya Basin: Inferences for the kinematics of the Malatya and Ovacık Fault Zones. Turk J Earth Sci 15:123–154.

Kaymakçı N, İnceöz M, Ertepınar P, Koç A (2010) Late Cretaceous to Recent kinematics of SE Anatolia (Turkey). In: Sosson M, Kaymakçı N, Stephenson RA, Bergerat F, Starostenko V (eds)

Sedimentary Basin Tectonics from the Black Sea and Caucasus to the Arabian Platform. Geol Soc Lond Spec Publ, 340:409–435.

Keskin M (2003) Magma generation by slab steepening and breakoff beneath a subduction-accretion complex: An alternative model for collision-related volcanism in Eastern Anatolia, Turkey. Geophys Res Lett 30:8046. doi:10.1029/2003GL018019.

Kociumbas M, Page RH (2009) The Cevizlidere Porphyry Deposit, Tunceli Province, Turkey. Technical report by Watts, Griffis and McQuat Limited for Anatolia Minerals Development Limited (www.alacergold.com). p. 94

Koçyiğit A, Beyhan A (1998) A new intracontinental transcurrent structure: the Central Anatolian Fault Zone, Turkey. Tectonophysics 284:317–336.

Kogiso T, Tatsumi Y, Nakano S (1997) Trace element transport during dehydration processes in the subducted crust: 1. Experiments and implications for the origin of ocean island basalts. Earth Planet Sci Lett 148:193–205.

Kuşcu İ, Gençalioğlu-Kuşcu G, Tosdal RM (2007) Tectonomagmatic-metallogenic framework of mineralization events in the southern NeoTethyan arc, southeastern Turkey. In: Andrew CJ et al (eds) Digging Deeper. Proceedings of the 9th Biennial SGA Meeting, Dublin, 20–23 August 2007, pp. 853–856.

Kuşcu İ, Gençalioğlu-Kuşcu G, Tosdal RM, Ulrich TD, Friedman R (2010) Magmatism in the southeastern Anatolian orogenic belt: transition from arc to post-collisional setting in an evolving orogen. In: Sosson M, Kaymakçı N, Stephenson RA, Bergerat F, Starostenko V (eds) Sedimentary Basin Tectonics from the Black Sea and Caucasus to the Arabian Platform. Geol Soc Lond Spec Publ 340:437–460.

Kuşcu İ, Tosdal RM, Gençalioğlu-Kuşcu G, Friedman R, Ullrich TD (2013) Late Cretaceous to Middle Eocene Magmatism and Metallogeny of a Portion of the Southeastern Anatolian Orogenic Belt, East-Central Turkey. Econ Geol 108:641–666.

Kürüm S, Önal A, Boztuğ D, Spell T, Arslan M (2008) ^{40}Ar/^{39}Ar age and geochemistry of the post-collisional Miocene Yamadağ volcanics in the Arapkir area (Malatya Province), eastern Anatolia, Turkey. J Asian Earth Sci 33:229–251.

Lo CH, Onstott TC (1989) ^{39}Ar recoil artifacts in chloritized biotite. Geochim Cosmochim Acta 53:2697–2711.

Maksaev V, Munizaga F, McWilliams M, Fanning M, Mathur R, Ruiz J, Zentilli M (2004)- New chronology for El Teniente, Chilean Andes, from U-Pb, ^{40}Ar/^{39}Ar, Re-Os, and fission track dating: Implications for the evolution of a supergiant porphyry Cu-Mo deposit. Soc Econ Geol Spec Publ 11:15–54.

Marinov D, Barra F, Alizade F (2011) Re-Os dating of molybdenite mineralisation from Turkish porphyry copper prospects. In: Let's Talk Ore Deposits, Proceedings of 11th Biennial SGA Meeting, Antofagasta (Chile), 26–29 September 2011.

Markey R, Stein HJ, Hannah JL, Selby D, Creaser RA (2007) Standardizing Re-Os geochronology: A new molybdenite Reference Material (Henderson, USA) and the stoichiometry of Os salts. Chem Geol 244:74–87.

Marsh TM, Einaudi MT, McWilliams M (1997) ^{40}Ar/^{39}Ar geochronology of Cu-Au and Au-Ag mineralization in the Potrerillos district, Chile. Econ Geol 92:784–806.

Masterman GJ, Cooke DR, Berry RF, Clark AH, Archibald DA, Mathur R, Walshe JL, Durán M (2004) ^{40}Ar/^{39}Ar and Re-Os geochronology of porphyry copper-molybdenum deposits and related copper-silver veins in the Collahuasi District, northern Chile. Econ Geol 99:673–690.

Michard A, Whitechurch H, Ricou LE, Montigny R, Yazgan E (1984) Tauric subduction (Malatya-Elazığ provinces) and its bearing on tectonics of the Tethyan realm in Turkey. In: Dixon JE, Robertson AHF (eds) The Geological Evolution of the Eastern Mediterranean. Geol Soc Lond Spec Publ 17:361–373.

Middlemost EAK (1994) Naming materials in the magma/igneous rock system. Earth Sci Rev 37:215–224.

Moore G, Carmichael ISE (1998) The hydrous phase equilibria (to 3 kbar) of an andesite and basaltic andesite from western Mexico: Constraints on water content and conditions of phenocryst growth. Contrib Mineral Petrol 130:304–319.

Muntean JL, Einaudi MT (2001) Porphyry-epithermal transition: Maricunga Belt, northern Chile. Econ Geol 96:743–772.

MTA (1989) Geologic map of Turkey. Ankara, MTA, scale 1:2,000,000.

Okay Aİ, Tüysüz O (1999) Tethyan sutures of northern Turkey. In: Durand B, Jolivet L, Horvath F, Seranne M (eds) Mediterranean Basins: Tertiary Extension within the Alpine Orogen. Geol Soc Lond Spec Publ 156:475–515.

Okay Aİ, Zattin M, Cavazza W (2010) Apatite fission-track data for the Miocene Arabia-Eurasia collision. Geology 38:35–38.

Önal A, Boztuğ D, Kürüm S, Harlavan Y, Arehart GB, Arslan M (2005) K-Ar age determination, whole-rock and oxygen isotope geochemistry of the post-collisional Bizmişen and Çaltı plutons, SW Erzincan, eastern Central Anatolia, Turkey. Geol J 40:457–476.

Özgül N, Turşucu A (1984) Stratigraphy of the Mesozoic carbonate sequence of the Munzur Mountains (Eastern Turkey). In: Tekeli O, Göncüoğlu MC (eds) Geology of the Taurus Belt. Proceedings of the International Tauride Symposium. Mineral Research and Exploration Institute of Turkey (MTA) Publications, Ankara, Turkey, pp 173–180.

Peccerillo A, Taylor SR (1976) Geochemistry of Eocene calc-alkaline volcanic rocks from the Kastamonu area, northern Turkey. Contrib Mineral Petr 58:63–81.

Richards JP (2003) Metallogeny of the Neo-Tethys arc in central Iran. In: Eliopoulos DG et al (eds) Proceedings of Mineral Exploration and Sustainable Development. Millpress, Rotterdam, pp 1237–1239.

Richards JP, Wilkinson D, Ullrich T (2006) Geology of the Sari Gunay epithermal gold deposit, northwest Iran. Econ Geol 101:1455–1496.

Richards JP, Spell T, Rameh E, Razique A, Fletcher T (2012) High Sr/Y magmas reflect arc maturity, high magmatic water content, and porphyry Cu ± Mo ± Au potential: examples from the Tethyan arcs of central and eastern Iran and western Pakistan. Econ Geol 107:295–332.

Rızaoğlu T, Parlak O, Höck V, Koller F, Hames WE, Billor Z (2009) Andean-type active margin formation in the eastern Taurides: Geochemical and geochronological evidence from the Baskil granitoid (Elazığ, SE Turkey). Tectonophysics 473:188–207.

Robertson AHF, Parlak O, Rızaoğlu T, Ünlügenç Ü, İnan N, Taşlı K, Ustaömer T (2007) Tectonic evolution of the South Tethyan ocean: evidence from the Eastern Taurus Mountains (Elazığ region, SE Turkey). In: Ries AC, Butler RWH, Graham RH (eds) Deformation of the Continental Crust: The Legacy of Mike Coward. Geol Soc Lond Spec Publ 272:231–270.

Selby D, Creaser RA (2004) Macroscale NTIMS and microscale LA-MC-ICP-MS Re-Os isotopic analysis of molybdenite: Testing spatial restrictions for reliable Re-Os age determinations, and implications for the decoupling of Re and Os within molybdenite. Geochim Cosmochim Acta 68:3897–3908.

Şengör AMC, Yılmaz Y (1981) Tethyan evolution of Turkey: a plate tectonic approach. Tectonophysics 75:181–241.

Shafiei B, Haschke, M, Shahabpour J (2009) Recycling of orogenic arc crust triggers porphyry Cu mineralization in Kerman Cenozoic arc rocks, southeastern Iran. Miner Deposit 44:265–283.

Smoliar MI, Walker RJ, Morgan JW (1996) Re-Os ages of Group IIA, IIIA, IVA, and IVB iron meteorites. Science 271:1099–1102.

Stein HJ, Markey RJ, Morgan JW, Hannah JL, Scherstén A (2001) The remarkable Re–Os chronometer in molybdenite: how and why it works. Terra Nova 13:479–486.

Stolz AJ, Jochum KP, Spettel B, Hofmann AW (1996) Fluid- and melt-related enrichment in the subarc mantle: Evidence from Nb/Ta variations in island-arc basalts. Geology 24:587–590.

Sun S-S, McDonough WF (1989) Chemical and isotopic systematics of oceanic basalts: Implications for mantle composition and processes. In: Saunders AD, Norry MJ (eds) Magmatism in the Ocean Basins. Geol Soc Lond Spec Publ 42:313–345.

Verdel C, Wernicke BP, Hassanzadeh J, Guest B (2011) A Paleogene extensional arc flare-up in Iran. Tectonics 30:TC3008. doi: 10.1029/2010TC002809.

Villeneuve M, Whalen JB, Anderson RG, Struik LC (2001) The Endako Batholith: Episodic plutonism culminating in formation of the Endako porphyry molybdenite deposit, north-central British Columbia. Econ Geol 96:171–196.

Westaway R, Arger J (2001) Kinematics of the Malatya-Ovacık fault zone. Geod Acta 14: 103-301.

Whitney DL, Dilek Y (1997) Core complex development in central Anatolia, Turkey. Geology 25:1023–1026.

Yazgan E, Chessex R (1991) Geology and tectonic evolution of Southeastern Taurus in the region of Malatya. Turk Assoc Petrol Geol Bull 3:1–42.

Yılmaz Y (1993) New evidence and model on the evolution of Southeast Anatolian orogen. Geol Soc Am Bull 105:251–271.

Yiğit Ö (2009) Mineral deposits of Turkey in relation to Tethyan metallogeny: implications for future mineral exploration. Econ Geol 104:19–51.

Zarasvandi A, Liaghat S, Zentilli M, Reynolds PH (2007) ^{40}Ar/^{39}Ar geochronology of alteration and petrogenesis of porphyry copper-related granitoids in the Darreh-Zerreshk and Ali-Abad area, Central Iran. Explor Min Geol 16:11–24.

CHAPTER 4: Hydrothermal Evolution of the Çöpler Porphyry-Epithermal Au Deposit, Erzincan Province, Central Eastern Turkey*

* A version of this chapter is intended to be submitted for journal publication as a co-authored article with co-authors Jeremy P. Richards (University of Alberta) and Karlis Muehlenbachs (University of Alberta)

4.1 Introduction

The Tauride-Anatolide Block (TAB) in Turkey is a roughly east–west-elongated continental fragment (Fig. 4.1) forming a sector of the extensive Tethyan Alpine-Himalayan orogenic belt. The TAB lies in between the Balkans to the northwest and Iran to the southeast, both regions being highly prospective for various types of base and precious metal deposits (Janković, 1977, 1997; Heinrich and Neubauer, 2002; Richards, 2003a; Marchev et al., 2005; von Quadt et al., 2005; Richards et al., 2012). Similar to its neighboring areas, the TAB hosts a variety of ore deposit types including porphyry Cu±Mo±Au, epithermal Au±Ag, Fe-skarn/IOCG, volcanic-hosted massive sulfide, and carbonate-hosted Pb-Zn deposits (Yiğit, 2009). Key to the formation of these deposits in Turkey is the subduction of the surrounding Neo-Tethyan ocean basins during the Mesozoic–Cenozoic, and the majority of these deposit types are spatially and temporally related to Late Cretaceous–Miocene igneous rocks that were generated in subduction-related and post-subduction settings (e.g., Erler, 1984; Kuşcu and Erler, 1998; Boztuğ et al., 2003; Yiğit, 2009; Kuşcu et al., 2010 and 2013; İmer et al., 2013, 2014).

Despite its prospectivity, Turkey was relatively underexplored, particularly for bulk tonnage porphyry Cu±Mo±Au and epithermal Au±Ag deposits, until the late 1990s. Following changes to the Turkish Mining Law in the early 2000s, the country's mining sector has become more industry-orientated, and has attracted significant amounts of foreign investment. This has led to a dramatic increase in exploration activity (mainly for Cu and Au) and the discovery of several important deposits, particularly in the western portion of the TAB (e.g., the Kışladağ porphyry Au deposit, and the Ovacık and Efemçukuru epithermal Au deposits). The eastern part of the TAB, on the other hand, has seen less exploration due to security issues, remoteness to infrastructure, and the relatively rough topography of the region. Despite these obstacles, several porphyry and epithermal deposits were discovered in the eastern TAB in the late 1990s and early 2000s, including the Çöpler epithermal Au and the Cevizlidere porphyry Cu-Mo-Au deposits.

The Çöpler Au deposit (39°25’N, 38°32’E) is located in the eastern Tauride mountain range about 120 km southwest of the city of Erzincan in central eastern Turkey (Fig. 4.1, 4.2). The deposit has combined measured and indicated resources of ~7.8 Moz Au, and consists of subeconomic porphyry-style Cu-Au mineralization overlain and overprinted by Au-bearing intermediate-sulfidation epithermal veinlet and manto-type carbonate-replacement orebodies. Gold-(copper) mineralization at Çöpler shows close spatial relationship to middle Eocene (~44 Ma) calc-alkaline intrusions of the Çöpler-Kabataş magmatic complex (Kuşcu et al., 2010, 2013; İmer et al., 2013), which were emplaced into a succession of variably metamorphosed Permian–Cretaceous siliciclastic and carbonate rocks exposed in the northern part of the Munzur Mountains (Fig. 4.2). The Karakartal porphyry Cu-Au deposit (formerly known as Kabataş) is also related to this magmatic complex, and occurs in association with calc-alkalic diorite to granodiorite intrusions of middle Eocene age (~48 Ma; Fig. 4.2; Kuşcu et al. 2013).

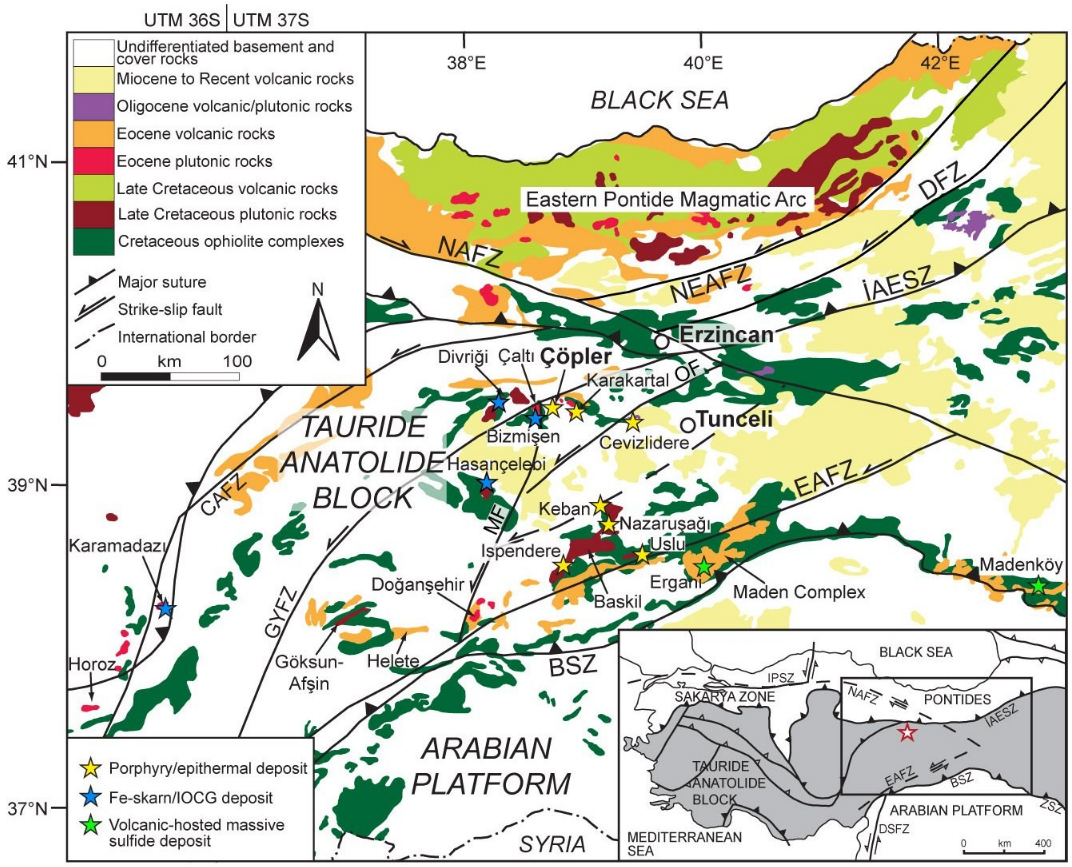

Figure 4.1 Simplified geological map of eastern Turkey showing igneous and ophiolitic rocks (after MTA, 1989, and Bozkurt, 2001). Also shown are the locations of major mineral deposits in eastern and southeastern Anatolia (excluding the Pontides). Inset map shows the main tectonic elements and major Tethyan sutures of Turkey (after Okay and Tüysüz, 1999). Abbreviations: BSZ = Bitlis Suture Zone, CAFZ = Central Anatolian Fault Zone, DFZ = Dumlu Fault Zone, DSFZ = Dead Sea Fault Zone, GYFZ = Göksu-Yazyurdu Fault Zone, İAESZ = İzmir-Ankara-Erzincan Fault Zone, IPSZ = Intra-Pontide Suture Zone, MF = Malatya Fault, NAFZ = North Anatolian Fault Zone, NEAFZ = North East Anatolian Fault Zone, OF = Ovacık Fault, ZSZ = Zagros Suture Zone.

Much of the earlier research in this region has focused on the general geology and stratigraphy of the sedimentary successions of the Çöpler and Kabataş areas (Özgül and Turşucu, 1984; Tunç et al., 1991; Özer, 1994), and more recently on the petrogenetic features, ages, and geodynamic significance of the shallow-level plutons of the Çöpler-Kabataş magmatic complex (Özer and Öner, 1999; Kuşcu et al., 2010 and 2013; İmer et al., 2013). In this paper, we investigate the nature of the ore forming fluids in the Çöpler porphyry-epithermal deposit. For this purpose, we report the results of detailed paragenetic studies of the hydrothermal alteration/mineralization assemblages, together with fluid inclusion and stable isotope data from vein samples of the porphyry and epithermal stages of mineralization.

4.2 Exploration History and Mineral Resources

The history of gold mining in the Çöpler area dates back to at least Roman times, with historical production estimated at about 50,000 ounces of gold together with smaller amounts of by-product copper and silver (D. Cliff and F. Alizade, unpub. presentation, PDAC 2004). Evidence for this comes mainly from several copper- and iron-rich slag piles located in the district from which the Çöpler village has drawn its name (Çöpler means “waste(s)” in Turkish). Prior to the discovery of Çöpler, however, this region was mainly the focus of artisanal mining activity for manganese oxide (between 1964 and 1992), and its precious and base metal potential was largely unknown.

Porphyry-related alteration and gold-copper mineralization was first discovered in the Çöpler-Kabataş district by Alacer Gold Corp. (formerly Anatolia Minerals Development Ltd.) geologists in 1998, during a regional exploration programme. This campaign was mainly aimed at following up several copper anomalies originally identified by the Mineral Research and Exploration Institute of Turkey (MTA) in the early 1990s. Following preliminary exploration work, Alacer formed a joint venture with Rio Tinto plc., and started an extensive drilling campaign. In 2004, Alacer acquired 100 percent ownership of the Çöpler deposit, and started commercial gold production in April 2011 (current ownership: 80% Alacer and 20% Anagold Mining).

As of December 2013, a combined measured and indicated oxide resource of 69.5 million metric tonnes at 1.1 g/t Au (0.3 g/t cut-off), 2.8 g/t Ag, and 0.1 wt. % Cu has been outlined at Çöpler, with an additional inferred oxide resource of 28.9 million tonnes at 1.0 g/t Au, 4.6 g/t Ag, and 0.1 wt. % Cu (unpublished report for AMDL, December 2013). Current production at Çöpler focuses on this shallow, oxidized part of the system, which is amenable to cyanide heap leaching. Measured and indicated resources for the more refractory sulfide ore underlying the oxidized zone are estimated to be 83.4 million tonnes grading 2.0 g/t Au (1.0 g/t cut-off), 5.7 g/t Ag, and 0.1 wt. % Cu, plus an inferred resource of 22.9 million tonnes at 1.9 g/t Au, 10.8 g/t Ag, and 0.1 wt. % Cu (unpublished report for AMDL, December 2013). Mine production at Çöpler between 2011 and 2013 totalled 645,237 ounces of Au (www.alacergold.com; June 2014).

4.3 Regional Geology and Metallic Mineral Deposits of Eastern Turkey

The Çöpler Au deposit is located within the eastern part of the Tauride mountain range, which stretches the length of Turkey from the Mediterranean coast in the southwest to the Iranian border in the southeast. The mountain range forms part of the much larger Tauride-Anatolide Block (TAB), a continental fragment of peri-Gondwana origin (Fig. 4.1). This E–W-elongated orogenic block mainly developed in conjunction with the Mesozoic–Cenozoic Alpine orogenic phase which saw the near complete elimination of the Neotethyan basins that once separated the northerly Eurasian continental fragments from the southerly Afro-Arabian continental margin.

In general, the Tauride belt exposes a stack of large nappe blocks mainly consisting of thick successions of Paleozoic and younger siliciclastic and carbonate rocks (and their metamorphic equivalents) developed in a passive margin setting. Based on the comprehensive work of Özgül et al. (1981), the eastern part of the TAB, which hosts the Çöpler Au deposit, comprises two of these major nappe blocks. The southern block, which is known as the Keban Unit, represents the lowermost basement succession in the region, and is dominated by Permo-Triassic low- to medium-grade (predominantly greenschist facies) metasedimentary rocks such as schist, marble, phyllite, and minor metaconglomerate and amphibolite (Fig. 4.2A; Özgül et al., 1981; Michard et al., 1984; Özgül and Turşucu, 1984; Yazgan, 1984; Yılmaz, 1993; Robertson et al., 2007).

The Keban Unit is structurally overlain by the Late Triassic–Cretaceous algal, stromatolitic, and rudist-bearing carbonate rocks of the Munzur Unit (Fig. 4.2A, B; Özgül and Turşucu, 1984; Tunç et al., 1991; Özer et al., 2004) representing shallower marine conditions proximal to the passive continental margin of the TAB. South-vergent overthrusting of the Munzur Unit onto the relatively autochthonous Keban Unit occurred in the early Late Cretaceous (Yılmaz, 1993; Elmas and Yılmaz, 2003; Robertson et al., 2013), leading to the regional metamorphism and folding of the latter (Michard et al., 1984). A second major episode of south-directed nappe movement in this region occurred during a period of contraction in the late Eocene–Oligocene associated with final collision along the Bitlis suture (Adamia et al., 1980; Kaymakçı et al., 2010; Robertson et al., 2013).

The Neotethyan evolution of the eastern Taurides was accompanied by widespread igneous activity, and associated mineralization. Only key points regarding these magmatic events are summarized below, and readers are referred to papers by Robertson et al. (2007), Şengör et al. (2008), Kaymakçı et al. (2010), Kuşcu et al. (2010 and 2013), and İmer et al. (2013) for details on the Late Mesozoic–Cenozoic geodynamics and tectonomagmatic history of the eastern Taurides.

In eastern Anatolia, the Southern Neotethys Arc is preserved in the Late Cretaceous calc-alkaline intrusive and extrusive rocks of the Baskil and Göksun-Afşin magmatic complexes (~88–74 Ma; Fig. 4.1; Yazgan and Chessex, 1991; Rızaoğlu et al., 2009; Kuşcu et al., 2013) and in the early to middle Eocene (Lutetian) calc-alkaline to mildly alkaline volcanic sequences of the Maden and Helete (Fig. 4.1; Yılmaz, 1993; Elmas and Yılmaz, 2003; Robertson et al., 2007). This swath of volcano-plutonic complexes defines an arcuate magmatic belt (Fig. 4.1) extending southeastwards to the Urumieh-Dokhtar magmatic zone in Iran.

Minor porphyry-related potassic (± phyllic) alteration has been reported from the Late Cretaceous arc magmatic assemblages in southeast Anatolia but most of these prospects (e.g., Nazaruşağı and Ispendere porphyry Cu-Au; Dumanlılar et al., 1999; Kuşcu et al. 2013; Fig. 4.1)

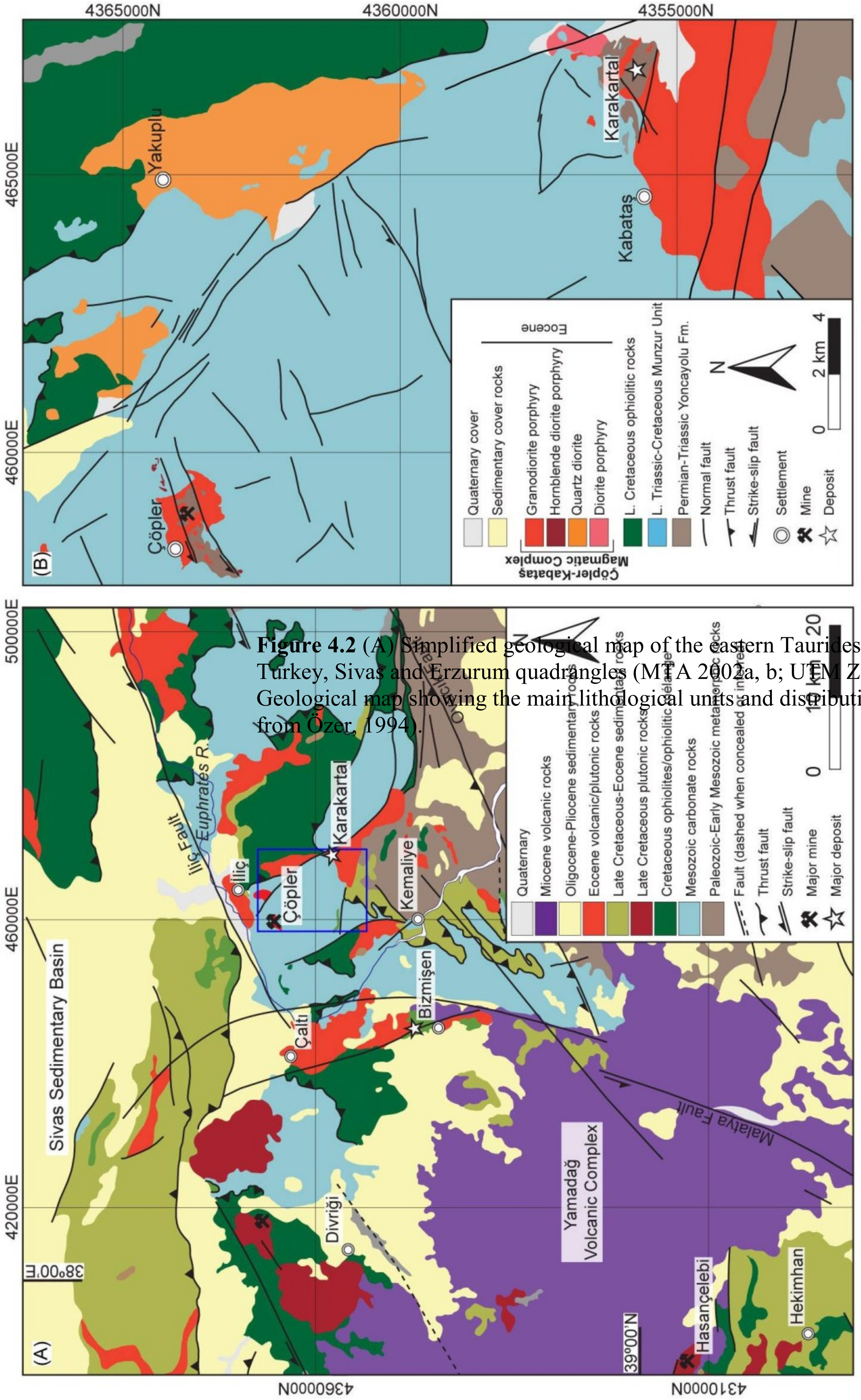

Figure 4.2 (A) Simplified geological map of the eastern Taurides and the surrounding region. Compi
Turkey, Sivas and Erzurum quadrangles (MTA 2002a, b; UTM Zone 37S). Structural data modified f
Geological map showing the main lithological units and distribution of major igneous rocks in the Çö
from Özer, 1994).

are either subeconomic or require further exploration. Middle Eocene mafic submarine volcanic rocks, on the other hand, are associated with volcanic-hosted massive sulfide mineralization and host some significant deposits such as Ergani (14.6 Mt at 1.39% Cu plus significant historic production; Yiğit, 2009) and Madenköy (24.2 Mt at 1.55% Cu; Erler, 1989; Fig. 4.1).

To the north of the Southern Neotethys Arc, subduction-related magmatism occurred in the Late Cretaceous and in the middle Eocene, with both magmatic phases relating to regional extension. The Late Cretaceous magmatic rocks (78–69 Ma; Leo et al. 1974; Boztuğ et al., 2007; Kuşcu et al., 2011 and 2013; İmer et al., 2013) crop out as large isolated intrusive bodies (Fig. 4.1, 4.2A) comprising calc-alkaline to mildly alkaline bimodal gabbro-diorite and syenite-quartz monzonite suites (Zeck and Ünlü, 1991; Boztuğ et al., 2007; Özgenç and İlbeyli, 2009; Kuşcu et al., 2011 and 2013; İmer et al., 2013). These bimodal intrusive complexes host some of the most significant Fe-skarn/IOCG deposits in Turkey, including the A-Kafa, B-Kafa, and C-Placer orebodies at Divriği (133.8 Mt at 56% Fe; Singer et al., 1993) and the Hasançelebi deposit (685 Mt at 19% Fe; Cihnioğlu et al., 1994) near Hekimhan (Fig. 4.1, 4.2A). In addition to these locations, the Keban district (Fig. 4.1) is another potentially prospective area containing a central porphyry Cu-Mo system that is zoned outward through skarn-type Mo-W and Pb-Zn veins, and carbonate-replacement zones (Yiğit, 2009; Kuşcu et al., 2013).

The middle Eocene calc-alkaline intrusive rocks including the Çöpler-Kabataş magmatic complex and the Bizmişen and Çaltı plutons (Fig. 4.1, 4.2A) were generated prior to the culmination of the same extensional tectonic phase (~ 48–44 Ma; Önal et al., 2005; Kuşcu et al., 2010 and 2013; İmer et al., 2013). Although a post-collisional tectonic setting was proposed for these middle Eocene intrusions (Önal et al., 2005; Kuşcu et al., 2010 and 2013), İmer et al. (2013) have argued that the middle Eocene eastern Tauride intrusions were emplaced in a rear-arc setting (i.e., an incipient back-arc) behind the contemporaneous Maden-Helete volcanic arc (Fig. 4.1). A similar tectonic setting was also proposed for the broadly coeval (51–45 Ma) calc-alkaline Doğanşehir, Karamadazı, and Horoz plutons (Fig. 4.1) located farther south and southwest of this region (İmer et al., 2013; Karaoğlan et al., 2013). Besides the Çöpler Au deposit, the Karakartal (formerly known as Kabataş; Fig. 4.1, 4.2A) porphyry Cu-Au prospect (13.8 Mt at 0.29% Cu and 0.5 g/t Au; www.alacergold.com; June 2014) and the Karamadazı Fe-skarn deposit (6.4 Mt at 54% Fe; Cihnioğlu et al., 1994) are the only significant deposits that are currently known to be associated with this stage of magmatism.

Following a period of regional contractional deformation and magmatic lull of ~20 m.y., igneous activity in the eastern Taurides resumed in the late Oligocene with sporadic calc-alkaline volcanism (Akay, 1989; Elmas and Yılmaz, 2003) and minor epizonal plutonism (İmer et al., 2014) within or marginal to extensional basins. This tectonic phase, possibly related to the breakoff of the Southern Neotethys slab (Kaymakçı et al., 2010; Guest and Matthews, 2010; İmer et al., 2014), resulted in formation of a cluster of porphyry prospects around ~25 Ma (İmer et al., 2014) in an area known as the Tunceli Porphyry Belt located immediately to the south of the Munzur Mountains. This belt includes the Cevizlidere porphyry Cu±Mo±Au deposit (~450 Mt at 0.38% Cu; İmer et al., 2014; Fig. 4.1), as well as a few smaller-sized porphyry prospects including Mamlis and Sin (İmer et al., 2014).

The final phase of igneous activity across the eastern Taurides commenced in the early to middle Miocene following the elimination of the Southern Neotethys basin through continent–continent collision between the TAB and the Arabian Platform. In eastern Anatolia, the early phase of collision-related magmatic activity is characterized by widespread bimodal calc-alkaline to mildly alkaline volcanism (17–11 Ma; Pearce et al., 1990; Keskin, 2003; Kürüm et al., 2008) which later progressed into alkaline intra-plate volcanism from ~8 Ma onwards (Pearce et al., 1990; Keskin, 2003). The middle Miocene to Recent volcanic rocks, formation of which are widely attributed to the delamination of the thickened eastern Anatolian mantle lithosphere (Pearce et al., 1990; Göğüş and Psyklwec; 2008), appear to be barren of any significant base and precious metal mineralization.

4.4 Geology of the Çöpler Deposit

The Çöpler Au deposit lies within a fault-controlled ENE-trending depression (~900-m-wide; Fig. 4.3), referred to herein as the Çöpler window, which is surrounded by the rolling hills of the Munzur Mountain range. This part of the Taurides is characterized by rugged topography with high mountain peaks (up to ~3,300 m a.s.l.) and intervening steep valleys. The Çöpler Au deposit flanks the northern edge of the Munzur Mountains, about 3 km south of the Euphrates River, where the mountain range merges into the relatively flat-lying eastern edge of the Sivas Basin (Fig. 4.2A). The deposit is centered around a composite stock in the northern sector of the Çöpler-Kabataş magmatic complex (Fig. 4.3; İmer et al., 2013), which was emplaced into a basement of Permo-Triassic metasedimentary and Cretaceous carbonate rocks in the middle Eocene (~44 Ma; Kuşcu et al., 2007, 2010; İmer et al., 2013).

4.4.1 Country rocks

The lowermost basement unit in the Çöpler area is an 800 m-thick variably metamorphosed turbiditic succession comprising a part of the Yoncayolu Formation of the Keban Unit (Fig. 4.2B; Özgül and Turşucu, 1984). This succession is dominated by thinly-bedded (usually <10 cm) greenschist-facies metapelites interbedded with minor metasandstone, and is only exposed within the Çöpler window and a similar structural corridor near Kabataş village (Fig. 4.2B, 4.3).

Unconformably overlying the metasedimentary package is the 1200 m-thick Kabataş Member of the Munzur Unit, which predominantly consists of rudist-bearing recrystallized limestones (Özgül and Turşucu, 1984; Tunç et al., 1991; Özer, 1994). The limestone unit is strongly recrystallized to marble within up to 500 m of the intrusive contacts (Fig. 4.3) with large (>0.5 cm) sugary crystals of calcite. In the contact aureole, metapelites and metasandstones have been transformed into either brown-colored biotite-rich or pale green-colored diopside-rich hornfels.

4.4.2 The Çöpler-Kabataş Magmatic Complex

The Paleozoic–Mesozoic succession is cut by porphyritic to equigranular intrusive bodies of varying composition and size. Regional geological mapping and airborne magnetic surveys reveal the presence of a cluster of shallow-level intrusive

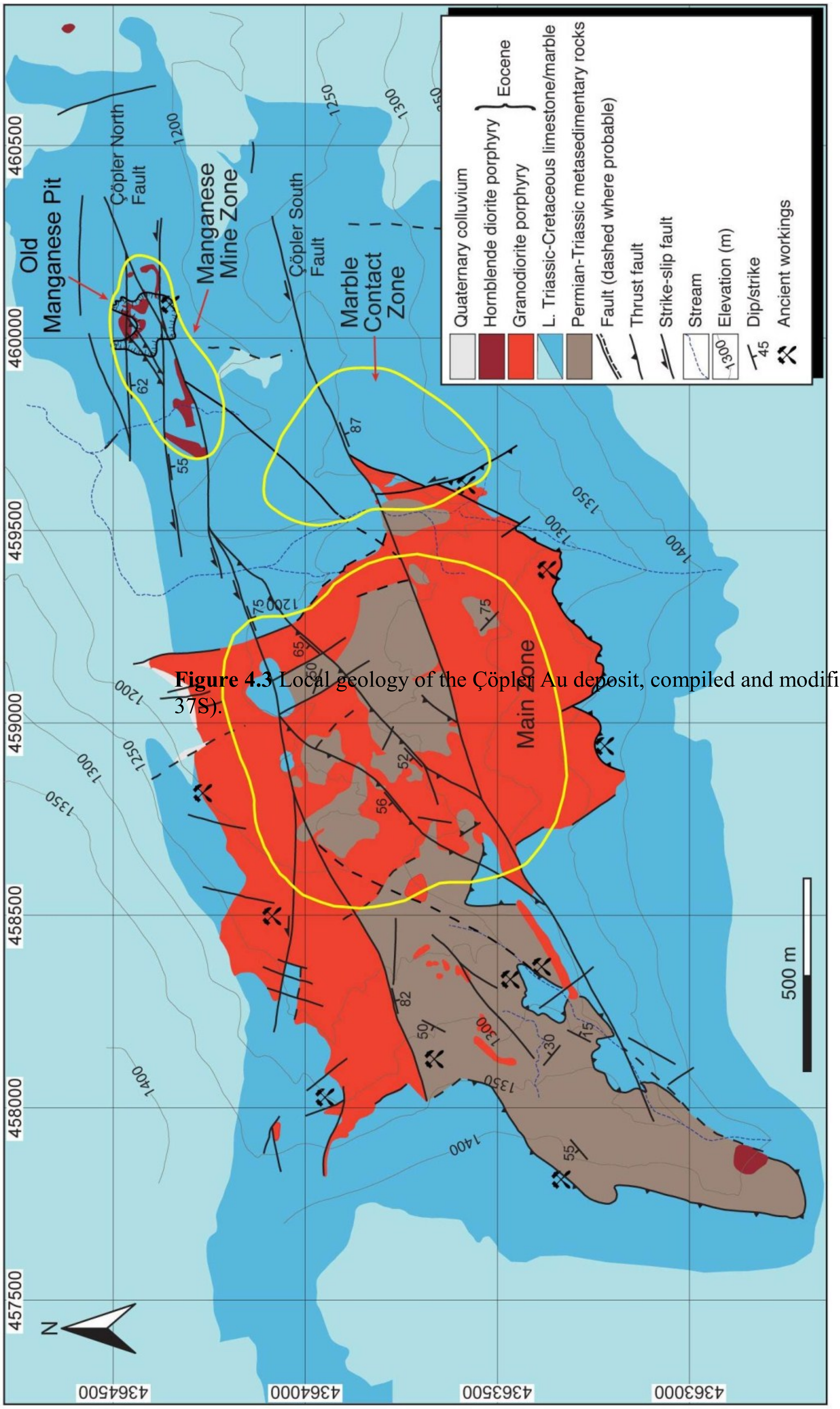

Figure 4.3 Local geology of the Çöpler Au deposit, compiled and modified from company maps prepared by
37S).

rocks scattered across an area of approximately 90 km^2 between the Çöpler and Kabataş villages and extending further southeast (Fig. 4.2A).

The predominant igneous phase at Çöpler is granodiorite porphyry, which occurs as a disrupted lobate body about 900 m wide, 1.5 km long, and at least 400 m deep (Fig. 4.3). Although it has mostly been altered and mineralized, relatively fresh drillcore intervals of granodiorite porphyry reveal a crowded, phenocryst-rich phase containing hornblende, plagioclase, and smaller amounts of biotite phenocrysts set in a plagioclase-quartz-magnetite groundmass. The granodiorite porphyry locally contains mafic xenoliths as well as fragments of the metasedimentary country rocks. A strong positive aeromagnetic anomaly exists underneath the thick limestone ridges to the southwest of the Çöpler window (Fig. 4.3), suggesting the presence of a buried intrusive body larger than the currently exposed granodiorite porphyry.

Relatively small exposures of hornblende diorite porphyry occur in the northeast and southwest sectors of the Çöpler system, in close spatial relationship with E–W-striking fault splays (Fig. 4.3). The hornblende diorite porphyry is also hydrothermally-altered, but least-altered samples collected from the northeastern area show a relatively phenocryst-poor phase consisting of thin, tabular hornblende phenocrysts (up to 3 cm long) and plagioclase phenocrysts embedded in a quartzofeldspathic and magnetite-bearing groundmass. Another distinctive feature of this unit compared to the granodiorite porphyry is that it lacks igneous biotite. The relationship between the hornblende diorite porphyry and the granodiorite porphyry is unclear and no crosscutting relationships have been observed. ^{40}Ar/^{39}Ar ages for these two units (reported below, Table 4.1) overlap, and preclude accurate determination of their relative timing.

A large quartz diorite body (also referred to as the Yakuplu Pluton by Özer and Öner, 1999) is exposed in the hanging wall block of an active NNW-striking reverse fault about 5 km east of Çöpler (Fig. 4.2B). The quartz diorite is equigranular and consists of hornblende, plagioclase, quartz, and biotite phenocrysts with minor magnetite. Although it is relatively fresh compared to the porphyry phases outcropping within the Çöpler window, the quartz diorite is also variably altered into an assemblage of chlorite-epidote-carbonate-pyrite in which chlorite replaces rims of hornblende and biotite phenocrysts, and subordinate epidote and carbonate mainly replace feldspars. The quartz diorite is also cut by occasional epidote veinlets, but no mineralization similar to Çöpler was observed in this unit.

To the south of this quartz diorite body, a relatively small exposure of plagioclase- and pyroxene-phyric, magnetite-bearing diorite porphyry was mapped (Fig. 4.2B). This unit is relatively unaltered and considerably more mafic than the other intrusive lithologies of the magmatic complex.

The southern margin of the magmatic complex is marked by a NW–SE-elongated porphyritic stock near Kabataş village (Fig. 4.2B). Although this stock has the largest surface exposure, it is the least known compared to the other sectors of the magmatic complex, and there are scarce data on its composition. A few samples collected from the northern part of this stock exhibit moderate degrees of alteration due to porphyry-related hydrothermal activity. Primary igneous textures are still preserved in these samples, which contain abundant plagioclase (mostly sericitized) alongside relict hornblende and biotite, indicating dioritic-granodioritic compositions, consistent with mapping by company geologists.

4.5 Structure

Although the Permo-Triassic metasedimentary rocks of the Yoncayolu Formation that form the structural basement in the Çöpler area are quite well-bedded in drillcore, bedding in this succession is commonly indistinct at surface. Where observed, the dips of the metasedimentary rocks are highly variable with no preferred strike orientation (Fig. 4.3), possibly due to disruption of these lithologies through block faulting and tilting at various stages throughout the structural development of the Çöpler window. Similarly, folds are observed in this succession only at the drillcore scale, but are reported to be well-developed in other regional exposures throughout the eastern Taurides (Michard et al., 1984; Özgül and Turşucu, 1984; Gücer and Aslan, 2014), and are attributed to regional low-grade Alpine metamorphism at 90–70 Ma (Gücer and Aslan, 2014).

The limestone succession and the equivalent marble immediately surrounding the deposit appear to be massive in outcrop and therefore no structural measurements were taken from these rocks. Nevertheless, thick limestone beds exposed along the hills approximately 1 km south of Çöpler clearly dip towards the north (~45°–55°) and this seems to be the general dipping trend within this section of the Munzur Unit.

The oldest mappable structure at Çöpler is the shallowly north-dipping tectonic contact separating the metasedimentary succession from the overlying carbonates. Özgül and Turşucu (1984) interpreted this structure as a regional sub-horizontal thrust surface along which the allochthonous Munzur Limestone was thrust over the upper parts of the Keban Unit. İmer et al. (2013) previously reported soft-sediment structures in the form of injections into the fracture zones at the base of the carbonate rocks, which likely indicates that the initial south-vergent movement along this thrust surface occurred at a pre-diagenetic stage. This is consistent with the regional tectonic models that suggest southerly nappe emplacement in the Turonian–Maastrichtian interval (Özgül and Turşucu, 1984; Özer 1994; Rice et al., 2009).

Following this major thrusting event, the Çöpler window underwent at least four stages of faulting. The earliest of these deformation phases resulted in formation of two prominent structures, the Çöpler North and South Faults, which define the main Çöpler window (Fig. 4.3). Both structures are ENE-striking, near vertical (steeply-dipping towards the south), and are characterized by oblique-slip displacement with a dominant sinistral component of slip. The amount of lateral displacement along the Çöpler North and South Faults is not known, but is probably small because of the overall coherence of the geological system. Although both structures were observed crosscutting the predominant granodiorite porphyry, a pre-magmatic origin is inferred in keeping with their close correlation with the İliç Fault (Fig. 4.2A; Kaymakçı et al., 2010), a major strand of the regional Göksu-Yazyurdu Fault Zone (Fig. 4.1), which was initiated during the early Paleogene (Koçyiğit and Beyhan, 1998). This implies that the Çöpler North and South Faults were reactivated during subsequent syn- and also probably post-mineral deformation stages (see below).

Two mineralized fault sets have been identified at Çöpler post-dating the ENE-trending structures. The first of these are E–W-striking, steeply south-dipping (~60°), short strike-length structures splaying out from the Çöpler North Fault (Fig. 4.3). These faults are best observed within and around the old manganese oxide pit in the northeastern sector (Fig. 4.3). Here, the original intrusion–marble contacts have been tectonically modified by the E–W-striking structures, and are now characterized by intervals of fault gouge and tectonic breccia (Fig. 4.4A, B). The fault gouge and breccia are not always mineralized, but where they are, they usually contain fragments of Au-mineralized carbonate-sulfide veinlets (see below). Some of these breccia zones were later cut by a second generation of epithermal-style veinlets (sooty pyrite veinlets) representing later stages of Au mineralization, as well as by barren post-mineral calcite veinlets indicating episodic fault reactivation along the E–W-trending faults.

The second set of mineralized faults consists of SW-striking, moderately to steeply NW-dipping (~50°–70°) tensional structures mainly observed in the central block linking the Çöpler North and South Faults and also in the southeastern part of Çöpler (Fig. 4.3). Discrete stages of epithermal-style veining similar to those mentioned above were also observed in close spatial relationship with the SW-striking faults. A significant reverse component of slip exhibited by the SW-striking structures suggests post-mineral fault reactivation under late compressional stress (C. Easterday, 2004, unpub. report for AMDL, 35 p.), possibly due to a change in the stress field in the late Eocene–Oligocene (Kaymakçı et al., 2010). This compressional event resulted in uplift of the central block along SW-striking faults, which was later eroded, exposing the altered and mineralized core of the porphyry orebody (Fig. 4.3). The bulk of the epithermal-style mineralization at Çöpler is hosted by the E–W- and SW-striking structures, but some of the highest grade (mainly supergene-enriched) ore shoots were encountered at the intersections of these structures with the Çöpler North and South Faults.

Another likely consequence of post-emplacement compression at Çöpler is the faulting of the intrusion–marble contact along the southern margin of the granodiorite porphyry (Fig. 4.3). Although the nature of displacement along this interpreted fault is not clear, it likely involves an element of thrusting because the hanging-wall breccias along this contact have steep (~60°–75°) attitudes towards the south (Fig. 4.4C)

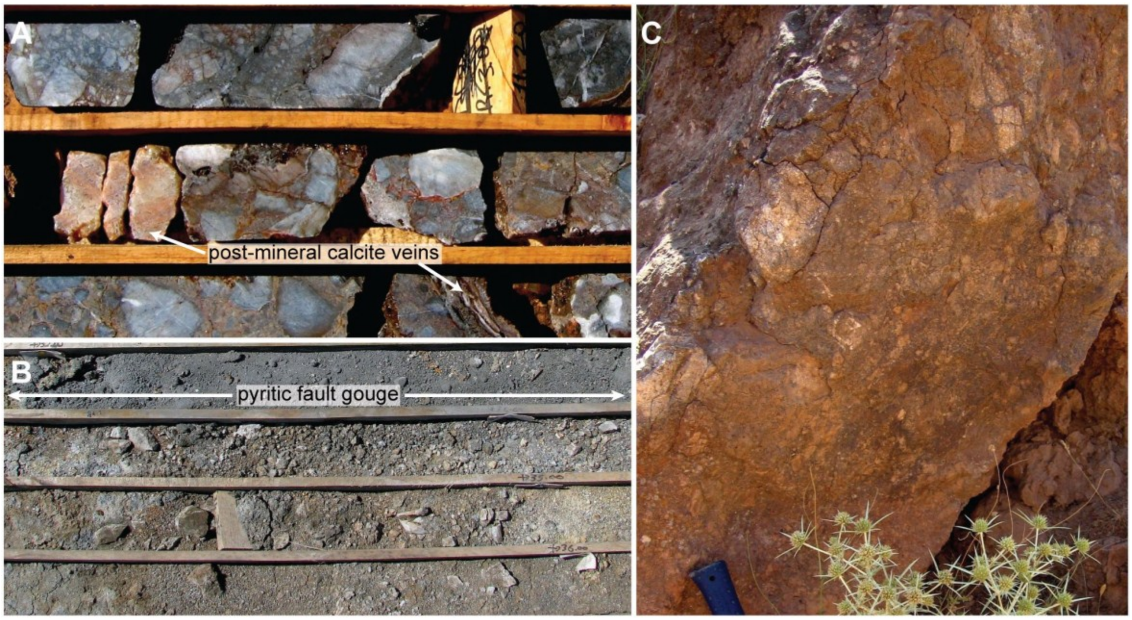

Figure 4.4. Contact relationships between the intrusive and carbonate rocks in drillcore and outcrop. (A) Brecciated marble at the intrusion–marble contact from the Manganese Mine Zone (CDD-159, 9.80–12.40 m; see Fig. 4.5 for drillhole location). Breccia is cut by late post-mineral calcite veins. (B) Partly mineralized fault gouge at the intrusion–marble contact. The interval at the top contains abundant pyrite indicated by gray color and has a grade of 7.7 g/t Au (CDD-157, 33.50–36.10 m; see Fig. 4.5 for drillhole location), whereas the remaining intervals are sulfide poor and have average grades <1 g/t Au. (C) Fault breccia developed in marble (hammer for scale), looking west along the southern granodiorite porphyry–marble contact (WGS84, 37S, 0459522E, 4363489N, 1,248 m a.s.l.).

A fourth set of NNW-striking high-angle (60°–80°) faults dipping NE occurs primarily within and around the Main Zone (Fig. 4.3). The NNW-striking structures truncate the granodiorite porphyry, and locally cut and displace the earlier fault sets by several meters. These post-mineral faults are probably still active because some of them cut Quaternary colluvium on the northern margin of the granodiorite porphyry (Fig. 4.3). In this respect, they may be correlated with the larger scale NNW-striking faults that extend from the east of Çöpler to Kabataş village (Fig. 4.2A), which have also been reported to be seismically active (Kaymakçı et al., 2010).

4.6 Timing of Magmatism and Hydrothermal Activity at Çöpler

The timing of magmatism and magmatic-hydrothermal activity in the Çöpler and Kabataş areas has been the subject of several recent studies. Table 4.1 summarizes the existing geochronological data obtained from step-heating ^{40}Ar/^{39}Ar analyses of igneous and porphyry-related hydrothermal mineral phases as well as from Re-Os analysis of vein molybdenite. The age of the overprinting epithermal system at Çöpler, however, could not be dated due to a lack of dateable minerals (e.g., adularia, alunite) that are typically found in epithermal deposits.

Kuşcu et al. (2007) reported an igneous biotite ^{40}Ar/^{39}Ar age of 44.43 ± 0.61 Ma for the diorite porphyry at Çöpler, as well as a biotite age of 48.51 ± 0.34 Ma from a weakly sericitized diorite porphyry from the Karakartal prospect near Kabataş, constraining the timing of magmatic activity in the complex to middle Eocene.

Marinov et al. (2009) dated molybdenite samples from four different Turkish porphyry systems including the Çöpler and Karakartal deposits. Their Re-Os analyses on two molybdenite separates from Çöpler were identical to each other (46.9 ± 0.30 Ma and 46.4 ± 0.30 Ma), but ~ 2.5 m.y. older than the age of the precursor pluton reported by Kuşcu et al. (2007) (Table 4.1). Similarly, the Re-Os molybdenite age obtained by Marinov et al. (2009) from the Karakartal prospect (51.1 ± 0.30 Ma) also appears to be ~ 2.5 m.y. older than the age of its causative pluton (48.51 ± 0.34 Ma; Kuşcu et al., 2007), leading one to suspect a systematic error in these Re-Os dates.

A more detailed study on the timing of magmatic and hydrothermal activity at Çöpler was later carried out by İmer et al. (2013). One igneous biotite and one hornblende sample obtained from the least-altered portions of the granodiorite porphyry and the hornblende diorite porphyry gave statistically similar ^{40}Ar/^{39}Ar plateau ages of 43.75 ± 0.26 Ma and 44.13 ± 0.38 Ma, respectively, whereas igneous biotite from a fresh quartz diorite to the east of Çöpler (Fig. 4.2B) yielded a plateau age of 44.19 ± 0.23 Ma (Table 4.1). A plateau age of 43.84 ± 0.26 Ma from hydrothermal biotite from the potassically-altered granodiorite porphyry and a sericite age of 44.44 ± 0.28 Ma from a quartz-sericite (phyllic) altered granodiorite porphyry closely overlap with the ages obtained from the igneous minerals as well as with the igneous biotite age reported by Kuşcu et al. (2007), and these dates are interpreted to reflect rapid cooling conditions at ~44 Ma (İmer et al., 2013). Two Re-Os ages (44.6 ± 0.2 and 43.9 ± 0.2 Ma) obtained from early stage molybdenite-bearing porphyry-style veinlets, although not overlapping with each other, are also in good agreement with the $^{40}Ar/^{39}Ar$ ages of hydrothermal alteration minerals. The slight difference in Re-Os molybdenite ages, on the other hand, probably reflects episodic precipitation of molybdenite at Çöpler (İmer et al., 2013).

A recent study by Kuşcu et al. (2013) reported three additional $^{40}Ar/^{39}Ar$ sericite ages from both the Çöpler and Karakartal deposits. The inverse isochron age for sericite (40.2 ± 6.8 Ma) from Çöpler has a large error and its significance is questionable, although it overlaps with the previously reported $^{40}Ar/^{39}Ar$ dates. In contrast, an inverse isochron age of 48.63 ± 0.62 Ma and a plateau age of 47.22 ± 0.49 Ma from sericite from the Karakartal porphyry deposit are statistically indistinguishable from the igneous biotite age reported by Kuşcu et al. (2007).

The combined $^{40}Ar/^{39}Ar$ and Re-Os data summarized above are in general internal agreement, with the exception of the Re-Os ages of Marinov et al. (2009), which we consider to be a result of systematic error. The data indicate that shallow-level magma emplacement in Çöpler area took place at ~44 Ma, and was closely followed by porphyry-style hydrothermal alteration and mineralization. There is no indication that the epithermal-style Au mineralization was not also closely related in time to this magmatic hydrothermal event, although the epithermal stage has not been directly dated.

4.7 Hydrothermal Alteration, Mineralization, and Vein Paragenesis

Various styles of Au-(Cu) mineralization including porphyry- and epithermal-type veinlets and carbonate-replacement zones were recognized at Çöpler based on field mapping and core logging. Spatial distribution of these mineralization styles throughout the deposit is largely dictated by the structural framework as well as by the distribution of lithologic units. Three major centers of mineralization (the Main Zone, the Marble Contact Zone, and the Manganese Mine Zone; Fig. 4.3, 4.5) were originally defined by company geologists on the basis of mineralization styles, and the same nomenclature is used here for convenience.

^{9}Ar and Re-Os geochronological data for the igneous and hydrothermal assemblages from the Çöpler-
yry mineralization

Lithology	Location	Methodology	Mineral	Age (Ma ± 2σ)[1]	Source
Igneous minerals					
Granodiorite porphyry	Çöpler	^{40}Ar/^{39}Ar	Biotite	44.43 ± 0.61	Kuşcu et al. (2007, 2010)
Diorite porphyry	Kabataş/Karakartal	^{40}Ar/^{39}Ar	Biotite	48.51 ± 0.34	Kuşcu et al. (2007, 2010)
Granodiorite porphyry	Çöpler	^{40}Ar/^{39}Ar	Biotite	43.75 ± 0.26	İmer et al. (2013)
Hornblende diorite porphyry	Çöpler	^{40}Ar/^{39}Ar	Hornblende	44.13 ± 0.38	İmer et al. (2013)
Quartz diorite	Çöpler east	^{40}Ar/^{39}Ar	Biotite	44.19 ± 0.23	İmer et al. (2013)
Hydrothermal minerals					
Sericitized granodiorite	Karakartal	^{40}Ar/^{39}Ar	Sericite	48.63 ± 0.62; inverse isochron	Kuşcu et al. (2007, 2010)
Potassically altered granodiorite porphyry	Çöpler	^{40}Ar/^{39}Ar	Biotite	43.84 ± 0.26	İmer et al. (2013)
Quartz-sericite altered granodiorite porphyry	Çöpler	^{40}Ar/^{39}Ar	Sericite	44.44 ± 0.28	İmer et al. (2013)
Sericitized diorite porphyry	Çöpler	^{40}Ar/^{39}Ar	Sericite	40.2 ± 6.8; inverse isochron	Kuşcu et al. (2013)
Granodiorite porphyry	Çöpler	^{40}Ar/^{39}Ar	Sericite		
Quartz-sulfide ± magnetite vein	Çöpler	Re-Os	Molybdenite	46.9 ± 0.3	Marinov et al. (2009)
Quartz-sulfide ± magnetite vein	Çöpler	Re-Os	Molybdenite	46.4 ± 0.3	Marinov et al. (2009)
Quartz-clay-molybdenite vein	Karakartal	Re-Os	Molybdenite	51.1 ± 0.4	Marinov et al. (2009)
Quartz-sulfide ± magnetite vein	Çöpler	Re-Os	Molybdenite	44.6 ± 0.2	İmer et al. (2013)
Quartz-sulfide ± magnetite vein	Çöpler	Re-Os	Molybdenite	43.9 ± 0.2	İmer et al. (2013)

[1] ^{40}Ar/^{39}Ar ages are reported as plateau ages unless indicated otherwise

Early stage porphyry mineralization is developed within the granodiorite porphyry intrusion, which is exposed primarily in the Main Zone, and is confined to a 300 x 500 m area delimited by the Çöpler North and South Faults (Figs. 4.3, 4.5). This zone also contains minor epithermal-style mineralization as a shallow overprint on the porphyry system, but it does not constitute a major gold resource. The bulk of the Au mineralization occurs in the Marble Contact and Manganese Mine Zones, mainly in the form of oxidized manto-type carbonate-replacement orebodies and carbonate-sulfide-quartz ± barite veinlets, respectively.

The relative timing of hydrothermal alteration and vein formation described in the following sections is mainly deduced from crosscutting and overprinting relationships observed in drillcore and thin section. A summary of these paragenetic relationships is given in Figure 4.8 and characteristics of vein types identified are listed in Table 4.2.

4.7.1 Hydrothermal alteration

Potassic alteration: The central part of the Çöpler system hosts subeconomic porphyry Cu-Au mineralization, which exhibits a broadly concentric pattern of hydrothermal alteration zoning (Fig. 4.5) similar to the alteration model of Lowell and Guilbert (1970). The core of the porphyry system is characterized by early potassic alteration, which is well developed at deeper levels (>150 m below surface) in the granodiorite porphyry within the Main Zone (Fig. 4.5). The alteration assemblage typically consists of abundant hydrothermal biotite and magnetite, and locally developed secondary K-feldspar (Fig. 4.7A–D). Fine-grained hydrothermal biotite occurs in the groundmass and as anhedral masses replacing igneous hornblende (Fig. 4.7C, D), whereas K-feldspar replaces both phenocrystic and groundmass plagioclase (Fig. 4.7B). K-feldspar is also present in early B veinlets in the central part of the potassic alteration zone.

Phyllic alteration: Potassic alteration grades laterally and vertically into phyllic alteration (Fig. 4.5). This is the most widespread alteration type at Çöpler, and is characterized by partial to complete replacement of plagioclase and mafic phenocrysts by sericite, and replacement of groundmass by fine-grained sericite and quartz (Fig. 4.7E–G), typically with abundant disseminated or veinlet pyrite (Fig. 4.7F, G).

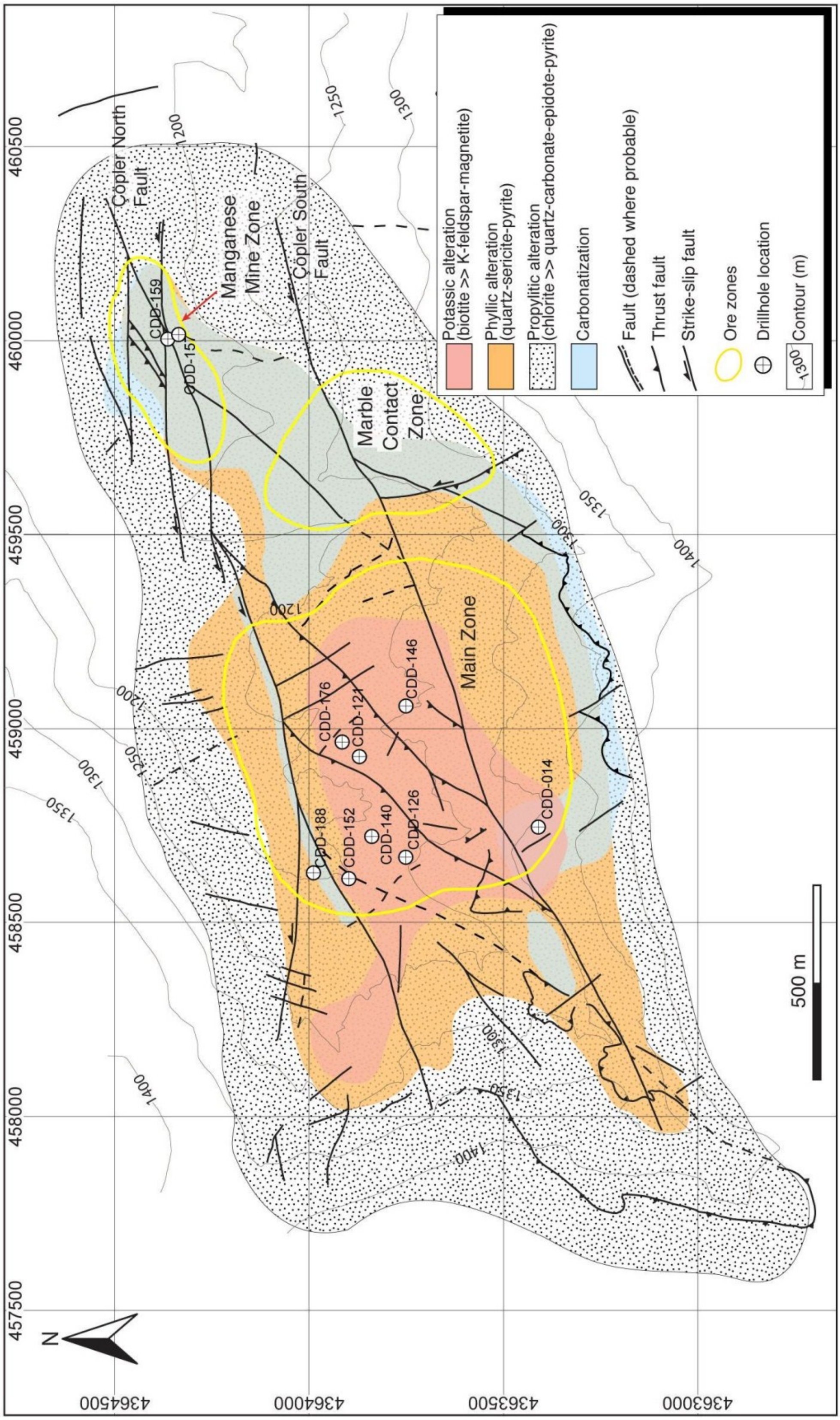

s (as defined by company geologists)
of drillholes mentioned in the text

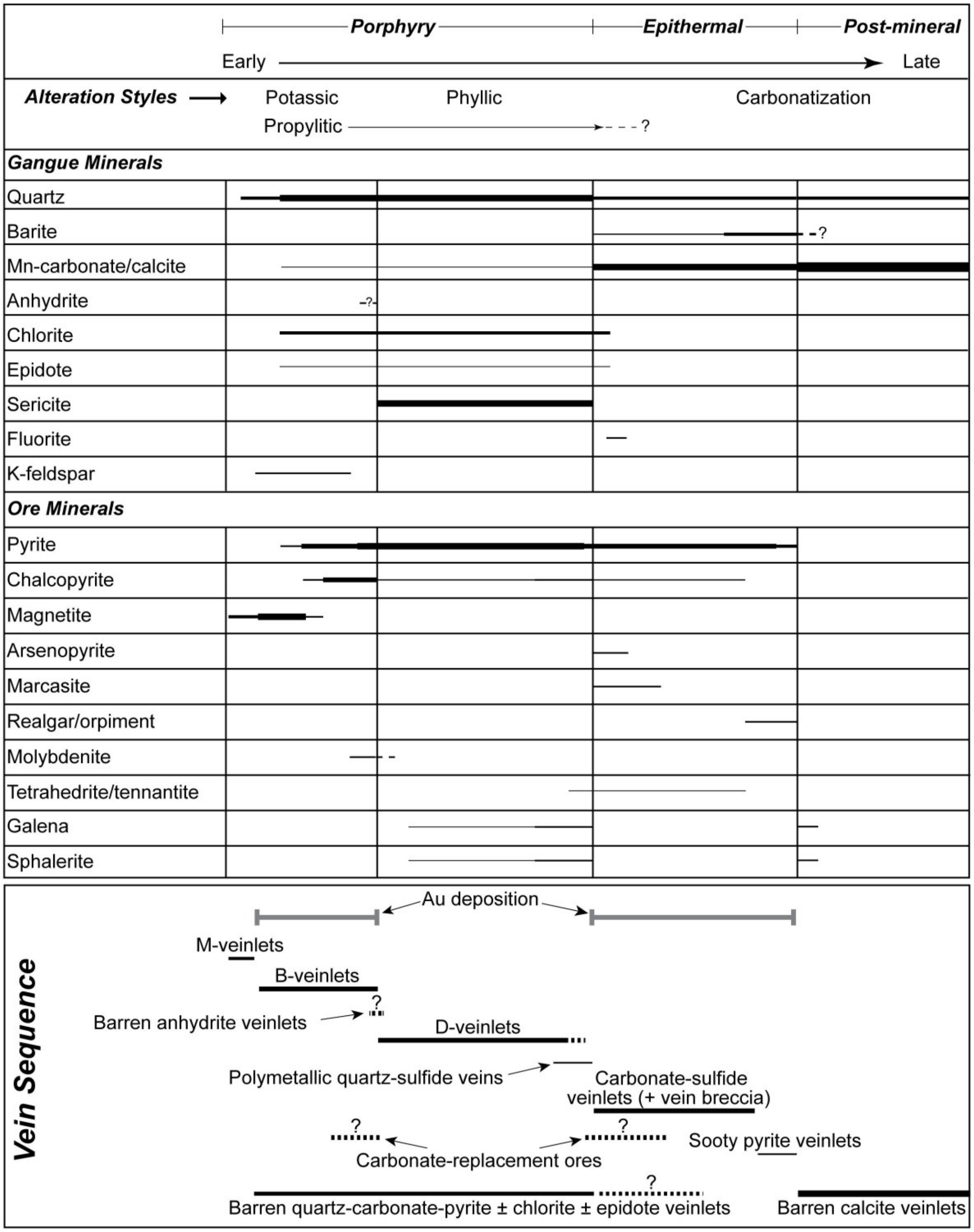

Figure 4.6 Paragenetic sequence of porphyry- and epithermal-style alteration and veining at Çöpler.

acteristics of major vein types identified at Çöpler

Veinlet type	Thickness	Opaque minerals	Gangue minerals	Alteration halo	Comments
M veinlets	Hairline to ~3 mm	Major: mag	-	-	Occur mostly as “bead-like” discontinuous structures.
B veinlets	0.5 cm to ~3 cm	Major: mag, py, cp Minor: mo	Major: qz Minor: Ksp, late carb (as centerline fillings), anh (?)	Mostly absent. Locally very weak/narrow Ksp halos.	Usually occur as sheeted arrays. Local vuggy centers
Anhydrite veinlets	~2 mm to 4 cm	-	anh	-	Wavy veinlet walls
D veinlets	~1 mm to 2 cm	Major: py Minor: cp, gn, sph, tet/ten Rare: mo	Major: qz, ser Rare: late carb	Prominent sericitic	Locally contain vuggy centers
Polymetallic quartz-sulfide veins	4 cm to 15 cm	Major: py, cp, gn, sph, tet/ten	Major: qz Minor: ser	Occasional sericitic halos possibly due to superimposition with D veinlets	Thicker than earlier veinlet groups. Banding is common. Some are brecciated due to later epithermal overprint.
Quartz-carbonate-sulfide ± chlorite ± epidote veinlets	~3 mm to 3 cm	Major: py Minor: cp	Major: qz, carb, chl, ep	Rare ep	
Carbonate-sulfide veinlets	1 cm to ~5 cm	Major: py, asp, cp Minor: asp, sph, gn, ten/tet	Major: Mn-ct/rhod, qz Minor: bar, late chal (as vug fillings)	-	Commonly superimposed on D veinlets and polymetallic quartz-sulfide veins
Sooty pyrite veinlets	< 1mm to ~8 cm	Major: py Minor: rea, orp	Major: rhod, qz, bar	-	Increased abundance of barite. Friable veinlets usually as irregular fracture fillings
Post-mineral calcite veins	From few mms up to ~20 cm	-	calcite	-	Colloform or crustiform banding common

Abbreviations: anh = anhydrite, asp = arsenopyrite, bar = barite, cp, chalcopyrite, ct = calcite, chal = chalced
feldspar, mag = magnetite, mar = marcasite, Mn-ct = manganocalcite, mo = molybdenite, orp = orpiment, py
rhodochrosite, ser = sericite, sph = sphalerite, ten = tennantite, tet = tetrahedrite

Propylitic alteration: Propylitic alteration forms the outer halo of the hydrothermal system at Çöpler (Fig. 4.5) affecting all lithologies (except limestone and marble) including intrusive phases exposed within the wider magmatic complex. Propylitic alteration assemblages consist of abundant chlorite (after mafic igneous minerals, secondary biotite, or sericite) and epidote with subordinate quartz, carbonate, and pyrite (Fig. 4.8A–C). This type of alteration is well developed at shallow levels and also at depth, the latter mainly in the form of a retrograde overprint of potassic-altered granodiorite porphyry (Fig. 4.8B, C). No economic mineralization is associated with propylitic alteration at Çöpler.

Carbonate alteration: Zones of extensive carbonate alteration were encountered in the intrusive rocks beneath the Manganese Mine Zone, in close proximity to intrusion–marble contacts (Fig. 4.5). Here, manganoan carbonates replace plagioclase phenocrysts (or pseudomorphous sericite) (Fig. 4.8D–F) and groundmass minerals with the exception of quartz. This type of alteration began during the Au-mineralizing epithermal stage, and continued well after this event. In cases where epithermal veinlets have been overprinted by later carbonatization, barite euhedra are replaced by calcite resulting in the formation of textures that resemble bladed calcite, as observed in boiling epithermal systems (although no evidence for boiling has been recorded at Çöpler).

Skarn alteration: Minor skarn alteration zones have been encountered particularly at the limestone–granodiorite porphyry contacts and in the peripheral metasedimentary rocks. Calcic endoskarn is characterized by a mineral assemblage consisting of garnet, diopside, epidote, pyrite, and calcite, whereas exoskarn is represented by small pods of massive magnetite replacing carbonate wall-rocks. Although these massive iron oxide occurrences exist only sporadically and very irregularly across the district, they might have been more widespread along the granodiorite-limestone/marble contacts, which have now been largely eroded following the uplift and unroofing of the Çöpler window.

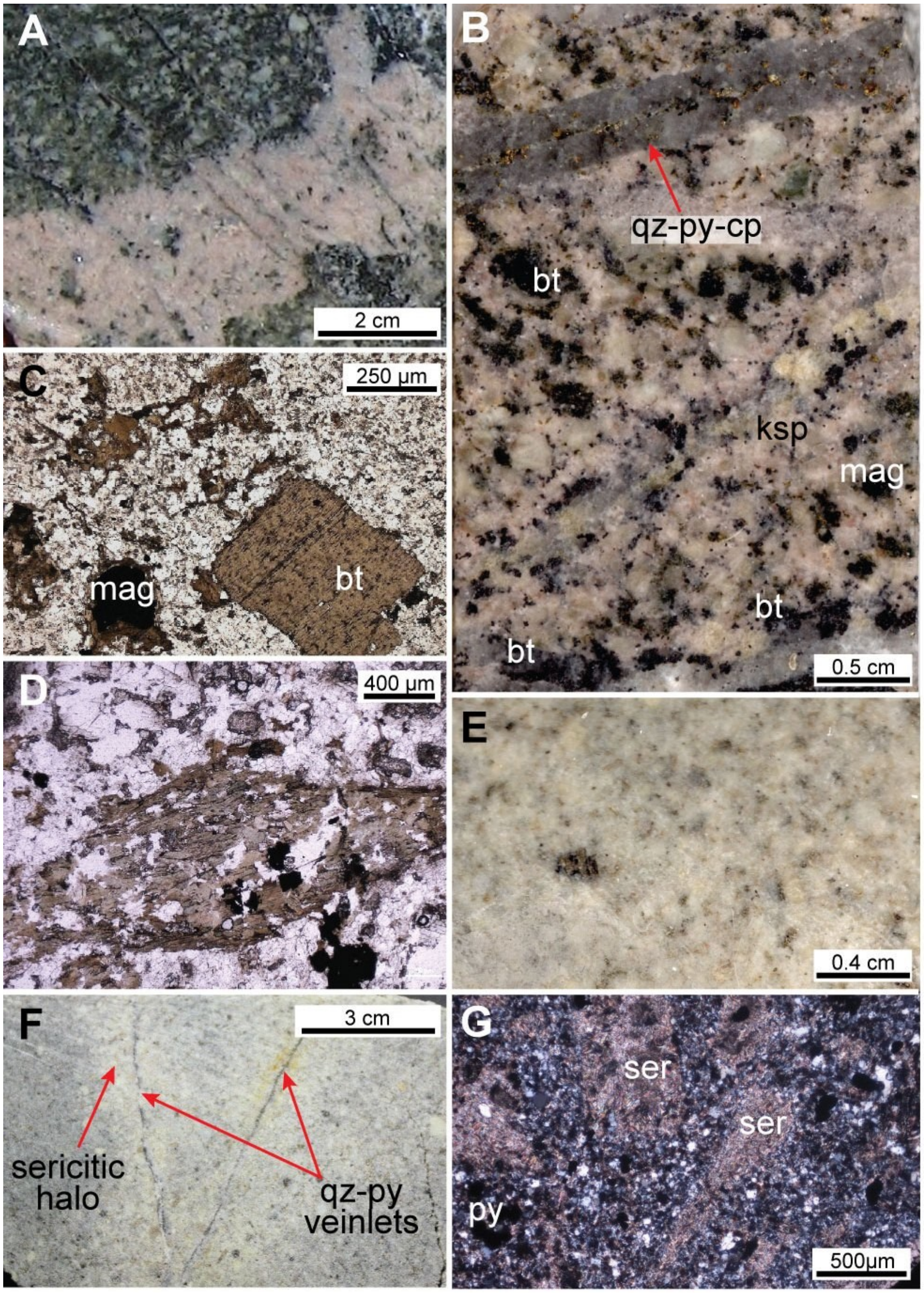

Figure 4.7 Early porphyry-related alteration styles from the Main Zone in hand specimen and thin section. (A) Strong potassic alteration in granodiorite porphyry with localized K-feldspar flooding (pink) and abundant secondary biotite (fine-grained black masses) with some relict primary biotite (CDD-140, 217.70–217.80 m). (B) Potassic-altered granodiorite porphyry with groundmass largely replaced by K-feldspar with abundant secondary biotite and magnetite (CDD-014, 361.30 m). Sample is crosscut by a B-type quartz-pyrite-chalcopyrite veinlet at the top of the photo. (C) Potassic-altered granodiorite porphyry showing a euhedral primary biotite grain surrounded by anhedral masses of secondary biotite (top left and center) and magnetite (sample C-169; plane-polarized transmitted light). (D) Hornblende phenocryst replaced by fine-grained secondary biotite in potassic-altered granodiorite porphyry (sample C-163; plane-polarized transmitted light). Biotite grains in this sample have been partially replaced by chlorite (green)

due to overprinting propylitic alteration. (E) Pervasive quartz-sericite alteration in granodiorite porphyry. A primary biotite grain in this sample is mostly altered to sericite (CDD-140, 178.20 m). (F) Narrow quartz-sericite halos surrounding the D-type quartz-pyrite veinlets in slightly propylitized granodiorite porphyry (CDD-140, 133.30 m). (G) Phyllic alteration in granodiorite porphyry: completely sericitized plagioclase phenocrysts embedded in a groundmass largely replaced by quartz. Opaque crystals are pyrite (sample C-225; cross-polarized transmitted light). Abbreviations: bt = biotite, cp = chalcopyrite, Ksp = K-feldspar, mag = magnetite, py = pyrite, qz = quartz, ser = sericite.

Supergene alteration: Supergene oxidation has affected all hypogene alteration/mineralization assemblages, and appears to be responsible for the locally high-grade (commonly 5–20 g/t Au, and locally up to 935 g/t over 1 m core intervals) nature of the Çöpler Au deposit. Oxidation penetrates to depths of 50 to 100 m in the Main Zone, but extends to depths of 250 m in intensely fractured areas, karstic zones, and along contacts between limestone/marble and the intrusive phases (e.g., in the Marble Contact Zone; Fig. 4.4). Much of the sericite (and possibly feldspar) has been replaced by supergene kaolinite at shallow depths, likely due to reaction with sulfuric acid generated by pyrite oxidation. In the oxidized zones, massive to semi-massive sulfide ores have been transformed into siliceous gossan, which mainly consists of variable amounts of jarosite, goethite, and limonite with lesser malachite and azurite. Large amounts of manganoan carbonate in the Manganese Mine Zone, on the other hand, have been weathered to manganese oxide (pyrolusite), forming large pods of fine-grained, friable manganese wad, together with supergene iron hydroxide minerals and relict quartz and barite. In the supergene-enriched zone, gold either occurs as free gold with grain sizes up to 400 µm, or as inclusions encapsulated by iron hydroxide minerals (after primary sulfides), and is readily liberated by leaching processes.

4.7.2 Porphyry-style mineralization

The earliest porphyry-style veinlets observed at Çöpler are the hairline magnetite veinlets (<2 mm, Fig. 4.8A), which cut the potassically-altered granodiorite porphyry and the adjacent metasedimentary rocks. The hairline magnetite veinlets, which may be analogous to the M-veinlets of Arancibia and Clark (1996), mostly occur as discontinuous bead-like structures, although more continuous examples were also encountered during sampling. The continuous hairline magnetite veinlets may be visually confused with dark colored veinlets and fractures containing secondary Mn-oxide, which are abundant in the metasedimentary rocks.

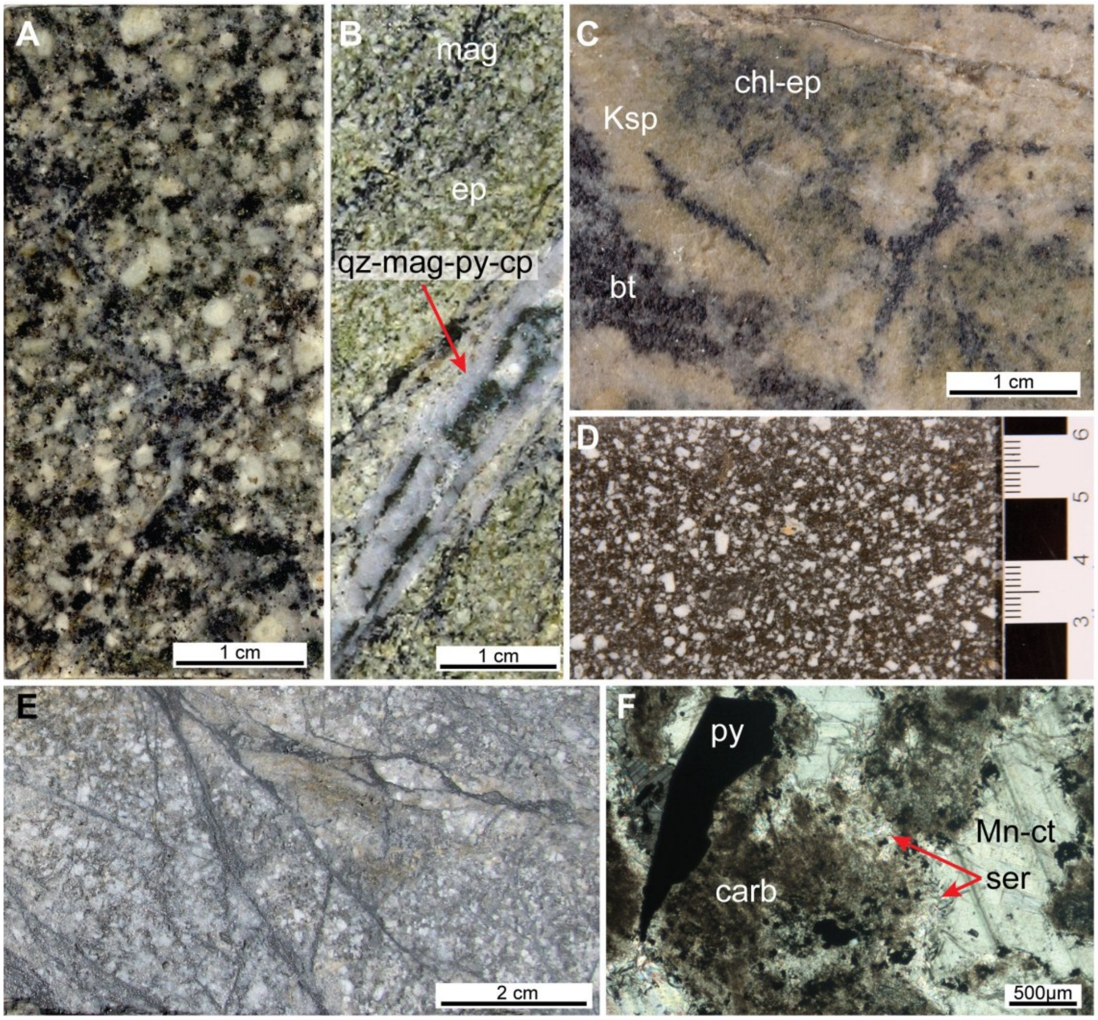

Figure 4.8 Propylitic and carbonate alteration in granodiorite porphyry. (A) Retrograde propylitic alteration overprinting weak potassic alteration. Propylitic and carbonate alteration in granodiorite porphyry**.** (A) Retrograde propylitic alteration overprinting weak potassic alteration. Secondary biotite (after hornblende) and feldspars in this sample have been partially altered to chlorite and epidote (CDD-014, 196.70 m). (B) Strong epidote-dominant propylitic overprint on earlier potassic alteration in granodiorite porphyry. Note the earlier magnetite and quartz-magnetite-pyrite-chalcopyrite veinlets associated with potassic alteration (CDD-121, 145.60 m). (C) Chlorite-epidote alteration overprinting potassically-altered granodiorite porphyry (K-feldspar flooding and fine-grained secondary biotite; CDD-126, 75.90 m). (D) Carbonate-altered intrusive rock from the Manganese Mine Zone. Dark appearance of the groundmass is due to partial oxidation of fine-grained manganoan carbonates (CDD-159, 169.00 m). (E) Carbonate alteration of granodiorite porphyry (CDD-184, 3.80 m). (F) Photomicrograph of carbonate alteration overprinting phyllic-altered granodiorite porphyry. Sericitized feldspar phenocrysts have been completely replaced by manganoan carbonates; relict sericite still present on the edges of phenocrysts (sample C-138; plane-polarized transmitted light). Abbreviations: bt = biotite, carb = carbonate, chl = chlorite, cp = chalcopyrite, ep = epidote, Ksp = K-feldspar, mag = magnetite, Mn-ct = manganocalcite, py = pyrite, qz = quartz.

The hairline magnetite veinlets are locally crosscut by aplite dikelets (Fig. 4.9A, B), which are restricted to deep levels (>200 m) in the granodiorite porphyry and the metasedimentary rocks. These dikelets are typically 2 to 5 cm thick and consist of fine-grained quartz and K-feldspar, and minor amounts of biotite and magnetite.

B-type quartz ± magnetite ± sulfide veinlets (Fig. 4.9 A, C–G; *sensu* Gustafson and Hunt, 1975) are the most common veinlet types associated with potassic alteration. They crosscut both the hairline magnetite veinlets and the aplite dikelets (Fig. 4.9A) and are best observed in drillholes CDD-121, -126, -140, and -152 (for locations, see Fig. 4.5). Thicknesses of these veinlets typically range from a few millimeters up to ~4 cm. B-type veinlets mostly occur as sheeted arrays with symmetrical and planar vein walls (Fig. 4.11C) but individual veinlets with slightly wavy walls (Fig. 4.9D, G) were also observed in the drillcore. Quartz is ubiquitous in B-type veinlets and occurs together with varying amounts of magnetite and sulfide minerals including pyrite, chalcopyrite, and molybdenite (Fig. 4.9C–G). Magnetite is typically present along the veinlet margins either as isolated grains or continuous bands (Fig. 4.9C), whereas sulfide minerals are either distributed randomly within the veinlets or form centrelines, except for molybdenite which occurs either in the veinlet margins (Fig. 4.9G) or centers. K-feldspar and late stage carbonate and quartz are also locally present as centreline fillings (Fig. 4.9C, G), and some veinlets exhibit vuggy centers. Prominent dark-colored actinolitic halos occur where these veinlets cut metasedimentary rocks.

In and around the B-type veinlets, chalcopyrite (Fig. 4.9D–F) is the only copper mineral except where it is partially or completely replaced by sparse secondary bornite, digenite, or covellite. Gold grades positively correlate with Cu and the density of quartz-sulfide ± magnetite veinlets. Average gold and copper grades in the potassic-altered granodiorite are ~0.2 % Cu and ~0.2 g/t Au, but grades as high as 0.5 % Cu and 0.5 g/t Au are locally observed where vein densities are high. Molybdenite, on the other hand, is present only in trace amounts at Çöpler, and its abundance positively correlates with the abundance of pyrite in the B-type veinlets rather than chalcopyrite.

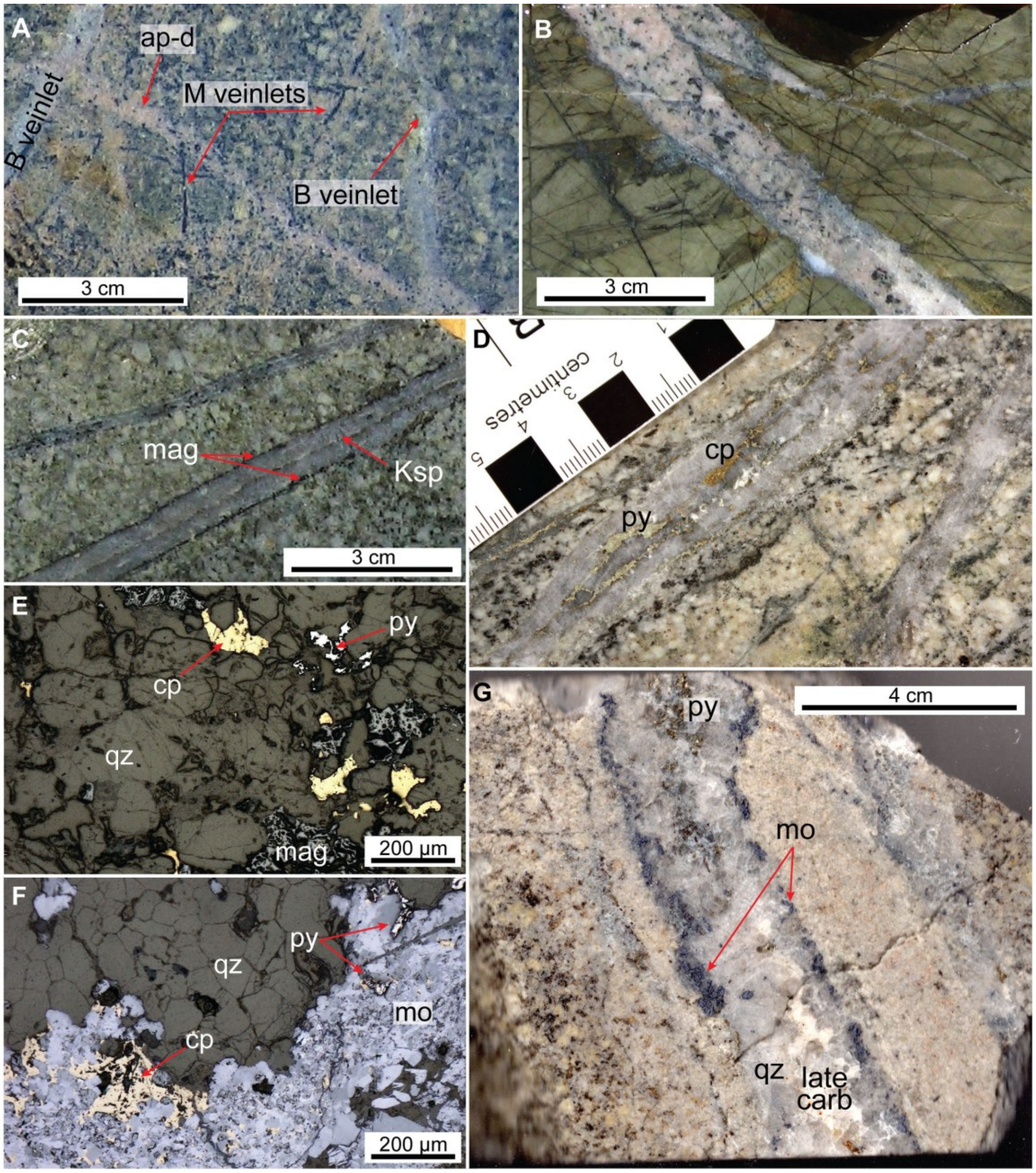

Figure 4.9 Early porphyry-style veinlets. (A) Crosscutting relationships in potassic-altered granodiorite porphyry: early magnetite (M) veinlets in this sample have been crosscut by an aplite dikelet, which itself has been cut and displaced by B-type quartz-magnetite veinlets (CDD-014, 373.0 m). (B) Aplite dikelet in metasedimentary rock (CDD-140, 157.70–157.80 m). (C) Early B-type quartz-magnetite veinlet with K-feldspar centerline (CDD-126, 229.00 m). (D) B-type quartz-chalcopyrite-pyrite vein in potassic-altered granodiorite porphyry. This meter-length interval has a grade of 0.22 g/t Au and 0.2 wt.% Cu (CDD-126, 95.00 m). (E) Photomicrograph of a B-type quartz-magnetite-chalcopyrite-pyrite veinlet (CDD-014, 361.3 m; reflected light). (F) Photomicrograph of a B-type quartz-chalcopyrite-pyrite-molybdenite veinlet (CDD-140, 180.00 m; reflected light). (G) B-type quartz-pyrite-molybdenite veinlet with late stage carbonate infill crosscutting phyllic-altered granodiorite porphyry (CDD-140, 30.90 m). Abbreviations: ap-d = aplite dikelet, carb = carbonate, cp = chalcopyrite, Ksp = K-feldspar, mag = magnetite, mo = molybdenite, py = pyrite, qz = quartz.

Rare barren anhydrite veinlets occur within the Main Zone, particularly in drillhole CDD-146 (Fig. 4.5). These veinlets are 2 mm- to 4 cm-thick and have irregular walls in contrast to the other veinlet types observed in the porphyry zone. Anhydrite veinlets are locally crosscut and offset by D veinlets (see below) associated with phyllic alteration, but their relative timing with respect to M- and B-type veinlets is unclear as no crosscutting relationships were observed between these veinlets.

Well-developed stockwork to sheeted quartz-pyrite veinlets, similar to the D veinlets of Gustafson and Hunt (1975), are closely associated with zones of phyllic alteration. D-type veinlets are characterized by straight to slightly wavy vein walls and their thicknesses range between 0.1 and 2 cm (Fig. 4.7F, 4.10A, B). Some of the D veinlets have vugs at the vein centers (Fig. 4.10B). These veinlets typically contain medium- to coarse-grained granular quartz and coarse-grained subhedral pyrite (Fig. 4.10A), with minor quantities of chalcopyrite and sparse galena, sphalerite, tetrahedrite/tennantite, and molybdenite. D-veinlets commonly have diffuse boundaries with prominent sericitic halos (Fig. 4.7F, 4.10A) but the intensity of alteration around these veinlets typically dies out rapidly away from the vein margin (e.g., within 1 cm; Fig. 4.7F) except in intervals with high vein density.

In the central part of the Main Zone, quartz-sericite-altered rocks also host polymetallic quartz-sulfide veins, which are most abundant in drillholes CDD-126 and CDD-146 (locations shown in Fig. 4.5). The polymetallic quartz-sulfide veins are similar to the D-type veinlets in terms of mineralogy and they also contain similar primary fluid inclusion types to those found in the D-type veinlets (see below). In contrast to typical D-type veinlets, the polymetallic quartz-sulfide veinlets are somewhat thicker (~4–15 cm) and they occur as individual veins (rather than as stockworks) close to the NE-trending structures, with relatively high abundances of chalcopyrite, galena, sphalerite, and tetrahedrite/tennantite (Fig. 4.10C, D). In this respect, these veinlets may be analogous to polymetallic veins described by Muntean and Einaudi (2001) from the Cerro Casale porphyry Au deposit in the Maricunga belt of northern Chile, which are also related to zones of quartz-sericite alteration.

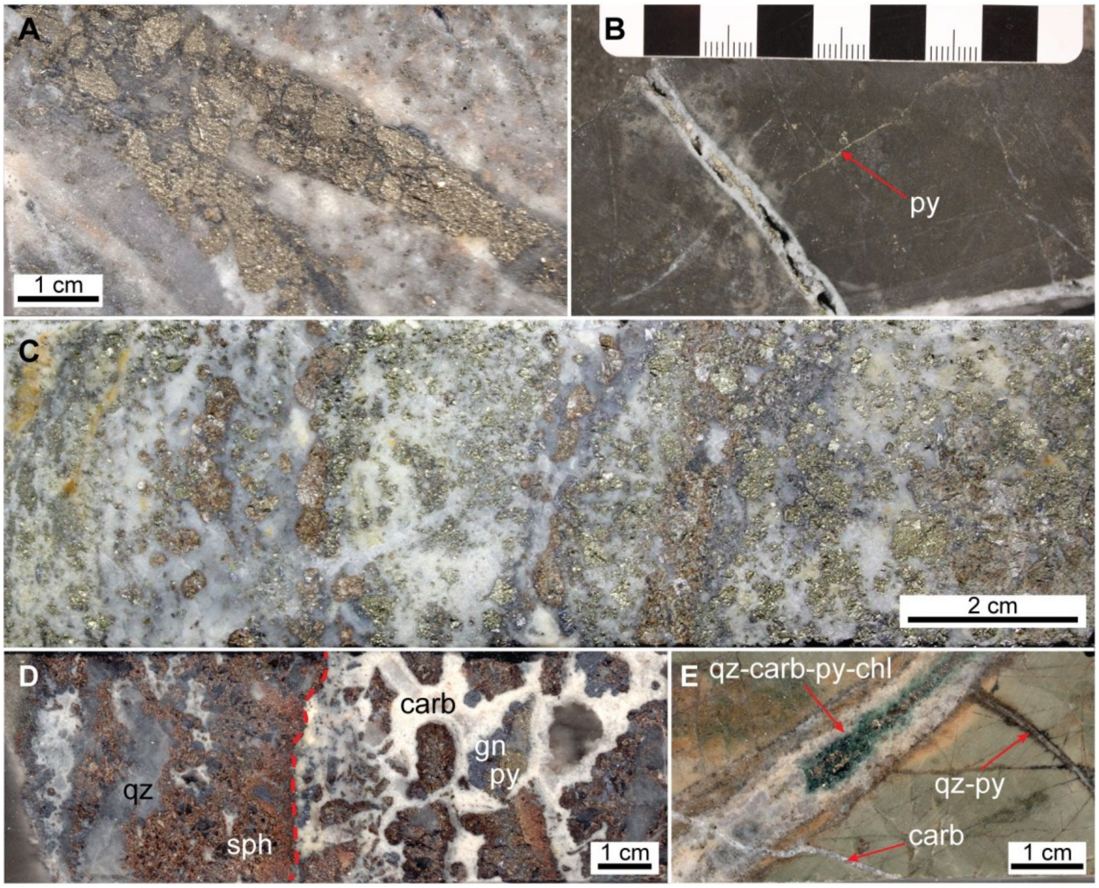

Figure 4.10 Porphyry-style veinlets associated with phyllic and propylitic alteration zones. (A) D-type veinlets with abundant coarse-grained subhedral pyrite and lesser quartz in phyllic-altered granodiorite porphyry (CDD-152, 192.00 m). (B) Vuggy D-type quartz-pyrite veinlet in metasedimentary rock (CDD-176, 112.00 m). (C) Thick polymetallic quartz-sulfide vein with pyrite, chalcopyrite, galena, and sphalerite (CDD-146, 294.40–294.60 m). (D) Brecciated polymetallic quartz-sulfide vein with galena and sphalerite. Sulfide-rich fragments derived from the polymetallic quartz-sulfide vein are cemented by manganocalcite on the right side of the photo (CDD-121, 100.70 m). (E) Quartz-carbonate-pyrite-chlorite veinlet associated with propylitic alteration. An earlier D-type quartz-pyrite veinlet is cut by this veinlet, which has itself been cut by a late (post-mineralization) carbonate veinlet (CDD-004, 128.40 m). Abbreviations: carb = carbonate, chl = chlorite, gn = galena, py = pyrite, qz = quartz, sph = sphalerite.

Quartz-calcite-pyrite ± chlorite ± epidote veinlets (Fig. 4.10E) are present mainly within the propylitized rocks in the outer zones of the porphyry system at Çöpler. Similar veinlets were also observed occasionally within the Main Zone, where propylitic alteration overprints the potassic- or phyllic-altered rocks.

4.7.3 Epithermal-style mineralization

Steeply-dipping, vuggy, auriferous carbonate-sulfide ± quartz ± barite veinlets (Fig. 4.11A–E) representing the main stage of Au mineralization at Çöpler are commonly observed as a shallow (usually <200 m depth) overprint on the porphyry system within the central part of the Main Zone, as well as in zones of carbonate alteration in the Manganese Mine Zone (Fig. 4.5).

The carbonate-sulfide ± quartz ± barite (hereafter termed “carbonate-sulfide”) veinlets have sharp walls without any visible alteration halos and their thicknesses vary between 0.5 cm and 5 cm (Fig. 4.11A, B). Carbonate minerals observed in these veinlets within the Main Zone are predominantly medium-grained white to creamy pink manganocalcite (Fig. 4.11A), whereas veinlets within the Manganese Mine Zone contain more distinctly pinkish rhodochrosite crystals, commonly displaying colloform bands (Fig. 4.11B) or rosette-like textures. In carbonate-sulfide veinlets, quartz usually occurs in microcrystalline form intergrown with manganocalcite or rhodochrosite, but coarse-grained quartz was also observed as late stage fillings (Fig. 4.11C). Barite is present in minor amounts in these veinlets, forming coarse-grained (>500 μm), subhedral to euhedral, bladed crystals. In the Main Zone, carbonate-sulfide veinlets commonly reopen or cut and offset porphyry stage veinlets (Fig. 4.7C). Locally this reopening and refilling is accompanied by fragmentation of the earlier veinlets and formation of vein breccias in which clasts of the earlier veinlets are cemented by epithermal minerals (Fig. 4.10D).

The ore mineralogy of the carbonate-sulfide veinlets is characterized by various sulfide and sulfosalt minerals. The predominant sulfide phase is euhedral pyrite overgrown by finely dispersed arsenical pyrite (Fig. 4.11D), which is commonly intergrown with minor chalcopyrite, arsenopyrite, marcasite, tennantite, tetrahedrite, galena, and compositionally-banded sphalerite (Fig. 4.11E). Gold grades within the carbonate-sulfide veinlets are typically 1 to 5 g/t Au, and locally as high as 8 g/t Au. The gold occurs as submicroscopic grains mainly within fine-grained arsenical pyrite, and to a lesser extent in arsenopyrite, tennantite, and tetrahedrite (see Appendix I for representative electron microprobe compositions).

A second pulse of epithermal-style Au mineralization is represented by sooty pyrite veinlets occurring as late stage infillings within the carbonate-sulfide veinlets or breccia zones. In these veinlets, gold occurs as submicroscopic grains in dark gray sooty pyrite (Appendix I), which is intergrown with realgar and orpiment together with

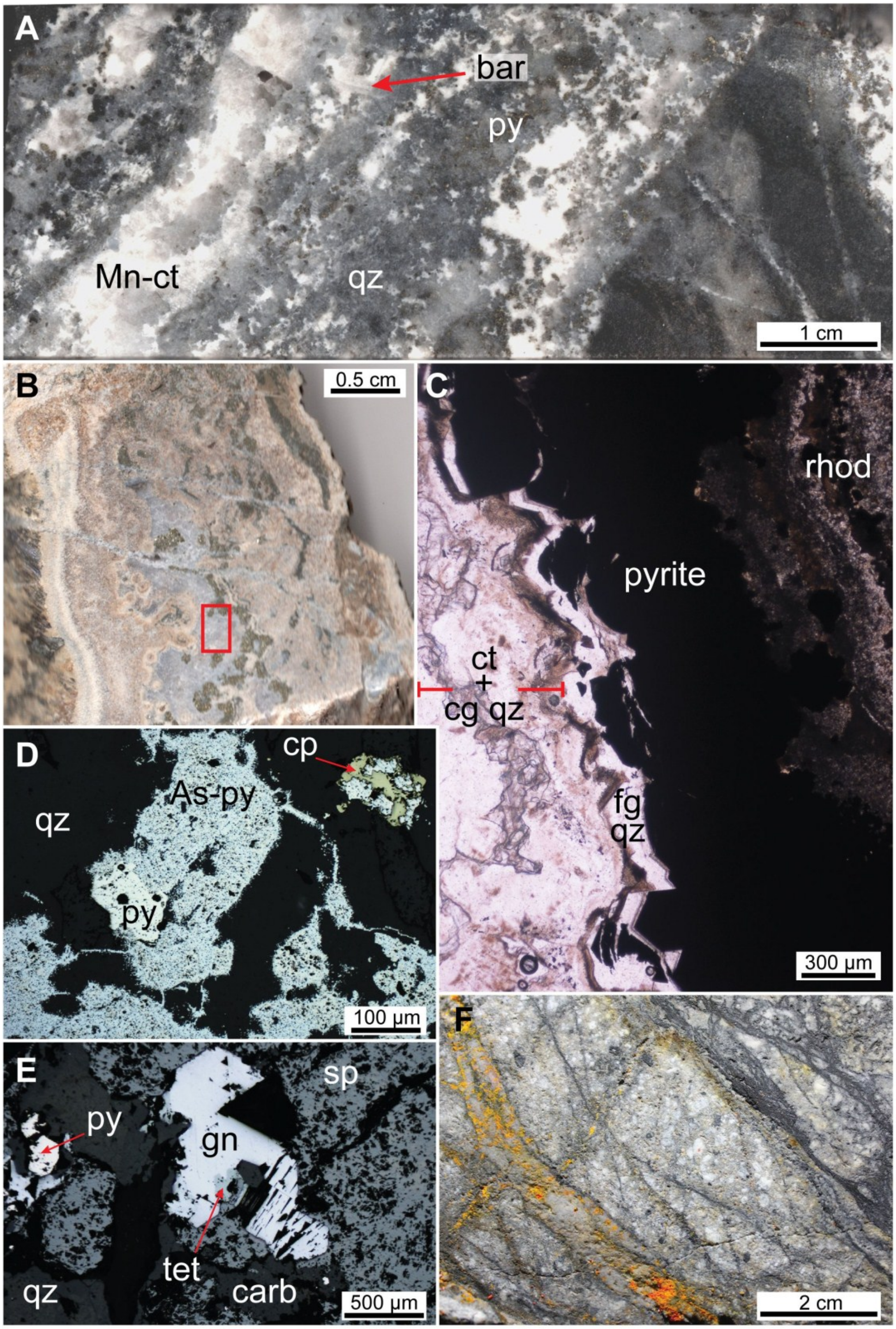
A
bar
py
Mn-ct
qz
1 cm
B
0.5 cm
C
rhod
pyrite
ct
+
cg qz
fg
qz
300 µm
D
cp
As-py
qz
py
100 µm
E
sp
py
gn
tet
qz
carb
500 µm
F
2 cm

Figure 4.11 Epithermal stage veinlets. (A) Carbonate-quartz-barite veinlet with fine-grained pyrite and lesser chalcopyrite, galena, sphalerite, and tetrahedrite/tennantite. This meter-length interval has an average grade of 1.4 g/t Au (CDD-146, 114.70 m). (B) Colloform-banded carbonate-sulfide-quartz veinlet with intergrown rhodochrosite, pyrite, and microcrystalline quartz. This meter-length interval has an average grade of 1.8 g/t Au (CDD-103, 80.65 m). (C) Detail of the area indicated with the red box in (B) under transmitted (plane-polarized) light. Band of rhodochrosite-pyrite is rimmed by fine-grained quartz followed by late calcite and coarse-grained quartz at the vein center. (D) Early subhedral pyrite overgrown by arsenical pyrite with lesser chalcopyrite (cp) and tetrahedrite/tennantite (not in this field of view) in a carbonate-sulfide-quartz-barite veinlet (under reflected light). This meter-length interval has an average grade of 6.5 g/t Au (CDD-176, 120.50–120.70 m). (E) Euhedral pyrite with coarse-grained galena and sphalerite and minor tetrahedrite in a carbonate-sulfide veinlet (under reflected light). This meter-length interval has an average grade of 1.7 g/t Au. (F) Fine-grained sooty pyrite (gray), realgar, and orpiment in a quartz-carbonate veinlet crosscutting carbonatized intrusive rock. This meter-length interval has an average grade of 4.6 g/t Au (CDD-184, 3.40 m). Abbreviations: As-py = arsenical pyrite, bar = barite, carb = carbonate, cg qz = coarse-grained quartz, cp = chalcopyrite, ct = calcite, fg qz = fine-grained quartz, gn = galena, Mn-ct = manganocalcite, py = pyrite, qz = quartz, rhod = rhodochrosite, sp = sphalerite, tet = tetrahedrite.

microcrystalline quartz, rhodochrosite, and barite gangue. These assemblages usually occur as late stage infillings within the carbonate-sulfide veinlets or breccia zones, and less commonly as discrete, friable veinlets in carbonatized rocks (Fig. 4.11F), particularly in the vicinity of ENE- and E–W-trending structures. Barite is more abundant in these sooty pyrite veinlets than in the earlier carbonate-sulfide veinlets.

4.7.4 Carbonate-replacement mineralization

Manto-type carbonate-replacement zones consisting of massive to semi-massive sulfides occur mainly in the Marble Contact Zone as well as below small uneroded marble blocks within the Main Zone. However, their presence within the Manganese Mine Zone is also suspected as evidenced by large masses of siliceous gossan, again underlying the carbonate succession. The carbonate-replacement zones are largely restricted to the structurally-modified intrusion–marble contacts in these localities, but mineralization locally extends into adjacent metasedimentary rocks.

The manto-type orebodies have sharp contacts with the surrounding rocks and their thicknesses vary from tens of centimeters up to several meters. The most significant of these zones were identified in drillhole CDD-188 (Fig. 4.12A; see Fig. 4.5 for drillhole location) with a ~20 m thick interval containing ~11 g/t Au and 0.77 % Cu. The ore assemblage of the carbonate-replacement zones typically consists of abundant arsenical pyrite, subordinate chalcopyrite, arsenopyrite, and marcasite, and minor sphalerite, galena, tennantite, and tetrahedrite (Fig. 4.12B, C). Small inclusions of pyrrhotite (<20 μm) were also detected within pyrite grains. Gangue mineralogy consists of quartz and carbonate, and late barite and chalcedonic quartz are present as fracture fillings (Fig. 4.12B). Gold in the carbonate-replacement ores mainly occurs as submicroscopic gold in pyrite and chalcopyrite and to a lesser extent in arsenopyrite, tetrahedrite, and tennantite (Appendix I).

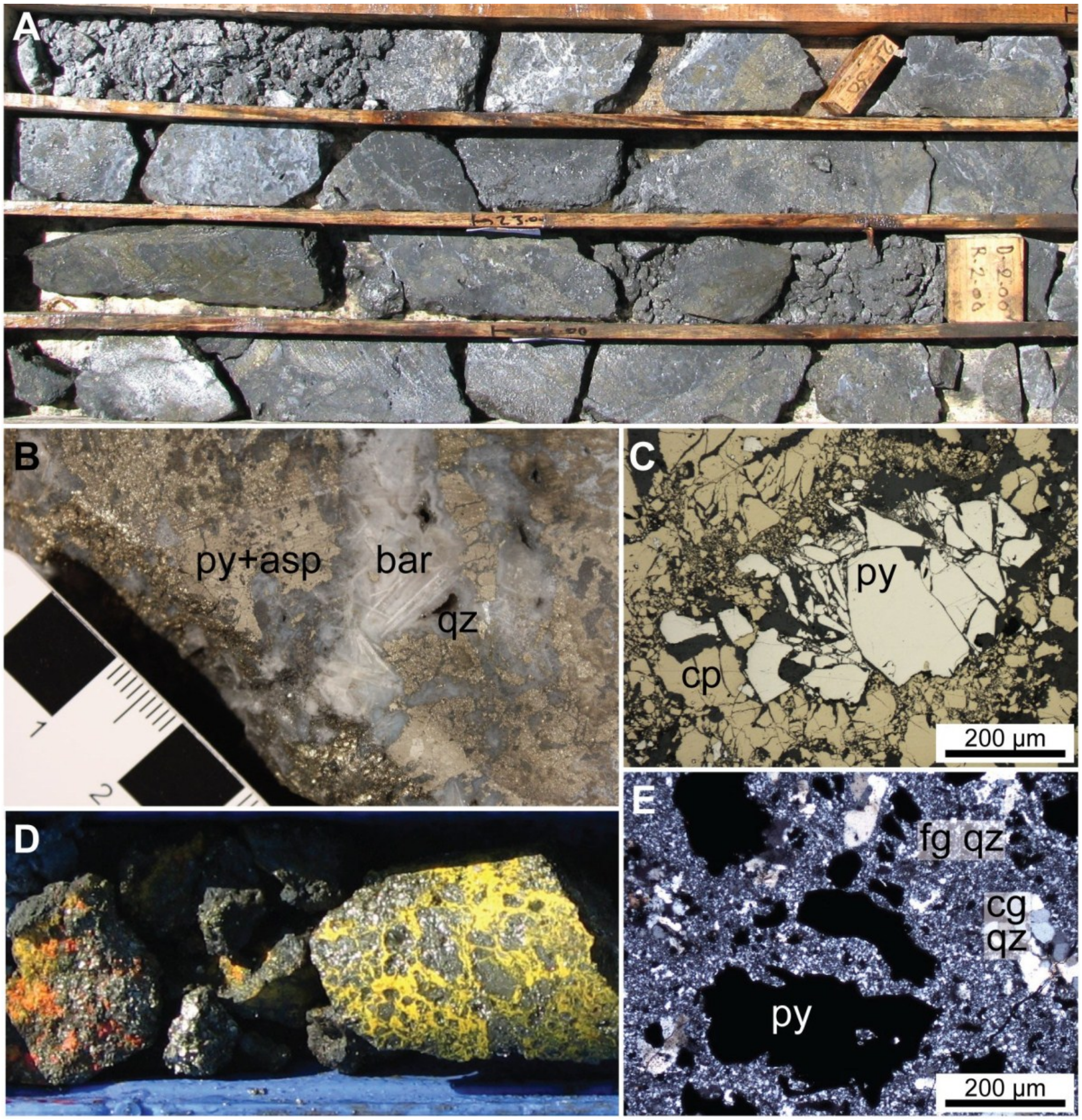

Figure 4.12 Textures of carbonate-replacement ores. (A) Approximately 4 m-long drillcore interval of deformed massive sulfide ore with an average grade of 8.6 g/t Au. Ore assemblage consists predominantly of pyrite and arsenopyrite with lesser chalcopyrite, marcasite, and sphalerite. Quartz and barite (white areas) occur as late stage fracture-filling material (CDD-188, 20.50–24.50 m). (B) Semi-massive zone of pyrite and arsenopyrite with late stage barite (bladed crystals) and chalcedonic quartz (vug linings) (CDD-

188, 11.00 m). (C) Broken pyrite and chalcopyrite fragments from a highly deformed carbonate-replacement zone (sample C-188027). (D) Realgar- and orpiment-impregnated pyritic breccia. This meter-length interval has an average grade of 16.6 g/t Au (CDD-087, 189.00 m). (E) Brecciated pyrite and coarse-grained (recrystallized) quartz fragments cemented by fine-grained quartz (sample C-188028). Abbreviations: asp = arsenopyrite, bar = barite, cg qz = coarse-grained quartz, cp = chalcopyrite, fg qz = fine-grained quartz, py = pyrite, qz = quartz.

In general, the carbonate-replacement zones show widespread evidence for multistage deformation. Recrystallization (e.g., granoblastic texture) and deformation (e.g., quartz and carbonate gangue with undulating extinction) textures are common, particularly in the quartz gangue. In addition, cataclastic breccias containing broken fragments of sulfide minerals were also observed. Matrices of these breccias typically consist of ore and gangue minerals characteristic of the sooty pyrite veinlets (Fig. 4.12D, E). This suggests that the carbonate-replacement ores were formed prior to sooty pyrite veinlets but their timing relative to the porphyry-style veinlets and later carbonate-sulfide veinlets is not known.

4.7.5 Post-mineralization veins

All of the vein types and mineralization styles mentioned above have been crosscut by later, barren calcite veins, particularly around the Manganese Mine and Marble Contact Zones. These veins are typically much thicker (4–20 cm) than the earlier veinlets and consist of colorless to creamy white calcite, forming colloform and crustiform bands. These veins do not contain any opaque mineral phases.

4.8 Analytical Methods

4.8.1 Fluid inclusion microthermometry

Microthermometric analyses of fluid inclusions in vein minerals from Çöpler were conducted in order to determine the temperatures and salinities of the mineralizing fluids, and to assess the spatiotemporal evolution of the hydrothermal system. Microthermometric analyses were performed on doubly polished wafers (~100–150 µm thick) using a Linkam THMSG600 freezing/heating stage. The stage was calibrated at -56.6°C, 0.0°C, and 374°C using Syn Flinc synthetic fluid inclusion standards, and measurements are accurate to ± 0.2°C for final ice melting temperatures recorded at subambient conditions and ± 2.0°C for temperatures above 100°C. Fluid inclusions hosted in quartz and sphalerite were initially cooled to -120°C, and then progressively heated until total homogenization was achieved, measuring all observed phase changes. In contrast, homogenization temperatures were measured first for fluid inclusions hosted by soft, cleavable minerals such as calcite, barite, and realgar to avoid stretching of the inclusions during freezing; some of the fluid inclusions in realgar and barite decrepitated upon heating, and yielded no data.

Salinity estimates for hypersaline fluid inclusions were derived from halite-melting temperatures using the equation of Sterner et al. (1988), whereas salinities of liquid-rich inclusions were calculated from final ice melting temperatures from the equation of Bodnar (1993). Concentrations of NaCl and KCl in hypersaline fluid inclusions that trapped both halite and sylvite daughter crystals were determined using the program SALTY (Bodnar et al., 1989).

4.8.2 Sulfur isotopes

A total of 16 samples (10 sulfide and 6 sulfate) were selected from different mineralization stages and analyzed for their sulfur isotope ratios ($^{34}S/^{32}S$) using continuous flow-isotope ratio mass spectrometry at the Isotope Science Laboratory of University of Calgary, Canada. Sulfur isotope values are reported in standard $\delta^{34}S$ notation relative to Canyon Diablo Troilite (CDT) with an analytical accuracy of ± 0.3‰ (2σ).

4.8.3 Oxygen and carbon isotopes

Oxygen isotopic compositions of 8 samples of quartz (4) and barite (4) separated from veinlets representing various stages of hydrothermal mineralization at Çöpler were analyzed using a Finnigan MAT 252 dual-inlet, multiple collector, magnetic-sector, gas mass spectrometer. Quartz and barite were handpicked from crushed samples and powdered for analysis. Oxygen isotope ratios are reported in standard $\delta^{18}O$ notation relative to V-SMOW (Vienna Standard Mean Ocean Water), with an accuracy of 0.2‰ (2σ).

In addition, 5 samples of vein carbonate were separated from mineralized epithermal veinlets and analyzed for their oxygen and carbon isotopic compositions in the Stable Isotope Geochemistry Laboratory at the University of Queensland, Australia. Carbonate samples were analyzed online using an Isoprime Dual Inlet Isotope Ratio Mass Spectrometer (DI-IRMS) with a multiprep attached. Analytical results are reported in standard $\delta^{18}O$ notation relative to V-SMOW for oxygen and in $\delta^{13}C$ notation relative to V-PDB (Vienna Pee Dee Belemnite) for carbon with analytical accuracy better than ± 0.2‰ (2σ).

4.9 Results

4.9.1 Fluid inclusion petrography

Vein samples representing different stages of mineralization at Çöpler contain abundant fluid inclusions. However, post-entrapment deformation due to fault reactivation and subsequent vein reopening is common throughout the district, and many of the inclusions observed have either been deformed (especially in softer minerals such as carbonates and sulfates) or are secondary inclusions lying along healed fractures (criteria of Roedder, 1984). Consequently, relatively few data were obtained from primary or pseudosecondary fluid inclusions in the epithermal veinlets. In contrast, such inclusions are well-preserved in some porphyry-style quartz veins. Microthermometric analyses were conducted on fluid inclusion assemblages (FIAs) based on the definition of Goldstein and Reynolds (1994), which allowed accurate characterization of separate fluid phases. During the petrographic investigations, five main types of primary and pseudosecondary inclusions were identified based on the phases present at ambient temperature conditions.

Halite-saturated hypersaline inclusions (denoted as "HS") are the predominant inclusion types in the porphyry-style B-, D-, and polymetallic quartz-sulfide veinlets, and they have been subdivided into HS1 and HS2 types based on the variety of daughter crystal phases they contain.

Early B veinlets consist of FIAs represented by coexisting polyphase brine (HS1) and vapor-rich (V) inclusions. HS1 inclusions contain halite, sylvite, and at least one other translucent daughter phase together with an opaque daughter crystal; they are typically equant or irregular shaped, with sizes ranging from <5 µm to ~ 50 µm (Fig. 4.13A–C). These inclusions are found either in clusters or as trails of pseudosecondary inclusions within early B-type quartz ± magnetite ± sulfide veinlets as well as in D-type quartz-pyrite and polymetallic quartz-sulfide veinlets. Halite crystals in these inclusions have typical cubic shapes, whereas sylvite crystals are smaller in size with slightly rounded corners (Fig. 4.13A, C). A birefringent, tabular-shaped daughter phase is also commonly present, and was tentatively identified as anhydrite. Chalcopyrite daughter crystals occur as small, triangular, brassy yellow inclusions (under reflected light), and cubic crystals of pyrite are not uncommon. Reddish brown grains of hematite were observed in few HS1 inclusions, and are interpreted to reflect post-entrapment oxidation because hematite is not observed in any of the hypogene ore assemblages.

Vapor-rich (V) inclusions in the same FIAs are characterized by either negative crystal shapes or as elongate elliptical inclusions, in which the vapor bubble makes up at least 70–85 volume percent of the total inclusion volume (Fig. 4.13B, C). They almost always coexist with HS1 inclusions in the early B-type veinlets (Fig. 4.13B, C) and were also found in D-type veinlets in smaller quantities. Vapor-rich inclusions also occur alone in trails of pseudosecondary inclusions, as well as in isolated clusters. Some of the V-type inclusions contain small opaque daughter minerals. Identification of these opaque phases was not possible for most of the V-type inclusions owing to their dark appearance, but in some large inclusions, chalcopyrite (Fig. 4.13C) and pyrite could be identified on the basis of their distinct crystal outlines.

Sugary quartz crystals in D-type quartz-pyrite and polymetallic quartz-sulfide veinlets commonly contain FIAs consisting of HS2 inclusions. These inclusions are similar to HS1 inclusions in containing halite daughter crystals as well as opaque phases, but they typically lack sylvite and other translucent daughter crystals (Fig. 4.13D). Sizes of HS2 inclusions range between 5 µm and ~20 µm with vapor bubbles occupying about 10–20 volume percent of the total inclusion volume.

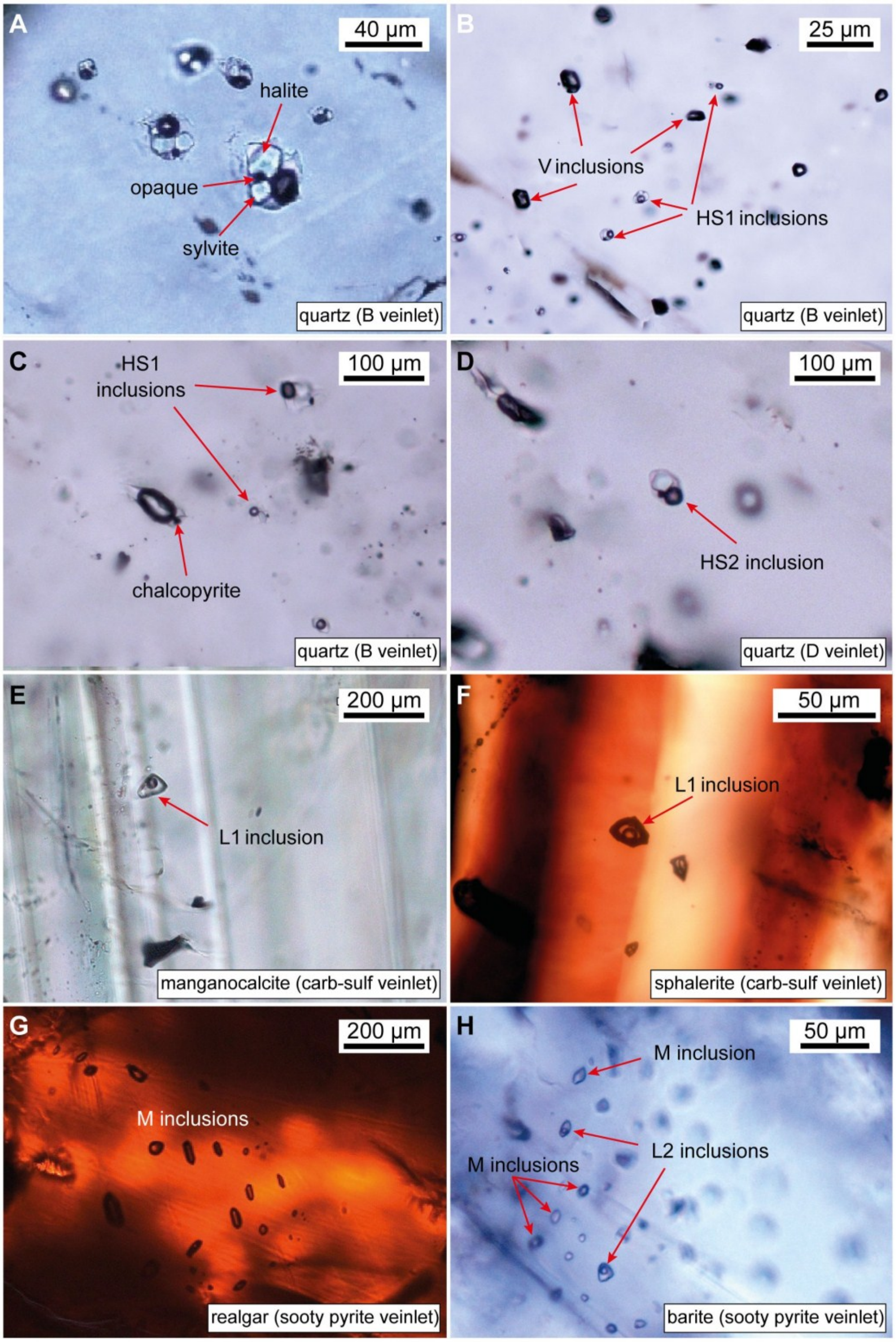

Figure 4.13. Transmitted light photomicrographs of fluid inclusions from mineralized veins. (A) Halite- and sylvite-bearing hypersaline (HS1) fluid inclusions in quartz from early B veinlet (sample C-126199). (B) Coexisting hypersaline (HS1) and vapor-rich (V) inclusions along boiling trails in quartz from early B veinlet (sample C-126199). (C) Vapor-rich (V) inclusion with chalcopyrite daughter coexisting with HS1 inclusions in quartz from early B veinlet (sample C-161). (D) Halite-bearing hypersaline inclusion (HS2) in quartz from a D-type quartz-pyrite veinlet (Sample C-225). (E) Isolated liquid-rich (L1) inclusion in

manganocalcite from carbonate-sulfide (carb-sulf) veinlet (Sample C-214). (F) Liquid-rich (L1) inclusion hosted in sphalerite from carbonate-sulfide (carb-sulf) veinlet (Sample C-222). (G) Monophase liquid (M) inclusions in realgar from a late sooty pyrite veinlet (Sample C-178). (H) Monophase liquid (M) and liquid-rich two-phase (L2) inclusions hosted in barite from a late sooty pyrite veinlet (Sample C-228).

Two-phase liquid-rich inclusions (L1) hosted within manganocalcite and sphalerite from auriferous epithermal veins are composed mainly of liquid with a small vapor bubble (~10–20 volume percent; Fig. 4.13E, F). These inclusions are typically 5–15 µm in size, and in manganocalcite they have elongated or irregular outlines. The majority of L1 inclusions in sphalerite have rounded shapes and they appear quite dark under transmitted light (Fig. 4.13F), hampering microthermometric analysis. In order to overcome this problem, measurements were primarily done on inclusions with elliptical or elongated shapes.

FIAs observed in barite and realgar from sooty pyrite veinlets contain primary monophase liquid (M) and liquid-rich two-phase (L2) inclusions (Fig. 4.13G, H). M-type inclusions are sub-rounded to elongate in shape with sizes typically ranging between <5 and 15 µm. Aqueous L2 inclusions with a small vapor bubble (5–10 vol. %) typically occur adjacent to the M-type inclusions (Fig. 4.13H), suggesting that the absence of a vapor bubble in the M-type inclusions is due to kinetic inhibition of bubble formation. Microthermometric measurements were only performed on these L2 inclusions due to metastability problems in monophase inclusions (Roedder, 1984).

4.9.2 Microthermometric data

A summary of the results of microthermometric analysis from a total of 196 inclusions from different paragenetic stages is provided in Table 4.3 and full data are listed in Appendix J. The relationship between measured homogenization temperatures and calculated salinity values is shown in Figure 4.16. No clathrate was observed in any of the fluid inclusion types during freezing runs and no liquid CO_2 was observed in any fluid inclusions at ambient to sub-ambient temperatures.

B veinlets: B-type veinlets are characterized by fluid inclusion assemblages consisting of polyphase hypersaline (HS1) fluid inclusions (Fig. 4.13A–C) that coexist with vapor-rich inclusions (Fig. 4.13B, C). First ice melting temperatures obtained only from a limited number of HS1 inclusions were between -24° and -23°C. This temperature range is close to the eutectic temperature for the H_2O-NaCl-KCl system (-22.9°C) consistent with the observed presence of halite and sylvite daughter crystals.

The majority of HS1 inclusions homogenized finally by halite dissolution at temperatures between 377°C and 424°C (mean = 394° ± 15°C, n = 25), with vapor bubble disappearance ($Th_{L-V(L)}$) at slightly lower temperatures between 318° and 403°C (mean = 368° ± 23°C). A few such inclusions failed to homogenize before decrepitation at temperatures above ~450°C. A minority of HS1 inclusions homogenized finally by vapor disappearance at temperatures between 347°C and 455°C (mean = 393° ± 32°C, n = 10), with Tm_{NaCl} values from 320° to 389°C (mean = 355° ± 34°C). Salinities obtained from halite dissolution temperatures from HS1 inclusions vary from 48 to 62 wt. % NaCl equiv. (mean = 55.6 ± 3.2 wt. % NaCl equiv., n = 33). This, combined with sylvite melting temperatures between 43°C and 214°C (mean = 123° ± 23°C, n = 33) correspond to an average NaCl:KCl ratio of ~2.1.

Microthermometric analysis of vapor-rich (V) inclusions in the B-type veinlets was difficult due to poor visibility of the meniscus in most cases, and therefore, the final homogenization temperatures of these inclusions could not be measured with confidence. Homogenization temperatures between 390° and 420°C were observed in V-type inclusions based on the apparent disappearance of the last visible liquid, but these should be regarded as minimum homogenization temperatures (Bodnar et al., 1985; Sterner, 1992). Final ice melting temperatures ranging from -3.5°C to -1.8°C (mean = -2.7° ± 0.6°C, n = 16) indicate salinity values between 3.1 and 5.7 wt. % NaCl equiv. (mean = 4.5 ± 1.0 wt. % NaCl equiv.). Vapor-rich and brine (HS1) inclusions observed in the same FIAs in quartz from B veinlets indicate that these assemblages were trapped under two-phase conditions, and therefore recorded homogenization temperatures represent trapping temperatures at the time of formation.

D veinlets and polymetallic quartz-sulfide veins: Hypersaline inclusions without a sylvite daughter (HS2) are the most abundant inclusion types observed in quartz crystals from the D-type quartz-pyrite (Fig. 4.13D) and polymetallic quartz-sulfide veinlets associated with phyllic alteration. These veinlets also contain relatively smaller amounts of HS1 inclusions but not in the same FIA.

HS2 inclusions homogenized finally by vapor bubble disappearance yielded homogenization temperatures between 284° and 367°C (mean = 337° ± 19°C, n = 21). Another fourteen HS2 inclusions finally homogenized by halite dissolution yielded homogenization temperatures ranging from 313°C and 397°C (mean = 347° ± 20°C). Salinity values corresponding to these homogenization temperatures were calculated to be between 36.8 and 45.4 wt.% NaCl equiv. (mean = 41.0 ± 1.5 wt. % NaCl equiv.).

Less abundant HS1 inclusions in D veinlets and polymetallic quartz-sulfide veins exhibit a similar range of homogenization temperatures. HS1 inclusions homogenized by halite dissolution yielded final homogenization temperatures between 358° and 385°C (mean = 369° ± 9°C, n = 10), whereas inclusions that homogenized by vapor bubble disappearance have overlapping homogenization temperatures ranging between 356° and 374°C (mean = 362° ± 11°C, n = 6). Salinities of these inclusions calculated from halite dissolution temperatures are higher compared to that of HS2 inclusions and are in the range 38.4 and 55.7 wt.% NaCl equiv. (mean = 52.2 ± 4.0 wt.% NaCl equiv.). The average NaCl:KCl ratio of ~1.7 calculated from halite and sylvite melting temperatures is slightly lower than the value (2.1) obtained from B-type veinlets.

Carbonate-sulfide veinlets: Rare primary and pseudosecondary fluid inclusions were found in manganocalcite and sphalerite from undeformed carbonate-sulfide veinlets (Fig. 4.13E, F). Microcrystalline quartz, on the other hand, contained no primary fluid inclusions.

Eutectic melting in two phase liquid-rich (L1) inclusions in manganocalcite occurred at temperatures from -21.5° to -20.4°C, close to the eutectic temperature of the H_2O-NaCl system (-21.2°C). L1 inclusions hosted in manganocalcite homogenized into the liquid phase at temperatures between 235° and 317°C (mean = 277° ± 19°C, n = 38). Final ice melting temperatures measured from these inclusions vary from -11.4°C to -2.2°C (mean = -6.3° ± 2.5°C, n = 38) indicating a relatively wide range of salinities from 3.7 to 15.4 wt.% NaCl equiv. (mean = 9.5 ± 3.2 wt.% NaCl equiv.).

Table 4.3 Summary of microthermometric data for fluid inclusion assemblages in porphyry- and epithermal-style veinlets

Sample	Assemblage ID	Boiling	Host	P/PS	Type	n	Tm$_{\text{ice}}$ (°C)	Tm$_{\text{sylvite}}$ (°C)	Th (°C)[1]	Tot. salinity (wt.% NaCl equiv.)
126199	1-1		qz	P	HS1	4		156±39	400±25	58.7±2.2
	1-2		qz	P	HS1	5		130±1	389±13	56.2±1.1
	1-3		qz	P	HS1	8		126±2	396±13	55.6±2.4
	1-4B	+	qz	P	HS1	2		123±0	406±2	57.3±0.2
	2-1B	+	qz	P	HS1	5		122±1	392±24	55.7±2.1
	2-2B	+	qz	PS	HS1	4		120±1	413±31	57.2±3.9
	2-3B	+	qz	PS	HS1	10		97±27	378±18	51.8±3.3
	1-4V	+	qz	PS	V	8	-2.6±0.7			4.1±1.0
	2-1V	+	qz	P	V	2	-3.5±0.1			5.7±0.1
	2-2V	+	qz	PS	V	3	-2.7±0.4			4.5±0.6
	2-3V	+	qz	PS	V	3	-2.7±0.5			4.5±0.8
C225	9-1		qz	P	HS2	8			346±22	40.9±1.9
	9-2		qz	PS	HS2	7			367±6	41.6±0.6
	9-3		qz	P	HS2	5			360±3	41.3±0.9
	10-1		qz	P	HS2	4			361±4	41.3±0.9
	10-2		qz	PS	HS1	9		122±9	366±8	53.0±1.7
C218	1-3		qz	PS	HS2	5			366±8	41.6±1.1
	1-4		qz	P	HS2	2			334±26	39.7±3.1
	2-1		qz	P	HS2	4			326±15	39.3±1.9
	2-2		qz	PS	HS2	3			368±21	53.2±2.4
	3-1		qz	P	HS2	4			368±7	49.8±7.6
C214	4-1		Mn-ct	PS	L1	5	-10.3±0.9		288±21	14.3±0.9
	4-2		Mn-ct	PS	L1	5	-8.7±1.1		286±12	12.4±1.3
	4-3		Mn-ct	P	L1	7	-5.9±1.8		289±16	9.0±2.6
	3-1		Mn-ct	PS	L1	8	-5.1±1.8		281±11	7.9±2.5
C216	1-1		Mn-ct	P	L1	6	-4.3±1.2		265±10	6.9±1.7
	1-2		Mn-ct	P	L1	4	-5.0±1.6		259±13	7.7±2.2
	1-3		Mn-ct	P	L1	3	-6.0±2.2		260±27	9.1±2.9
C222	1-1		sp	P	L1	4	-2.5±0.5		273±11	4.2±0.8
	1-2		sp	P	L1	4	-4.7±2.0		273±12	7.3±2.8
	2-1		sp	P	L1	5	-5.8±0.1		267±2	8.9±0.2
	3-1		sp	P	L1	3	-4.7±0.3		267±1	7.5±0.4
	3-3		sp	PS	L1	6	-6.1±0.2		261±7	9.3±0.3
C178	1-2		rea	PS	L2	4	-6.2±1.7		102±19	8.3±5.5
	2-1		rea	PS	L2	2	-7.1±3.3		129±6	10.3±0.6
	2-2		rea	PS	L2	3	-4.7±1.2		102±17	6.2±2.1
	2-4		rea	PS	M	6	-4.2±2.5			6.1±2.7
	2-5		rea	PS	M	2	-4.0±1.7			5.8±1.7
C161	1-2		bar	PS	L2	3	-3.2±2.3		113±17	8.0±1.0
	2-1		bar	PS	L2	3	-3.9±2.5		93±10	7.0±5.6
	2-2		bar	P	L2	4	-5.1±3.1		87±17	6.5±3.1
C228	1-2		bar	P	L2	4	-4.1±2.2		98±21	4.8±2.3
	5-2		bar	P	L2	3	-3.0±1.5		104±5	7.6±2.8

[1] Temperature of final homogenization either by halite dissolution or vapor bubble disappearance

Abbreviations: bar = barite, Mn-ct = manganocalcite, P = primary, PS = pseudosecondary, qz = quartz, rea = realgar, sp = sphalerite

Homogenization temperatures measured from L1 inclusions hosted in sphalerite fall between 251° and 289°C (mean = 268° ± 9°C, n = 22), similar to the range of L1 inclusions in manganocalcite. Final ice melting temperatures, measured only from a small number of these inclusions due to their dark appearance, range between -7.0° and -2.2°C (mean = -4.6° ± 1.6°C, n = 13). These temperatures correspond to salinity values of 3.7–10.5 wt.% NaCl equiv. (mean = 7.2 ± 2.4 wt.% NaCl equiv.), which also overlap with the salinity range determined from L_1 inclusions hosted in manganocalcite (Table 4.3).

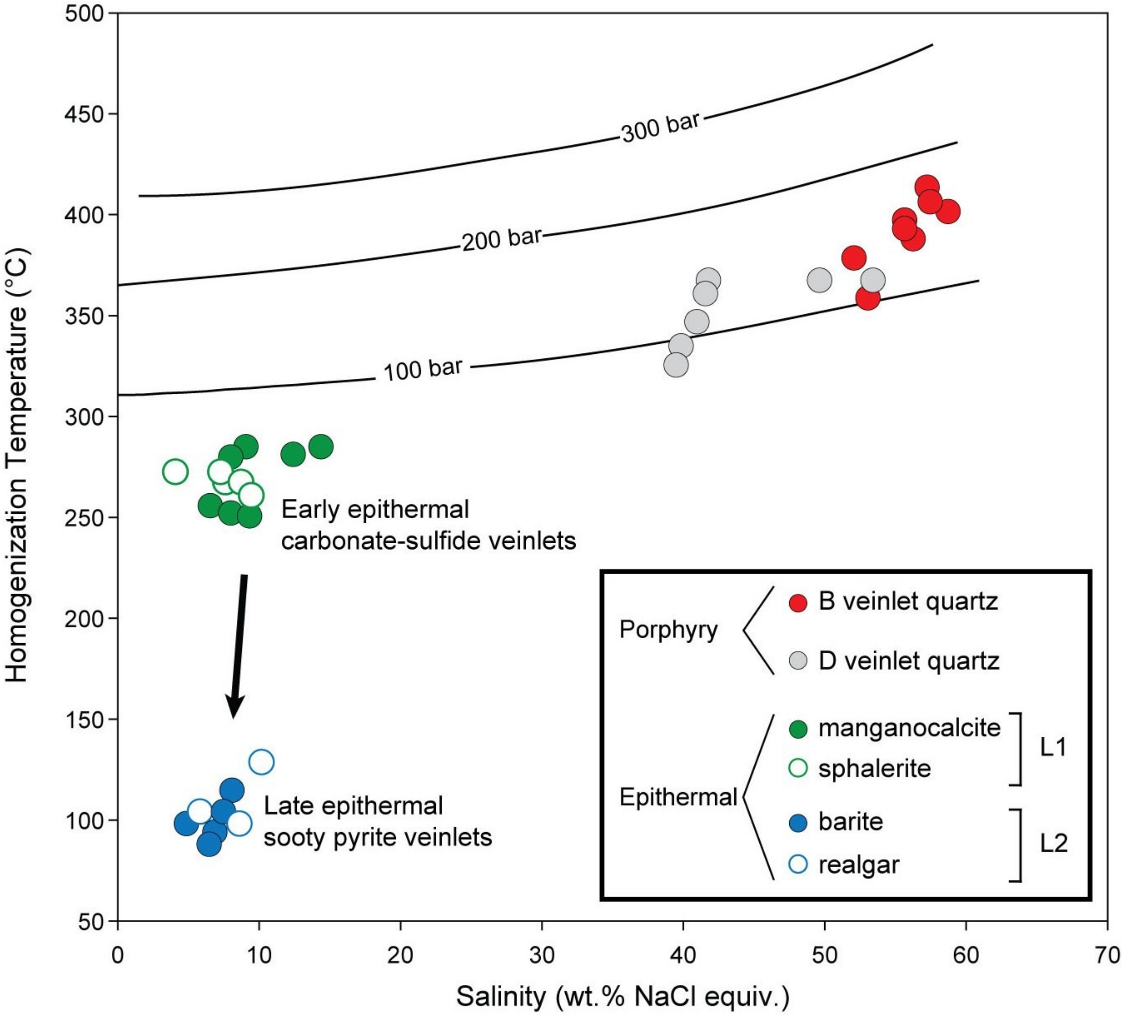

Figure 4.14 Salinity (wt.% NaCl equiv.) versus final homogenization temperature (Th) plot of fluid inclusion assemblages. Isobars for hypersaline inclusions were calculated based on the H_2O-NaCl system (Driesner and Heinrich, 2007).

Sooty pyrite veinlets: Barite and realgar from sooty pyrite veinlets host abundant primary monophase (M) inclusions (Fig. 4.13G, H), in some fluid inclusion assemblages together with sparse L2 inclusions with small vapor bubbles (Fig. 4.13H). The absence of a vapor phase in the M-type inclusions due to metastability (Roedder, 1984) precludes determination of homogenization temperatures, but the accompanying L2 inclusions were measured to provide an estimate of homogenization temperature and salinity for both M and L2 inclusions. In samples lacking L2 inclusions, the M-type inclusions were deliberately stretched by heating to nucleate a vapor bubble, which allowed measurement of ice melting temperatures.

L2 inclusions hosted by barite and realgar in late sooty pyrite veinlets homogenized to the liquid phase at temperatures between 76° and 133°C (mean = 102° ± 17°C, n = 26). This temperature range is consistent with the suggestion that monophase inclusions generally form at temperatures below 100°C (Roedder, 1984; Goldstein and Reynolds, 1994). Ice melting temperatures of L2 and stretched M inclusions range between -13.6° and -0.7°C (mean = -4.4° ± 2.3°C, n = 34) and indicate a wide range of salinities between 1.2 and 13.6 wt.% NaCl equiv. (mean = 7.0 ± 3.1 wt.% NaCl equiv.).

4.9.3 Trapping conditions of fluid inclusions

Homogenization temperatures recorded during microthermometric analysis of fluid inclusions provide a minimum estimate of temperature at the time of trapping, unless 2-phase conditions such as boiling were occurring. In B-veinlets polyphase brine (HS1) inclusions were observed coexisting with abundant vapor-rich fluid inclusions suggesting boiling conditions. However, most of the analyzed HS1 inclusions were homogenized finally by halite dissolution, and due to phase equilibria constraints these inclusions could only be trapped in the absence of a vapor phase in the liquid-stable field. In addition, the freezing point depression and homogenization temperatures recorded from vapor-rich inclusions are usually inaccurate, and as a result, microthermometric data obtained from brine inclusions that homogenized finally by halite dissolution and coexisting with vapor-rich inclusions cannot be used for estimating the trapping depth and pressures of B veinlets.

On the other hand, in some FIAs HS1 inclusions exhibiting different final homogenization behaviors (halite dissolution or vapor bubble disappearance) were observed together. This can be explained either by movement along the P-T space during cooling (Bodnar, 1994), by pressure fluctuations during entrapment at relatively constant temperatures (Cline and Bodnar, 1994), or by post-entrapment modification of inclusions due to H_2O loss or shrinkage (Sterner et al., 1988; Klemm et al., 2008). For Çöpler, the latter scenario is likely the case since most of the early veinlets have been deformed and necking is suspected particularly in the relatively large (>20 μm) HS1 inclusions. In addition, the tendency of these large brine inclusions to occur as isolated groups, and the coexistence of small-sized brine inclusions (usually <10 μm) together with vapor-rich inclusions commonly along boiling trails may further indicate post-entrapment modification of at least some of the HS1 inclusions (Audétat and Günther, 1999). Thus, HS1 inclusions are inferred to have originally formed during boiling or near-boiling conditions, such that their homogenization temperatures and pressures approximate to their actual temperatures and pressures at the time of entrapment.

The minimum trapping pressures of HS1 inclusions that finally homogenized by halite dissolution were determined using the HOKIEFLINCS_H2O-NaCl software (Steele-MacInnis et al., 2012) based on the numerical model of Lecumberri-Sanchez et al. (2012). Although pressure values obtained by this method vary widely from 120 to 1000 bars (n=30), approximately 85 percent of the data clustered between 150 and 500 bars with an average value of 385 bars. The outlying (apparently higher pressure) data likely reflects post-entrapment effects (stretching or leakage) as mentioned above. The calculated pressure range corresponds to depths of ~0.6–2 km and the average pressure of 385 bars correspond to a depth of ~1.5 km under lithostatic conditions, assuming a specific gravity of 2.5 g/cm^3 for the overlying carbonate rocks.

Minimum trapping pressures for inclusions that reach final homogenization by halite dissolution can also be determined using an alternate method, which utilizes the relationship between halite melting temperatures and liquid-vapor homogenization temperatures (Becker et al., 2008). On the Tm_{halite} versus Th_{L-V} diagram, FIAs containing hypersaline (HS1 and HS2) inclusions from porphyry-style veinlets are scattered along a wide pressure range between <250 bars and ~750 bars (Fig. 4.15). A lithostatic depth of ~1.4 km corresponding to an average pressure value of ~350 bars is close to the depth estimate obtained using Lecumberri-Sanchez et al.'s model.

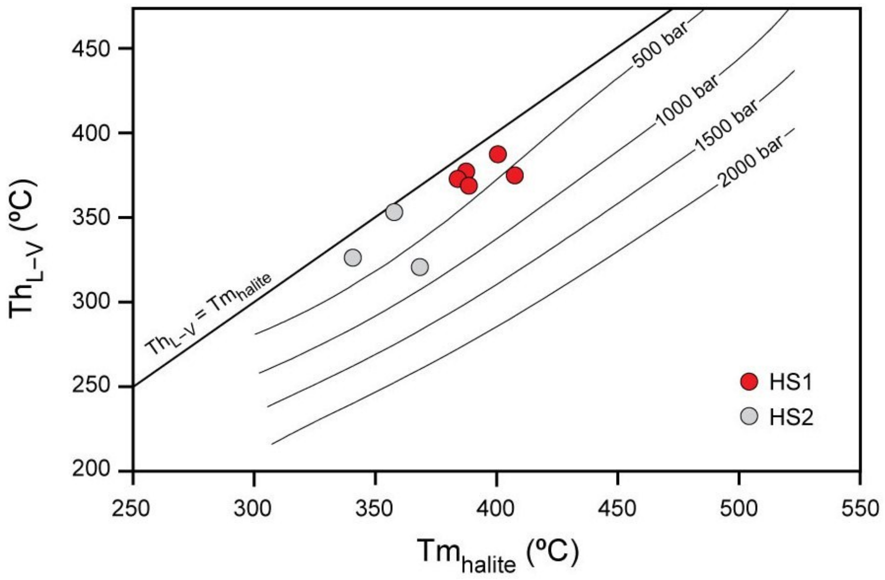

Figure 4.15 Tm$_{halite}$ versus Th$_{(L-V)}$ plot of fluid inclusion assemblages containing hypersaline inclusions that homogenized finally by halite dissolution (after Becker et al., 2008).

Homogenization (and trapping) pressures for the less abundant group of HS1 inclusions, which homogenized finally by vapor bubble disappearance, were determined using the SoWat software (Driesner, 2007). Calculated pressure values between ~100–300 bars (n=10) correspond to minimum formation depths of between 0.4 and 1.2 km (under lithostatic conditions), and the average pressure value of 180 bars translates into a minimum trapping depth of 700 m.

For comparison, minimum trapping pressures of fluid inclusions have also been calculated using the equations for the H_2O-NaCl binary system (Driesner and Heinrich, 2007). Trapping pressures of hypersaline inclusions determined using this model are mostly between 100 and 200 bars (Fig. 4.14), corresponding to depths of 400 to 800 m, which are significantly lower than the above estimates. One major problem regarding this method, however, is that it does not take other salt phases (e.g., KCl) and minor amounts of dissolved CO_2 into account. This may lead to uncertainties in the range of 100–200 bars (Landtwing et al., 2010), thereby resulting in underestimation of minimum trapping pressures.

Field geological evidence indicates that both porphyry phases at Çöpler have been emplaced directly below the Munzur limestone. Previous studies by Özgül and Turşucu

(1984) and Tunç et al. (1991) estimated the maximum thickness of this carbonate succession to be 1,200 m. These studies also indicated that ophiolitic blocks and some ophiolitic mélange were thrust onto the northern margin of the Munzur Unit prior to the middle Eocene, but it is not clear whether the carbonate rocks surrounding the Çöpler deposit was overlain by such lithologies at the time of emplacement of the intrusions. The porphyritic texture of the intrusive rocks and the absence of ophiolitic rocks in the immediate vicinity of the deposit area suggest that the intrusive system at Çöpler was formed at shallow depths and that the thickness of the overlying rock column above the orebody was close to the estimated maximum thickness of the Munzur limestone. A depth of ~1.2 km is also in good agreement with the estimated average pressure for HS1 inclusions that homogenized finally by halite dissolution, and also with the higher pressure estimate obtained from HS1 inclusions that homogenized finally by vapor bubble disappearance. Taking into account that the high temperature B veinlets were mainly sampled from depths of 150 to 300 m below surface, and assuming that the erosion along the Çöpler window did not vertically extend significantly into the host granodiorite porphyry following the removal of the overlying carbonate rocks, a depth of 1.5 km seems to be a reasonable approximation for the depth of formation of the porphyry-type B veinlets.

No evidence for boiling was observed in the paragenetically late D-type quartz-pyrite and polymetallic quartz-sulfide veinlets, and therefore a pressure correction is required to estimate trapping temperatures of HS2 inclusions in these veinlets. Assuming that both veinlet types were formed broadly around the same depth of ~1.5 km with the B veinlets and a salinity of 40 wt.% NaCl equiv. (average of salinities from HS2 inclusions), a temperature correction of ~15°C is calculated indicating trapping temperatures of ~370° ± ~20°C.

Similarly, a temperature correction of ~10°C is calculated for the L1 inclusions hosted in carbonate-sulfide veinlets assuming a maximum depth of 1.5 km and a salinity of 10 wt. % NaCl equiv. (average of salinities from L1 inclusions). This translates into an average trapping temperature of ~290° ± ~20°C for the L1 inclusions, which should be regarded as a maximum trapping temperature because these veinlets presumably formed during the early stages of unroofing of the Çöpler window, such that their formation depth is likely to be less than 1.5 km. Later sooty pyrite epithermal veinlets, on the other hand, are inferred to have formed under shallower and cooler conditions as indicated by the abundance of monophase liquid inclusions. Therefore, a negligible pressure correction is required for L2 inclusions in these assemblages, and trapping temperatures were likely close to the homogenization temperatures of ~100°C.

4.9.4 Sulfur isotopes

The overall $\delta^{34}S$ compositions of sulfide samples from Çöpler exhibit a narrow range between 2.3 and 4.9 ‰ (Table 4.4). One pyrite separate extracted from a B-type veinlet yielded a $\delta^{34}S$ value of 4.8‰, whereas pyrite from a D-type veinlet has a $\delta^{34}S$ composition of 4.9‰. The $\delta^{34}S$ values for two galena (2.3 and 3.7‰) and two sphalerite (3.8 and 4.6‰) separates from polymetallic quartz-sulfide veinlets are slightly lower than the range of pyrite samples. The range of compositions from these earlier porphyry-related veinlet groups are comparable with the sulfur isotopic compositions of typical I-type granitoids (Ishihara and Sasaki, 1989), and also with values reported from many porphyry systems (Ohmoto and Rye, 1979; Taylor, 1987).

The $\delta^{34}S$ compositions of sulfides from later epithermal veinlets indicate values within the range of compositions obtained from porphyry stage veinlets (Table 4.4). Two pyrite separates obtained from carbonate-sulfide and sooty pyrite epithermal veinlets returned $\delta^{34}S$ values of 3.4 and 4.1‰, respectively. In addition, one pyrite sample extracted from massive sulfide manto ore yielded a similar $\delta^{34}S$ value of 3.4‰ (Table 4.4).

All of the sulfate minerals from the Çöpler deposit yielded relatively enriched $\delta^{34}S$ values compared to the tightly grouped sulfide minerals (Table 4.4). Two anhydrite samples from barren anhydrite veinlets have $\delta^{34}S$ values of 13.5 and 14.3‰. One gypsum sample extracted from a polymetallic quartz-sulfide veinlet returned a $\delta^{34}S$ value of 14.0‰, similar to the anhydrite data (Table 4.4). This gypsum, which was only observed as a late stage filling in some of the polymetallic quartz-sulfide veinlets, may be a product of hydration of early stage magmatic anhydrite, and may thus have inherited its sulfur isotopic composition from the precursor anhydrite. Two barite samples from epithermal carbonate-sulfide ± quartz ± barite (sooty pyrite) veinlets have higher $\delta^{34}S$ isotopic compositions of 17.7 and 19.0‰, whereas two other barite samples from carbonate-replacement ores yielded $\delta^{34}S$ values of 16.1 and 16.9‰ (Table 4.4).

Sulfur isotope thermometry was attempted to provide independent estimates of crystallization temperature for certain veinlet types. Sphalerite and galena pairs from two polymetallic quartz-sulfide veinlets yielded temperatures of 627°C (+660°/-203°C) and 424°C (+203°/-108°C) based on the fractionation equations of Ohmoto and Rye (1979). These calculated temperatures are significantly higher than the temperatures obtained from microthermometric analyses. Similarly, a temperature of 378°C (+15°/-13°C) was calculated from a barite-pyrite pair from a sooty pyrite veinlet using the fractionation equation of Ohmoto and Lasaga (1982), which is much higher than the estimated trapping temperature of fluid inclusions in these veinlets (100°C). These geologically unreasonable temperature estimates are either related to difficulties in obtaining pure mineral separates (e.g., due to abundant chalcopyrite inclusions in sphalerite) or they may reflect sulfur isotopic disequilibrium during crystallization of galena-sphalerite and pyrite-barite pairs, despite petrographic evidence for textural equilibrium.

4.9.5 Oxygen isotopes

The $\delta^{18}O$ isotopic compositions of three quartz separates from the mineralized veinlets associated with the early potassic and phyllic alteration assemblages range between 9.1 and 11.5‰ (Table 4.5). One microcrystalline quartz separate from a Stage I carbonate-quartz-sulfide veinlet has a slightly heavier $\delta^{18}O$ value of 13.2‰.

Manganocalcite from a carbonate-sulfide epithermal veinlet has a $\delta^{18}O$ composition of 11.9‰, whereas two rhodochrosite separates from similar veinlets yielded higher values of 16.3 and 16.5‰ (Table 4.5). Two other rhodochrosite samples from sooty pyrite epithermal veinlets have the highest $\delta^{18}O_{carbonate}$ values of 17.5 and 18.9‰ (Table 4.5).

Table 4.4 $\delta^{34}S$ compositions of sulfide and sulfate minerals from various mineralization stages from Çöpler

Sample no.	**Mineral**	**Paragenetic stage**	**$\delta^{34}S$ (‰, V-CDT)**
C-041	Anhydrite	Anhydrite veinlet	13.5
C-047	Anhydrite	Anhydrite veinlet	14.3
C-152222	Pyrite	B veinlet	4.8
C-225	Pyrite	D veinlet	4.9
C-146293	Galena	Polymetallic quartz-sulfide vein	2.3
C-146293	Sphalerite	Polymetallic quartz-sulfide vein	3.8
C-224	Gypsum	Polymetallic quartz-sulfide vein	14.0
C-224	Galena	Polymetallic quartz-sulfide vein	3.7
C-224	Sphalerite	Polymetallic quartz-sulfide vein	4.6
C-197	Pyrite	Carbonate-replacement ore	3.4
C-214	Pyrite	Carbonate-sulfide veinlet	4.1
C-228	Barite	Sooty pyrite veinlet	19.0
C-176090	Barite	Carbonate-replacement ore	16.1
C-176121	Barite	Carbonate-replacement ore	16.9
C-188011	Pyrite	Sooty pyrite veinlet	3.4
C-188011	Barite	Sooty pyrite veinlet	17.7

The shift in $\delta^{18}O$ values in carbonate minerals from carbonate-sulfide veinlets may be related to a change in physicochemical properties of the ore fluids such as temperature or composition, or it may be related to different isotopic fractionation factors for manganocalcite and rhodochrosite. Fluid inclusion data collected from carbonate-sulfide veinlets indicates a narrow temperature interval (~30°C; Table 4.3) for the fluids associated with this stage, and therefore, temperature change is not expected to have a pronounced effect on the observed variations in oxygen isotopic compositions. On the other hand, the presence of rhodochrosite in relatively shallow carbonate-sulfide veinlets instead of manganocalcite may be due to fluid buffering by manganese-bearing metasedimentary rocks indicating significant change in fluid composition. Unfortunately, fractionation factors for manganocalcite do not exist, and therefore, the latter possibility cannot be tested.

Barite from a sooty pyrite veinlet has a $\delta^{18}O$ value of 14.8‰, whereas three other barite samples associated with carbonate-replacement ores have heavier $\delta^{18}O$ compositions between 18.7 and 22.8‰ (Table 4.5).

The $\delta^{18}O$ isotopic compositions of hydrothermal fluids representing different mineralization stages were calculated based on published water isotopic fractionation equations (O'Neil et al., 1969; Clayton, 1972; Kusakabe and Robinson, 1977) and using the trapping temperature estimates from microthermometric analysis of fluid inclusions (Table 4.5). Calculated $\delta^{18}O_{fluid}$ values from quartz for the fluids associated with early potassic alteration and porphyry-style mineralization are 4.8 and 7.2‰ (based on a temperature estimate of 390°C), and a $\delta^{18}O_{fluid}$ value of 6.7‰ was calculated from quartz associated with phyllic alteration using a temperature estimate of 370°C. These values are similar to the $\delta^{18}O$ compositions reported for primary magmatic waters (5.5–10.0‰; Taylor, 1974; Giggenbach, 1992).

Early carbonate-sulfide epithermal veinlets have calculated $\delta^{18}O_{fluid}$ values (based on a pressure-corrected T_h of 290°C) between 5.9 and 9.3‰ with the higher values obtained from rhodochrosite samples with relatively heavier $\delta^{18}O$ mineral values (Table 4.5). Nevertheless, this temperature range, which is broadly similar to the range for porphyry-related veinlets, also suggests a predominantly magmatic source for the fluids in the early epithermal veinlets. $\delta^{18}O_{fluid}$ values of 1.8 and 0.4‰ were calculated for rhodochrosite from later sooty pyrite veins, based on a temperature estimate of 100°C, and are similar to a $\delta^{18}O_{fluid}$ composition of 0.5‰ calculated for barite from the second sample (Table 4.5). The range of calculated $\delta^{18}O_{fluid}$ compositions for the later sooty pyrite veinlets is significantly lower than that of porphyry-style and early epithermal veinlets, suggesting the late stage involvement of meteoric waters.

4.9.6 Carbon isotopes

Carbonate minerals from epithermal carbonate-sulfide and sooty pyrite veinlets have $\delta^{13}C$ values that fall in a narrow range between -2.0 and 0.6‰ (Table 4.5). Three samples from carbonate-sulfide veinlets yielded $\delta^{13}C$ compositions between -2.0 and 0.0‰. Two samples from later sooty pyrite veinlets have slightly higher but partly overlapping $\delta^{13}C$ values of -0.3 and 0.6‰.

arbonate, and barite and $\delta^{13}C$ data for carbonate with fluid compositions calculated using
on analyses

Sample no.	Sample description	Mineral	$\delta^{18}O_{mineral}$ (‰, V-SMOW)	$\delta^{13}C_{mineral}$ (‰, V-PDB)	Temperature Estimate (°C)	$\delta^{18}O_{fluid}$ (‰, V-SMOW)[1,2]
C-126199	B veinlet	Quartz	9.1		390 (±20)	4.8 (4.3–5.3)
C-152222	B veinlet	Quartz	11.[illegible]		390 (±20)	7.2 (6.7–7.7)
C-225	D veinlet	Quartz	11.[illegible]		370 (±20)	6.7 (6.2–7.2)
C-176097	Carb-sulf veinlet	Quartz	13.[illegible]		290 (±20)	5.9 (5.1–6.6)
C-214	Carb-sulf veinlet	Mn-ct	11.9	-2.0	290 (±20)	5.7 (5.3–6.6)
C-217	Carb-sulf veinlet	Rhod	16.[illegible]	-1.3	290 (±20)	9.1 (8.7–10.0)
C-157109	Carb-sulf veinlet	Rhod	16.[illegible]	0.0	290 (±20)	9.3 (9.0–10.2)
C-157	Sooty py veinlet	Rhod	18.[illegible]	-0.3	100 (±15)	1.8 (0.1–3.3)
C-228	Sooty py veinlet	Rhod	17.[illegible]	0.6	100 (±15)	0.4 (-1.3–1.9)
C-228	Sooty py veinlet	Barite	14.[illegible]		100 (±15)	0.5 (-1.3–2.1)
C-188024	CRO	Barite	22.[illegible]			
C-176090	CRO	Barite	18.[illegible]			
C-176121	CRO	Barite	22.[illegible]			

Abbreviations: carb = carbonate, CRO = carbonate-replacement ore, Mn-ct = manganocalcite, py = pyrite, rhod = rhodochrosite, sulf = sulfide

[1] Fluid $\delta^{18}O$ calculations based on the fractionation equations of Clayton (1972) for quartz, O'Neil et al. (1969) for carbona
and Kusakabe and Robinson (1977) for barite

[2] Ranges of $\delta^{18}O_{fluid}$ values given in parentheses are calculated based on the errors in the average T_h values

4.10 Discussion

4.10.1 Early porphyry-style Cu-Au mineralization

Locally pervasive and areally restricted potassic alteration assemblages, characterized by predominant secondary biotite and lesser secondary K-feldspar, are the earliest manifestations of the porphyry-related magmatic-hydrothermal activity. No sulfide precipitation occurred at this stage but hydrothermal magnetite was abundant (up to 5 vol. %) either as hairline magnetite veinlets or as disseminations, in keeping with many other gold-rich porphyry systems (Sillitoe, 1997; Ulrich and Heinrich, 2002; Perelló et al., 2003).

Cu and Au deposition occurred subsequently, during formation of sheeted B-type quartz ± magnetite ± sulfide veinlets albeit not in significant amounts to develop an economic porphyry system. Magnetite and chalcopyrite are the predominant ore minerals in the earlier and deeper B veinlets, whereas veinlets with larger quantities of pyrite and molybdenite are usually found marginal to the Cu-rich zone possibly indicating a slight temperature decline from chalcopyrite-magnetite-rich B-veinlets towards more pyrite-molybdenite-rich B veinlets, as is commonplace in Cu-Au porphyry deposits (Ulrich and Heinrich, 2002; Profett, 2003; Sillitoe, 2010).

B veinlets trapped polyphase hypersaline (~47–62 wt.% NaCl equiv.; HS1) inclusions and low salinity (~3–5.5 wt.% NaCl equiv.), low density vapor-rich inclusions which are interpreted to have formed near-boiling conditions. These fluids likely originated from unmixing of a low to moderate salinity supercritical fluid exsolved from a magmatic source at temperatures of ~390°C. Stratigraphic reconstructions coupled with theoretical estimates using homogenization temperatures of HS1 inclusions indicate that these fluids were probably trapped at depths of ~1.5 km and under lithostatic pressures of ~400 bars.

Cooling of the high salinity magmatic fluid in response to downward retreat of the thermal gradient resulted in characteristic feldspar-destructive phyllic (quartz-sericite-pyrite) overprinting of the earlier potassic alteration assemblages. D-type quartz-pyrite veinlets associated with this volumetrically more extensive alteration zone trapped abundant brine (HS2) inclusions with slightly lower temperatures (~370° ± 20°C) and salinities (37–42 wt.% NaCl equiv.) compared to the fluids associated with the potassic alteration. Sparse polymetallic quartz-sulfide veinlets with relatively high abundances of chalcopyrite, galena, sphalerite, and tennantite/tetrahedrite developed in the central part of the Main Zone, again in close association with the phyllic alteration zone. Although significant variations in terms of temperature and salinity were not observed between D veinlets and polymetallic quartz-sulfide veins, the contrasting mineralogy of the latter group combined with their greater thickness and textural evidence for open-space filling may indicate a change in the formation conditions (lower pressures), possibly in response to a switch from ductile to brittle deformation (Fournier, 1999). It can be argued, therefore, that the polymetallic quartz-sulfide veins represent the transition from porphyry to epithermal conditions at Çöpler.

The apparent absence of argillic or advanced argillic assemblages above the phyllic-altered zone at Çöpler can be explained either as a consequence of lithologic controls during the evolution of the hydrothermal system, or by deep erosion within Çöpler window. Although the carbonate succession once overlying the Çöpler intrusive system has now been almost completely removed throughout the deposit area, it is not clear whether this erosion has extended deeply into the granodiorite porphyry, and some blocks of remnant marble may represent roof pendants or relicts of the roof rocks. If the depth estimate of ~1.5 km for formation of the B-veinlets is accurate, then this suggests that erosion within the Çöpler window was mostly restricted to the carbonate rocks, and therefore that low-temperature argillic alteration assemblages were never formed. According to this scenario, weakly acidic magmatic-hydrothermal fluids were neutralized upon contact with limestone/marble, and did not evolve to more acidic compositions during cooling. The carbonate roof rocks may have acted as an impermeable barrier to upward fluid flow, concentrating ore deposition at their base (*cf.* Sillitoe et al., 2006). It can also be speculated that hydrothermal weakening of the carbonate rocks directly above the porphyry system rendered them more susceptible to later erosion, thus explaining the existence of the Çöpler window directly over the orebody.

4.10.2 Overprinting epithermal-style Au mineralization

The main stage of Au mineralization at Çöpler took place with formation of carbonate-sulfide veinlets following the switch from ductile to brittle conditions. Significant amounts of arsenical pyrite (containing submicroscopic gold) and various other sulfide/sulfosalts phases precipitated alongside with carbonate, quartz, and barite gangue. Homogenization temperatures of ~290° ± 20°C and salinity values of 4 to 15 wt.% NaCl equiv. (avg = 10.7 ± 2.7 wt.% NaCl equiv.) obtained from liquid-rich two-phase (L1) inclusions from these veinlets indicate a marked change in fluid compositions towards relatively dilute and low temperature ore fluids. This range of salinities is higher than that of fluids associated with high- and low-sulfidation epithermal systems and is similar to the salinities (<10 up to 23 wt.% NaCl equiv.; Sillitoe and Hedenquist, 2003; Simmons et al., 2005) reported from many intermediate-sulfidation systems worldwide. An intermediate-sulfidation-type epithermal system is also confirmed by the abundance of Mn-carbonates and sulfide/sulfosalt phase minerals, and a stable mineral assemblage of chalcopyrite, sphalerite, and tetrahedrite/tennantite (Hedenquist and Sillitoe, 2003). Such fluid compositions in intermediate-sulfidation systems are commonly, if not always, attributed to contribution from a high salinity magmatic source (Simmons, 1991; Albinson et al., 2001). A magmatic origin for the fluids associated with auriferous carbonate-sulfide veinlets is further attested by the $\delta^{34}S$ compositions of pyrite (3.4 and 4.1‰; Table 4.4) as well as by the calculated $\delta^{18}O_{fluid}$ compositions (5.3–10.1‰; Table 4.5) obtained from quartz and carbonate gangue from the same veinlets.

According to Cooke and Simmons (2000), simple cooling of fluids alone is not a viable mechanism for effective precipitation of Au in the epithermal environment, especially when compared to other processes such as boiling or fluid mixing. In the early carbonate-sulfide epithermal veinlets, there is no fluid inclusion (coexisting liquid- and vapor-rich inclusions), textural (bladed calcite), or mineralogical (adularia) evidence for boiling, and fluid mixing is not supported by the oxygen isotope data.

Apart from cooling, another plausible mechanism that likely contributed to gold deposition is the neutralization of slightly acidic magmatic fluids by wall-rock reaction. Carbonate minerals (either manganocalcite or rhodochrosite) are ubiquitous in the epithermal veinlets and their presence indicates that the ore fluids of this stage were near-neutral pH. These carbonate minerals were unlikely to have been precipitated from the original magmatic fluid as neither visible CO_2 nor clathrate melting was observed in any of the fluid inclusions, although minor amounts of dissolved CO_2 (<0.85 mol.%; Hedenquist and Henley, 1985) could still be present in them. Rather, the presence of carbonate minerals can be explained in terms of buffering with carbonate country rocks. The involvement of wall-rock induced neutralization in gold precipitation is also supported by the predominance of rhodochrosite over manganocalcite in epithermal veinlets away from the source granodiorite porphyry (both at shallower levels and also towards the Manganese Mine Zone), as manganese was probably derived from the metasedimentary succession. Therefore, it seems more likely that the main stage of Au mineralization associated with carbonate-sulfide veinlets resulted from progressive cooling and neutralization of the high-salinity fluids that were derived from the deeper porphyry environment.

Gold is transported in epithermal systems primarily as sulfide complexes rather than as chloride complexes, but the latter are more important for base metal transport (Seward and Barnes, 1997). Cooling and neutralization of slightly acidic and saline fluids of magmatic origin would have led to a decrease in the solubility of chloride complexed base metals, and the precipitation of significant amounts of base metal sulfide and sulfosalt phases in the polymetallic quartz-sulfide veins in advance of epithermal mineralization. This process would have reduced the concentration of sulfide in the hydrothermal fluids, thus reducing the solubility of gold (Benning and Seward, 1996), and causing co-precipitation with sulfide minerals.

On the other hand, the close similarity between the ore mineral assemblages of carbonate-replacement zones and epithermal carbonate-sulfide veinlets may be indicative of a genetic connection between these two mineralization styles. Although the exact timing of carbonate-replacement mineralization at Çöpler is unknown, late stage sooty pyrite veinlets locally crosscutting the carbonate-replacement zones provide an upper age limit for the latter style of mineralization, and therefore, the carbonate-replacement mineralization may be broadly synchronous with the auriferous carbonate-sulfide veinlets.

Alternatively the carbonate-replacement ores could have formed earlier, contemporaneously with the porphyry-style mineralization. Experimental studies from a variety of magmatic-hydrothermal ore deposit types indicate that significant amounts of base and precious metals can be transported by magmatic vapors (Williams-Jones and Heinrich, 2005). As noted earlier, if the ascending low-pH, low-density vapors separated from high density brine were neutralized at the base of the carbonate rocks, they could have precipitated some gold together with other sulfide and sulfosalt phases to form carbonate-replacement zones. The relatively higher abundance of chalcopyrite in the carbonate-replacement zones compared to carbonate-sulfide veinlets may also support this hypothesis as vapor-rich inclusions trapped in B veinlets commonly contain chalcopyrite daughters (Fig. 4.13B). Unfortunately, it was not possible to test these models since the carbonate-replacement ores at Çöpler have been mostly oxidized and their locally observed non-oxidized counterparts have been intensely deformed (i.e., brecciated and/or recrystallized) due to repeated tectonic activity along the intrusive-carbonate contacts.

The final stage of gold mineralization occurred with the deposition of sooty pyrite veinlets in which submicroscopic gold is intimately associated with fine-grained pyrite intergrown with realgar, orpiment, rhodochrosite, microcrystalline quartz, and increased amounts of barite. These veinlets generated grades locally as high as 10 g/t Au, but their occurrence is sporadic, localized around E–W- and NE-striking structures.

Ore fluids of this stage are significantly cooler (100°C) and slightly less saline (7.6 ± 3.0 wt.% NaCl equiv.) compared to the fluids associated with carbonate-sulfide veining. Despite a significant temperature drop, the marginal decrease in salinities does not support a simple cooling trend from the earlier epithermal fluids. Although $\delta^{13}C$ compositions of carbonates from epithermal carbonate-sulfide and sooty pyrite veinlets do not show significant variations, a plot of $\delta^{13}C$ against $\delta^{18}O$ compositions of these carbonate minerals reveals a clear shift in isotopic compositions from relatively depleted values in carbonate-sulfide stage towards relatively enriched values in the late sooty pyrite stage (Fig. 4.16). This may indicate entrainment of an external fluid, which was possibly buffered by the surrounding carbonate rocks. Similarly, the relatively depleted $\delta^{18}O_{fluid}$ compositions of the later epithermal fluids in the sooty pyrite veins (0.6–2.0‰; Table 4.5) suggest mixing between the earlier magmatic fluids and a more dilute external fluid (likely of meteoric groundwater origin). The occurrence of evaporites in the sedimentary basin to the north of the Çöpler (Tekin et al., 2001; Palmer et al., 2004) may explain the elevated salinities in the inferred groundwater.

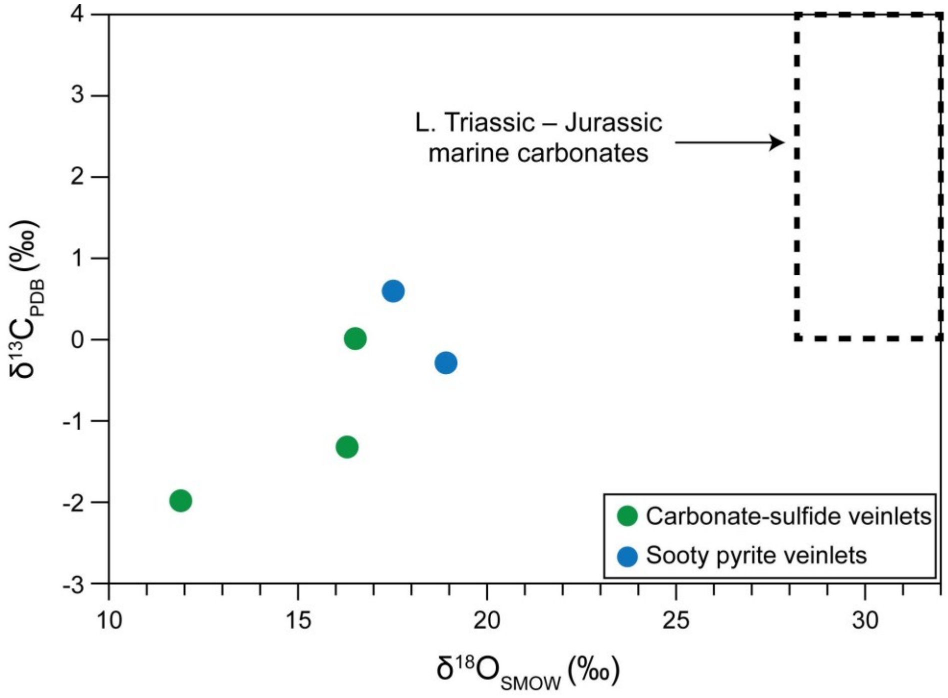

Figure 4.16 $\delta^{18}O_{SMOW}$ versus $\delta^{13}C_{PDB}$ plot of carbonate minerals from epithermal carbonate-sulfide and sooty pyrite veinlets. Range of compositions for the Late Triassic–Jurassic marine carbonates is taken from Veizer et al. (1999).

Overall, observed crosscutting relationships at Çöpler suggest a progression from early high-temperature porphyry-style alteration and mineralization assemblages towards a late, lower temperature intermediate-sulfidation epithermal-style mineralization. The hydrothermal system seems to have evolved from a single magmatic source until the very late stages, during which some involvement of external fluids was recorded. This implies a genetic link between the early porphyry and overprinting intermediate-sulfidation epithermal mineralization. Similar relationships have been reported from many other districts such as Baguio and Mankayan in Luzon in Philippines (Cooke and Bloom, 1990; Claveria, 2001; Cooke et al., 2011), Wafi-Golpu in Papua New Guinea (Sillitoe, 2010), and Maricunga (Sillitoe et al., 2013) in northern Chile. The Çöpler Au deposit is similar to these porphyry-epithermal systems in many aspects including tectonic setting (broadly arc-related), nature of magmatism, alteration/mineralization styles, and fluid characteristics.

At Çöpler, the confinement of discrete mineralization styles to the top 300–400 meters of the igneous intrusions and to the adjoining metasedimentary and carbonate rocks suggests strong telescoping of porphyry-epithermal mineralization. This telescoping was likely due to rapid cooling of the magmatic-hydrothermal system, which in turn was controlled by a combination of lithologic and structural factors including shallow emplacement of the intrusive rocks at the base of the thick limestone succession and repeated fault activity along favorable structural zones enhancing fluid focusing. The carbonate cover rocks played a further critical role in the build up of the magmatic-hydrothermal system as they likely acted as a seal to maintain fluid overpressures and also as a neutralizing agent due to their highly receptive nature.

4.10.3 Çöpler in comparison with other Tethyan epithermal systems

Several other porphyry deposits occur in the eastern Taurides, such as Karakartal and Cevizlidere (Fig. 1.1., 4.1), but other epithermal Au deposits similar to Çöpler have not been discovered in this region to date.

The Mastra Au-Ag-(Cu-Pb-Zn) deposit (0.7 Moz Au, ~0.3 Moz Ag), located about 200 km NE of Çöpler in the eastern Pontides (Fig. 1.1), is geographically the closest known occurrence of an intermediate-sulfidation epithermal deposit. At Mastra, andesitic porphyries of inferred Eocene age host an approximately 2.5 km-long vein system in adularia-quartz-sericite-carbonate altered rocks (Tüysüz et al., 1995), throughout which two stages of epithermal mineralization were recognized. Locally brecciated stockwork zones contain an early Ag-rich base metal sulfide mineralization associated with hydrothermal fluids of 240°–300°C and 5–11 wt.% NaCl equiv. Later

Au-rich (base metal-poor) mineralization was precipitated from cooler (160°–260°C) fluids, but with similar salinities (6–9 wt.% NaCl equiv., Tüysüz et al., 1995).

Several other analogous systems are found in western Turkey, particularly in the highly prospective Biga Peninsula. Middle to late Eocene andesitic to dacitic porphyries in the Şahinli area (Fig. 1.1) host breccia veins containing Au-Ag and base metal mineralization (Yılmaz et al., 2010). Moderate temperature (mostly 250°–300°C) and low to moderate salinity (4–7 wt.% NaCl equiv.) fluids were reported from Şahinli for the main stage mineralization (Yılmaz et al., 2010). The late Cenozoic Efemçukuru Au deposit to the south of this region (Fig. 1.1) was originally classified as a low-sulfidation epithermal system (Oyman et al., 2003), although its high base metal content, abundance of manganese carbonates and silicates, and ore fluids with a range of salinities between 0 to 9 wt.% NaCl equiv. are more consistent with an intermediate-sulfidation classification. It should be noted however that none of the intermediate-sulfidation epithermal deposits mentioned above are known to be associated with underlying porphyry-like systems, although porphyry-related mineralization is suspected in Şahinli (Yılmaz et al., 2013).

The telescoped porphyry-epithermal Fakos deposit is exposed to the west of the Biga Peninsula on Limnos Island in the northern Aegean Sea, in close association with ~20 Ma monzonitic and shoshonitic hypabyssal rocks (Fornadel et al., 2012). Although the relatively alkaline nature of the host magmatic rocks is consistent with its collision-related setting, and the close association of Au with tellurides resembles the low-sulfidation, porphyry-related epithermal systems of the western Pacific (e.g., Emperor, Ladolam), moderate salinities (up to 9.7 wt.% NaCl equiv.) and the ore mineralogy of late stage fluids suggest an intermediate-sulfidation classification (Fornadel et al., 2012).

In the Eastern Rhodope Massif of southeast Bulgaria, the late Eocene Madjarovo district (Fig. 1.1) contains a base metal-rich intermediate-sulfidation system and small skarn orebodies centered around a potassic-altered zone suggesting the presence of an underlying porphyry system, similar to Çöpler (Marchev et al., 2002). Intermediate-sulfidation epithermal mineralization at Madjarovo is contained in an array of quartz-carbonate-barite-sulfide veins hosted within zones of quartz-carbonate-sericite-adularia alteration and distal propylitic alteration (Marchev et al., 2005). Fluid inclusion data suggests that Pb-Zn and precious metal mineralization developed at moderate to low temperatures (210°–280°C) from low salinity (2–4.5 wt.% NaCl equiv.) fluids (Marchev et al., 2005).

The Apuseni Mountains of Romania also host several important intermediate-sulfidation epithermal deposits. Among these, the Miocene Roşia Montană Au-Ag and Sacarimb deposits are broadly contemporaneous and they were formed in relation to post-subduction magmatism developed at 14–12 Ma (Alderton and Fallick, 2000; Wallier et al., 2006). In Roşia Montană (Fig. 1.1), epithermal mineralization is mainly hosted in adularia- and phyllic-altered breccia zones of volcanic-hydrothermal origin. Gold mineralizing occurred from low salinity (0.2–2.2 wt.% NaCl equiv.) and low to moderate temperature (200°–280°C) fluids with strong magmatic signatures (Wallier et al., 2006). Nevertheless, geochronological evidence suggests that these fluids are not related to the underlying porphyry system, which developed significantly later (Wallier et al., 2006). Similarly fluid characteristics (0–6 wt.% NaCl equiv., 200°–300°C) were also observed in Sacarimb, but unlike Roşia Montană, there is no evidence for porphyry-style mineralization in this deposit (Alderton and Fallick, 2000).

The presence of intermediate-sulfidation epithermal systems has also been confirmed from the Iranian part of the Tethyan Metallogenic Belt, but many of these deposits are either small or detailed documentation of their paragenetic features is not available. The most significant and well-known deposit from this region is the Miocene Chah Zard Au-Ag deposit (Fig. 1.1), which contains low- to intermediate-sulfidation veins and breccias that contain abundant sulfides and sulfosalts within quartz-sericite-carbonate-adularia-altered host rocks (Kouhestani et al., 2013). Ranges of salinities (8.4–13.7 wt.% NaCl equiv.) and temperatures (260°–345°C) reported from Chah Zard (Kouhestani et al., 2013) indicate fluids that are quite similar to the Stage I fluids from Çöpler.

4.11 Conclusions

The Çöpler Au deposit is the most significant discovery in a region previously unrecognized for Cu-Au mineralization. The deposit features a highly telescoped porphyry-epithermal system and also contains peripheral zones of irregular and poorly-preserved carbonate-replacement orebodies that have been largely oxidized. Gold-copper mineralization is centered around a shallowly emplaced composite stock of middle Eocene (~44 Ma) age which has been exposed within an ENE-trending structural corridor.

Early porphyry mineralization began with formation of a central potassic alteration zone and associated M-type magnetite and B-type quartz ± magnetite ± sulfide veinlets. B-veinlets trapped coexisting brine (~39–60 wt.% NaCl equiv.) and low salinity (~3–6 wt.% NaCl equiv.) vapor-rich inclusions at temperatures of ~390°C and depths of ~1.5 km, generating subeconomic Cu-Au mineralization. Extensive phyllic overprinting of the potassically altered core was developed in relation to slightly cooler (~370°C) and relatively less saline fluids (~37–45 wt.% NaCl equiv.), which were trapped along sheeted to stockwork D-type quartz-pyrite and polymetallic quartz-sulfide veinlets. Flashing of sulfide and sulfosalt minerals were recorded in the latter veinlets most likely due to a switch from ductile to brittle conditions.

Main stage of gold mineralization developed along carbonate-sulfide veinlets which contain abundant arsenical pyrite and relatively smaller amounts of arsenopyrite, marcasite, chalcopyrite, galena, sphalerite, and tennantite/tetrahedrite. In these veinlets gold mainly occurs as submicroscopic grains in pyrite, arsenopyrite, and tennantite/tetrahedrite. Liquid-rich two-phase inclusions in manganocalcite and sphalerite indicated temperatures of ~290°C and salinities between 4 and 15 wt.% NaCl equiv.

Carbonate-sulfide veinlets are crosscut by late epithermal sooty pyrite veinlets in which gold occurs in association with fine-grained pyrite which was intergrown with lesser realgar and orpiment. These veinlets were formed from almost equally saline (1.2–14 wt.% NaCl equiv.) but significantly cooler (~100°C) fluids.

A synthesis of paragenetic, fluid inclusion, and stable isotope data revealed that the paragenetically-late intermediate-sulfidation epithermal mineralization was formed from progressive cooling and neutralization of magmatic fluids derived from the deeper porphyry environment. This is more evident in the early carbonate-sulfide veinlets, whereas some mixing with meteoric fluids possibly occurred during formation of the later sooty pyrite veinlets.

The sealing effect provided by the now-eroded Munzur limestone and the shallow emplacement of the porphyry system at the base of this carbonate succession were particularly effective for the localization of Au mineralization at Çöpler. Rapid cooling of the magmatic-hydrothermal system and unroofing of the Çöpler window resulted in significant telescoping of the porphyry and epithermal assemblages, and were also critical for the locally-deep supergene oxidation of Au mineralization. Such a close relationship between porphyry and intermediate-sulfidation epithermal mineralization styles is not unique to Çöpler, and is commonly observed in many districts including the Baguio and Mankayan districts in Philippines and in the El Indio and Maricunga belts in Chile.

4.12 References

Adamia S, Bergougnan H, Fourquin C, Haghipour A, Lordkipanidze M, Özgül N, Ricou LE, Zakariadze G (1980) The Alpine Middle East between the Aegean and the Oman traverses: 26th International Geological Congress, Paris, C5, p. 122–136.

Akay E, Erkan E, Ünay E (1989) Muş Tersiyer havzasının stratigrafisi. Bull Min Res Explor Inst Turkey (MTA) 109:59–76 (in Turkish).

Akay E (1989) Evolution of the post-collisional cratonic basins in eastern Taurus: Bulletin of Mineral Research and Exploration Institute of Turkey (MTA), 109:53–64.

Albinson T, Norman DI, Cole D, Chomiak B (2001) Controls on formation of low-sulfidation epithermal deposits in Mexico: Constraints from fluid inclusion and stable isotope data: Soc Econ Geol Spec Publ 8:1–32.

Alderton DHM, Fallick AE (2000) The nature and genesis of gold-silver-tellurium mineralization in the Metaliferi Mountains of western Romania. Econ Geol 95:495–515.

Arancibia O, Clark AH (1996) Early magnetite-amphibole-plagioclase alteration-mineralization in the Island Copper porphyry copper-gold-molybdenum deposit, British Columbia. Econ Geol 91: 402–438.

Beane RE, Bodnar RJ (1995) Hydrothermal Fluids and Hydrothermal Alteration in Porphyry Copper Deposits In: Pierce, FW and Bohm JG (eds.) Porphyry Copper Deposits of the American Cordillera. Arizona Geol Soc Digest 20, Tuscon, AZ, p. 83–93.

Becker SP, Fall A, Bodnar RJ (2008) Synthetic fluid inclusions. XVII. PVTX properties of high salinity H_2O–NaCl solutions (>30 wt.% NaCl): application to fluid inclusions that homogenize by halite disappearance from porphyry copper and other hydrothermal ore deposits. Econ Geol 103:539–554.

Benning LG, Seward TM (1996) Hydrosulfide complexing of Au (I) in hydrothermal solutions from 150–400°C and 500–1500 bar. Geochim Cosmochim Acta 60:1849–1871.

Bodnar RJ (1993) Revised equation and table for determining the freezing point depression of H_2O-NaCl solutions. Geochim Cosmochim Ac 57:683–684.

Bodnar RJ (1994) Synthetic fluid inclusions: XII. The system H_2O–NaCl. Experimental determination of the halite liquidus and isochores for a 40 wt% NaCl solution. Geochim Cosmochim Acta 58:1053–1063.

Bodnar RJ, Burnham CW, Sterner M (1985) Synthetic fluid inclusions in natural quartz. III. Determination of phase equilibrium properties in the system H_2O-NaCl to 1000°C and 1500 bars. Geochim Cosmochim Acta 49:1861–1873.

Bodnar RJ, Sterner SM, Hall DL (1989) SALTY: a Fortran program to calculate compositions of fluid inclusions in the system NaCl–KCl–H2O. Computers Geosci 15:19–41.

Bodnar RJ, Vityk MO (1994) Interpretation of Microtermometric data for H_2O-NaCl fluid inclusions. In: de Vivo D, Frezzotti ML (eds) Fluid Inclusions in Minerals, Virginia Tech, Blacksburg, VA, p. 117–130.

Boulton SJ (2009) Record of Cenozoic sedimentation from the Amanos Mountains, Southern Turkey: Implications for inception and evolution of the Arabia–Eurasia continental collision. Sediment Geol 216:29–47.

Boztuğ D, Harlavan Y, Arehart GB, Satır M, Avcı N (2007) K-Ar age, whole-rock and isotope geochemistry of A-type granitoids in the Divriği-Sivas region, eastern-central Anatolia, Turkey. Lithos 97:193–218.

Boztuğ D, Kuşcu İ, Erçin Aİ, Avcı N, Şahin SY (2003) Mineral deposits associated with the pre-, syn- and post-collisional granitoids of the NeoTethyan convergence system between the Eurasian and Anatolian plates in NE and central Turkey. Mineral Exploration and Sustainable Development, 7th Biennial SGA Meeting, Athens, Greece, August 24–28, 2003, Proceedings, p. 1141.

Cihnioğlu M, Isbasarir O, Ceyhan U, Adiguzel O (1994) Iron inventory of Turkey. Ankara, MTA Publication, 408 p. (in Turkish).

Claveria RJR (2001) Mineral paragenesis of the Lepanto copper and gold and the Victoria gold deposits, Mankayan mineral district, Philippines. Resource Geology 51:97–106.

Clayton RN, O'Neil J., Mayeda TK (1972) Oxygen isotope exchange between quartz and water. J. Geophys. Res. 77:3057–3067.

Cline JS, Bodnar RJ (1994) Direct evolution of brine from a crystallizing silicic melt at the Questa, New Mexico, molybdenum deposit. Econ Geol 89: 1780–1802.

Cooke DR, Bloom MS (1990) Epithermal and subjacent porphyry mineralization, Acupan, Baguio District, Philippines: a fluid-inclusion and paragenetic study. J Geochem Expl 35:297–340.

Cooke DR, Simmons SF (2000) Characteristics and genesis of epithermal gold deposits. Rev. Econ. Geol. 13:221–244.

Cooke DR, Deyell CL, Waters PJ, Gonzales RI, Zaw K (2011) Evidence for magmatic-hydrothermal fluids and ore-forming processes in epithermal and porphyry deposits of the Baguio District, Philippines. Econ Geol 106:1399–1424.

Dewey JF, Hempton MR, Kidd WSF, Şaroğlu F, Şengör AMC (1986) Shortening of continental lithosphere: the neotectonics of Eastern Anatolia – a young collision zone. In: Coward MP, Ries AC (eds) Collision Tectonics. Geol Soc Lond Spec Publ 19:3–36.

Dhont D, Chorowicz J, Luxey P (2006) Anatolian escape tectonics driven by Eocene crustal thickening and Neogene-Quaternary extensional collapse in the eastern Mediterranean region. In: Dilek Y, Pavlides S (eds) Postcollisional Tectonics and Magmatism in the Mediterranean Region and Asia. Geol Soc Am Spec Pap 409:441–462.

Driesner T (2007) The system H_2O-NaCl. Part II: Correlations for molar volume, enthalpy and isobaric heat capacity from 0 to 1000°C, 1 to 5000 bar, and 0 to 1 X_{NaCl}. Geochim Cosmochim Acta 71:4902–4919.

Driesner T, Heinrich CA (2007) The system H_2O-NaCl. Part I: Correlation formulae for phase relations in temperature-pressure-composition space from 0 to 1000°C, 1 to 5000 bar, and 0 to 1 X_{NaCl}. Geochim Cosmochim Acta 71:4880–4901.

Dumanlılar H, Aydal D, Dumanlılar Ö (1999) Geology, mineralogy and geochemistry of sulfide mineralization in the Ispendere region (Malatya). Bull Min Res Explor Inst Turkey (MTA) 121:57–82.

Elmas A (1994) An example of the active continental margin volcanism in the Late Lutetian–Late Oligocene interval in southeast Anatolia: Gövelek volcanics (Van-Erçek). Turk J Earth Sci 3:43–54.

Elmas A, Yılmaz Y (2003) Development of an oblique subduction zone – tectonic evolution of the Tethys suture zone in southeast Turkey. Int Geol Rev 45:827–840.

Erler (1989) Geochemical character of the hydrothermal alteration zones around the Madenkoy-Siirt massive sulfide deposit and implications of geochemical exploration. J Geochem Explor 32:405–407.

Erler A (1984) Tectonic setting of the massive sulfide deposits of the southeast Anatolian thrust belt. In: Tekeli O, Göncüoğlu MC (eds) Geology of the Taurus Belt. Proceedings of the International Tauride Symposium. Mineral Research and Exploration Institute of Turkey (MTA) Publications, Ankara, Turkey, pp 309–316.

Fornadel AP, Voudoris PCh, Spry PG, Melfos V (2012) Mineralogical, stable isotope, and fluid inclusion studies of spatially related porphyry Cu and epithermal Au-Te mineralization, Fakos Peninsula, Limnos Island, Greece. Miner Petrol 105:85–111.

Fournier RO (1999) Hydrothermal processes related to movement of fluid from plastic into brittle rock in the magmatic-epithermal environment. Econ Geol 94:1193–1211.

Giggenbach WF (1992) Isotopic shifts in waters from geothermal and volcanic systems along convergent plate boundaries and their origin. Earth Planet Sc Lett 113:495–510.

Göğüş OH, Pysklywec RN (2008) Mantle lithosphere delamination driving plateau uplift and synconvergent extension in eastern Anatolia. Geology 36:723–726.

Goldstein R.H. and Reynolds T.J. (1994) Systematics of fluid inclusions in diagenetic minerals: Society for Sedimentary Geology Short Course 31, 199 pp.

Gücer MA, Aslan Z (2014) ^{40}Ar-^{39}Ar age, petrography and geochemistry of the Yoncayolu Metamorphic Rocks (NE Turkey): Subduction-related metamorphism under greenschist facies conditions. J Min Geochem 191, 257–276.

Guest B, Matthews WA (2011) A reassessment of the timing of the Arabia-Eurasia collision with regional and global implications. Geological Society of America Annual Meeting Abstracts with Programs 43, no.5, 141.

Gustafson LB, Hunt JP (1975) The porphyry copper deposit at El Salvador, Chile. Econ Geol 70:857–912.

Harris AC, Golding SD (2002) New evidence of magmatic-fluid-related phyllic alteration: Implications for the genesis of porphyry Cu deposits. Geology 30: 335-338.

Hayba DO, Bethke PM, Heald P, Foley NK (1985) Geologic, mineralogic, and geochemical characteristics of volcanic-hosted epithermal precious metal deposits. Reviews in Economic Geology 2:129–167.

Heinrich CA, Neubauer F (2002) Cu – Au – Pb – Zn – Ag metallogeny of the Alpine – Balkan – Carpathian – Dinaride geodynamic province. Miner Deposit 37:533–540.

Hetzel R, Reischmann T (1996) Intrusion age of Pan-African augen gneisses in the southern Menderes massif and age of cooling after Alpine ductile extensional deformation. Geol Mag 133:565–572.

Hüsing SK, Zachariasse W-J, van Hinsbergen DJJ, Krijgsman W, İnceöz M, Harzhauser M, Mandic O, Kroh A (2009) Oligocene–Miocene basin evolution in SE Anatolia, Turkey: constraints on the closure of the eastern Tethys gateway. In: van Hinsbergen DJJ, Edwards MA, Gowers R (eds) Collision and Collapse at the Africa-Arabia-Eurasia Subduction Zone. Geol Soc Lond Spec Publ 311:107–132.

İmer A, Richards JP, Creaser RA (2013) Age and tectonomagmatic setting of the Çöpler-Kabataş magmatic complex and porphyry-epithermal Au deposit, east central Anatolia, Turkey. Miner Deposit 48:557–583.

İmer A, Richards JP, Creaser RA, Spell TL (2014) The Late Oligocene Cevizlidere Cu-Au-Mo deposit, Tunceli Province, eastern Turkey. Miner Deposit, in press.

Ishihara, S., and Sasaki, A., 1989, Sulfur isotopic ratios of the magnetite-series and ilmenite-series granitoids of the Sierra Nevada batholith—a reconnaissance study: Geology, v. 17, p. 788–791.

Janković S (1977) The copper deposits and geotectonic setting of the Tethyan Eurasian Metallogenic Belt. Miner Deposita 12:37–47.

Janković S (1997) The Carpatho-Balkanides and adjacent area: a sector of the Tethyan Eurasian metallogenic belt. Miner Deposit 32:426–433.

Karaoğlan F, Parlak O, Robertson A, Thöni M, Klötzli U, Koller F, Okay Aİ (2013) Evidence of Eocene high-temperature/high-pressure metamorphism of ophiolitic rocks and granitoid intrusion related to Neotethyan subduction processes (Dogansehir area, SE Anatolia). In: Robertson AHF, Parlak O, Ünlügenç UC (eds) Geological Development of Anatolia and the Easternmost Mediterranean Region. Geol Soc Lond Spec Publ 372:249–272.

Kaymakçı N, İnceöz M, Ertepınar P (2006) 3D-architecture and Neogene evolution of the Malatya Basin: Inferences for the kinematics of the Malatya and Ovacık Fault Zones. Turk J Earth Sci 15:123–154.

Kaymakçı N, İnceöz M, Ertepınar P, Koç A (2010) Late Cretaceous to Recent kinematics of SE Anatolia (Turkey). In: Sosson M, Kaymakçı N, Stephenson RA, Bergerat F, Starostenko V (eds) Sedimentary Basin Tectonics from the Black Sea and Caucasus to the Arabian Platform. Geol Soc Lond Spec Publ, 340:409–435.

Keskin M (2003) Magma generation by slab steepening and breakoff beneath a subduction-accretion complex: An alternative model for collision-related volcanism in Eastern Anatolia, Turkey. Geophys Res Lett 30:8046. doi:10.1029/2003GL018019.

Klemm LM, Pettke T, Heinrich CA (2008) Fluid and source magma evolution of the Questa porphyry Mo deposit, New Mexico, USA. Miner Deposit 43:533–552.

Koçyiğit A, Beyhan A (1998) A new intracontinental transcurrent structure: the Central Anatolian Fault Zone, Turkey. Tectonophysics 284:317–336.

Kouhestani H, Ghaderi M, Chang Z, Zhaw K (2013) Constraints on the ore fluids in the Chah Zard breccia-hosted epithermal Au–Ag deposit, Iran: Fluid inclusions and stable isotope studies. Ore Geol Rev, doi:10.1016/j.oregeorev.2013.06.003.

Kröner A, Şengör AMC (1990) Archean and Proterozoic ancestry in late Precambrian to early Paleozoic crustal elements of southern Turkey as revealed by single-zircon dating. Geology 18:1186–1190.

Kürüm S, Önal A, Boztuğ D, Spell T, Arslan M (2008) ^{40}Ar/^{39}Ar age and geochemistry of the post-collisional Miocene Yamadağ volcanics in the Arapkir area (Malatya Province), eastern Anatolia, Turkey. J Asian Earth Sci 33:229–251.

Kusakabe M, Robinson BW (1977) Oxygen and sulfur isotope equilibria in the BaSO4-HSO4-H2O system from 110 to 350ºC and applications. Geochim Cosmochim Ac 41:1033–1040.

Kuşcu İ, Erler A (1998) Mineralization events in a collision-related setting: the Central Anatolian Crystalline Complex, Turkey. Int Geol Rev 40: 552–565.

Kuşcu İ, Gençalioğlu-Kuşcu G, Tosdal RM (2007) Tectonomagmatic-metallogenic framework of mineralization events in the southern NeoTethyan arc, southeastern Turkey. In: Andrew CJ et al (eds) Digging Deeper. Proceedings of the 9th Biennial SGA Meeting, Dublin, 20-23 August 2007, p. 853–856.

Kuşcu İ, Gençalioğlu-Kuşcu G, Tosdal RM, Ulrich TD, Friedman R (2010) Magmatism in the southeastern Anatolian orogenic belt: transition from arc to post-collisional setting in an evolving orogen. In: Sosson M, Kaymakçı N, Stephenson RA, Bergerat F, Starostenko V (eds) Sedimentary Basin Tectonics from the Black Sea and Caucasus to the Arabian Platform. Geol Soc Lond Spec Publ 340:437–460.

Kuşcu İ, Tosdal RM, Gençalioğlu-Kuşcu G, Friedman R, Ullrich TD (2013) Late Cretaceous to Middle Eocene Magmatism and Metallogeny of a Portion of the Southeastern Anatolian Orogenic Belt, East-Central Turkey. Econ Geol 108:641–666.

Kuşcu İ, Yılmazer E, Güleç N, Bayır S, Demirela G, Gençalioğlu-Kuşcu G, Sezerer Kuru G, Kaymakçı N (2011) U-Pb and 40Ar-39Ar geochronology and isotopic constraints on the genesis of copper-gold-bearing iron oxide deposits in the Hasançelebi district, eastern Turkey. Econ Geol 106:261–288.

Landtwing MR, Furrer C, Redmond PB, Pettke T, Guillong M, Heinrich CA (2010) The Bingham Canyon porphyry Cu-Mo-Au deposit. III. Zoned copper-gold ore deposition by magmatic vapor expansion. Econ Geol 105:91–118.

Lecumberri-Sanchez P., Steele-MacInnis M, Bodnar RJ (2012) A numerical model to estimate trapping conditions of fluid inclusions that homogenize by halite disappearance. Geochim Cosmochim Acta 92:14–22.

Leo, GW, Marwin RF, Mehnert HH (1974) Geologic framework of the Kuluncak-Sofular area, east central Turkey, and K-Ar ages of igneous rocks. Geol Soc Am Bull 85:1785–1788.

Lickfold V, Cooke DR, Smith SG, Ullrich TD (2003) Endeavour copper-gold porphyry deposits, Northparkes, New South Wales: intrusive history and fluid evolution. Econ Geol 98:1607–1636.

Lowell JD, Guilbert JM (1970) Lateral and vertical alteration-mineralization zoning in porphyry ore deposits. Econ Geol 65:373–408.

Marchev P, Singer B (2002) ^{40}Ar/^{39}Ar geochronology of magmatism and hydrothermal activity of the Madjarovo base–precious metal ore district, eastern Rhodopes, Bulgaria. In: Blundell DJ, Neubauer F, von Quadt A (eds) The Timing and Location of Major Ore Deposits in an Evolving Orogen. Geol Soc Lond Spec Publ 204:137–150.

Marchev P, Downes H, Thirlwall MF, Mortiz R (2002) Small-scale variations of ^{87}Sr/^{86}Sr isotope composition of barite in the Madjarovo low-sulphidation epithermal system, SE Bulgaria: implications for sources of Sr, fluid fluxes and pathways of the ore-forming fluids. Mineral Deposit 37:669–677.

Marchev P, Kaiser-Rohrmeier M, Heinrich C, Ovtcharova M, von Quadt A, Raicheva R (2005) 2: Hydrothermal ore deposits related to post-orogenic extensional magmatism and core complex formation: The Rhodope Massif of Bulgaria and Greece. Ore Geol Rev 27:53–89.

Marinov D, Barra F, Alizade F (2011) Re-Os dating of molybdenite mineralisation from Turkish porphyry copper prospects. In: Let's Talk Ore Deposits, Proceedings of 11th Biennial SGA Meeting, Antofagasta (Chile), 26–29 September 2011.

McInnes BIA, Crocket JH, Goodfellow WD, The Laforma deposit, an atypical epithermal-Au system at Freegold Mountain, Yukon Territory, Canada. L Geochem Expl 36:73–102.

Michard A, Whitechurch H, Ricou LE, Montigny R, Yazgan E (1984) Tauric subduction (Malatya-Elazığ provinces) and its bearing on tectonics of the Tethyan realm in Turkey. In: Dixon JE, Robertson AHF (eds) The Geological Evolution of the Eastern Mediterranean. Geol Soc Lond Spec Publ 17:361–373.

MTA (1989) Geologic map of Turkey. Ankara, MTA, scale 1:2,000,000.

MTA (2002a) Geologic map of Turkey (Sivas Quadrangle). Ankara, MTA, scale 1:500,000.

Muntean JL, Einaudi MT (2001) Porphyry-epithermal transition: Maricunga Belt, northern Chile. Econ Geol 96:743–772.

Ohmoto H (1986) Stable isotope geochemistry of ore deposits. In *Reviews in Mineralogy* 16 (Stable Isotopes), 491–559. Blacksburg, Virginia: Min. Soc. Am.

Ohmoto H, Lasaga AC (1982) Kinetics of reactions between aqueous sulfates and sulfides in hydrothermal systems. Geochim Cosmochim Acta 46:1727–1745.

Ohmoto H, Rye RO (1979) Isotopes of sulfur and carbon. In: Barnes, H.L. (ed), Geochemistry of Hydrothermal Ore Deposits, 2nd ed. Wiley, New York, p. 509–567.

Okay Aİ, Tüysüz O (1999) Tethyan sutures of northern Turkey. In: Durand B, Jolivet L, Horvath F, Seranne M (eds) Mediterranean Basins: Tertiary Extension within the Alpine Orogen. Geol Soc Lond Spec Publ 156:475–515.

Okay Aİ, Zattin M, Cavazza W (2010) Apatite fission-track data for the Miocene Arabia-Eurasia collision. Geology 38:35–38.

Önal A, Boztuğ D, Kürüm S, Harlavan Y, Arehart GB, Arslan M (2005) K-Ar age determination, whole-rock and oxygen isotope geochemistry of the post-collisional Bizmişen and Çaltı plutons, SW Erzincan, eastern Central Anatolia, Turkey. Geol J 40:457–476.

Oyman T, Minareci F, Piskin O (2003) Efemcukuru B-rich epithermal gold deposit (Izmir, Turkey). Ore Geol Rev 23:35–53.

Özer E (1994) Stratigraphy of the Munzur mountains (Kemah-İliç-Erzincan). Bull Geol Soc Turk 37:53–64 (in Turkish with English abstract).

Özer E (2004) Stratigraphical evidence for the depression of the northern margin of the Menderes–Tauride Block (Turkey) during the Late Cretaceous. J Asian Earth Sci 22:401–412.

Özer E, Öner F (1999) Geochemical characteristics and tectonic interpretation of the Yakuplu Pluton in the northeastern Taurid Mountains, eastern Turkey. Chemie Erde 59:173–182. (in German with English abstract)

Özgenç İ, İlbeyli N (2009) Geochemical constraints on petrogenesis of Late Cretaceous alkaline magmatism in east-central Anatolia (Hasançelebi-Başören, Malatya), Turkey. Miner Petrol 95:71–85.

Özgül N, Turşucu A (1984) Stratigraphy of the Mesozoic carbonate sequence of the Munzur Mountains (Eastern Turkey). In: Tekeli O, Göncüoğlu MC (eds) Geology of the Taurus Belt. Proceedings of the International Tauride Symposium. Mineral Research and Exploration Institute of Turkey (MTA) Publications, Ankara, Turkey, pp 173–180.

Özgül N, Turşucu A, Özyardımcı N, Şenol M, Bingöl İ, Uysal S (1981) Munzur dağlarının jeolojisi. Min Res Explor Inst Turkey (MTA) Report 6995, Ankara (unpublished).

Palmer MR, Helvaci C, Fallick AE (2004) Sulphur, sulphate oxygen and strontium isotope composition of Cenozoic Turkish evaporites. Chem Geol 209:341–356.

Parlak O (2006) Geodynamic significance of granitoid magmatism in the southeast Anatolian orogen: geochemical and geochronological evidence from Göksun-Afşin (Kahramanmaraş, Turkey) region. Int J Earth Sci 95:609–627.

Pearce JA, Bender JF, De Long SE, Kidd WSF, Low PJ, Güner, Saroglu F, Yilmaz Y, Moorbath S, Mitchell JG (1990) Genesis of collision volcanism in Eastern Anatolia, Turkey. J Volcanol Geoth Res 44:189–229.

Perelló J, Carlotto V, Zárate A, Ramos P, Posso H, Neyra C, Caballero A, Fuster N, Muhr R (2003) Porphyry-style alteration and mineralization of the middle Eocene to early Oligocene Andahuaylas-Yauri Belt, Cuzco Region, Peru. Econ Geol 98:1575–1605.

Proffett JM (2003) Geology of the Bajo de la Alumbrera porphyry copper-gold deposit, Argentina. Econ Geol 98:1535−1574.

Rice SP, Robertson AHF, Ustaömer T, İnan N, Tasli K (2009) Late Cretaceous–Early Eocene tectonic development of the Tethyan suture zone in the Erzincan area, Eastern Pontides, Turkey. Geol Mag 146:567–590.

Richards JP (2003a) Metallogeny of the Neo-Tethys arc in central Iran. In: Eliopoulos DG et al (eds) Proceedings of Mineral Exploration and Sustainable Development. Millpress, Rotterdam, pp 1237–1239.

Richards JP (2003b) Tectono-magmatic precursors for porphyry Cu-(Mo-Au) deposit formation. Econ Geol 98:1515–1533.

Richards JP, Spell T, Rameh E, Razique A, Fletcher T (2012) High Sr/Y magmas reflect arc maturity, high magmatic water content, and porphyry Cu ± Mo ± Au potential: examples from the Tethyan arcs of central and eastern Iran and western Pakistan. Econ Geol 107:295–332.

Rızaoğlu T, Parlak O, Höck V, Koller F, Hames WE, Billor Z (2009) Andean-type active margin formation in the eastern Taurides: geochemical and geochronological evidence from the Baskil granitoid (Elazığ, SE Turkey). Tectonophysics 473:188–207.

Robertson AHF, Parlak O, Metin Y, Vergili Ö, Taslı K, İnan N, Soycan H (2013) Late Palaeozoic–Cenozoic tectonic development of carbonate platform, margin and oceanic units in the Eastern Taurides, Turkey. In: Robertson AHF, Parlak O, Ünlügenç UC (eds) Geological Development of Anatolia and the Easternmost Mediterranean Region. Geol Soc London Spec 372:167–218.

Robertson AHF, Parlak O, Rızaoğlu T, Ünlügenç Ü, İnan N, Taşlı K, Ustaömer T (2007) Tectonic evolution of the South Tethyan ocean: evidence from the Eastern Taurus Mountains (Elazığ region, SE Turkey). In: Ries AC, Butler RWH, Graham RH (eds) Deformation of the Continental Crust: The Legacy of Mike Coward. Geol Soc Lond Spec Publ 272:231–270.

Roedder E (1984) Fluid inclusions. Rev Mineral, vol. 12, 644 p.

Rusk BG, Reed MH, Dilles JH (2008) Fluid inclusion evidence for magmatic-hydrothermal fluid evolution in the porphyry copper-molybdenum deposit at Butte, Montana. Econ Geol 103:307–334.

Seedorff E, Einaudi MT (2004) Henderson porphyry molybdenum system, Colorado: II. decoupling of introduction and deposition of metals during geochemical evolution of hydrothermal fluids. Econ Geol 99:39–72.

Şengör AMC, Yılmaz Y (1981) Tethyan evolution of Turkey: a plate tectonic approach. Tectonophysics 75:181–241.

Sillitoe RH (1997) Characteristics and controls of the largest porphyry copper-gold and epithermal gold deposits in the circum-Pacific region. Australian Journal of Earth Sciences 44:373–388.

Sillitoe RH (2010) Porphyry copper systems. Econ Geol 105:3–41.

Sillitoe RH, Hedenquist JW (2003) Linkages between volcanotectonic settings, ore-fluid compositions, and epithermal precious metal deposits. Soc Econ Geol Spec Publ 10:315–343.

Sillitoe RH, Hall DJ, Redwood, SD, Waddell AH (2006) Pueblo Viejo high-sulfidation epithermal gold-silver deposit, Dominican Republic: a new model of formation beneath barren limestone cover. Econ Geol 101:1427–1435.

Simmons SF (1991) Hydrologic implications of alteration and fluid inclusion studies in the Fresnillo district, Mexico: Evidence for a brine reservoir and a descending water table during the formation of hydrothermal Ag-Pb-Zn orebodies. Econ Geol 86: 1579–1601.

Simmons SF, Browne PRL (1997) Saline fluid inclusions in sphalerite from the Broadlands-Ohaaki geothermal system: a coincidental trapping of fluids being boiled towards dryness. Econ Geol 92:485–489.

Simmons SF, White NC, John DA (2005) Geological characteristics of epithermal precious and base metal deposits. Economic Geology 100th Anniversary Volume: 485–522.

Singer DA, Mosier DL, Menzie WD (1993) Digital grade and tonnage data for 50 types of mineral deposits. U.S. Geolological Survey open-file report, no. 93-280, 102 p.

Sterner SM (1992) Homogenization of fluid inclusions to the vapor phase: the apparent homogenization phenomenon. Econ Geol 87:1616–1623.

Sterner SM, Hall DL, Bodnar RJ (1988) Synthetic fluid inclusions. V. Solubility reactions in the system NaCl-KCl-H_2O under vapor-saturated conditions. Geochimica et Cosmochimica Acta 52:989–1005.

Taylor HP Jr. (1974) The application of oxygen and hydrogen isotope studies to problems of hydrothermal alteration and ore deposition. Econ Geol 69:843–883.

Taylor BE (1987) Stable isotope geochemistry of low-temperature fluids. Mineral Assoc Can Shourt Course Series 13:337–445.

Tekin E (2001) Stratigraphy, geochemistry and depositional environment of the celestine-bearing gypsiferous formation of the Tertiary Ulaş-Sivas Basin, east-central Anatolia (Turkey). Turkish J Earth Sci 10:35–49.

Tekin E, Varol B, Ayan Z, Satir M (2002) Epigenetic origin of celestite deposits in the Tertiary Sivas Basin: new mineralogical and geochemical evidence. Neues Jb Miner Monat 7:289–318.

Tunç M, Özçelik O, Tutkun Z, Gökçe A (1991) Basic geological characteristics of the Divriği-Yakuplu-İliç-Hamo (Sivas) area. Turk J Eng Environ Sci 15:225–245 (in Turkish with English abstract).

Tüysüz N, Sadıklar B, Er M, Yılmaz Z (1995) An epithermal gold-silver deposit in the Pontide island arc, Mastra Gümüşhane, northeast Turkey. Econ Geol 90:1301–1309.

Ulrich T, Heinrich CA (2002) Geology and alteration geochemistry of the porphyry Cu-Au deposit at Bajo de la Alumbrera, Argentina. Econ Geol 97:1865–1888.

von Quadt, Moritz R, Peytcheva I, Heinrich CA (2005) 3: Geochronology and geodynamics of Late Cretaceous magmatism and Cu–Au mineralization in the Panagyurishte region of the Apuseni–Banat–Timok–Srednogorie belt, Bulgaria. Ore Geol Rev 27:95–126.

Wallier S, Rey R, Kouzmanov K, Pettke T, Heinrich CH, Leary S, O'Connor G Tamas CG, Vennemann T, Ullrich T (2006) Magmatic fluids in the breccia-hosted epithermal Au-Ag deposit of Rosia Montana, Romania. Econ Geol 101:923–954.

White WH, Bookstrom AA, Kamilli RJ, Ganster MW, Smith RP, Ranta DE, Steininger RC (1981) Character and origin of Climax-type molybdenum deposits. Econ Geol 75th Anniv. Vol, 270–316.

Yazgan E (1984) Geodynamic evolution of the Eastern Taurus region In: Tekeli O, Göncüoğlu MC (eds) Geology of the Taurus Belt. Proceedings of the International Tauride Symposium. Mineral Research and Exploration Institute of Turkey (MTA) Publications, Ankara, Turkey, pp 199–208.

Yazgan E, Chessex R (1991) Geology and tectonic evolution of Southeastern Taurus in the region of Malatya. Turk Assoc Petrol Geol Bull 3:1–42.

Yiğit Ö (2009) Mineral deposits of Turkey in relation to Tethyan metallogeny: implications for future mineral exploration. Econ Geol 104:19–51.

Yılmaz Y (1993) New evidence and model on the evolution of Southeast Anatolian orogen. Geol Soc Am Bull 105:251–271.

Yılmaz H, Oyman T, Sonmez FN, Arehart GB, Billor Z (2010) Intermediate sulfidation epithermal gold-base metal deposits in Tertiary subaerial volcanic rocks, Sahinli/Tespih Dere (Lapseki/Western Turkey). Ore Geol. Rev. 37:236–258.

Zeck HP, Ünlü T (1991) Shoshonitic, monzonitic pluton near Murmano, eastern Central Turkey–a preliminary note. Mineral Res Explor Bull 112:47–58.

CHAPTER 5: Conclusions

Major findings of this project relating to the regional tectonic and magmatic controls involved in formation of the Çöpler and Cevizlidere deposits, and conditions of porphyry-epithermal mineralization at Çöpler are as follows:

- The shallow-level intrusive rocks of the Çöpler-Kabataş magmatic complex were emplaced into a succession of Paleozoic–Mesozoic metasedimentary and Mesozoic carbonate rocks along the northern section of the Munzur Mountains in central eastern Anatolia.

- Combined ^{40}Ar/^{39}Ar and Re-Os data revealed that emplacement of the precursor plutons took place at ~44 Ma, closely followed by porphyry-style alteration and mineralization. This suggests rapid cooling of the magmatic-hydrothermal system in ≤1 m.y., consistent with the simple intrusive history and shallow depth of emplacement.

- Magmatism and porphyry-epithermal Au-(Cu) mineralization at Çöpler coincided with a period of transtension, which commenced in the latest Mesozoic–early Paleogene as a result of roll-back of the northward subducting Southern Neotethys slab. This transtensional period led to initiation of a series of ENE-trending regional structural zones (e.g., the Göksu-Yazyurdu and Central Anatolian Fault Zones; Fig. 2.1), which allowed focussing of shallow-level magmatism. The Çöpler North and South Faults, defining the main Çöpler window, follow the same regional fabric, and therefore, are inferred to have initiated prior to formation of the Çöpler deposit.

- The Cevizlidere porphyry Cu-Mo-Au deposit was formed along the southern margin of the same mountain range, also during a period of extension, possibly relating to breaking off of the Southern Neotethys slab. The source granodiorite porphyry at Cevizlidere was dated at ~25.5 Ma, and porphyry mineralization developed at ~25 Ma, suggesting a short-lived magmatic-hydrothermal system (≤0.7 m.y) similar to Çöpler.

- The intrusive rocks at Çöpler and Cevizlidere are geochemically very similar to each other as both magmatic suites are composed of calc-alkaline, LILE- and LREE-enriched and relatively MREE- and HREE-depleted rocks derived from hydrous and oxidized magmas. These overall geochemical characteristics resemble magmas that are generated in subduction-related settings. However, given its distal positioning relative to the contemporaneous Maden-Helete volcanic arc system, the Çöpler deposit is interpreted to have formed in an incipient back-arc setting to the north of the Southern Neotethys subduction zone. A similar tectonic setting is also inferred for the Cevizlidere deposit, which closely predated the Arabia–Eurasia continent-continent collision.

- Although early porphyry Cu-Au mineralization at Çöpler is subeconomic, its Au-rich nature and tectonic setting resembles some giant porphyry Cu-Au systems such as Bajo de la Alumbrera (Argentina) and Bingham Canyon (USA). This may have implications for future exploration of similar Au-rich porphyry systems, not only in central eastern Turkey, but also in the adjacent orogenic belts in southeastern Europe and in northwest Iran.
- The Cevizlidere deposit, on the other hand, may be correlated with some Oligocene–Miocene porphyry-epithermal systems in Iran such as the Dalli porphyry Cu-Au, and the Darreh-Zerreshk and Ali-Abad porphyry Cu deposits as well as the deposits located within the Kerman porphyry belt.
- Three major hypogene mineralization styles have been identified in the Copler Au deposit:
    - Early porphyry-style Cu-Au mineralization developed mainly in the central granodiorite porphyry
    - Overprinting low-temperature epithermal Au mineralization
    - Manto-type carbonate-replacement orebodies
- The early potassic alteration (biotite-magnetite-K-feldspar) is associated with hairline magnetite and crosscutting B-type quartz ± magnetite ± sulfide veinlets. The latter vein group generated low-grade Cu-Au mineralization, and is interpreted to have formed from immiscible brine (~47–62 wt.% NaCl equiv.) and vapor (~3–5.5 wt.% NaCl equiv.) exsolved from a cooling magma at temperatures of ~390°C. The depth of entrapment of these fluids is estimated as ~1.5 km.

- These fluids evolved to slightly lower temperature (~370° ± 20°C) and lower salinity (~37–45 wt.% NaCl equiv.) fluids upon further cooling, forming an extensive phyllic alteration halo around the potassically-altered core. Abundant D-type quartz-pyrite and less abundant polymetallic quartz-sulfide veinlets formed during this stage.

- These earlier assemblages were overprinted by epithermal veinlets mainly in two stages. The bulk of the gold mineralization is associated by carbonate-sulfide veinlets in which gold occurs as submicroscopic grains mainly in arsenical pyrite as well as in arsenopyrite and tetrahedrite/tennantite. These veinlets were formed from moderate temperature (~290° ± 20°C) and moderate salinity (4–15 wt.% NaCl equiv.) fluids which were likely derived from earlier (slightly acidic) magmatic fluids as a result of progressive cooling and neutralization.

- The final stage of epithermal Au mineralization occurred in sooty pyrite veinlets consisting of abundant fine-grained pyrite (with submicroscopic gold) alongside with realgar and orpiment. Fluid inclusion data indicates much cooler (~100°C), low to moderate salinity (1.2–13.6 wt.% NaCl equiv.) fluids, possibly formed at near-surface conditions. Involvement of meteoric waters is evident for this stage as indicated by oxygen and carbon isotopic data.

- Manto-type carbonate-replacement ores predate the epithermal sooty pyrite veinlets but their timing could not be constrained accurately due to widespread post-mineral faulting and intense supergene oxidation throughout the deposit area. Nevertheless, they are inferred to have formed synchronously with either the early porphyry-style mineralization or with the epithermal carbonate-sulfide veinlets.

- Presence of low pH and moderate temperature/salinity fluids of magmatic origin in the main stage of epithermal mineralization is indicative of a typical intermediate-sulfidation system, which is also confirmed by the abundance of Mn-carbonate gangue and an ore assemblage consisting of chalcopyrite, sphalerite, tetrahedrite/tennantite. Porphyry and epithermal mineralization at Çöpler seem to be genetically linked, as is commonly observed elsewhere.

- Repeated fault reactivation has a major control over Au mineralization as ore fluids of discrete stages were channelized along favorable structural zones. The thick carbonate cover succession (now mostly eroded) may have acted as an effective barrier to the ascending reactive fluids, thus acting both as a neutralizing agent a pressure seal.

- Supergene oxidation of the porphyry-epithermal system following uplift and unroofing of the Çöpler window was critical for the locally high-grade nature of Au mineralization at Çöpler.

APPENDIX A:

Whole-rock, $^{40}Ar/^{39}Ar$, and Re-Os geochronological sample locations and descriptions

Sample	**Location**	**UTM Easting (WGS84-37S)**	**UTM Northing (WGS84-37S)**	**Drillhole: depth interval (m)**	**Description (based on field names)**
C-014	Çöpler-Kabataş	458661	4363576	CDD-003: 292.95-294.50	Hbl diorite porphyry (Çöpler Mn Mine Zone). Hbl-Plag phenocrysts within Plag-Qz groundmass. Hbl phenocrysts partially chloritized, Plag phenocrysts weakly sericitized. Sparse Ep-Carb-Mt in groundmass.
C-104	Çöpler-Kabataş	458753	4363430	CDD-014: 370.10-372.75	Granodiorite porphyry (Çöpler Main Zone). Abundant Hbl-Plag phenocrysts with lesser Biot grains. Qz-Plag-rich groundmass. Hb-Biot phenocrysts weakly chloritized along the rims. Sparse Ep-Carb-Mt present.
C-138	Çöpler-Kabataş	459831	4364348	CDD-064: 78.00-78.10	Hbl diorite porphyry (Çöpler Mn Mine Zone). Intense and pervasive Ser-Qz alteration. Late interstitial Carb with rare Fl. Euhedral Py common throughout together with less abundant sulfide phases (Cp, Gn, Sp, Tet/Ten).
C-161	Çöpler-Kabataş	458723	4363842	-	Qz-Cp-Py-Mo vein (Çöpler Main Zone). ~ 4 cm-thick vein with predominant coarse Qz crystals and lesser sulfides. Late infills of chalcedony and coarse/tabular Bar crystals also present.
C-162	Çöpler-Kabataş	458802	4363880	CDD-140: 180.00-180.10	Granodiorite porphyry (Çöpler Main Zone). Pervasive phyllic alteration with abundant Ser replacing Plag and other mafics. Qz and disseminated Py grains also common throughout. Crosscut by a Qz-Cp-Py-Mo veinlet (1–2 cm thick). Mo is present in substantial amounts in the veinlet.
C-163	Çöpler-Kabataş	457958	4366457	BHD-001: 101.90-105.30	Granodiorite porphyry (Çöpler Main Zone). Altered Hbl phenocrysts with Plag and rare Biot phenocrysts. Secondary Biot as pseudomorphs after Hbl. Late chloritization of Biot/Hbl. Plag phenocrysts weakly sericitized. Mt common throughout with rare Py-Cp.
C-164	Çöpler-Kabataş	458723	4363842	CDD-140: 106.00-106.20	Granodiorite porphyry (Çöpler Main Zone). Biot-Plag phenocrysts as well as clusters of small/anhedral secondary Biot grains. Plag phenocrysts are partially sericitized. Groundmass consists of Plag and Qz. Sparse Carb present. Disseminations of Py-Cp-Mt.
C-166	Çöpler-Kabataş	460072	4364353	CDD-159: 26.00-26.30	Hbl diorite porphyry (Çöpler Mn Mine Zone). Abundant Hbl and Plag phenocrysts. Hbl partially chloritized. Plag-Qz makes up bulk of the groundmass. Late Carb present both in the groundmass and also as veinlets. Py-Mt common throughout. Hem partially replacing Mt.
C-169	Çöpler-Kabataş	458723	4363842	CDD-140: 128.30-128.60	Granodiorite porphyry (Çöpler Main Zone). Hbl-Plag and minor Biot phenocrysts surrounded by Plag-Qz groundmass. Anhedral secondary Biot grains present. Plag phenocrysts weakly sericitized. Mt grains common throughout with lesser Py-Cp.
C-173	Çöpler-	458723	4363842	CDD-140:	Granodiorite porphyry (Çöpler Main Zone). Hbl-Plag-Biot phenocrysts within

	Kabataş			183.20-183.30	a Plag-Qz groundmass. Secondary anhedral Biot present. Biot grains commonly contain inclusions of Qz and partially altered to Chl. Plag phenocrysts weakly sericitized. Some Carb in the groundmass. Disseminated Py-Cp-Mt grains. Mt grains partially altered to Hem.
CR-01	Çöpler-Kabataş	461485	4365002	-	Qz diorite (boulder from the Waste Dam area). Equigranular with abundant Plag-Qz-Biot-Hbl phenocrysts. Biot and Hbl partially chloritized. Carb and Ep other alteration phases. Rare Mt and Py disseminated. Crosscut by epidote veinlets. Mafic xenoliths common.
CR-02	Çöpler-Kabataş	464761	4362274	-	Qz diorite (near Yakuplu village). Equigranular with abundant Plag-Qz-Biot-Hbl phenocrysts. Weakly chloritized rims of Biot and Hbl. Rare Carb, Ep, and Mt present. Relatively fresh compared to CR-01.
CR-03	Çöpler-Kabataş	467648	4356200	-	Diorite porphyry (Kabataş N). Unaltered. Porphyritic with Plag microcrysts and Plag-Cpx phenocrysts. Oscillatory zoning observed in Plag. Plag and Cpx phenocrysts occur as glomeroporphyritic clusters. Mt grains common throughout.
CR-05	Çöpler-Kabataş	466789	4355978	-	Granodiorite porphyry (from near Kabataş village). Few Plag-Biot phenocrysts are still partially intact. Intensely Ser-Chl altered Plag-Biot-(Hbl?) phenocrysts. Inclusions of Py-Mt in Biot phenocryst.
CR-07	Divriği	422307	4364732	-	Qz monzonite. Unaltered. Equigranular. Predominant Ksp-Qz-Hbl-Biot phenocrysts. Plag phenocrysts less abundant. Rare Mt present as partially hematized grains.
CR-08	Divriği South	396959	4346187	-	Qz monzonite. Unaltered. Equigranular. Ksp and Qz phenocrysts common throughout. Rare Plag and Biot phenocrysts present. Ksp phenocrysts commonly perthitic. Few grains of Hem observed.
CR-09	Divriği South	396959	4346187	-	Alkali feldspar granite dyke next to CR-08. Equigranular. Similar to CR-08 but smaller crystal size. Ksp grains are perthitic and weakly sericitized. Biot phenocrysts fresh. Sparse Hem grains present.
CR-10	Yamadağ	407237	4347905	-	Glassy, vesicular, Ol-Plag-phyric lava. Ol commonly altered to Idd. Ol-Plag phenocrysts within a matrix consisting of microcrysts of same minerals. Vesicles partly filled with sparse Carb. Mt microcrysts common throughout.
CR-11	Çaltı	445281	4356231	-	Tonalite. Unaltered. Equigranular. Consists of Qz and Plag phenocrysts. Less abundant Biot and Hbl in equal amounts. Rare Mt grains.
CR-12	Bizmişen	446382	4340356	-	Diorite. Unaltered. Equigranular with abundant Plag and brown Hbl phenocrysts. Rare Biot, Qz, and Mt.
CR-14	Çöpler-Kabataş	460177	4364452	-	Hbl diorite porphyry (Çöpler Mn Mine Zone). Abundant Plag-Hbl phenocrysts in a Plag-Qz groundmass. Plag phenocrysts partially sericitized and Hbl phenocrysts commonly chloritized. Ep-Carb in groundmass. Mt grains common.
CR-24	Doğanşehir	395319	4220805	-	Tonalite. Equigranular to porphyritic. Abundant Plag-Qz-Hbl with lesser Biot. Plag phenocrysts weakly sericitized. Sparse Mt present.

CR-28	Karamadazı	703821	4226225	-	Granite. Equigranular. Abundant Ksp and Qz phenocrysts with lesser Plag and Biot phenocrysts. Ksp commonly perthitic.
CR-31	Horoz	659869	4150565	-	Granodiorite. Unaltered. Equigranular to porphyritic. Plag-Ksp-Qz-Biot phenocrysts with lesser Qz microcrysts. Rare Mt grains throughout.

Abbreviations: Bar = barite, Biot = biotite, Carb = carbonate, Chl = chlorite, Cp = chalcopyrite, Cpx = clinopyroxene, Ep = epidote, Fl = fluorite, Gn = galena, Hbl = hornblende, Hm = hematite, Idd = iddingsite, Ksp = Potassium feldspar, Mo = molybdenite, Mt = magnetite, Ol = olivine, Plag = plagioclase, Py = pyrite, Qz = quartz, Ser = sericite, Sph = sphalerite, Tet/Ten = tetrahedrite/tennantite

APPENDIX B:

Major and trace element analyses of least altered and altered igneous rocks from the Çöpler-Kabataş magmatic complex and least altered igneous lithologies from the surrounding area

Sample no.		**C-014**	**C-104**	**C-163**	**C-164**	**C-166**	**C-169**	**C-173**	**CR-01**	**CR-02**
Lithology		Hbl Diorite Porphyry	Grd. Porphyry	Grd. Porphyry	Grd. Porphyry	Hbl Diorite Porphyry	Grd. Porphyry	Grd. Porphyry	Quartz Diorite	Quartz Diorite
Alteration		Least alt.	Least alt.	Alt. (prop)	Alt. (prop)	Alt. (prop)	Alt. (K)	Least alt.	Least alt.	Least alt.
Location		Çöpler-Kabataş								
Weight (%)	*Method (detection limit)*									
SiO_2	Fusion-ICP (0.01)	64.05	64.44	59.01	60.63	54.29	62.69	65.25	67.50	65.75
Al_2O_3	Fusion-ICP (0.01)	15.98	16.37	16.06	16.64	16.30	16.48	15.88	65.75	16.13
$Fe_2O_{3(T)}$	Fusion-ICP (0.01)	4.79	4.01	5.37	4.15	4.78	4.44	4.20	3.59	4.33
MnO	Fusion-ICP (0.001)	0.10	0.06	0.03	0.09	0.24	0.04	0.05	0.05	0.07
MgO	Fusion-ICP (0.01)	1.74	1.76	2.50	1.55	0.91	1.99	1.53	1.64	1.74
CaO	Fusion-ICP (0.01)	5.11	3.61	4.44	5.54	11.30	4.26	3.90	3.98	4.68
Na_2O	Fusion-ICP (0.01)	3.37	3.02	1.76	2.50	2.65	2.78	2.85	3.50	3.60
K_2O	Fusion-ICP (0.01)	3.05	3.50	2.75	2.82	2.98	3.46	3.11	2.44	2.20
TiO_2	Fusion-ICP (0.001)	0.46	0.41	0.532	0.54	0.55	0.52	0.44	0.35	0.43
P_2O_5	Fusion-ICP (0.01)	0.21	0.18	0.24	0.26	0.25	0.23	0.19	0.11	0.15
LOI	Fusion-ICP (0.01)	1.61	2.77	6.50	5.18	6.65	3.90	3.30	1.19	0.85
Total		100.50	100.10	99.18	99.91	100.90	100.80	100.70	100.30	99.94
ppm (except unless indicated)										
Au (ppb)	INAA (1)	42	17	53	70	8	138	14	< d.l.	< d.l.
Ag	MULT INAA/TD-ICP-MS (0.5)	< d.l.	< d.l.	< d.l.	< d.l.	< d.l.	< d.l.	< d.l.	< d.l.	< d.l.
As	INAA (1)	2	2	< d.l.	14	8	3	6	< d.l.	< d.l.
Ba	Fusion-ICP (1)	771	717	561	634	762	691	736	623	665
Be	Fusion-ICP (1)	2	2	2	2	2	2	2	1	1
Bi	Fusion-ICP-MS (0.1)	0.1	0.1	0.1	0.2	0.3	0.4	0.1	0.1	2.7
Br	INAA (0.5)	< d.l.	0.9	< d.l.	< d.l.	1	< d.l.	1.3	< d.l.	1
Cd	TD-ICP (0.5)	< d.l.	< d.l.	< d.l.	0.5	< d.l.	< d.l.	< d.l.	< d.l.	< d.l.
Co	INAA (0.1)	9.2	5	10	10.6	16.9	10	7.1	7.4	8.7
Cr	INAA (0.5)	10.8	7.7	8.2	6.6	< d.l.	5.5	5.6	9.5	13.5
Cs	Fusion-ICP-MS (0.1)	0.4	1.1	2.3	4.1	1.6	1.9	1.5	0.9	0.9
Cu	TD-ICP (1)	185	149	561	221	20	734	246	143	26
Ga	Fusion-ICP-MS (1)	18	17	16	16	17	18	17	14	16
Ge	Fusion-ICP-MS (0.5)	1.6	1.5	1.3	0.9	0.9	1.7	1.6	1.4	1.5
Hf	Fusion-ICP-MS (0.1)	3.3	3.1	2.7	3.1	2.8	3.3	3.6	2.9	3
Hg	INAA (1)	< d.l.	< d.l.	< d.l.	< d.l.	< d.l.	< d.l.	< d.l.	< d.l.	< d.l.
In	Fusion-ICP-MS (0.1)	< d.l.	< d.l.	< d.l.	< d.l.	< d.l.	< d.l.	< d.l.	< d.l.	< d.l.
Ir (ppb)	INAA (1)	< d.l.	< d.l.	< d.l.	< d.l.	< d.l.	< d.l.	< d.l.	< d.l.	< d.l.
Nb	Fusion-ICP-MS (0.2)	8.6	8.3	6.9	8.7	7.1	8.1	8.4	6.4	6.8
Ni	TD-ICP (1)	3	3	3	74	96	21	22	3	5
Pb	TD-ICP (5)	9	9	8	37	10	< d.l.	5	7	7
Rb	Fusion-ICP-MS (2)	63	76	66	83	68	101	91	62	61
S (%)	TD-ICP (0.001)	0.26	0.49	0.59	1.75	1.86	0.76	0.315	0.013	0.002
Sb	INAA (0.1)	< d.l.	0.5	< d.l.	1	0.8	0.3	0.3	< d.l.	< d.l.
Sc	INAA (0.01)	9.4	8.26	11.8	11.7	11.8	10.6	8.33	7.18	7.92
Se	INAA (0.5)	< d.l.	< d.l.	< d.l.	< d.l.	< d.l.	< d.l.	< d.l.	< d.l.	< d.l.
Sn	Fusion-ICP-MS (1)	< d.l.	< d.l.	< d.l.	< d.l.	< d.l.	< d.l.	< d.l.	< d.l.	< d.l.
Sr	Fusion-ICP (2)	549	449	263	408	615	426	391	271	394
Ta	Fusion-ICP-MS (0.1)	0.7	0.7	0.6	0.6	0.6	0.6	0.7	0.7	0.5
Th	Fusion-ICP-MS (0.05)	7.55	7.95	5.96	9.21	5.88	9.44	7.21	8.06	5.49
U	Fusion-ICP-MS (0.05)	1.95	1.89	1.56	3.25	3.3	2.33	2.44	1.62	1.55
V	Fusion-ICP (5)	102	84	134	130	131	117	86	67	75
W	INAA (1)	< d.l.	< d.l.	< d.l.	< d.l.	< d.l.	< d.l.	< d.l.	2	< d.l.
Y	Fusion-ICP (1)	19	16	17	16	19	17	17	10	12
Zn	MULT INAA/TD-ICP-MS (1)	32	28	32	116	48	34	28	25	29
Zr	Fusion-ICP-MS (1)	125	113	100	148	121	149	152	104	119
La	Fusion-ICP-MS (0.05)	27.1	20.3	21.7	20.1	27.7	25.2	26.4	21.7	22.7
Ce	Fusion-ICP-MS (0.1)	53.2	39.9	41.5	35.6	46.9	43.7	45.8	37.1	39
Pr	Fusion-ICP-MS (0.02)	5.94	4.51	4.59	4.1	5.29	4.92	5.19	3.72	4.07
Nd	Fusion-ICP-MS (0.05)	22.2	17.4	17.9	13.6	17.2	15.8	16.6	12.7	15.1
Sm	Fusion-ICP-MS (0.01)	4.21	3.54	3.48	2.82	3.59	3.26	3.31	2.14	2.85
Eu	Fusion-ICP-MS (0.005)	1.24	1.01	1.06	0.856	1.05	0.979	0.93	0.733	0.974
Gd	Fusion-ICP-MS (0.02)	3.5	2.92	2.93	2.88	3.5	3.04	3.05	1.76	2.33
Tb	Fusion-ICP-MS (0.01)	0.59	0.49	0.51	0.49	0.57	0.51	0.52	0.3	0.39
Dy	Fusion-ICP-MS (0.02)	3.45	2.92	3.08	2.63	3.1	2.83	2.86	1.78	2.26
Ho	Fusion-ICP-MS (0.01)	0.69	0.58	0.61	0.53	0.61	0.57	0.57	0.37	0.47
Er	Fusion-ICP-MS (0.01)	2.03	1.79	1.79	1.6	1.83	1.75	1.74	1.18	1.4
Tl	Fusion-ICP-MS (0.05)	0.25	0.45	0.5	1	0.63	0.63	0.63	0.28	0.86
Tm	Fusion-ICP-MS (0.005)	0.31	0.283	0.27	0.244	0.279	0.261	0.266	0.188	0.224
Yb	Fusion-ICP-MS (0.01)	2.08	1.91	1.8	1.67	1.87	1.74	1.79	1.31	1.54
Lu	Fusion-ICP-MS (0.002)	0.32	0.285	0.282	0.289	0.305	0.29	0.302	0.219	0.24

CR-03	**CR-05**	**CR-07**	**CR-08**	**CR-09**	**CR-10**	**CR-11**	**CR-12**	**CR-14**	**CR-24**	**CR-28**	**CR-31**
Diorite Porphyry	Quartz Diorite	Quartz Monzonite	Quartz Monzonite	Alk. Feld. Granite	Basaltic Andesite	Tonalite	Diorite	Hbl Diorite Porphyry	Tonalite	Granite	Granite
Diorite Porphyry	Quartz Diorite	Quartz Monzonite	Quartz Monzonite	Alk. Feld. Granite	Basaltic Andesite	Tonalite	Diorite	Hbl Diorite Porphyry	Tonalite	Granite	Granite
Least alt.	Alt. (phyl)	Least alt.	Least alt.	Least alt.	Least alt.	Least alt.	Least alt.	Alt. (prop)	Least alt.	Least alt.	Least alt.
Çöpler-Kabataş		Divriği			Yamadağ	Çaltı	Bizmişen	Çöpler-Kabataş	Doğanşehir	Karamadazı	Horoz
57.11	62.58	62.98	65.10	72.04	55.11	65.19	54.92	54.23	65.91	76.48	73.11
17.73	15.53	16.36	17.16	14.04	16.26	15.84	16.46	16.11	16.47	12.20	14.38
6.96	3.89	4.26	2.70	1.50	8.21	4.32	8.95	5.20	4.08	0.90	2.05
0.08	0.14	0.06	0.03	0.02	0.13	0.05	0.15	0.03	0.01	0.03	0.01
2.36	1.12	1.64	0.16	0.13	4.87	1.68	4.11	1.80	1.74	0.08	0.67
7.30	4.71	3.64	2.34	0.47	7.71	4.66	8.20	11.19	4.52	0.66	2.18
3.36	2.92	4.23	4.97	3.88	3.78	3.51	3.59	2.57	4.33	3.30	3.82
1.76	3.21	4.37	5.46	6.05	1.14	2.27	1.77	4.09	1.76	4.72	3.52
0.78	0.36	0.57	0.41	0.18	1.17	0.41	0.95	0.59	0.46	0.09	0.22
0.16	0.16	0.25	0.10	0.02	0.20	0.15	0.18	0.26	0.15	0.03	0.11
1.45	4.49	0.45	1.83	0.71	0.61	1.09	0.89	4.59	0.81	0.25	0.64
99.05	99.11	98.82	100.3	99.02	99.19	99.18	100.20	100.70	100.20	98.72	100.70
< d.l.	2	< d.l.	1	6	< d.l.	< d.l.	< d.l.	6	< d.l.	< d.l.	< d.l.
< d.l.	< d.l.	< d.l.	< d.l.	< d.l.	< d.l.	< d.l.	< d.l.	< d.l.	< d.l.	< d.l.	< d.l.
< d.l.	2	3	7	8	< d.l.	< d.l.	< d.l.	8	< d.l.	< d.l.	2
290	571	983	547	108	245	708	464	836	733	125	534
1	2	5	7	6	2	1	1	3	3	3	3
0.3	0.3	0.2	0.4	0.3	< d.l.	0.1	0.3	< d.l.	< d.l.	< d.l.	< d.l.
1.1	< d.l.	< d.l.	1.4	2.1	< d.l.	< d.l.	1.3	< d.l.	< d.l.	1	< d.l.
< d.l.	< d.l.	< d.l.	< d.l.	< d.l.	0.5	< d.l.	< d.l.	< d.l.	< d.l.	< d.l.	< d.l.
15.7	8.6	7.8	2.9	2.5	31.3	8.8	21.8	14	8	3	5
5.7	13.6	14.9	4.8	6.7	135	14.5	22.7	29	61	66	26
0.6	1.1	2.3	3.5	3.2	2.1	0.7	1	0.9	0.2	2.2	1
23	40	9	9	9	38	9	14	33	13	4	3
19	16	19	23	22	17	15	17	17	17	11	16
1.4	1.4	1.3	1.4	1.4	1.1	1.4	1.5	1.2	1.3	1.7	1.2
3.7	3.2	6.5	10.7	5.4	3.2	2.8	3.3	2.8	3.5	4.5	3
< d.l.	< d.l.	< d.l.	< d.l.	< d.l.	< d.l.	< d.l.	< d.l.	< d.l.	< d.l.	< d.l.	< d.l.
< d.l.	< d.l.	< d.l.	< d.l.	< d.l.	< d.l.	< d.l.	< d.l.	< d.l.	< d.l.	< d.l.	< d.l.
< d.l.	< d.l.	< d.l.	< d.l.	< d.l.	< d.l.	< d.l.	< d.l.	21	< d.l.	< d.l.	< d.l.
5.4	8.3	21	71.5	54.8	6.8	7.4	7.2	7.4	13.1	26.3	12.3
3	8	5	1	1	45	5	5	5	9	4	4
7	13	12	11	7	10	7	7	17	< d.l.	6	< d.l.
40	49	167	218	308	36	54	36	82	36	190	80
< d.l.	0.016	< d.l.	0.002	0.003	0.003	0.002	0.052	0.62	0.006	0.002	0.001
0.3	3	0.4	1.3	1.9	< d.l.	< d.l.	< d.l.	0.9	0.1	0.1	0.1
17.7	7.4	6.49	1.88	0.86	20.7	8.93	27.2	11.9	7.5	1.9	2.8
< d.l.	< d.l.	< d.l.	< d.l.	< d.l.	< d.l.	< d.l.	< d.l.	0.5	0.5	0.5	0.5
< d.l.	< d.l.	4	4	4	< d.l.	< d.l.	1	1	1	2	1
473	214	348	202	34	333	347	350	642	356	40	439
0.4	0.8	2.1	8.1	8.5	0.6	0.7	0.4	0.5	1.1	3.2	1.1
4.81	8.98	18.9	70.3	116	6.45	6.73	3.7	5.75	8.88	32.1	14.9
1.6	2.74	7.89	12.5	8.26	2.19	1.69	1.35	2.19	1.95	7.93	2.69
193	63	60	17	< d.l.	154	79	241	188	79	5	33
< d.l.	< d.l.	< d.l.	3	< d.l.	< d.l.	< d.l.	< d.l.	2	< d.l.	< d.l.	< d.l.
23	13	22	36	36	22	13	29	19	16	11	12
57	63	24	15	10	62	19	52	37	21	14	20
127	112	265	381	131	127	106	113	110	132	112	111
18.4	26.5	40.8	65.6	79.3	16.3	23.7	19.6	25.7	28.4	30.5	32.5
39.9	47.7	79.5	123	152	32.6	43.1	42	45.5	49	47.3	55.8
4.91	4.91	8.42	11.8	13.4	3.76	4.47	5.28	4.7	4.61	4.52	5.2
20.2	17.4	29.8	38.8	40.2	15	16	21.8	17.1	14.7	11.8	15.2
4.43	3.1	5.37	6.63	7.06	3.45	2.96	4.99	3.79	2.98	1.83	2.73
1.32	0.903	1.22	1.24	0.476	1.31	0.887	1.41	1.17	0.833	0.232	0.694
4.05	2.56	4.25	5.11	5.23	3.59	2.31	4.75	3.68	2.67	1.36	2.08
0.71	0.42	0.74	0.98	1.12	0.67	0.41	0.86	0.57	0.45	0.24	0.32
4.39	2.45	4.09	6.08	6.78	4.2	2.46	5.41	3.37	2.76	1.62	1.87
0.88	0.5	0.8	1.23	1.31	0.84	0.49	1.09	0.69	0.58	0.39	0.39
2.61	1.54	2.42	4	4.23	2.46	1.48	3.25	2.09	1.8	1.48	1.27
0.17	0.26	0.64	0.49	0.68	0.29	0.23	0.14	0.48	0.15	1.25	0.28
0.39	0.237	0.373	0.659	0.697	0.364	0.238	0.489	0.31	0.277	0.293	0.203
2.46	1.58	2.4	4.43	4.42	2.33	1.6	3.11	2.02	1.85	2.25	1.43
0.363	0.247	0.367	0.641	0.614	0.355	0.249	0.46	0.32	0.306	0.38	0.241

Abbreviations: alk feld = alkali feldspar; alt = altered; d.l. = detection limit, grd = granodiorite; hbl = hornblende; ICP-MS = inductively coupled plasma mass spectrometry; INAA = instrumental neutron activation analysis; K = potassic; LOI = loss-on-ignition; MULT = multiple analytical methods; phyl = phyllic; prop = propylitic; TD = total dis

APPENDIX C:

Ar-Ar isotopic data for samples from the Çöpler-Kabataş magmatic complex and nearby intrusions. Errors reported as 2σ

C-164: Biotite										
Laser Power(%)	$^{40}\mathrm{Ar}/^{39}\mathrm{Ar}$	$^{38}\mathrm{Ar}/^{39}\mathrm{Ar}$	$^{37}\mathrm{Ar}/^{39}\mathrm{Ar}$	$^{36}\mathrm{Ar}/^{39}\mathrm{Ar}$	Ca/K	Cl/K	%^{40}Ar atm	f ^{39}Ar	$^{40}\mathrm{Ar}^{*}/^{39}\mathrm{Ar}_K$	Apparent age (Ma)
2	18.4031 ± 0.0185	0.0612 ± 0.1875	0.0500 ± 0.1472	0.0500 ± 0.0572	0.079	0.008	76.26	0.32	3.803 ± 0.824	35.54 ± 7.63
2.3	7.0180 ± 0.0243	0.0691 ± 0.0711	0.0612 ± 0.0664	0.0123 ± 0.0815	0.507	0.012	49.23	2.79	3.397 ± 0.315	31.79 ± 2.92
2.6	12.4936 ± 0.0195	0.1388 ± 0.0427	0.1361 ± 0.0372	0.0276 ± 0.0376	1.192	0.028	63.94	2.93	4.383 ± 0.314	40.91 ± 2.90
2.9	6.0691 ± 0.0085	0.1804 ± 0.0228	0.0053 ± 0.0905	0.0046 ± 0.0785	0.032	0.038	20.91	7.54	4.688 ± 0.116	43.72 ± 1.07
3.1	5.2286 ± 0.0068	0.1872 ± 0.0133	0.0032 ± 0.1047	0.0018 ± 0.0860	0.02	0.04	8.97	13.37	4.674 ± 0.056	43.59 ± 0.52
3.3	4.9356 ± 0.0051	0.1877 ± 0.0125	0.0029 ± 0.0844	0.0008 ± 0.0646	0.02	0.04	3.6	19.42	4.686 ± 0.029	43.70 ± 0.26
3.5	4.8390 ± 0.0066	0.1893 ± 0.0153	0.0026 ± 0.1387	0.0004 ± 0.1417	0.016	0.04	1.17	16.84	4.704 ± 0.035	43.86 ± 0.33
3.7	4.8428 ± 0.0060	0.1907 ± 0.0145	0.0022 ± 0.1122	0.0004 ± 0.2088	0.012	0.041	1.46	15.31	4.689 ± 0.040	43.73 ± 0.37
4	4.8310 ± 0.0051	0.1950 ± 0.0143	0.0020 ± 0.0887	0.0004 ± 0.1384	0.012	0.042	1.4	21.48	4.694 ± 0.029	43.77 ± 0.27
Total/Average	5.2585 ± 0.0013	0.1841 ± 0.0030	0.0358 ± 0.0031	0.0020 ± 0.0143	0.066	0.032		100	4.642 ± 0.011	
Volume $^{39}\mathrm{Ar}_K$ =		380.35								
Integrated Date =		43.29 ± 0.21								
C-166: Hornblende										
Laser Power(%)	$^{40}\mathrm{Ar}/^{39}\mathrm{Ar}$	$^{38}\mathrm{Ar}/^{39}\mathrm{Ar}$	$^{37}\mathrm{Ar}/^{39}\mathrm{Ar}$	$^{36}\mathrm{Ar}/^{39}\mathrm{Ar}$	Ca/K	Cl/K	%^{40}Ar atm	f ^{39}Ar	$^{40}\mathrm{Ar}^{*}/^{39}\mathrm{Ar}_K$	Apparent age (Ma)
2	2542.0518 ± 1.6253	1.5608 ± 1.8448	1.7717 ± 2.6069	8.9582 ± 1.6284	-8.379	-0.03	105.1	0	19.334 ± 391.048	173.84 ± 3352.03
2.2	422.3886 ± 0.1366	1.0094 ± 0.2598	2.3150 ± 0.1901	1.4378 ± 0.1626	24.676	0.267	98.95	0.01	4.330 ± 73.267	40.41 ± 676.25
2.4	278.2450 ± 0.0359	1.0228 ± 0.1412	1.6379 ± 0.0986	0.9147 ± 0.0508	11.631	0.203	96.78	0.15	8.754 ± 10.571	80.80 ± 95.41
2.8	48.2264 ± 0.0263	0.3327 ± 0.0952	3.1071 ± 0.0384	0.1456 ± 0.0647	21.345	0.069	85.71	0.56	6.309 ± 2.644	58.59 ± 24.16
3.2	15.9700 ± 0.0161	0.1644 ± 0.0759	3.0844 ± 0.0229	0.0402 ± 0.0581	20.998	0.033	66.18	2.46	5.058 ± 0.684	47.12 ± 6.29
3.6	7.8730 ± 0.0104	0.5772 ± 0.0270	0.5617 ± 0.0238	0.0101 ± 0.1024	3.804	0.13	25.98	2.66	5.080 ± 0.315	47.33 ± 2.89
4	5.5438 ± 0.0048	0.9148 ± 0.0119	1.5314 ± 0.0126	0.0043 ± 0.0486	10.361	0.208	12.22	28.07	4.769 ± 0.066	44.46 ± 0.61

4.2	5.1977 ± 0.0124	0.9201 ± 0.0170	1.4839 ± 0.0213	0.0031 ± 0.0534	10.044	0.209	5	14.57	4.751 ± 0.079	44.30 ± 0.73
4.4	4.9509 ± 0.0084	1.0040 ± 0.0110	1.7600 ± 0.0263	0.0028 ± 0.0442	11.922	0.229	3.39	27.27	4.677 ± 0.055	43.61 ± 0.51
4.6	5.2193 ± 0.0130	0.9549 ± 0.0221	1.6128 ± 0.0491	0.0034 ± 0.1091	10.932	0.218	4.25	10.09	4.736 ± 0.129	44.15 ± 1.19
4.8	5.1649 ± 0.0163	0.9900 ± 0.0187	1.7637 ± 0.0393	0.0033 ± 0.0569	11.83	0.226	4.17	14.17	4.760 ± 0.099	44.38 ± 0.91
Total/Average	6.0495 ± 0.0020	0.9247 ± 0.0032	6.0711 ± 0.0022	0.0060 ± 0.0109	11.158	0.16		100	4.766 ± 0.022	
Volume $^{39}Ar_K$ =		154.68								
Integrated Date =		44.43 ± 0.42								
CR-2: Biotite										
Laser Power(%)	$^{40}Ar/^{39}Ar$	$^{38}Ar/^{39}Ar$	$^{37}Ar/^{39}Ar$	$^{36}Ar/^{39}Ar$	Ca/K	Cl/K	%^{40}Ar atm	f ^{39}Ar	$^{40}Ar^*/^{39}Ar_K$	Apparent age (Ma)
2	207.3801 ± 0.0146	0.3390 ± 0.0774	0.0558 ± 0.1584	0.7116 ± 0.0359	0.25	0.047	101.65	0.03	-3.842 ± 7.845	-54.60 ± 113.17
2.2	99.7598 ± 0.0106	0.2196 ± 0.0404	0.0448 ± 0.0989	0.3212 ± 0.0200	0.165	0.034	95.33	0.1	4.744 ± 1.711	65.21 ± 23.10
2.5	22.1819 ± 0.0065	0.1433 ± 0.0287	0.0641 ± 0.0446	0.0707 ± 0.0311	0.22	0.027	94.19	0.26	1.254 ± 0.648	17.47 ± 8.98
2.8	10.8869 ± 0.0052	0.1411 ± 0.0219	0.0502 ± 0.0385	0.0277 ± 0.0255	0.169	0.028	75.16	0.85	2.657 ± 0.208	36.81 ± 2.86
3	5.7634 ± 0.0049	0.1363 ± 0.0177	0.0312 ± 0.0236	0.0094 ± 0.0332	0.105	0.028	47.44	1.52	2.972 ± 0.093	41.13 ± 1.28
3.2	4.1941 ± 0.0041	0.1382 ± 0.0117	0.0215 ± 0.0260	0.0035 ± 0.0245	0.072	0.028	24.25	2.98	3.125 ± 0.029	43.21 ± 0.40
3.4	3.6877 ± 0.0049	0.1375 ± 0.0117	0.0319 ± 0.0205	0.0017 ± 0.0402	0.106	0.028	12.73	4.75	3.171 ± 0.026	43.85 ± 0.35
3.6	3.4989 ± 0.0042	0.1371 ± 0.0129	0.0181 ± 0.0262	0.0010 ± 0.0352	0.06	0.028	7.52	5.77	3.190 ± 0.017	44.11 ± 0.24
3.8	3.4279 ± 0.0046	0.1379 ± 0.0122	0.0152 ± 0.0233	0.0007 ± 0.0478	0.051	0.029	5.54	8.44	3.196 ± 0.018	44.19 ± 0.25
4	3.4006 ± 0.0052	0.1387 ± 0.0120	0.0137 ± 0.0200	0.0006 ± 0.0325	0.046	0.029	4.37	8.06	3.210 ± 0.018	44.37 ± 0.25
4.2	3.3781 ± 0.0041	0.1400 ± 0.0113	0.0121 ± 0.0293	0.0005 ± 0.0617	0.041	0.029	3.95	7.64	3.202 ± 0.017	44.26 ± 0.23
4.4	3.3391 ± 0.0050	0.1456 ± 0.0100	0.0168 ± 0.0188	0.0004 ± 0.0459	0.056	0.03	3.18	8.48	3.191 ± 0.017	44.12 ± 0.24
4.6	3.3305 ± 0.0088	0.1417 ± 0.0137	0.0171 ± 0.0214	0.0004 ± 0.0656	0.058	0.029	2.73	8.24	3.197 ± 0.030	44.20 ± 0.41
4.8	3.3204 ± 0.0043	0.1436 ± 0.0114	0.0186 ± 0.0154	0.0003 ± 0.0667	0.063	0.03	2.51	8.41	3.195 ± 0.016	44.17 ± 0.21
5	3.3105 ± 0.0044	0.1394 ± 0.0103	0.0164 ± 0.0220	0.0003 ± 0.0678	0.055	0.029	2.3	9.08	3.193 ± 0.016	44.14 ± 0.22
5.2	3.3010 ± 0.0041	0.1393 ± 0.0111	0.0161 ± 0.0179	0.0003 ± 0.0506	0.054	0.029	1.79	7.82	3.199 ± 0.014	44.22 ± 0.19
5.5	3.2844 ± 0.0043	0.1385 ±	0.0135 ±	0.0002 ±	0.046	0.029	1.64	10.96	3.190 ± 0.015	44.11 ± 0.20

		0.0092	0.0146	0.0680						
5.9	3.3046 ± 0.0043	0.1416 ± 0.0123	0.0160 ± 0.0181	0.0003 ± 0.0633	0.053	0.029	1.72	6.63	3.203 ± 0.015	44.28 ± 0.21
Total/Average	3.6802 ± 0.0007	0.1403 ± 0.0016	0.0318 ± 0.0016	0.0016 ± 0.0047	0.058	0.03		100	3.195 ± 0.004	
Volume ^{39}Ar$_K$ =		3334.34								
Integrated Date =		43.97 ± 0.11								
C-169: Biotite										
Laser Power(%)	^{40}Ar/^{39}Ar	^{38}Ar/^{39}Ar	^{37}Ar/^{39}Ar	^{36}Ar/^{39}Ar	Ca/K	Cl/K	%^{40}Ar atm	f ^{39}Ar	^{40}Ar*/^{39}Ar$_K$	Apparent age (Ma)
2	209.5148 ± 0.3841	0.0023 ± 100.4156	0.0642 ± 5.6724	0.7113 ± 0.4146	3.905	-0.047	0.35	0	-47.950 ± 362.806	-521.11 ± 4571.37
2.2	83.7175 ± 0.0351	0.1585 ± 0.1431	0.0782 ± 0.3044	0.2858 ± 0.0561	0.581	0.022	100.83	0.07	-0.668 ± 3.928	-6.31 ± 37.20
2.4	30.1391 ± 0.0108	0.1199 ± 0.0812	0.1061 ± 0.0866	0.0964 ± 0.0530	0.725	0.02	93.94	0.24	1.672 ± 1.503	15.71 ± 14.07
2.7	22.2238 ± 0.0087	0.1414 ± 0.0326	0.4597 ± 0.0180	0.0644 ± 0.0282	3.076	0.027	84.98	1.59	3.260 ± 0.547	30.52 ± 5.07
3	9.3672 ± 0.0105	0.1753 ± 0.0179	0.2581 ± 0.1951	0.0180 ± 0.0281	1.725	0.036	55.27	3.1	4.083 ± 0.158	38.14 ± 1.46
3.2	7.4259 ± 0.0066	0.1944 ± 0.0151	0.0173 ± 1.7090	0.0096 ± 0.0278	0.116	0.041	37.01	4.53	4.570 ± 0.087	42.63 ± 0.80
3.4	5.9049 ± 0.0056	0.1995 ± 0.0155	0.0241 ± 0.8057	0.0040 ± 0.0446	0.162	0.043	18.82	7.63	4.703 ± 0.060	43.85 ± 0.56
3.6	7.1102 ± 0.0057	0.2003 ± 0.0200	0.0098 ± 4.2177	0.0082 ± 0.0258	0.066	0.043	32.99	5.06	4.660 ± 0.069	43.46 ± 0.64
3.8	5.7644 ± 0.0051	0.2031 ± 0.0145	0.0070 ± 1.7731	0.0034 ± 0.0428	0.047	0.043	16.76	9.98	4.719 ± 0.051	44.00 ± 0.47
4	7.0837 ± 0.0067	0.1983 ± 0.0161	0.0024 ± 0.0738	0.0079 ± 0.0272	0.016	0.042	32.09	6.08	4.717 ± 0.073	43.98 ± 0.67
4.2	6.0245 ± 0.0053	0.2008 ± 0.0123	0.0019 ± 0.0763	0.0043 ± 0.0338	0.013	0.043	20.4	8.55	4.712 ± 0.052	43.93 ± 0.48
4.4	6.2201 ± 0.0067	0.2006 ± 0.0167	0.0015 ± 0.1773	0.0049 ± 0.0417	0.011	0.043	22.47	7.7	4.735 ± 0.069	44.15 ± 0.64
4.6	11.9516 ± 0.0056	0.1880 ± 0.0200	0.0049 ± 0.1254	0.0248 ± 0.0269	0.034	0.039	60.97	5.1	4.590 ± 0.197	42.81 ± 1.82
4.8	7.9398 ± 0.0049	0.1863 ± 0.0096	0.0027 ± 0.1037	0.0110 ± 0.0248	0.019	0.039	40.5	12.76	4.664 ± 0.083	43.50 ± 0.77
5	6.0458 ± 0.0062	0.1918 ± 0.0130	0.0030 ± 0.1137	0.0045 ± 0.0360	0.021	0.041	21.14	9.53	4.689 ± 0.056	43.73 ± 0.52
5.2	5.0726 ± 0.0042	0.1987 ± 0.0108	0.0022 ± 0.0461	0.0011 ± 0.0441	0.015	0.042	5.71	12.15	4.707 ± 0.026	43.89 ± 0.24
5.4	5.2285 ± 0.0074	0.1924 ± 0.0182	0.0025 ± 0.0758	0.0018 ± 0.0446	0.017	0.041	8.21	5.94	4.683 ± 0.043	43.67 ± 0.40
Total/Average	6.9529 ± 0.0008	0.1944 ± 0.0020	0.0775 ± 0.0227	0.0078 ± 0.0046	0.142	0.033		100	4.634 ± 0.013	
Volume ^{39}Ar$_K$ =		770.21								

Integrated Date =		43.22 ± 0.24								
C-138: Sericite										
Laser Power(%)	^{40}Ar/^{39}Ar	^{38}Ar/^{39}Ar	^{37}Ar/^{39}Ar	^{36}Ar/^{39}Ar	Ca/K	Cl/K	%^{40}Ar atm	f ^{39}Ar	^{40}Ar*/^{39}Ar$_K$	Apparent age (Ma)
2	7.6303 ± 0.0099	0.0227 ± 0.0437	0.0311 ± 0.0544	0.0114 ± 0.0469	0.186	0.002	41.06	1.44	4.257 ± 0.166	39.75 ± 1.53
2.1	7.6295 ± 0.0072	0.0177 ± 0.0707	0.0487 ± 0.0504	0.0065 ± 0.0766	0.29	0.001	22.33	1.89	5.684 ± 0.155	52.88 ± 1.42
2.2	6.0091 ± 0.0078	0.0152 ± 0.0782	0.1681 ± 0.0393	0.0032 ± 0.0921	0.998	0	13.17	4.14	5.078 ± 0.097	47.32 ± 0.89
2.3	5.6454 ± 0.0059	0.0138 ± 0.0285	0.3496 ± 0.0145	0.0025 ± 0.0442	2.075	0	10.74	8.53	4.955 ± 0.046	46.18 ± 0.42
2.4	5.2752 ± 0.0059	0.0128 ± 0.0441	0.2529 ± 0.0164	0.0015 ± 0.0478	1.531	0	6.3	14.05	4.876 ± 0.037	45.46 ± 0.34
2.5	5.1136 ± 0.0067	0.0125 ± 0.0414	0.1806 ± 0.0741	0.0010 ± 0.0367	1.093	0	4.34	16.18	4.829 ± 0.036	45.02 ± 0.33
2.6	4.9869 ± 0.0068	0.0122 ± 0.0194	0.0545 ± 0.1490	0.0006 ± 0.0704	0.33	0	2.54	16.89	4.796 ± 0.035	44.72 ± 0.33
2.7	5.0151 ± 0.0057	0.0127 ± 0.0184	0.0180 ± 0.6226	0.0008 ± 0.0674	0.109	0	3.5	11.3	4.761 ± 0.032	44.40 ± 0.29
2.8	5.0829 ± 0.0105	0.0128 ± 0.0336	0.0319 ± 0.0445	0.0010 ± 0.0851	0.193	0	4.55	7.4	4.752 ± 0.058	44.31 ± 0.53
2.9	5.1105 ± 0.0114	0.0130 ± 0.0592	0.0486 ± 0.0480	0.0012 ± 0.1245	0.294	0	4.73	4.91	4.736 ± 0.072	44.17 ± 0.66
3	5.0254 ± 0.0067	0.0139 ± 0.0390	0.0383 ± 0.0274	0.0008 ± 0.1258	0.232	0	3.15	7.21	4.764 ± 0.045	44.43 ± 0.41
3.2	5.0817 ± 0.0115	0.0138 ± 0.0338	0.0135 ± 0.0638	0.0011 ± 0.0802	0.082	0	4.45	5.27	4.729 ± 0.063	44.10 ± 0.58
3.6	8.2300 ± 0.0306	0.0367 ± 0.0594	0.0117 ± 0.1918	0.0173 ± 0.0413	0.074	0.005	58.84	0.81	3.098 ± 0.259	29.02 ± 2.41
Total/Average	5.2134 ± 0.0012	0.0134 ± 0.0059	0.4023 ± 0.0038	0.0014 ± 0.0104	0.736	0		100	4.817 ± 0.008	
Volume ^{39}Ar$_K$ =		796.47								
Integrated Date =		44.91 ± 0.16								
CR-11: Biotite										
Laser Power(%)	^{40}Ar/^{39}Ar	^{38}Ar/^{39}Ar	^{37}Ar/^{39}Ar	^{36}Ar/^{39}Ar	Ca/K	Cl/K	%^{40}Ar atm	f ^{39}Ar	^{40}Ar*/^{39}Ar$_K$	Apparent age (Ma)
2	62.2847 ± 0.0309	0.2262 ± 0.0997	0.0984 ± 0.1277	0.2074 ± 0.0477	0.341	0.041	98.63	0.03	0.814 ± 2.849	11.36 ± 39.65
2.4	23.4940 ± 0.0163	0.1214 ± 0.0492	0.1188 ± 0.0445	0.0725 ± 0.0343	0.411	0.022	91.21	0.22	2.010 ± 0.727	27.93 ± 10.03
2.8	9.5351 ± 0.0119	0.1059 ± 0.0315	0.0338 ± 0.0260	0.0238 ± 0.0246	0.117	0.02	73.72	0.78	2.451 ± 0.175	34.00 ± 2.40
3	4.8109 ± 0.0172	0.1101 ± 0.0246	0.0156 ± 0.0481	0.0060 ± 0.0326	0.054	0.022	36.31	2.44	3.012 ± 0.085	41.70 ± 1.16
3.2	3.6768 ± 0.0145	0.1128 ± 0.0179	0.0076 ± 0.0378	0.0017 ± 0.0324	0.026	0.023	13.44	4.84	3.137 ± 0.051	43.40 ± 0.70

3.4	3.5297 ± 0.0046	0.1104 ± 0.0135	0.0027 ± 0.0757	0.0007 ± 0.0335	0.01	0.022	5.73	6.4	3.283 ± 0.017	45.40 ± 0.24
3.6	3.4255 ± 0.0066	0.1112 ± 0.0166	0.0021 ± 0.0648	0.0005 ± 0.0582	0.007	0.022	3.58	7.37	3.260 ± 0.024	45.08 ± 0.32
3.8	3.3290 ± 0.0086	0.1134 ± 0.0135	0.0026 ± 0.0550	0.0004 ± 0.0288	0.009	0.023	2.97	11.78	3.191 ± 0.028	44.14 ± 0.39
4	3.3624 ± 0.0089	0.1129 ± 0.0234	0.0032 ± 0.0454	0.0004 ± 0.0587	0.011	0.023	3.26	9.69	3.212 ± 0.030	44.43 ± 0.41
4.2	3.2977 ± 0.0040	0.1145 ± 0.0105	0.0042 ± 0.0337	0.0002 ± 0.0608	0.015	0.023	1.76	10.32	3.200 ± 0.014	44.26 ± 0.19
4.4	3.2874 ± 0.0040	0.1145 ± 0.0107	0.0050 ± 0.0332	0.0002 ± 0.0787	0.017	0.023	1.56	10.6	3.196 ± 0.014	44.21 ± 0.19
4.6	3.2775 ± 0.0044	0.1148 ± 0.0122	0.0054 ± 0.0335	0.0002 ± 0.0840	0.019	0.023	1.56	10.18	3.186 ± 0.015	44.07 ± 0.21
4.8	3.3053 ± 0.0045	0.1126 ± 0.0113	0.0052 ± 0.0469	0.0003 ± 0.2068	0.018	0.023	1.89	4.21	3.193 ± 0.023	44.16 ± 0.31
5	3.3133 ± 0.0043	0.1141 ± 0.0124	0.0076 ± 0.0328	0.0003 ± 0.1354	0.027	0.023	2.22	4.9	3.192 ± 0.019	44.16 ± 0.26
5.2	3.2643 ± 0.0043	0.1142 ± 0.0102	0.0073 ± 0.0255	0.0002 ± 0.1177	0.026	0.023	1.26	8.8	3.182 ± 0.016	44.02 ± 0.21
5.5	3.2800 ± 0.0041	0.1134 ± 0.0105	0.0064 ± 0.0364	0.0002 ± 0.1002	0.023	0.023	1.34	7.44	3.193 ± 0.015	44.17 ± 0.20
Total/Average	3.4772 ± 0.0010	0.1134 ± 0.0021	0.0104 ± 0.0028	0.0009 ± 0.0061	0.019	0.024		100	3.206 ± 0.004	
Volume ^{39}Ar$_{K}$ =		2985.4								
Integrated Date =		44.11 ± 0.11								
CR-12: Hornblende										
Laser Power(%)	^{40}Ar/^{39}Ar	^{38}Ar/^{39}Ar	^{37}Ar/^{39}Ar	^{36}Ar/^{39}Ar	Ca/K	Cl/K	%^{40}Ar atm	f ^{39}Ar	^{40}Ar*/^{39}Ar$_{K}$	Apparent age (Ma)
2	176.1797 ± 0.0661	0.8049 ± 0.1239	0.4676 ± 0.1777	0.6071 ± 0.0760	5.12	0.412	102	0.02	-9.336 ± 21.331	-135.77 ± 322.18
2.4	226.8937 ± 0.0215	1.6768 ± 0.0324	1.1291 ± 0.0283	0.7710 ± 0.0303	4.121	0.38	100.58	0.42	-1.442 ± 5.379	-20.31 ± 76.20
2.8	218.9034 ± 0.0079	2.0197 ± 0.0188	2.0795 ± 0.0173	0.7436 ± 0.0188	7.198	0.446	100.48	1	-1.128 ± 3.984	-15.88 ± 56.30
3	128.3148 ± 0.0185	1.0244 ± 0.0296	1.6806 ± 0.0358	0.4253 ± 0.0250	5.945	0.226	97.95	0.63	2.730 ± 2.292	37.84 ± 31.44
3.2	119.1241 ± 0.0102	1.0372 ± 0.0309	2.0197 ± 0.0211	0.3993 ± 0.0231	7.035	0.228	99.01	0.86	1.188 ± 2.592	16.57 ± 35.98
3.4	67.5540 ± 0.0079	1.1236 ± 0.0209	2.4929 ± 0.0158	0.2168 ± 0.0218	8.568	0.254	94.44	1.25	3.807 ± 1.377	52.56 ± 18.73
3.6	15.2634 ± 0.0061	1.8100 ± 0.0124	4.1768 ± 0.0134	0.0438 ± 0.0293	14.05	0.417	80.52	5.62	2.942 ± 0.383	40.76 ± 5.25
3.8	8.0259 ± 0.0062	1.2453 ± 0.0118	4.3157 ± 0.0129	0.0187 ± 0.0305	14.478	0.285	60.31	9.86	3.143 ± 0.172	43.50 ± 2.35
4	9.2547 ± 0.0128	1.3253 ± 0.0168	3.8919 ± 0.0179	0.0226 ± 0.0558	13.12	0.305	64.81	4.08	3.187 ± 0.378	44.10 ± 5.16
4.2	8.7878 ± 0.0066	1.9158 ±	4.5121 ±	0.0214 ±	15.12	0.441	63.92	15.22	3.141 ± 0.127	43.48 ± 1.74

		0.0120	0.0143	0.0195						
4.4	5.8428 ± 0.0071	1.4274 ± 0.0114	4.3822 ± 0.0139	0.0113 ± 0.0319	14.669	0.327	45.06	23.66	3.178 ± 0.110	43.98 ± 1.50
4.6	4.2544 ± 0.0062	1.2085 ± 0.0115	4.4500 ± 0.0134	0.0060 ± 0.0216	14.9	0.277	24.77	21.72	3.158 ± 0.044	43.71 ± 0.60
4.8	5.6055 ± 0.0111	1.2487 ± 0.0205	3.9618 ± 0.0185	0.0106 ± 0.0397	13.302	0.287	43.87	7.37	3.072 ± 0.132	42.52 ± 1.80
5.1	4.8609 ± 0.0078	1.3024 ± 0.0101	4.2467 ± 0.0142	0.0082 ± 0.0415	14.256	0.299	34.86	8.29	3.089 ± 0.106	42.76 ± 1.45
Total/Average	12.5596 ± 0.0012	1.4344 ± 0.0024	7.7269 ± 0.0018	0.0343 ± 0.0037	14.218	0.327		100	3.143 ± 0.040	
Volume ^{39}Ar$_{K}$ =		313.88								
Integrated Date =		42.36 ± 1.11								
CR-9: Biotite										
Laser Power(%)	^{40}Ar/^{39}Ar	^{38}Ar/^{39}Ar	^{37}Ar/^{39}Ar	^{36}Ar/^{39}Ar	Ca/K	Cl/K	%^{40}Ar atm	f ^{39}Ar	^{40}Ar*/^{39}Ar$_{K}$	Apparent age (Ma)
2	99.0605 ± 0.0198	0.2306 ± 0.1354	0.1422 ± 0.1203	0.3408 ± 0.0480	0.513	0.036	102	0.09	-2.017 ± 4.618	-28.46 ± 65.68
2.4	13.1854 ± 0.0048	0.1078 ± 0.0253	0.0336 ± 0.0349	0.0331 ± 0.0298	0.119	0.02	74.1	2.25	3.351 ± 0.291	46.32 ± 3.97
2.7	11.4640 ± 0.0057	0.1538 ± 0.0228	0.0122 ± 0.0343	0.0240 ± 0.0212	0.043	0.031	61.45	2.35	4.340 ± 0.151	59.75 ± 2.04
3	6.6084 ± 0.0051	0.1528 ± 0.0144	0.0042 ± 0.0488	0.0045 ± 0.0226	0.015	0.032	19.67	14.02	5.257 ± 0.041	72.13 ± 0.55
3.2	5.6440 ± 0.0047	0.1532 ± 0.0133	0.0033 ± 0.0453	0.0007 ± 0.0538	0.012	0.032	3.21	16.8	5.410 ± 0.028	74.20 ± 0.38
3.4	5.6416 ± 0.0050	0.1551 ± 0.0129	0.0056 ± 0.0871	0.0007 ± 0.1148	0.02	0.032	3.09	11.33	5.407 ± 0.036	74.15 ± 0.49
3.6	5.6765 ± 0.0055	0.1525 ± 0.0193	0.0094 ± 0.0518	0.0008 ± 0.0653	0.033	0.032	3.38	9.53	5.419 ± 0.034	74.32 ± 0.46
3.9	5.6496 ± 0.0051	0.1501 ± 0.0124	0.0160 ± 0.0321	0.0007 ± 0.0513	0.056	0.031	3.2	12.84	5.412 ± 0.030	74.21 ± 0.41
4.2	5.6394 ± 0.0044	0.1504 ± 0.0133	0.0084 ± 0.0582	0.0007 ± 0.0506	0.03	0.031	3.04	13.87	5.412 ± 0.026	74.22 ± 0.35
4.7	5.6704 ± 0.0045	0.1476 ± 0.0138	0.0060 ± 0.0698	0.0007 ± 0.0883	0.021	0.031	3.28	12.07	5.426 ± 0.032	74.40 ± 0.42
5.2	6.1548 ± 0.0071	0.1542 ± 0.0226	0.0067 ± 0.0661	0.0025 ± 0.0869	0.023	0.032	10.83	4.86	5.399 ± 0.075	74.04 ± 1.01
Total/Average	6.1652 ± 0.0009	0.1510 ± 0.0025	0.0156 ± 0.0045	0.0028 ± 0.0066	0.029	0.031		100	5.414 ± 0.008	
Volume ^{39}Ar$_{K}$ =		711.84								
Integrated Date =		72.89 ± 0.22								

APPENDIX D:

Whole-rock and $^{40}Ar/^{39}Ar$ sample locations and descriptions from the Cevizlidere deposit

Sample no.	UTM Coordinates (Zone 37S, WGS84)		Drillhole: depth (m)	Drillhole elevation, azimuth/dip	Sample description
	Easting	Northing			
K-1180	504582	4344844	KIZ-001: 180–182m	1625m, 190/-85°	Propylitized diorite porphyry with Chl (after Hb)-Biot (mostly fresh)-Plag-Qz-Ep-Carb-Py
K-1427	504582	4344844	KIZ-001: 427–429m	1625m, 190/-85°	Weakly propylitized diorite porphyry (incipient Chl on Biot); minor sericite on Plag and sparse Py in the groundmass
K-1492	504582	4344844	KIZ-001: 493–493.50m	1625m, 190/-85°	Moderately-altered (potassic) granodiorite porphyry with Biot (mostly primary and lesser overgrowths of secondary)-Mt-Kspar; minor retrograde Chl-Carb-Ep
K-4385	505156	4344350	KIZ-004: 385.50–386.50m	1710m, 250/-75°	Weakly propylitized granodiorite porphyry; Hb phenocrysts replaced by Chl and minor retrograde Chl surrounding Biot; minor sericite on Plag
K-4403	505156	4344350	KIZ-004: 404–406.50m	1710m, 250/-75°	Weakly Propylitized diorite porphyry (Hb partially to completely replaced by Chl but Biot looks fresh); minor sericite on Plag
K-4415	505156	4344350	KIZ-004: 415.40–415.80m	1710m, 250/-75°	Diorite porphyry with Chl (after Hb) and fresh Biot-Plag-Mt (primary); sparse Carb and lesser Py
K-5425	504297	4345154	KIZ-005: 425–427m	1578m, vertical	Weakly sericite-Qz altered and propylitized (Chl and minor Ep-Carb) granodiorite porphyry; contains sparse partially Chl altered primary Biot
K-7420	504961	4344624	KIZ-007: 232.50–232.70m	1673m, vertical	Potassically-altered (secondary Biot-Kspar-Mt) granodiorite porphyry, minor cross-cutting Biot veinlets

Abbreviations: Biot = biotite, Carb = carbonate, Chl = chlorite, Ep = epidote, Hb = hornblende, Kspar = K-feldspar, Plag = plagioclase, Py = pyrite, Qz = quartz

APPENDIX E:

Description and procedures for $^{40}Ar/^{39}Ar$ dating at the Nevada Isotope Geochronology Laboratory

Samples were wrapped in Al foil and stacked in 6 mm inside-diameter sealed fused silica tubes. Individual packets averaged 3 mm thick and neutron flux monitors (FC-2, Fish Canyon Tuff sanidine) were placed every 5 to 10 mm along the tube. Synthetic K-glass and optical grade CaF_2 were included in the irradiation packages to monitor neutron induced argon interferences from K and Ca. Loaded tubes were packed in an Al container for irradiation. Samples were irradiated at the U.S. Geological Survey TRIGA Reactor, Denver, CO, were in-core for 7 hours in the In-Core Radiation Tube (ICIT) of the 1 MW TRIGA type reactor. Correction factors for interfering neutron reactions on K and Ca were determined by repeated analysis of K-glass and CaF_2 fragments. Measured $(^{40}Ar/^{39}Ar)_K$ values were 2.05 (±33.35%) x 10^{-2}. Ca correction factors were $(^{36}Ar/^{37}Ar)_{Ca} = 2.67$ (±1.87%) x 10^{-4} and $(^{39}Ar/^{37}Ar)_{Ca} = 6.91$ (±1.19%) x 10^{-4}. J factors were determined by fusion of 4 to 8 individual crystals of neutron flux monitors which gave reproducibilities of 0.16% to 0.43% at each standard position. Variation in neutron flux along the 100 mm length of the irradiation tubes was <4%. Matlab curve fit was used to determine J and uncertainty in J at each standard position. No significant neutron flux gradients were present within individual packets of crystals as indicated by the excellent reproducibility of the single crystal flux monitor fusions.

Samples were analyzed by furnace step-heating method utilizing a double vacuum resistance furnace similar to the Staudacher et al. (1978) design. Reactive gases were removed by three GP-50 SAES getters prior to being admitted to a MAP 215-50 mass spectrometer by expansion. The relative volumes of the extraction line and mass spectrometer allow 76% for furnace heating analyses. Peak intensities were measured using a Balzers electron multiplier by peak hopping through 7 cycles; initial peak heights were determined by linear regression to the time of gas admission. Mass spectrometer discrimination and sensitivity was monitored by repeated analysis of atmospheric argon aliquots from an on-line pipette system. Measured $^{40}Ar/^{36}Ar$ ratios were 280 ± 0.67% during this work, thus a discrimination correction of 1.0523 (4 AMU) was applied to measured isotope ratios. The sensitivity of the mass spectrometer was ~6 x 10^{-17} mol mV^{-1} with multiplier operated at a gain of 36 over the Faraday. Line blanks averaged 6.91 mV for mass 40 and 0.03 mV for mass 36 for furnace heating analyses. Discrimination, sensitivity, and blanks were relatively constant over the period of data collection. Computer automated operation of the sample stage, extraction line and mass spectrometer as well as final data reduction and age calculations were done using LabSPEC software written by B. Idleman (Lehigh University). An age of 28.02 Ma (Renne et al., 1998) was used for the Fish Canyon Tuff sanidine flux monitor in calculating ages for samples.

For $^{40}Ar/^{39}Ar$ analyses, a plateau segment age is defined as consisting of three or more contiguous gas fractions having analytically indistinguishable ages (i.e., all plateau steps overlap in age ±2σ analytical error) and comprising a significant proportion of the total gas released (typically >50%). Total gas (integrated) ages are calculated by weighing by the amount of ^{39}Ar released, whereas plateau ages are weighted by the inverse of the variance. For each sample, inverse isochron diagrams are examined to check for the effects of excess argon. Reliable isochrons are based on the MSWD criteria of Wendt and Carl (1991) and, as for plateaus, must comprise contiguous steps and a significant fraction of the total gas released. All analytical data are reported at the confidence level of 1σ.

References

Renne PR, Swisher CC, Deino AL, Karner DB, Owens TL, DePaolo DJ (1998) Intercalibration of standards, absolute ages and uncertainties in $^{40}Ar/^{39}Ar$ dating. Chem Geol 145:117–152.

Staudacher TH, Jessberger EK, Dorflinger D, Kiko J (1978) A refined ultrahigh-vacuum furnace for rare gas analysis. J Phys E Sci Instrum 11:781–784.

Wendt I, Carl C (1991) The statistical distribution of the mean squared weighted deviation. Chem Geol 86:275–285.

APPENDIX F:

Procedure for Re-Os dating at the University of Alberta Radiogenic Isotope Facility

Molybdenite separates were prepared by pulverizing the vein samples in a porcelain disk mill, and molybdenite was separated from other sulfide and gangue phases using heavy liquid techniques, magnetic separation, and by flotation using high-purity water. Finally, molybdenite grains were handpicked under a binocular microscope.

The ^{187}Re and ^{187}Os concentrations in molybdenite were determined by isotope dilution mass spectrometry at the University of Alberta Radiogenic Isotope Facility. Dissolution of molybdenite separates and equilibration of sample and tracer Re and Os were done using the Carius tube method (Shirey and Walker, 1995).

Samples were dissolved and equilibrated with a known amount of ^{185}Re and isotopically normal Os in 3 ml of reverse aqua regia (2:1, 16 *N* HNO_3: 12 *N* HCl) at 240°C for 24 hours. Os and Re were separated by solvent extraction, microdistillation, and anion chromatography techniques (Selby and Creaser, 2004). The purified Os and Re fractions were loaded onto Ba-coated Pt filaments and measured with Faraday collectors using negative thermal ionization mass spectrometry (Creaser et al., 1991; Völkening et al., 1991) on a Micromass Sector 54 mass spectrometer. Total procedure blanks are on the order of <5 pg for Re, and <2 pg for Os.

Model Re-Os ages were calculated (after Stein et al. 2001) based on the equation: $t = \ln(^{187}\mathrm{Os}/^{187}\mathrm{Re} + 1)/\lambda$, where t is the model age, and λ is the ^{187}Re decay constant (1.666×10^{-11} a^{-1}; Smoliar et al. 1996). Errors (2σ) include uncertainties in Re and Os isotopic measurements, spike and standard Re and Os isotope compositions, calibration and gravimetric uncertainties of ^{185}Re and ^{187}Os, and uncertainties in the ^{187}Re decay constant. Uncertainties in weights of sample and tracer solution do not affect the calculated age and are not considered.

The molybdenite powder HLP-5 (Markey et al., 1998) is analyzed to assess the accuracy in Re-Os molybdenite age determinations. The average Re-Os age for this standard over a four-year period is 221.59 ± 0.45 Ma (1σ uncertainty, n = 11), which is identical to the value of 221.0 ± 1.0 Ma reported by Markey et al. (1998). The Henderson molybdenite standard is also analyzed to assess accuracy, and yielded an age of 27.71 ± 0.13 Ma in accord with the recommended age value (Markey et al., 2007).

References

Creaser RA, Papanastassiou DA, Wasserburg GJ (1991) Negative thermal ion mass spectrometry of osmium, rhenium and iridium. Geochim Cosmochim Acta 55:397–401.

Markey RJ, Stein HJ, Morgan JW (1998) Highly precise Re-Os dating for molybdenite using alkaline fusion and NTIMS. Talanta 45:935–946.

Markey RJ, Stein HJ, Hannah JL, Selby D, Creaser RA (2007) Standardizing Re-Os geochronology: A new molybdenite Reference Material (Henderson, USA) and the stoichiometry of Os salts. Chem Geol 244:74–87.

Selby D, Creaser RA (2004) Macroscale NTIMS and microscale LA-MC-ICP-MS Re-Os isotopic analysis of molybdenite: Testing spatial restrictions for reliable Re-Os age determinations, and implications for the decoupling of Re and Os within molybdenite. Geochim Cosmochim Acta 68:3897–3908.

Shirey SB, Walker RJ (1995) Carius tube digestion for low-blank rhenium-osmium analysis. Anal Chem 67:2136–2141.

Smoliar MI, Walker RJ, Morgan JW (1996) Re-Os ages of Group IIA, IIIA, IVA, and IVB iron meteorites. Science 271:1099–1102.

Stein HJ, Markey RJ, Morgan JW, Hannah JL, Scherstén A (2001) The remarkable Re–Os chronometer in molybdenite: how and why it works. Terra Nova 13:479–486.

Völkening J, Walczyk T, Heumann K (1991) Osmium isotope ratio determinations by negative ion mass spectrometry. Int J Mass Spectrom Ion Proc 105:147–159.

APPENDIX G:

Whole-rock geochemical data for the least-altered and altered rock samples from the Cevizlidere deposit

Sample →		**K-1427**	**K-4385**	**K-4403**	**K-4415**	**K-1180**	**K-1492**	**K-5425**	**K-7420**
Field name →	Method[1] ↓	Di. por.	Grd. por.	Di. por.	Di. por.	Di. por.	Grd. por.	Grd. por.	Grd. por.
		Least-altered				Altered			
Alteration		Wk. prop.	Wk. prop.	Wk. prop.	Wk. prop.	Mod. prop.	Mod. pot.	Wk. phy/ prop.	Mod. pot.
SiO_2 (wt.%)	Fusion-ICP	63.81	65.08	60.81	61.43	56.04	65.34	60.58	63.43
Al_2O_3	Fusion-ICP	15.67	15.86	15.93	15.93	15.78	15.58	15.29	14.72
$Fe_2O_{3(T)}$	Fusion-ICP	4.99	5.12	5.66	6.69	6.07	3.74	4.83	4.45
MnO	Fusion-ICP	0.007	0.054	0.008	0.047	0.021	0.025	0.006	0.034
MgO	Fusion-ICP	2.09	2.22	2.62	3.09	4.38	1.89	2.3	2.08
CaO	Fusion-ICP	4.22	4.65	4.58	4.69	6.04	3.86	4.5	4.07
Na_2O	Fusion-ICP	4.20	4.03	4.03	3.80	3.20	4.29	4.34	3.76
K_2O	Fusion-ICP	1.06	1.37	1.42	1.24	1.49	1.19	1.13	1.29
TiO_2	Fusion-ICP	0.428	0.465	0.501	0.548	0.596	0.418	0.426	0.393
P_2O_5	Fusion-ICP	0.12	0.13	0.11	0.14	0.14	0.11	0.1	0.11
LOI	Fusion-ICP	2.05	1.76	2.84	2.41	5.51	4.14	5.43	6.19
Total	Fusion-ICP	98.64	100.7	98.5	100.0	99.26	100.6	98.93	100.5
As (ppm)	INAA	< 1	< 1	2	< 1	< 1	< 1	< 1	< 1
Ba	Fusion-ICP	134	212	129	137	216	240	140	194
Be	Fusion-ICP	3	1	2	1	3	2	2	1
Co	INAA	10	7.3	11	11.9	15	6.5	13	9.1
Cr	INAA	53	57.4	103	67.1	219	43.5	69	44
Cs	Fusion-MS	0.5	0.4	0.5	0.4	1.7	0.5	0.4	0.3
Cu	TD-ICP	448	329	911	1040	39	2520	1410	2550
Ga	Fusion-MS	17	17	18	18	17	14	16	14
Ge	Fusion-MS	1.3	1.6	1.1	1.7	1.3	1.9	1.4	1.6
Hf	Fusion-MS	3	2.5	2.7	2.3	2.8	2.7	2.4	2.4
Nb	Fusion-MS	6.2	6.1	6.2	6.1	8	7.2	7	5.6
Ni	TD-ICP	13	14	15	24	47	13	18	15
Pb	TD-ICP	< 5	< 5	< 5	< 5	< 5	< 5	< 5	< 5
Rb	Fusion-MS	22	26	29	27	41	23	23	18
S (%)	TD-ICP	0.263	0.242	0.475	0.517	0.685	0.695	1.18	1.44
Sb	INAA	0.1	0.4	0.1	0.3	0.3	0.7	0.1	0.6
Sc	INAA	8.9	9.48	12.4	13.1	17.6	8.84	10.5	7.85
Se	INAA	0.5	< 0.5	0.5	< 0.5	0.5	< 0.5	0.5	< 0.5
Sn	Fusion-MS	1	< 1	3	< 1	2	2	2	3
Sr	Fusion-ICP	388	406	377	379	300	361	361	299
Ta	Fusion-MS	0.5	0.46	0.5	0.61	0.6	0.63	0.6	0.52
Th	Fusion-MS	5.02	5.15	4.18	4.28	4.48	6.15	4.7	4.93
U	Fusion-MS	0.77	0.96	0.82	0.81	1.36	1.66	1.01	0.75
V	Fusion-ICP	96	98	117	122	140	81	100	82
Y	Fusion-ICP	9	12	12	11	17	13	10	9
Zn	MULT	32	52	38	41	49	25	28	19
Zr	Fusion-MS	118	131	116	112	107	119	96	104
La	Fusion-MS	13.1	13	12.5	9.91	17.8	18.4	16.2	11.1
Ce	Fusion-MS	22.3	24.4	21.4	19.9	33.8	34.8	29.5	20.7
Pr	Fusion-MS	2.25	2.80	2.22	2.43	3.52	3.74	2.90	2.27
Nd	Fusion-MS	8.09	10.4	8.32	9.96	13.1	13.4	9.96	8.54
Sm	Fusion-MS	1.77	2.21	1.90	2.30	2.93	2.63	2.10	1.63
Eu	Fusion-MS	0.621	0.685	0.630	0.645	0.832	0.688	0.665	0.495
Gd	Fusion-MS	1.73	1.92	1.92	2.12	2.98	2.13	1.99	1.50
Tb	Fusion-MS	0.26	0.34	0.32	0.36	0.5	0.33	0.32	0.25
Dy	Fusion-MS	1.59	2.07	1.87	2.06	3.1	1.93	1.89	1.42
Ho	Fusion-MS	0.34	0.38	0.38	0.42	0.64	0.39	0.39	0.28
Er	Fusion-MS	1.03	1.19	1.17	1.32	1.93	1.16	1.18	0.85
Tl	Fusion-MS	0.26	0.14	0.27	0.21	0.63	0.36	0.21	0.17
Tm	Fusion-MS	0.155	0.196	0.182	0.210	0.291	0.200	0.182	0.136
Yb	Fusion-MS	1.04	1.40	1.20	1.39	1.88	1.38	1.22	0.96
Lu	Fusion-MS	0.174	0.214	0.194	0.220	0.292	0.206	0.197	0.146

Di = diorite, Grd = granodiorite, ICP = inductively-coupled plasma, INAA = instrumental neutron activation analysis, MS = mass spectrometry, MULT = multiple, Phy = phyllic, Por = porphyry, Pot = potassic, Prop = propylitic, TD = total dissolution, Wk = weak

APPENDIX H:

Ar-Ar isotopic data for samples from the Cevizlidere deposit. Errors reported as 1σ.

K-1427, Biotite, 2.40 mg, J = 0.001726 ± 0.17%

4 amu discrimination = 1.0523 ± 0.67%, 40/39K = 0.0205 ± 33.35%, 36/37Ca = 0.000267 ± 1.87%, 39/37Ca = 0.000691 ± 1.19%

step	T (C)	t (min.)	^{36}Ar	^{37}Ar	^{38}Ar	^{39}Ar	^{40}Ar	%^{40}Ar*	% ^{39}Ar rlsd	Ca/K	^{40}Ar*/^{39}ArK	Age (Ma)	1s.d.
1	720	12	7.518	0.101	2.714	16.202	2276.69	7.3	5.5	0.295925492	10.326552	31.87	3.09
2	810	12	0.407	0.027	1.802	21.246	293.414	62.4	7.2	0.060323354	8.537689	26.39	0.32
3	880	12	0.207	0.026	2.383	29.371	296.717	82.0	9.9	0.042019523	8.218414	25.41	0.26
4	930	12	0.249	0.027	1.677	20.728	237.915	72.8	7.0	0.061830884	8.202129	25.36	0.27
5	980	12	0.237	0.036	2.272	27.263	290.938	79.0	9.2	0.062679866	8.323625	25.73	0.26
6	1010	12	0.109	0.028	2.625	33.455	303.699	92.0	11.3	0.03972768	8.251637	25.51	0.23
7	1040	12	0.087	0.024	3.056	39.269	343.157	94.8	13.3	0.029010566	8.202129	25.36	0.23
8	1070	12	0.094	0.024	2.668	33.525	295.248	93.2	11.3	0.033981137	8.106383	25.07	0.22
9	1100	12	0.090	0.026	2.247	28.929	256.678	92.7	9.8	0.042661539	8.088473	25.01	0.23
10	1170	12	0.125	0.030	3.015	38.310	342.932	93.4	12.9	0.037171063	8.097591	25.04	0.22
11	1400	12	0.560	0.031	0.677	7.539	218.611	39.8	2.5	0.195193091	10.914886	33.67	0.59
								Cumulative %39Ar rlsd =	100.0		Total gas age =	25.95	0.16
note: isotope beams in mV, rlsd = released, error in age includes J error, all errors 1 sigma											Plateau age =	25.29	0.17
(^{36}Ar through ^{40}Ar are measured beam intensities, corrected for decay for the age calculations)												(steps 3-10)	
											Isochron age =	25.10	0.14
												(steps 2-10)	

K-4403, Biotite, 1.90 mg, J = 0.001715 ± 0.21%

4 amu discrimination = 1.0523 ± 0.67%, 40/39K = 0.0205 ± 33.35%, 36/37Ca = 0.000267 ± 1.87%, 39/37Ca = 0.000691 ± 1.19%

step	T (C)	t (min.)	^{36}Ar	^{37}Ar	^{38}Ar	^{39}Ar	^{40}Ar	%^{40}Ar*	% ^{39}Ar rlsd	Ca/K	^{40}Ar*/^{39}ArK	Age (Ma)	1s.d.
1	650	12	1.283	0.111	0.606	4.47	386.126	7	2.141830379	1.133317436	5.990500198	18.44	1.958
2	725	12	1.216	0.038	0.869	7.8	409.67	17	3.737422137	0.222283007	8.902462736	27.336	1.11
3	815	12	0.315	0.034	1.268	14.371	209.68	59.6	6.885960709	0.107942949	8.558670171	26.288	0.337
4	905	12	0.225	0.03	1.818	22.155	245.371	76.1	10.61571634	0.061779705	8.327509838	25.583	0.269
5	980	12	0.219	0.056	2.188	25.61	272.911	79.5	12.27120268	0.099765351	8.351441396	25.656	0.265
6	1040	12	0.206	0.122	5.644	67.802	617.008	91.6	32.4877815	0.082094924	8.330460252	25.592	0.235

7	1100	12	0.135	0.505	4.771	54.267	479.196	93.5	26.00239578	0.424618813	8.228515597	25.281	0.228
8	1150	12	0.078	0.065	0.818	9.172	97.231	90.4	4.394825108	0.323355139	8.256704323	25.367	0.24
9	1200	12	0.09	0.027	0.178	2.048	42.212	59.5	0.981312889	0.601589942	8.182629849	25.141	0.384
10	1400	12	0.324	0.047	0.157	1.007	105.486	20.6	0.482510781	2.130760228	14.76268325	45.107	1.971
								Cumulative %39Ar rlsd =	100.0009583		Total gas age =	25.55804708	0.203111647
note: isotope beams in mV, rlsd = released, error in age includes J error, all errors 1 sigma											Plateau age =	25.54366327	0.203566689
(^{36}Ar through ^{40}Ar are measured beam intensities, corrected for decay for the age calculations)											(steps 2-9)		
											Isochron age =	25.49	0.1
											(steps 2-9)		

K-7420, Biotite, 3.20 mg, J = 0.001722 ± 0.18%

4 amu discrimination = 1.0523 ± 0.67%, 40/39K = 0.0205 ± 33.35%, 36/37Ca = 0.000267 ± 1.87%, 39/37Ca = 0.000691 ± 1.19%

step	**T (C)**	**t (min.)**	**^{36}Ar**	**^{37}Ar**	**^{38}Ar**	**^{39}Ar**	**^{40}Ar**	**%^{40}Ar***	**% ^{39}Ar rlsd**	**Ca/K**	**^{40}Ar*/^{39}ArK**	**Age (Ma)**	**1s.d.**
1	720	12	8.529	0.273	3.199	23.068	2672.02	10.4	5.7	0.55070161	12.141782	37.33	2.41
2	810	12	0.911	0.027	2.148	29.444	508.377	50.3	7.3	0.04266427	8.675776	26.75	0.40
3	880	12	0.191	0.028	2.509	37.541	353.705	86.2	9.3	0.034701521	8.081804	24.93	0.24
4	930	12	0.157	0.024	2.340	35.154	323.010	88.2	8.7	0.031763798	8.019470	24.74	0.23
5	980	12	0.209	0.030	3.335	49.798	460.775	88.5	12.4	0.028028819	8.156548	25.16	0.24
6	1020	12	0.122	0.025	6.265	97.781	820.299	96.5	24.3	0.011895395	8.115095	25.04	0.22
7	1060	12	0.094	0.021	5.563	88.509	730.068	97.2	22.0	0.011038882	8.026323	24.76	0.22
8	1100	12	0.067	0.019	1.423	22.874	200.709	94.0	5.7	0.038646336	8.045251	24.82	0.22
9	1160	12	0.084	0.016	0.833	13.164	127.793	91.3	3.3	0.056549827	7.912767	24.42	0.24
10	1400	12	0.475	0.024	0.448	5.405	185.989	34.7	1.3	0.206601892	9.849477	30.34	0.86
								Cumulative %39Ar rlsd =	100.0		Total gas age =	25.83	0.17
note: isotope beams in mV, rlsd = released, error in age includes J error, all errors 1 sigma											Plateau age =	24.84	0.18
(^{36}Ar through ^{40}Ar are measured beam intensities, corrected for decay for the age calculations)											(steps 3-9)		
											Isochron age =	24.73	0.08
											(steps 2-10)		

APPENDIX I:

Representative EMPA compositions of selected Au-bearing sulfide and sulfosalt phases from the Çöpler deposit

Sample	C188027	C188027	C188011	C222	C222	C226	C224	C178
Mineral	Cp	Py	Asp	As-Py	Asp	Ten	Tet/ten	Py
Ore Type	CRO	CRO	CRO	Carb-sulf veinlet	Carb-sulf veinlet	Carb-sulf veinlet	Carb-sulf veinlet	Sooty py veinlet
Element (wt.%)								
Ag	0.035	-	0.094	0.14	0.031	0.253	0.835	0.006
Fe	29.44	44.02	33.16	46.8	38.85	0.886	0.927	45.6
Pb	0.152	0.199	0.324	0.267	0.279	0.101	0.156	0.211
As	0.044	0.035	44.13	1.34	26.69	18.19	12.07	0.028
Au	0.147	0.046	0.217	0.035	0.073	0.141	0.015	0.051
Sb	0.017	0.005	0.196	-	0.355	3.11	12.71	0.084
S	36.09	53.98	21.72	53.09	34.31	29.35	27.86	53.39
Cu	33.45	0.016	0.244	0.03	0.098	41.14	39.63	0.035
Zn	-	3.93	0.011	-	0.016	6.76	6.62	0
Total	99.375	102.231	100.095	101.702	100.702	99.931	100.823	99.405

Abbreviations: As-Py = arsenical pyrite, Asp = arsenopyrite, carb = carbonate, Cp = chalcopyrite, CRO = carbonate replacement ore, Py = pyrite, sulf = sulfur, Ten = tennantite, Tet = tetrahedrite

APPENDIX J:

Fluid inclusion data

Sample-chip-group #	Incl. #	Mineral	Vein type	P/PS	Type	Tm$_{ice}$ (°C)	Corr. Tm$_{ice}$ (°C)	Tm$_{sylvite}$ (°C)	Tm$_{halite}$ (°C)	Th$_{V\text{-}L}$ (°C)	NaCl (wt.%)	KCl (wt.%)	Total salinity (wt.% NaCl equiv.)	NaCl:KCl
126199-01-01	1	qz	B	P	HS1			214	378	374	32.4	27.8	60.2	1.2
	2	qz	B	P	HS1			145	424	403	41.1	19.0	60.1	2.2
	3	qz	B	P	HS1			135	418	398	40.7	18.3	59.0	2.2
	4	qz	B	P	HS1			131	380	380	36.1	19.4	55.5	1.9
126199-01-02	1	qz	B	P	HS1			131	387	379	37.0	19.1	56.1	1.9
	2	qz	B	P	HS1			130	384	368	36.6	19.2	55.8	1.9
	3	qz	B	P	HS1			130	379	351	36.0	19.4	55.3	1.9
	4	qz	B	P	HS1			130	381	375	36.2	19.3	55.5	1.9
	7	qz	B	P	HS1			128	412	379	40.1	18.0	58.1	2.2
126199-01-03	1	qz	B	P	HS1			128	386	373	36.9	18.9	55.8	2.0
	2	qz	B	P	HS1			128	416	376	40.7	17.7	58.4	2.3
	3	qz	B	P	HS1			128	385	359	36.9	18.9	55.7	2.0
	4	qz	B	P	HS1			127	386	364	37.0	18.7	55.8	2.0
	5	qz	B	P	HS1			125	418	399	41.0	17.5	58.5	2.3
	8	qz	B	P	HS1			125	394	318	38.1	18.3	56.4	2.1
	10	qz	B	P	HS1			125	347	390	32.6	19.9	52.5	1.6
	13	qz	B	P	HS1			124	341	397	32.1	20.0	52.1	1.6
126199-01-04	1	qz	B	PS	V	-2.4	-2.6				4.3		4.3	
	2	qz	B	PS	V	-1.6	-1.8				3.1		3.1	
	3	qz	B	PS	V	-1.7	-1.9				3.2		3.2	
	4	qz	B	PS	V	-1.9	-2.1				3.6		3.6	
	5	qz	B	PS	V	-3.2	-3.4				5.6		5.6	
	6	qz	B	P	HS1			124	405	372	39.4	17.8	57.2	2.2
	7	qz	B	P	HS1			123	408	379	39.9	17.6	57.5	2.3
	8	qz	B	PS	V	-1.6	-1.8				3.1		3.1	
	10	qz	B	PS	V	-3.2	-3.4				5.6		5.6	
	13	qz	B	PS	V	-2.5	-2.7				4.5		4.5	
126199-02-01	1	qz	B	P	V	-3.2	-3.4				5.6		5.6	
	2	qz	B	P	V	-3.3	-3.5				5.7		5.7	
	3	qz	B	P	HS1			123	385	345	37.0	18.5	55.5	2.0
	4	qz	B	P	HS1			122	377	362	36.1	18.6	54.7	1.9
	5	qz	B	P	HS1			122	382	362	36.7	18.4	55.1	2.0

Sample-chip-group #	Incl. #	Mineral	Vein type	P/PS	Type	Tm_{ice} (°C)	Corr. Tm_{ice} (°C)	$Tm_{sylvite}$ (°C)	Tm_{halite} (°C)	Th_{V-L} (°C)	NaCl (wt.%)	KCl (wt.%)	Total salinity (wt.% NaCl equiv.)	NaCl:KCl
	6	qz	B	P	HS1			122	365	381	34.7	19.0	53.7	1.8
	7	qz	B	P	HS1			121	428	434	42.6	16.7	59.3	2.6
126199-02-02	1	qz	B	PS	HS1			121	362	455	46.3	15.6	61.8	3.0
	2	qz	B	PS	HS1			120	414	383	40.7	17.1	57.8	2.4
	3	qz	B	PS	HS1			120	400	400	39.0	17.6	56.6	2.2
	4	qz	B	PS	HS1			118	351	383	33.4	19.0	52.5	1.8
	5	qz	B	PS	V	-2.4	-2.6				4.3		4.3	
	6	qz	B	PS	V	-3.0	-3.2				5.3		5.3	
	7	qz	B	PS	V	-2.2	-2.4				4.0		4.0	
126199-02-03	1	qz	B	PS	HS1			117	389	399	37.8	17.7	55.5	2.1
	2	qz	B	PS	HS1			116	380	348	36.8	17.8	54.6	2.1
	3	qz	B	PS	HS1			110	321	347	30.7	19.1	49.7	1.6
	4	qz	B	PS	HS1			110	394	326	38.6	16.9	55.5	2.3
	5	qz	B	PS	HS1			103	321	364	30.9	18.3	49.2	1.7
	6	qz	B	PS	HS1			78	320	380	32.1	15.5	47.6	2.1
	7	qz	B	PS	HS1			43	384	324	40.7	10.0	50.7	4.1
	8	qz	B	PS	V	-2.1	-2.3				3.9		3.9	
	9	qz	B	PS	V	-2.3	-2.5				4.2		4.2	
	10	qz	B	PS	V	-3.1	-3.3				5.4		5.4	
C225-09-01	1	qz	D	P	HS2				333	309	40.3		40.3	
	2	qz	D	P	HS2				335	331	40.5		40.5	
	3	qz	D	P	HS2				334	308	40.5		40.5	
	4	qz	D	P	HS2				326	336	39.9		39.9	
	5	qz	D	P	HS2				337	311	40.7		40.7	
	6	qz	D	P	HS2				340	326	40.9		40.9	
	7	qz	D	P	HS2				397	329	45.4		45.4	
	8	qz	D	P	HS2				320	359	39.4		39.4	
C225-09-02	1	qz	D	PS	HS2				348	379	41.6		41.6	
	2	qz	D	PS	HS2				345	371	41.3		41.3	
	3	qz	D	PS	HS2				348	367	41.5		41.5	
	4	qz	D	PS	HS2				348	361	41.5		41.5	
	5	qz	D	P	HS2				345	369	41.3		41.3	
	6	qz	D	P	HS2				364	361	42.8		42.8	
	7	qz	D	P	HS2				341	361	41.0		41.0	
C225-09-03	1	qz	D	P	HS2				341	362	41.0		41.0	
	2	qz	D	P	HS2				347	360	41.4		41.4	

Sample-chip-group #	Incl. #	Mineral	Vein type	P/PS	Type	Tm_{ice} (°C)	Corr. Tm_{ice} (°C)	$Tm_{sylvite}$ (°C)	Tm_{halite} (°C)	Th_{V-L} (°C)	NaCl (wt.%)	KCl (wt.%)	Total salinity (wt.% NaCl equiv.)	NaCl:KCl
	3	qz	D	P	HS2				353	363	41.9		41.9	
	4	qz	D	P	HS2				326	358	39.8		39.8	
	6	qz	D	P	HS2				357	356	42.2		42.2	
C225-10-01	1	qz	D	P	HS2				345	356	41.3		41.3	
	2	qz	D	P	HS2				361	359	42.6		42.6	
	3	qz	D	P	HS2				341	366	41.0		41.0	
	4	qz	D	P	HS2				335	360	40.5		40.5	
C225-10-02	1	qz	D	PS	HS1			124	323	372	30.2	20.5	50.7	1.5
	2	qz	D	PS	HS1			126	350	368	32.9	19.9	52.8	1.7
	3	qz	D	PS	HS1			131	379	363	36.0	19.4	55.4	1.9
	4	qz	D	PS	HS1			101	338	360	32.7	17.6	50.3	1.9
	5	qz	D	PS	HS1			120	358	356	33.8	19.1	53.0	1.8
	6	qz	D	PS	HS1			123	351	356	33.1	19.6	52.7	1.7
	7	qz	D	PS	HS1			125	374	353	35.7	19.0	54.7	1.9
	8	qz	D	PS	HS1			121	360	350	34.2	19.0	53.3	1.8
	9	qz	D	PS	HS1			129	364	348	34.4	19.7	54.1	1.7
C218-01-03	1	qz	PQS	PS	HS2				339	360	40.8		40.8	
	5	qz	PQS	PS	HS2				348	366	41.5		41.5	
	6	qz	PQS	PS	HS2				367	377	43.0		43.0	
	7	qz	PQS	PS	HS2				331	372	40.2		40.2	
	8	qz	PQS	PS	HS2				357	351	42.2		42.2	
C218-01-04	1	qz	PQS	P	HS2				352	289	41.9		41.9	
	2	qz	PQS	P	HS2				294	315	37.5		37.5	
C218-02-01	1	qz	PQS	P	HS2				313	312	38.9		38.9	
	2	qz	PQS	PS	HS2				284	313	36.8		36.8	
	3	qz	PQS	P	HS2				333	321	40.4		40.4	
	4	qz	PQS	PS	HS2				344	340	41.2		41.2	
C218-02-02	1	qz	PQS	PS	HS1			125	354	374	33.4	19.7	53.0	1.7
	2	qz	PQS	PS	HS1			114	334	344	31.8	19.1	50.9	1.7
	3	qz	PQS	PS	HS1			128	385	344	36.8	18.9	55.8	1.9
C218-03-01	1	qz	PQS	P	HS1			119	362	334	34.5	18.8	53.3	1.8
	2	qz	PQS	P	HS1			117	361	333	34.5	18.6	53.1	1.9
	3	qz	PQS	P	HS1			119	374	314	36.0	18.4	54.3	2.0
	4	qz	PQS	P	HS1			98	374	298	17.1	21.3	38.4	0.8
C214-04-01	1	Mn-ct	carb-sulf	PS	L1	-11.2	-11.4			294.6	15.4		15.4	
	2	Mn-ct	carb-sulf	PS	L1	-10.9	-11.1			287.5	15.1		15.1	

Sample-chip-group #	Incl. #	Mineral	Vein type	P/PS	Type	Tm$_{ice}$ (°C)	Corr. Tm$_{ice}$ (°C)	Tm$_{sylvite}$ (°C)	Tm$_{halite}$ (°C)	Th$_{V-L}$ (°C)	NaCl (wt.%)	KCl (wt.%)	Total salinity (wt.% NaCl equiv.)	NaCl:KCl
	3	Mn-ct	carb-sulf	PS	L1	-9.4	-9.6			316.9	13.5		13.5	
	4	Mn-ct	carb-sulf	PS	L1	-9.5	-9.7			257.9	13.6		13.6	
	5	Mn-ct	carb-sulf	PS	L1	-9.6	-9.8			284.3	13.7		13.7	
C214-04-02	1	Mn-ct	carb-sulf	PS	L1	-9.6	-9.8			269.8	13.7		13.7	
	2	Mn-ct	carb-sulf	PS	L1	-7.1	-7.3			287.9	10.9		10.9	
	3	Mn-ct	carb-sulf	PS	L1	-8.6	-8.8			285.6	12.6		12.6	
	4	Mn-ct	carb-sulf	PS	L1	-9.5	-9.7			283.4	13.6		13.6	
	5	Mn-ct	carb-sulf	PS	L1	-7.5	-7.7			304.4	11.3		11.3	
C214-04-03	1	Mn-ct	carb-sulf	PS	L1	-7.1	-7.3			289.9	10.9		10.9	
	2	Mn-ct	carb-sulf	PS	L1	-2	-2.2			302.1	3.7		3.7	
	3	Mn-ct	carb-sulf	P	L1	-6.3	-6.5			288.3	9.9		9.9	
	4	Mn-ct	carb-sulf	P	L1	-5.6	-5.8			249.4	8.9		8.9	
	5	Mn-ct	carb-sulf	P	L1	-5.1	-5.3			292.7	8.3		8.3	
	6	Mn-ct	carb-sulf	P	L1	-7.4	-7.6			289.1	11.2		11.2	
	7	Mn-ct	carb-sulf	PS	L1	-6.7	-6.9			308.9	10.4		10.4	
C214-03-01	1	Mn-ct	carb-sulf	PS	L1	-4.5	-4.7			286.7	7.5		7.5	
	2	Mn-ct	carb-sulf	PS	L1	-3.2	-3.4			290.3	5.6		5.6	
	3	Mn-ct	carb-sulf	PS	L1	-7.5	-7.7			285.5	11.3		11.3	
	4	Mn-ct	carb-sulf	PS	L1	-6.3	-6.5			291.8	9.9		9.9	
	5	Mn-ct	carb-sulf	PS	L1	-4.7	-4.9			282.7	7.7		7.7	
	6	Mn-ct	carb-sulf	PS	L1	-2.1	-2.3			269.8	3.9		3.9	
	7	Mn-ct	carb-sulf	PS	L1	-4.5	-4.7			284.5	7.5		7.5	
	8	Mn-ct	carb-sulf	P	L1	-6.5	-6.7			259.9	10.1		10.1	
C216-01-01	1	Mn-ct	carb-sulf	P	L1	-5.8	-6			262.1	9.2		9.2	
	2	Mn-ct	carb-sulf	P	L1	-2.7	-2.9			249.2	4.8		4.8	
	3	Mn-ct	carb-sulf	P	L1	-3.7	-3.9			270.9	6.3		6.3	
	4	Mn-ct	carb-sulf	P	L1	-3.8	-4			271.4	6.5		6.5	
	5	Mn-ct	carb-sulf	P	L1	-3.4	-3.6			257.5	5.9		5.9	
	7	Mn-ct	carb-sulf	P	L1	-5.3	-5.5			276.1	8.6		8.6	
C216-01-02	1	Mn-ct	carb-sulf	P	L1	-4.5	-4.7			262.9	7.5		7.5	
	2	Mn-ct	carb-sulf	P	L1	-4.6	-4.8			243.9	7.6		7.6	
	3	Mn-ct	carb-sulf	P	L1	-6.9	-7.1			253.1	10.6		10.6	
	4	Mn-ct	carb-sulf	P	L1	-3	-3.2			275.1	5.3		5.3	
C216-01-03	1	Mn-ct	carb-sulf	P	L1	-3.4	-3.6			253.8	5.9		5.9	
	2	Mn-ct	carb-sulf	P	L1	-6.5	-6.7			235.5	10.1		10.1	
	3	Mn-ct	carb-sulf	P	L1	-7.6	-7.8			289.3	11.5		11.5	

Sample-chip-group #	Incl. #	Mineral	Vein type	P/PS	Type	Tm$_{ice}$ (°C)	Corr. Tm$_{ice}$ (°C)	Tm$_{sylvite}$ (°C)	Tm$_{halite}$ (°C)	Th$_{V-L}$ (°C)	NaCl (wt.%)	KCl (wt.%)	Total salinity (wt.% NaCl equiv.)	NaCl:KCl
C222-01-01	1	sp	carb-sulf	PS	L1	-2.1	-2.3			283.2	3.87		3.87	
	2	sp	carb-sulf	P	L1	-2.9	-3.1			259.6	5.11		5.11	
	3	sp	carb-sulf	P	L1	-2	-2.2			281.7	3.71		3.71	
	4	sp	carb-sulf	P	L1					268.0				
C222-01-02	1	sp	carb-sulf	P	L1	-2.2	-2.4			272.8	3.87		3.87	
	2	sp	carb-sulf	P	L1	-6.8	-7			288.7	10.49		10.49	
	3	sp	carb-sulf	P	L1	-5.1	-5.3			261.1	8.28		8.28	
	4	sp	carb-sulf	P	L1	-3.8	-4			268.3	6.45		6.45	
C222-02-01	1	sp	carb-sulf	P	L1	-5.7	-5.9			268.5	9.08		9.08	
	2	sp	carb-sulf	P	L1					266.1				
	3	sp	carb-sulf	P	L1					268.4				
	4	sp	carb-sulf	P	L1					268.1				
	5	sp	carb-sulf	P	L1	-5.5	-5.7			265.1	8.81		8.81	
C222-03-01	1	sp	carb-sulf	P	L1	-4.3	-4.5			267.7	7.17		7.17	
	2	sp	carb-sulf	P	L1	-4.7	-4.9			268.2	7.73		7.73	
	3	sp	carb-sulf	P	L1					266.2				
C222-03-03	1	sp	carb-sulf	PS	L1	-5.7	-5.9			270.2	9.08		9.08	
	2	sp	carb-sulf	PS	L1	-6	-6.2			267.7	9.47		9.47	
	3	sp	carb-sulf	PS	L1					255.8				
	4	sp	carb-sulf	PS	L1					250.9				
	5	sp	carb-sulf	PS	L1					264.4				
	6	sp	carb-sulf	PS	L1					259.0				
C178-01-02	1	rea	sooty py	PS	L2	-4.2	-4.4			90.7	1.74		1.74	
	2	rea	sooty py	PS	L2	-6.3	-6.5			130.0	13.62		13.62	
	3	rea	sooty py	PS	L2	-8.1	-8.3			94.5	12.05		12.05	
	5	rea	sooty py	PS	L2	-5.3	-5.5			91.2	5.86		5.86	
C178-02-01	1	rea	sooty py	PS	L2	-4.5	-4.7			132.9	10.73		10.73	
	2	rea	sooty py	PS	L2	-9.2	-9.4			124.4	9.86		9.86	
C178-02-02	1	rea	sooty py	PS	L2	-4.1	-4.3			121.2	6.3		6.3	
	2	rea	sooty py	PS	L2	-3.6	-3.8			96.7	6.01		6.01	
	3	rea	sooty py	PS	L2	-5.8	-6.0			88.6	9.861		9.861	
C161-01-02	1	bar	sooty py	P	L2	-2.9	-3.1			129.7	8.55		8.55	
	2	bar	sooty py	PS	L2	-5.3	-5.5			113.9	8.55		8.55	
	3	bar	sooty py	PS	L2	-0.8	-1.0			95.7	6.88		6.88	
C161-02-01	1	bar	sooty py	PS	L2	-6.3	-6.5			88.6	5.11		5.11	
	2	bar	sooty py	PS	L2	-1.3	-1.5			104.6	2.57		2.57	

Sample-chip-group #	Incl. #	Mineral	Vein type	P/PS	Type	Tm_{ice} (°C)	Corr. Tm_{ice} (°C)	$Tm_{sylvite}$ (°C)	Tm_{halite} (°C)	Th_{V-L} (°C)	NaCl (wt.%)	KCl (wt.%)	Total salinity (wt.% NaCl equiv.)	NaCl:KCl
	3	bar	sooty py	P	L2	-3.5	-3.7			86.4	13.29		13.29	
C161-02-02	1	bar	sooty py	P	L2	-9.5	-9.7			111.4	9.34		9.34	
	2	bar	sooty py	P	L2	-3.8	-4.0			75.9	8.14		8.14	
	3	bar	sooty py	P	M	-3.4	-3.6			86.2	2.24		2.24	
	4	bar	sooty py	P	L2	-2.9	-3.1			76.2	6.45		6.45	
C228-01-02	1	bar	sooty py	P	L2	-5.9	-6.1			129.1	5.11		5.11	
	2	bar	sooty py	P	L2	-3.7	-3.9			80.7	1.7		1.7	
	3	bar	sooty py	P	L2	-5.1	-5.3			89.6	7.45		7.45	
	4	bar	sooty py	P	L2	-0.8	-1.0			92.1	4.8		4.8	
C228-05-02	1	bar	sooty py	P	L2	-4.1	-4.3			109.6	10.11		10.11	
	2	bar	sooty py	P	L2	-3.2	-3.4			98.7	8		8	
	3	bar	sooty py	P	L2	-1.1	-1.3			103.7	4.65		4.65	
C178-02-04	1	rea	sooty py	PS	M	-6.5	-6.7				1.23		1.23	
	2	rea	sooty py	PS	M	-0.5	-0.7				9.21		9.21	
	3	rea	sooty py	PS	M	-7.1	-7.3				5.56		5.56	
	4	rea	sooty py	PS	M	-4.5	-4.7				6.16		6.16	
	5	rea	sooty py	PS	M	-2.6	-2.8				7.45		7.45	
	6	rea	sooty py	PS	M	-2.7	-2.9				6.88		6.88	
C178-02-05	1	rea	sooty py	PS	M	-5.0	-5.2				7.02		7.02	
	2	rea	sooty py	PS	M	-2.6	-2.8				4.65		4.65	

Abbreviations: bar = barite, carb = carbonate, corr = corrected, Mn-ct = manganocalcite, incl = inclusion, P = primary, PQS = polymetallic quartz-sulfide, PS = pseudosecondary, py = pyrite, qz = quartz, rea = realgar, sp = sphalerite, sulf = sulfide